DYNAMICS OF DWARF GALAXIES

Satellite associations and internal kinematics as probes of ΛCDM



Mariana P. Júlio

Dynamics of dwarf galaxies

Satellite associations and internal kinematics as probes of ΛCDM

Mariana Pouseiro Júlio

Uni.-Diss.
zur Erlangung des akademischen Grades
“doctor rerum naturalium”
(Dr. rer. nat.)
in der Wissenschaftsdisziplin
Astrophysik

eingereicht an der
Mathematisch-Naturwissenschaftlichen Fakultät
Institut für Physik und Astronomie
der Universität Potsdam
und
Leibniz-Institut für Astrophysik Potsdam





Leibniz-Institut für Astrophysik Potsdam
1700 - 2025
325 Jahre

Betreuer:
Prof. dr. M.-R. Cioni
Leibniz-Institut für Astrophysik Potsdam / Universität Potsdam
Dr. M. S. Pawlowski
Leibniz-Institut für Astrophysik Potsdam

Gutatcher:
Prof. dr. M. Collins
University of Surrey
Dr. M. S. Pawlowski
Leibniz-Institut für Astrophysik Potsdam
Prof. dr. M. M. Roth
Leibniz-Institut für Astrophysik Potsdam / Universität Potsdam

Datum der Disputation:
Potsdam, 13.10.2026

Cover image: Visualisation of the Local Group, showing the Milky Way, Andromeda and some of their satellites galaxies. Adapted from Andrew Z. Colvin.

Summary

The standard cosmological model, Λ cold dark matter (ΛCDM), has been remarkably successful at describing the large-scale structure of the Universe. On the scales of galaxy clusters and beyond, its predictions are in excellent agreement with observations. However, on galactic and sub-galactic scales, a number of long-standing tensions persist, many of which are most clearly expressed in dwarf galaxies. These systems probe the smallest scales at which ΛCDM makes robust predictions and where the interplay between dark matter, baryonic physics, and environment becomes particularly complex.

Dwarf galaxies in the Local Group exhibit a diverse range of properties that challenge simple theoretical expectations. Their spatial distributions and orbital configurations around massive hosts raise questions about the hierarchical nature of structure formation, particularly in light of the observed coherence of satellite systems and the presence of close satellite associations. At the same time, their internal dynamics reveal unexpected regularities in empirical scaling relations established at higher masses, and allow us to place tight constraints on the nature of dark matter and on proposed alternatives to it. Together, these phenomena indicate that the challenges posed by dwarf galaxies are not independent, but are likely linked through common underlying physical processes, and must be studied in detail and in a consistent way.

This thesis uses dwarf galaxies as dynamical probes to investigate two of the most significant unsolved challenges at small scales. First, it explores phase-space correlations among satellite galaxies — namely pairs and groups — motivated by their potential role in shaping the spatial and kinematic structure of satellite systems in the Local Group. Using high-precision proper motion measurements, orbital modelling, and comparisons with cosmological simulations, this work explores observational evidence for such associations and evaluates whether their incidence and properties are consistent with expectations from hierarchical structure formation in ΛCDM. Second, this thesis analyses the internal mass distributions of low-mass dwarf galaxies in the context of the radial acceleration relation, extending it for the first time to radially resolved measurements at extremely low accelerations.

By addressing both the external and internal dynamics of dwarf galaxies, this thesis highlights them as unique laboratories for probing small-scale cosmology. It shows that satellite pairs and group infall in the Local Group are consistent with ΛCDM simulations, providing direct insight into the origin of phase-space correlations. It also presents the first radially resolved measurements of the radial acceleration relation in ultra-faint dwarfs, providing clear evidence for dark matter at extremely low accelerations. Together, these results bring us one step closer to understanding how galaxies form and evolve in a ΛCDM universe.

Zusammenfassung

Das Standardmodell der Kosmologie, Λ Cold Dark Matter (ΛCDM), hat sich als außerordentlich erfolgreich bei der Beschreibung der großskaligen Struktur des Universums erwiesen. Auf den Skalen von Galaxienhaufen und darüber hinaus stimmen seine Vorhersagen hervorragend mit Beobachtungen überein. Auf galaktischen und subgalaktischen Skalen bestehen jedoch seit langem einige Spannungen, von denen viele in Zwerggalaxien besonders deutlich zutage treten. Diese Systeme sondieren die kleinsten Skalen, auf denen ΛCDM robuste Vorhersagen macht und auf denen das Zusammenspiel von Dunkler Materie, baryonischer Physik und Umgebung besonders komplex wird.

Zwerggalaxien in der Lokalen Gruppe zeigen eine große Vielfalt an Eigenschaften, die einfachen theoretischen Erwartungen widersprechen. Ihre räumlichen Verteilungen und Bahnkonfigurationen um massereiche Wirtsgalaxien werfen Fragen zur hierarchischen Natur der Strukturbildung auf, insbesondere angesichts der beobachteten Kohärenz von Satellitensystemen und des Auftretens enger Satellitenassoziationen. Gleichzeitig offenbaren ihre internen Dynamiken unerwartete Regularitäten in empirischen Skalierungsrelationen, die bei größeren Massen etabliert wurden, und erlauben strenge Einschränkungen hinsichtlich der Natur der Dunklen Materie sowie vorgeschlagener Alternativen. Zusammengenommen deuten diese Phänomene darauf hin, dass die von Zwerggalaxien aufgeworfenen Herausforderungen nicht unabhängig voneinander sind, sondern wahrscheinlich durch gemeinsame zugrunde liegende physikalische Prozesse verknüpft sind und daher detailliert und konsistent untersucht werden müssen.

Diese Dissertation nutzt Zwerggalaxien und ihre Dynamik, um zwei der bedeutendsten ungelösten Probleme auf kleinen Skalen zu untersuchen. Erstens werden Phasenraumkorrelationen zwischen Satellitengalaxien — insbesondere Paare und Gruppen — analysiert, motiviert durch ihre mögliche Rolle bei der Prägung der räumlichen und kinematischen Struktur von Satellitensystemen in der Lokalen Gruppe. Mithilfe hochpräziser Eigenbewegungsmessungen, Bahnmodellierung und Vergleichen mit kosmologischen Simulationen untersucht diese Arbeit die beobachteten Hinweise auf solche Assoziationen und bewertet, ob ihre Häufigkeit und Eigenschaften mit den Erwartungen der hierarchischen Strukturbildung im Rahmen von ΛCDM vereinbar sind. Zweitens analysiert diese Dissertation die internen Massenverteilungen massearmer Zwerggalaxien im Kontext der Radialbeschleunigungsrelation und erweitert diese erstmals auf radial aufgelöste Messungen bei extrem niedrigen Beschleunigungen.

Durch die gemeinsame Betrachtung der externen und internen Dynamik von Zwerggalaxien hebt diese Arbeit ihre Rolle als einzigartige Laboratorien zur Untersuchung der Kosmologie auf kleinen Skalen hervor. Sie zeigt, dass Satellitenpaare und Gruppenakkretion in der Lokalen Gruppe mit ΛCDM-Simulationen vereinbar sind und direkte Einblicke in den Ursprung von Phasenraumkorrelationen liefern. Zudem präsentiert sie die ersten radial aufgelösten Messungen der Radialbeschleunigungsrelation in ultralichtschwachen Zwerggalaxien und liefert klare Hinweise auf Dunkle Materie bei extrem niedrigen Beschleunigungen. Zusammengenommen bringen diese Ergebnisse uns einen Schritt näher an das Verständnis, wie Galaxien in einem ΛCDM-Universum entstehen und sich entwickeln.

Contents

Summary iii

Zusammenfassung v

1 Introduction 1
- 1.1 The cosmological context 1
- 1.2 Small-scale problems in the ΛCDM paradigm 3
  - 1.2.1 The abundance of satellites 4
  - 1.2.2 Internal structure of dwarf galaxies 5
  - 1.2.3 The spatial and kinematic coherence of satellite galaxies 5
  - 1.2.4 Regularity in galaxy scaling relations 8
- 1.3 Dwarfs as tracers of structure formation 10
  - 1.3.1 How small can galaxies be? 10
  - 1.3.2 Insights from dwarf galaxy dynamics 12
  - 1.3.3 Stellar populations and evolutionary histories 15
  - 1.3.4 Dwarf galaxies as ideal laboratories for small-scale tests 15
- 1.4 Scope and structure of this thesis 15

Part I: External dynamics 17

2 Satellite group infall into the Milky Way: exploring the Crater-Leo case with new HST proper motions 19
- 2.1 Introduction 20
- 2.2 The proposed Crater-Leo group 22
  - 2.2.1 Properties 22
  - 2.2.2 Proper motions 24
  - 2.2.3 New HST proper motions of Leo IV and Leo V 24
- 2.3 Methods 26
  - 2.3.1 Lynden-Bell method 26
  - 2.3.2 Intrinsic scatter 28
  - 2.3.3 Looking for additional members 28
- 2.4 Results 29
  - 2.4.1 Orbital poles 29
  - 2.4.2 Predicted proper motions 29
  - 2.4.3 Removing Crater II 30
  - 2.4.4 Additional members 31
  - 2.4.5 Orbital dynamics 32
  - 2.4.6 Effect of the LMC on the orbital poles 36
- 2.5 Discussion and Conclusions 39

Acknowledgements 40

Appendix 41

- 2.A Intrinsic scatter 41
- 2.B Effect of the MW mass 42
- 2.C Additional members 42
- 2.D Orbital histories 43
- 2.E Effect of the LMC 43

3 Spatial and kinematic signatures of satellite pairs in the Local Group 45
- 3.1 Introduction 46
- 3.2 Data 47
  - 3.2.1 Observations 47

3.2.2 Simulations 48
3.3 Methods 49
3.4 Results and discussion 51
3.4.1 Statistical analysis 51
3.4.2 Pair candidates 53
3.4.2.1 Kinematic coherence 56
3.4.2.2 Mass similarity 56
3.4.2.3 Motion alignment 59
3.4.2.4 Gravitational binding 60
3.5 Conclusion 64
Acknowledgements 67
Appendices 68
3.A Cumulative radial distribution of simulations 68
3.B *P*-value distributions of opposite host analogues 68
3.C Kinematic coherence of pair candidates 69

Part II: Internal dynamics 73

4 The radial acceleration relation at the EDGE of galaxy formation: testing its universality in low-mass dwarf galaxies 75
4.1 Introduction 76
4.2 Data 77
4.2.1 Observational data 77
4.2.1.1 Dwarf spheroidals 78
4.2.1.2 MUSE-Faint dwarfs 78
4.2.2 EDGE simulation data 79
4.3 Methods 80
4.3.1 The radial relation acceleration 80
4.3.2 GravSphere 81
4.3.3 Priors 83
4.3.4 Recovering the RAR from mock data 83
4.4 Results 84
4.4.1 RAR of the observations 84
4.4.2 RAR of the EDGE simulations 85
4.5 Discussion 86
4.5.1 The origin of scatter in the RAR of low-mass dwarf galaxies 86
4.5.2 Comparing isolated EDGE dwarfs to observed satellite dwarfs 87
4.5.3 The external field effect 88
4.5.4 Challenges to interpretation 88
4.6 Conclusions 90
Acknowledgements 90
Appendices 91
4.A Adding rotation to GravSphere 91
4.B Additional sources of scatter 91
4.C GravSphere fits 92
4.D Tracer density profile 94
4.E Galaxies with gas 95

5 Conclusions 97

Bibliography 101

List of publications 113

Acknowledgements 115

1 Introduction

1.1 The cosmological context

Dark matter was originally introduced as a response to a sequence of observational inconsistencies that could not be explained within a Universe composed solely of baryonic matter. Early evidence came to light from studies of galaxy clusters, where the observed velocity dispersions of member galaxies implied gravitational potentials far deeper than those inferred from the luminous mass alone (Zwicky, 1933). On galactic scales, this discrepancy became even more striking with the measurement of rotation curves of spiral galaxies, which were found to remain approximately flat well beyond the stellar disc (Bosma, 1981; Rubin et al., 1980).

Over the decades following the first dynamical indications for dark matter, several lines of observational evidence led to the same conclusion: the majority of matter in the Universe does not emit, absorb, or scatter light, yet dominates gravitational dynamics. These include X-ray observations of hot intracluster gas, which revealed gravitational potentials far deeper than implied by the baryonic mass alone (e.g. Forman & Jones, 1982; Sarazin, 1986); gravitational lensing measurements providing direct, mappings of mass distributions independent of the dynamical state of the system (e.g. Tyson et al., 1990); the dynamics of galaxy groups and the Local Group itself (e.g. Kahn & Woltjer, 1959; Ostriker et al., 1974); and the observed growth of large-scale structure, which cannot be reproduced in a purely baryonic Universe (e.g. Blumenthal et al. 1984; Peebles 1982). Attempts to explain these phenomena through unseen baryonic components or observational systematics proved insufficient, motivating the introduction of a new, non-baryonic matter component: dark matter (see e.g. Bertone & Hooper 2018 for a historical overview).

As cosmological observations improved in precision and scope, it became clear that dark matter alone could not fully account for the observed properties of the Universe. Measurements of the anisotropies of the cosmic microwave background (CMB) revealed a spatially flat geometry and a total matter density well below the critical value (e.g. de Bernardis et al., 2000; Spergel et al., 2003), while observations of distant Type Ia supernovae demonstrated that cosmic expansion is accelerating (e.g. Perlmutter et al., 1999; Riess et al., 1998). Together, these findings pointed to the existence of an additional energy component with negative pressure, commonly modelled as a cosmological constant, Λ (e.g. Peebles & Ratra, 2003; Weinberg, 1989). The resulting Λ Cold Dark Matter (ΛCDM) model combines cold, collisionless dark matter with a cosmological constant and has, since then, been considered the standard model of cosmology, since it is able to simultaneously explain a broad range of independent observations. These include the successful predictions of Big Bang Nucleosynthesis (e.g. Olive et al., 2000; Wagoner et al., 1967), the detailed statistical properties of the CMB anisotropies (Planck Collaboration et al., 2016; Spergel et al., 2003), the large-scale distribution of galaxies (Peacock et al., 2001; Tegmark et al., 2004), and the observed matter–energy budget of the Universe (Planck Collaboration et al., 2016).

To make quantitative predictions for structure formation, the ΛCDM model is most commonly explored through cosmological N-body simulations, which follow the nonlinear gravitational evolution of collisionless dark matter from cosmological initial conditions. These simulations have proven remarkably successful at reproducing the large-scale distribution of matter, including the existence of filaments, haloes, and voids that characterise the cosmic web (Springel et al., 2006).

A central prediction of collisionless cold dark matter simulations is that dark matter haloes follow a universal density profile. Navarro et al. (1996b) demonstrated that haloes spanning a wide range of masses are well described by the Navarro-Frenk-White (NFW) profile,

$$\rho_{\rm CDM}(r) = \frac{\rho_0}{(r/r_s)(1 + r/r_s)^2}, \tag{1.1}$$

where r_s is the scale radius and ρ_0 is the characteristic density, which is expressed as

$$\rho_0 = \rho_{\rm crit}\, \Delta\, c_{200}^3 g_c / 3, \tag{1.2}$$

with $r_s = r_{200}/c_{200}$. Here $\rho_{\rm crit} = 3H^2/8\pi G$ is the critical density of the Universe, r_{200} is the virial radius enclosing a mean overdensity $\Delta \simeq 200$ relative to $\rho_{\rm crit}$, and c_{200} is the concentration parameter. This parameter quantifies the relative extent of the inner and outer regions of the halo and is not independent of halo mass: in ΛCDM simulations, lower-mass haloes are typically more concentrated than higher-mass haloes at fixed redshift (e.g. Dutton & Macciò, 2014; López-Cano et al., 2022; Neto et al., 2007). This is illustrated in Figure 1.1. The function g_c is defined as

$$g_c = \frac{1}{ln(1 + c_{200}) - c_{200}/(1 + c_{200})}. \tag{1.3}$$

This profile provides an excellent description of haloes in dark matter only simulations, being the reference to test deviations induced by baryonic effects.

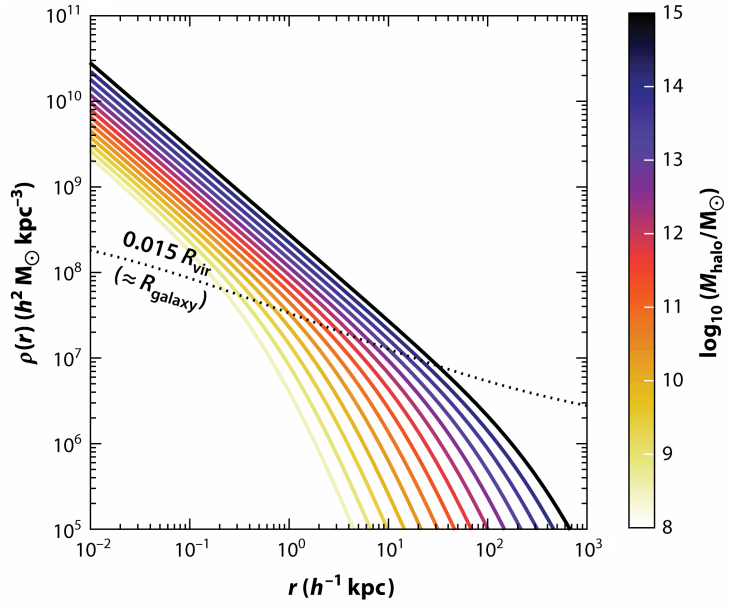


FIGURE 1.1: Median NFW density profiles at $z = 0$ for dark matter haloes spanning several orders of magnitude in virial mass. The profiles demonstrate the universal structure predicted by collisionless ΛCDM simulations and the mass dependence encoded in the concentration–mass relation. Adapted from Bullock & Boylan-Kolchin (2017).

Within the ΛCDM paradigm, structure grows hierarchically. This means that small objects are formed first and eventually collapse under the influence of their own gravity, merging with each other to form more massive and larger objects (e.g. White & Rees, 1978, Blumenthal et al., 1984). Figure 1.2 provides a visual example of this hierarchical growth, showing how a massive halo builds up over cosmic time through the successive merging of smaller structures in the Millennium-II Simulation (Boylan-Kolchin et al., 2009), a large N-body simulation of dark matter evolution in ΛCDM.

In this scenario, the small objects (satellites) can orbit their host halo, but will ultimately merge with it or be tidally disrupted by it (e.g. Gao et al., 2004). In this hierarchical scenario, a substantial fraction of low-mass haloes survive as bound substructures orbiting within larger host haloes. Analytical arguments and numerical simulations have shown that while many satellites are tidally stripped or disrupted, a significant population is expected to persist to the present day (Gao et al., 2004). High-resolution simulations of Milky Way (MW)–like haloes predict large numbers of surviving subhaloes (Springel et al., 2008) and indicate that a non-negligible fraction are accreted in groups rather than individually, a scenario already anticipated by Lynden-Bell (1976).

Despite its success on large and intermediate scales, ΛCDM faces persistent challenges on galactic and sub-galactic scales (see Bullock & Boylan-Kolchin, 2017; Sales et al., 2022 for a complete overview), where baryonic physics, and environmental processes become increasingly important. Dwarf galaxies, which inhabit low-mass dark matter haloes that form early and experience limited subsequent growth, are particularly sensitive to these effects, including stellar feedback, reionisation, and tidal interactions (Read et al., 2019; Simon, 2019). As the most dark matter dominated systems known,

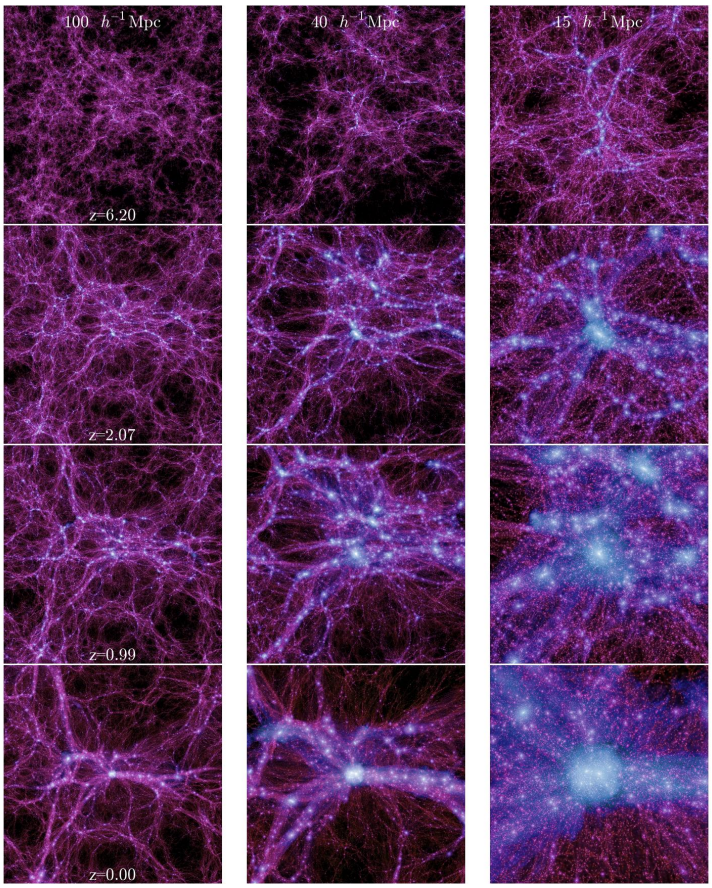


FIGURE 1.2: Example of hierarchical halo growth from Boylan-Kolchin et al. (2009). The panels show the formation of the most massive halo at four redshifts ($z = 6, 2, 1, 0$) and on three comoving scales (100, 40, and 15 Mpc/h, left to right). This sequence illustrates how small structures merge over time to form larger haloes, with surviving subhaloes representing satellites within the host at later times.

dwarf galaxies occupy a unique position for testing whether observed discrepancies arise from incomplete baryonic modelling or more fundamental limitations of ΛCDM (e.g. Bullock & Boylan-Kolchin, 2017).

1.2 Small-scale problems in the ΛCDM paradigm

A number of long-standing challenges, often referred to as the small-scale problems of ΛCDM, arise when comparing theoretical predictions to observations of dwarf galaxies and satellite systems (Bullock & Boylan-Kolchin, 2017; Sales et al., 2022). While none of these issues alone has yet conclusively falsified the standard model, their persistence motivates a careful and systematic investigation. These include:

- **Abundance of satellites:** dark matter only simulations predict far more low-mass subhaloes than the number of observed satellite galaxies around MW–like hosts, giving rise to the classical *missing satellites problem* (Klypin et al., 1999; Moore et al., 1999). More recently, improved observations of faint systems have revealed a complementary tension in which the observed number of dwarf galaxies appears to exceed theoretical expectations in certain environments, leading to the *too-many satellites problem* (Kanehisa et al., 2024; Müller et al., 2024).
- **Internal structure of dwarfs:** observations suggest shallower central density profiles than predicted by collisionless simulations, giving rise to the *core-cusp problem* (de Blok, 2010) and the *too-big-to-fail problem* (Boylan-Kolchin et al., 2011).
- **Spatial and kinematic coherence:** thin, coherent planes of satellites, such as around the MW (Pawlowski et al., 2012) and Andromeda (M31; Ibata et al., 2013), as well as the pronounced lopsidedness of the M31 satellite distribution (Kanehisa et al., 2025), challenge expectations from isotropic accretion in ΛCDM (e.g. Pawlowski, 2018).

- **Regularity in galaxy scaling relations:** galaxies from several mass ranges often follow surprisingly tight relations between stellar mass, size, and dynamical mass, which is unexpected in the stochastic regime of ΛCDM (e.g. McGaugh, 2004; McGaugh et al., 2016).

By focusing on these specific small-scale issues, the following sections explore how dwarf galaxies serve as probes of both baryonic processes and the underlying dark matter distribution. To address small-scale challenges to the ΛCDM paradigm, it is therefore essential to investigate the formation and dynamics of the lowest-mass structures in the Universe.

1.2.1 The abundance of satellites

One of the first identified challenges to the ΛCDM paradigm concerns the predicted abundance of low-mass dark matter haloes relative to the observed population of dwarf galaxies. Early dark matter only simulations of MW-like haloes showed a steeply rising subhalo mass function, implying the existence of hundreds to thousands of bound substructures with masses comparable to those expected to host dwarf galaxies (Klypin et al., 1999; Moore et al., 1999). In contrast, only a few dozen satellite galaxies were known around the MW at the time, giving rise to the so-called *missing satellites problem*.

Posterior observations have dramatically increased the census of faint dwarf galaxies, particularly through wide-field surveys such as the Sloan Digital Sky Survey (SDSS), the Dark Energy Survey (DES) and the Panoramic Survey Telescope & Rapid Response System (Pan-STARRS), resulting in the discovery of numerous ultra-faint dwarfs (Belokurov et al., 2007; Drlica-Wagner et al., 2015; Simon, 2019; Willman et al., 2005). In parallel, adding baryonic physics to theoretical models has shown that processes such as cosmic reionisation, stellar feedback, and tidal stripping can strongly suppress star formation in low-mass haloes, resulting in many dark subhaloes (Bullock et al., 2000; Sawala et al., 2016; Somerville, 2002). Taken together, and when corrected for sky coverage and detection limits, the inferred satellite luminosity function now appears broadly consistent with ΛCDM expectations (Koposov et al., 2008; Newton et al., 2018). As a result, the original tension has been substantially alleviated, and many consider it already solved.

However, there are still important tensions to solve between simulated dark matter subhaloes and observed dwarf galaxies. In particular, recent work has identified a complementary discrepancy referred to as the *too-many satellites problem* (e.g. Homma et al., 2024; Kanehisa et al., 2024; Li et al., 2026; Müller et al., 2024). This tension arises beyond the Local Group, where simulations calibrated to reproduce satellite populations in MW–like environments appear to underpredict the number of luminous satellites around certain nearby galaxies. These studies suggest that models calibrated to reproduce satellite populations in MW–like environments may not robustly capture the diversity of satellite systems across different host galaxies and environments. The discrepancy does not appear to be driven by obvious observational incompleteness or by resolution limits in current simulations, but instead points to uncertainties in the galaxy–halo connection, the stochasticity of star formation in low-mass haloes, and the environmental dependence of satellite survival.

The abundance of satellites is therefore not simply a question of counting objects, but of understanding how star formation, feedback, and environmental processes regulate which subhaloes are able to form and retain stars across different host galaxies. Proposed resolutions span several categories. Improved modelling of baryonic physics can suppress star formation and enhance satellite disruption through disc shocking and tidal stripping, reducing the number of surviving luminous satellites (Kelley et al., 2019; Sawala et al., 2016). Alternatively, modifications to the nature of dark matter, such as warm or self-interacting dark matter, can reduce the formation of low-mass haloes altogether, altering the predicted subhalo mass function at early times (Lovell et al., 2014; Vogelsberger et al., 2014). Observationally, deeper surveys and improved completeness corrections remain essential for establishing robust constraints on satellite populations beyond the Local Group (Drlica-Wagner et al., 2020). While uncertainties remain, the broad agreement between corrected satellite luminosity functions and ΛCDM predictions suggests that abundance alone is no longer the most severe small-scale challenge to the standard cosmological model (e.g. Sales et al., 2022). Instead, remaining discrepancies in satellite abundances appear to be highly sensitive to modelling choices, host-to-host variation, and observational selection effects. As such, they provide important context for galaxy formation physics, but are unlikely on their own to distinguish between competing cosmological models.

1.2.2 Internal structure of dwarf galaxies

Another tension between observations and ΛCDM predictions is about the internal mass distribution of dwarf galaxies. Dark matter only cosmological simulations predict that haloes follow centrally steep density profiles characterised by a power-law "cusp" towards the centre (Navarro et al., 1996b). In contrast, dynamical studies of dwarf galaxies often favour approximately constant-density inner regions, commonly referred to as "cores". This apparent discrepancy is known as the *core-cusp problem* and has been identified as one of the small-scale challenges to the standard cosmological model.

Closely related is the *too-big-to-fail* (TBTF) problem, which arises from the fact that the most massive subhaloes in ΛCDM simulations are denser than any of the observed classical dwarf spheroidal galaxies. These subhaloes are predicted to be massive enough to form stars and therefore should not have "failed" to produce visible galaxies, but observational counterparts with the required central densities are yet to be found (Boylan-Kolchin et al., 2011). While originally identified for satellites of MW–like hosts, similar discrepancies have also been reported for isolated dwarf galaxies in the field, where the inner dynamical masses are systematically lower than those predicted for haloes of comparable abundance (Ferrero et al., 2012; Garrison-Kimmel et al., 2014), showing that the TBTF problem extends beyond satellite systems. Together, the core-cusp and TBTF problems point to potential mismatches between the predicted inner structure of dark matter haloes and the observed kinematics of dwarf galaxies.

A wide range of explanations to solve these problems has been explored: one possibility is that systematic effects in the data or modelling assumptions bias the inferred inner density profiles. Limited spatial resolution, departures from dynamical equilibrium, triaxiality, and unmodelled velocity anisotropies can all affect mass estimates derived from stellar kinematics (e.g. Battaglia et al., 2013; de Blok, 2010; Genina et al., 2018; Hayashi & Chiba, 2012; Read & Steger, 2017). While such effects may be important in individual cases, extensive tests using mock observations suggest that they are unlikely to systematically transform cuspy haloes into cores across the dwarf galaxy population (Read et al., 2018).

A more radical possibility is that the nature of dark matter itself differs from the cold, collisionless assumption of ΛCDM. Models such as self-interacting dark matter naturally produce cored density profiles and can reduce central densities in massive subhaloes, offering an alternative explanation for both the core-cusp and TBTF problems (e.g. Elbert et al., 2015; Kaplinghat et al., 2016). Modified gravity theories have also been proposed as a means to explain dwarf galaxy dynamics without invoking dark matter (see Clifton et al., 2012, for a review), though such models face significant challenges across a wide range of astrophysical scales (e.g. Dodelson, 2011; Ibata et al., 2011; Natarajan & Zhao, 2008; Read et al., 2019).

Once again, perhaps the most plausible solution is the inclusion of baryonic physics in simulations. Hydrodynamical simulations have demonstrated that repeated, bursty episodes of star formation can drive rapid gas inflows and outflows, inducing fluctuations in the gravitational potential that transfer energy to dark matter particles and lower the central density (Fitts et al., 2019; Navarro et al., 1996a; Pontzen & Governato, 2012). This mechanism can simultaneously alleviate both the core-cusp and TBTF problems for galaxies with sufficiently extended star formation histories. However, the efficiency of this process depends strongly on stellar mass. In the ultra-faint dwarf regime ($M_\star \lesssim 10^5\ \mathrm{M}_\odot$; Simon 2019), where star formation is extremely limited, the available supernova energy is likely insufficient to significantly modify the dark matter distribution, and cuspy profiles are therefore expected to persist in ΛCDM (Orkney et al., 2021; Peñarrubia et al., 2012). Indeed, to date, no ultra-faint dwarf has been observed to exhibit a cored inner density profile.

Overall, baryonic physics appear capable of reconciling both the internal structure of dwarf galaxies with ΛCDM predictions and their abundance (Sales et al., 2022), but the continued study of dwarf galaxy kinematics is essential for solving other small-scale challenges.

1.2.3 The spatial and kinematic coherence of satellite galaxies

One of the most striking and persistent small-scale challenges to the ΛCDM paradigm is the apparent existence of thin, spatially flattened and kinematically coherent planes of satellite galaxies around several nearby hosts. The best-studied examples are found in the Local Group, where the high quality

of distance, velocity, and proper motion data allows detailed characterisation of satellite configurations (see Pawlowski, 2018, 2021b, for a review).

Around the MW, satellite galaxies are distributed in a highly anisotropic structure roughly perpendicular to the Galactic disc, commonly referred to as the Vast Polar Structure (VPOS; Pawlowski et al., 2012). The brightest satellites define a thin, disc-like configuration with a root-mean-square (RMS) thickness of $\sim$ 20–30 kpc, a radial extent of $\sim$ 250 kpc, and an axis ratio $c/a \simeq 0.2$–0.3 (Pawlowski et al., 2012; Pawlowski & Kroupa, 2020). Proper motion measurements indicate that many of these satellites share a common direction of orbital motion, suggesting phase-space coherence (Li et al., 2021; Taibi et al., 2024).

A comparable structure has been identified around M31, known as the Great Plane of Andromeda (GPoA; Conn et al., 2013; Ibata et al., 2013). Roughly half of M31's satellites lie within a thin plane with $c/a \sim 0.1$, exhibiting strong line-of-sight velocity coherence consistent with rotation (Ibata et al., 2013). Recent proper motion measurements support the interpretation that at least some satellites are co-orbiting within this structure (Casetti-Dinescu et al., 2024; Pawlowski & Tony Sohn, 2021; Sohn et al., 2020). In addition to its pronounced planar structure, the satellite system of M31 exhibits a marked spatial asymmetry. A large fraction of its satellites are preferentially located on the near side of the host with respect to the MW, resulting in a strongly lopsided distribution that is difficult to reconcile with expectations from isotropic accretion (Conn et al., 2013; Kanehisa et al., 2025; Savino et al., 2022). This asymmetry appears to be long-lived and statistically significant, further aggravating the challenge posed by the GPoA.

Beyond the Local Group, similarly flattened and kinematically correlated satellite systems have been reported around Centaurus A (Cen A satellite plane, CASP; Kanehisa et al., 2023b; Müller et al., 2021, 2018; Tully et al., 2015), and more recently around NGC 4490 (Karachentsev & Kroupa, 2024; Pawlowski et al., 2024). These satellite planes are represented in Figure 1.3. Systematic surveys of nearby galaxies, such as the MATLAS low-to-moderate density fields, have found that dwarf satellites around massive early-type hosts also exhibit flattened distributions, indicating that planar satellite arrangements may be a more general phenomenon beyond the Local Group (Heesters et al., 2021). While observational constraints outside the Local Group remain more limited, these systems suggest that planar structures may not be a unique feature of our surroundings.

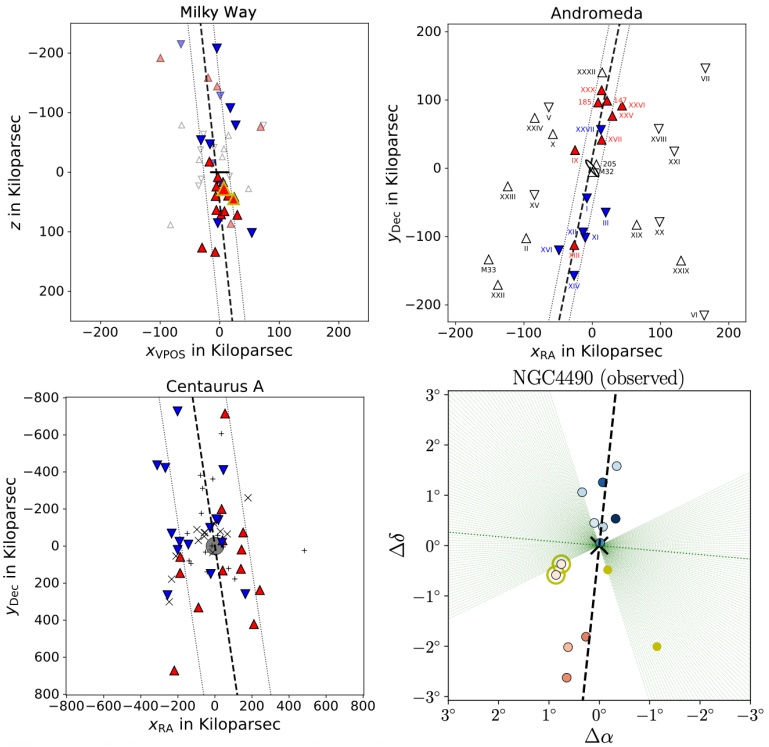


FIGURE 1.3: Edge-on views of prominent satellite planes around nearby galaxies: the Milky Way (VPOS), M31 (GPoA), Cen A (CASP), and NGC 4490 adapted from Pawlowski, 2018; Pawlowski et al., 2024. Colours indicate line-of-sight velocity relative to the host (blue/red), and dashed lines show the best-fitting planar structures. Together, these systems illustrate flattened satellite configurations with coherent kinematics in both the Local Group (top) and nearby galaxies (bottom).

Comparisons with cosmological simulations indicate that satellite systems as flattened and kinematically coherent as those observed are rare in ΛCDM. Studies focusing on MW analogues typically find that configurations matching both the spatial flattening and velocity coherence of the VPOS occur in

fewer than one in several hundred systems (Pawlowski, 2018, 2021b; Samuel et al., 2021). Similar conclusions have been reached for M31, Cen A and NGC 4490 analogues (Ibata et al., 2014; Müller et al., 2021; Pawlowski et al., 2024; Pawlowski & Tony Sohn, 2021). This apparent mismatch between observations and theoretical expectations has become known as the *planes of satellites problem* (see Pawlowski, 2018, 2021b, for a review).

A wide range of explanations has been proposed to account for the existence of satellite planes. These include anisotropic accretion along filaments of the cosmic web (Libeskind et al., 2011; Lovell et al., 2011), baryonic effects (Pawlowski et al., 2019, 2015a), perturbations induced by massive satellites such as the Large Magellanic Cloud (LMC; Garavito-Camargo et al., 2021; Pawlowski et al., 2022; Vasiliev, 2023), galaxy mergers (Kanehisa et al., 2023a; Smith et al., 2016), tidal dwarf galaxy scenarios (Banik et al., 2022; Fouquet et al., 2012; Pawlowski, 2021a), and accretion of satellites in groups (Li & Helmi, 2008; Metz et al., 2009b).

While each of these mechanisms can produce planar configurations under certain conditions, no single explanation consistently reproduces all observed properties across different hosts. As a result, the statistical significance, longevity, and broader cosmological relevance of satellite planes remain actively debated, particularly given the small number of well-characterised systems and the sensitivity of inferred properties to selection effects and analysis methods.

Among the proposed scenarios, group infall is a particularly promising mechanism for generating both correlated satellite orbits and flattened distributions in a natural cosmological context. However, its ability to reproduce the full range of observed spatial and kinematic properties has not yet been systematically investigated. Moreover, clear observational evidence for group infall within satellite systems remains limited, with the hierarchical Magellanic Clouds association representing the only well-established case to date. This scenario is discussed in more detail below.

Group infall as a possible origin of satellite planes

In the hierarchical structure formation paradigm, satellite galaxies are not necessarily accreted individually, but may fall into larger haloes as members of bound groups. Early simulations showed that such group infall events are a natural outcome of ΛCDM structure formation (D'Onghia & Lake, 2008; Li & Helmi, 2008).

Cosmological simulations predict that a substantial fraction of present-day satellites were accreted in groups. Estimates range from $\sim$ 20% in dark matter only simulations (Bakels et al., 2021) to 30–60% in hydrodynamical simulations, depending on satellite mass and host halo properties (Shao et al., 2018; Wetzel et al., 2015). Group infall fractions are generally higher for fainter satellites, suggesting that correlated structures may be most prominent in the ultra-faint dwarf regime.

Group infall has therefore been proposed as a mechanism capable of producing both the spatial flattening and kinematic coherence observed in satellite planes (D'Onghia & Lake, 2008; Li & Helmi, 2008; Metz et al., 2009b). This idea was anticipated observationally by Lynden-Bell (1976) and later discussed through phase-space arguments by Lynden-Bell & Lynden-Bell (1995), who showed that satellites accreted together should share similar specific angular momentum and energy, potentially retaining spatial and kinematic coherence for several gigayears.

The Magellanic system provides a nearby example of group accretion, with several ultra-faint dwarfs dynamically associated with the LMC (D'Onghia & Lake, 2008; Kallivayalil et al., 2018; Patel et al., 2020). Cosmological models predict that LMC-mass haloes should host several satellites of their own (Dooley et al., 2017; Jahn et al., 2019), broadly consistent with current observational constraints.

Despite its appeal, clear observational evidence for past group infall events beyond the Magellanic system remains scarce. Proposed satellite associations in the MW and M31 have largely relied on spatial and line-of-sight velocity correlations (Fattahi et al., 2013; Lynden-Bell, 1982), with only limited confirmation from proper motion measurements (Sohn et al., 2020). As a result, the role of group infall in shaping satellite planes remains an open question, motivating systematic comparisons between observed systems and cosmological simulations.

1.2.4 Regularity in galaxy scaling relations

A longstanding challenge for galaxy formation in the ΛCDM model is the existence of tight empirical scaling relations linking baryonic galaxy properties to their observed dynamics. Relations connecting stellar mass, luminosity, size, surface brightness, metallicity, and characteristic velocities are observed across many orders of magnitude in mass and across diverse galaxy morphologies. In a cosmological model where galaxies form through hierarchical assembly, stochastic accretion histories, and complex baryonic physics, such regularity is not an obvious outcome (e.g. Bullock & Boylan-Kolchin 2017).

Classical examples include the Tully–Fisher relation for rotationally supported galaxies (Tully & Fisher, 1977) and the Faber–Jackson relation for pressure-supported systems (Faber & Jackson, 1976), which relate stellar luminosity or baryonic mass to characteristic velocities that probe the depth of the gravitational potential, implying a close coupling between stellar content and halo mass.

More generally, a variety of galaxy scaling relations indicate that galaxy structure and dynamics follow tight empirical correlations, despite the expected sensitivity to feedback, mergers, environment, and halo assembly history (e.g. McGaugh, 2004; McGaugh et al., 2016). Within the ΛCDM framework, these relations are commonly interpreted as the outcome of the coupled evolution of baryons and dark matter haloes, rather than as fundamental laws directly linking mass and dynamics (Dutton et al., 2010; Sales et al., 2022). However, reproducing this level of regularity across the full galaxy population, particularly in the low-mass, dark matter dominated regime, remains an ongoing challenge for galaxy formation models.

A prominent and widely discussed example is the family of relations connecting baryonic mass distributions to dynamical accelerations, including the mass discrepancy acceleration relation (McGaugh, 2004) and its spatially resolved form, the radial acceleration relation (RAR; Lelli et al. 2017; McGaugh et al. 2016), which relates the baryonic and total accelerations at each radius within individual galaxies. These relations imply a close, nearly one-to-one correspondence between baryonic and total gravitational acceleration over a wide dynamic range. While correlations of this kind can arise in ΛCDM as a consequence of galaxy–halo scaling relations (e.g. Garaldi et al. 2018; Ludlow et al. 2017; Tenneti et al. 2018), reproducing their tightness, characteristic acceleration scale, and apparent universality has proven challenging.

Figure 1.4 illustrates the RAR over nearly eight orders of magnitude in baryonic acceleration. The left panel shows the original RAR as derived from resolved rotation curves of late-type galaxies, where the total gravitational acceleration at each radius closely follows that expected from the baryonic mass distribution (McGaugh et al., 2016). This relation shows remarkably low scatter over a wide range of galaxy masses and surface brightnesses. The right panel extends this relation to dwarf spheroidal galaxies (dSphs), for which $g_{\rm obs}$ is estimated from stellar velocity dispersions rather than rotation curves (Lelli et al., 2017). Classical dwarfs tend to occupy a region broadly consistent with the extrapolation of the RAR defined by more massive galaxies, while ultra-faint show larger deviations, which, as argued by Lelli et al. (2017), can be due to both observational uncertainties and the greater susceptibility of these galaxies to non-equilibrium effects.

This behaviour highlights the important role of dwarf galaxies in understanding the physical origin of galaxy scaling relations. The persistence of correlations between baryons and dynamics (McGaugh, 2004; McGaugh et al., 2016) into the low-acceleration regime (Lelli et al., 2017) places tight constraints on models of galaxy formation within ΛCDM, while the increased scatter and systematic uncertainties observed in dwarf systems mark the regime where the robustness and origin of these relations can be tested. As the most dark matter dominated and least evolved galaxies, dwarfs therefore are crucial systems to distinguish between baryonic processes, halo assembly effects, or even potential departures from the standard gravitational framework (Famaey & McGaugh, 2012; Milgrom, 1983).

Testing cosmology with dwarf galaxies

Taken together, the small-scale challenges to the ΛCDM paradigm highlight a recurring theme: the formation and evolution of the smallest galaxies seem to be driven by a balance between dark matter, baryonic physics, and environment that is not yet fully understood. Tensions related to the abundance of satellite galaxies, their internal mass distributions, their spatial and kinematic coherence, and their obedience to (or deviations from) empirical scaling relations are often discussed separately, yet they

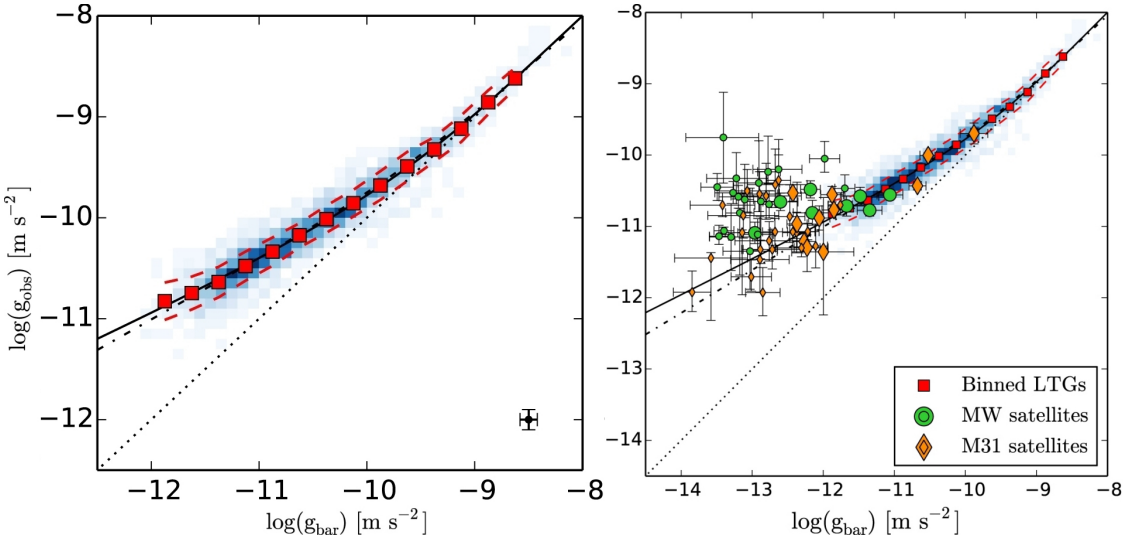


FIGURE 1.4: Radial acceleration relation (RAR) across a wide range of galaxy masses. **Left:** The resolved RAR for late-type galaxies, showing the relation between the observed gravitational acceleration, $g_{\rm obs}$, inferred from rotation curves, and the baryonic acceleration, $g_{\rm bar}$, computed from the distribution of stars and gas adapted from McGaugh et al. (2016). **Right:** Extension of the RAR to dSphs using stellar kinematic data adapted from Lelli et al. (2017). Circles and diamonds distinguish Milky Way and M31 satellites, respectively; large symbols denote classical dwarfs, while smaller symbols indicate ultra-faint and more isolated systems.

are deeply connected.

Many of the proposed solutions invoke baryonic processes such as cosmic reionisation, stellar feedback, and tidal interactions, which are expected to be most effective in low-mass systems (e.g. Bullock & Boylan-Kolchin, 2017; Read et al., 2018; Sales et al., 2022). Others require environmental effects, anisotropic accretion, or group infall (e.g. Pawlowski, 2018, 2021b), while more radical explanations explore modifications to the nature of dark matter (e.g. **Júlio et al.**, 2023) or gravity itself (e.g. Milgrom, 1983). But these mechanisms are not independent: the same physical processes that suppress star formation may reshape inner density profiles, influence orbital coherence, and might even be the ones that introduce scatter into scaling relations.

A useful summary of the current status of these issues is provided by Sales et al. (2022), who classify the historical and present-day tensions between ΛCDM predictions and dwarf galaxy observations after accounting for known baryonic effects (Figure 1.5). In this framework, some long-standing problems — such as the missing satellites and core–cusp tensions — are substantially alleviated, while others persist as more severe challenges. Notably, the diversity of galaxy rotation curves and the existence of spatially and kinematically coherent satellite structures are identified as among the strongest remaining tensions with the standard cosmological model.

These two challenges are particularly compelling because they probe complementary aspects of dwarf galaxy physics. The diversity of rotation curves directly tests the connection between baryonic components and dark matter haloes, as inferred by empirical relations such as the radial acceleration relation (RAR), especially in the low-acceleration regime inhabited by dwarf galaxies. In contrast, the presence of satellite planes and correlated satellite orbits probes the hierarchical assembly of galaxies, the role of anisotropic accretion, and the importance of group infall in shaping satellite systems.

Dwarf galaxies therefore occupy a unique position in this debate. Their shallow potential wells amplify the impact of feedback and environmental effects (e.g. Mayer et al., 2006; Pontzen & Governato, 2012; Read et al., 2006), while their large numbers and diversity of formation histories provide a statistically significant test bed (e.g. Tolstoy et al., 2009; Weisz et al., 2014a) in which competing theoretical models can be assessed (e.g. Fitts et al., 2019). Moreover, the dwarf galaxies regime displays multiple small-scale problems simultaneously, so they are a unique laboratory for distinguish whether observed tensions arise from incomplete modelling of baryonic physics, environmental preprocessing, or more fundamental shortcomings of the standard cosmological model (e.g. Bullock & Boylan-Kolchin, 2017; Simon, 2019).

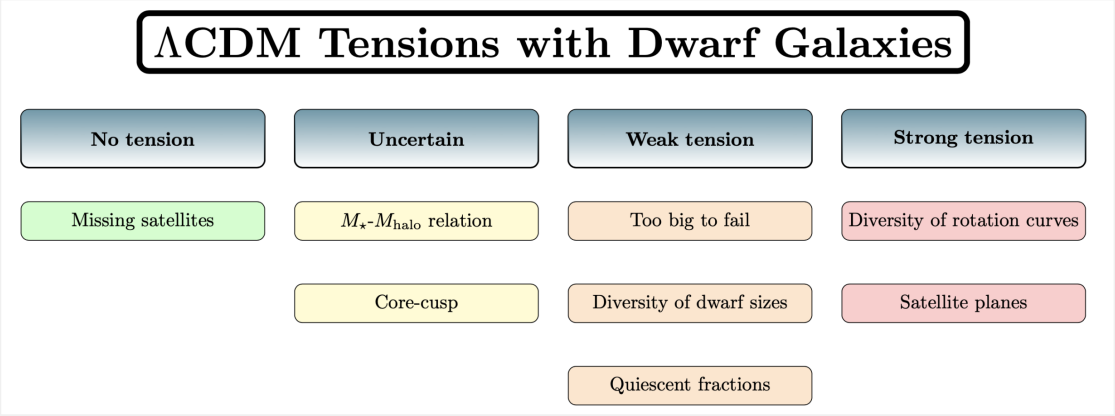


FIGURE 1.5: Historical and current tensions between ΛCDM theory and observations of dwarf galaxies taken from Sales et al. (2022). These tensions are classified according to the level of tension/challenge they present to the cosmological ΛCDM scenario, after the critical effects of baryonic physics have been considered.

1.3 Dwarfs as tracers of structure formation

Unlike more massive galaxies, where baryons dominate the central potential (e.g. Lelli et al., 2016), dwarf galaxies are strongly dark matter dominated even in their inner regions (Read et al., 2019; Walker et al., 2009b), providing a more direct connection between observed kinematics and the underlying gravitational potential. This allows us to test dark matter halo structure, the efficiency and impact of baryonic feedback, and the role of environment in shaping galaxy evolution (e.g. Fitts et al., 2019; Genina et al., 2022; Read et al., 2019). Furthermore, dwarf galaxies span a wide range of environments — from isolated field systems to satellites embedded within the influence of their massive hosts (see Figure 1.6) — allowing to study the influence of tidal forces, ram-pressure stripping, and group preprocessing on galaxy properties.

The Local Group offers an unparalleled opportunity in this regard. Its proximity allows dwarf galaxies to be resolved into individual stars, enabling detailed measurements of stellar populations, chemical abundances, internal velocity dispersions, and, increasingly, full six-dimensional phase-space information through proper motions (see McConnachie, 2012; Pace, 2025, for a review). Combined with the rapidly growing census of faint and ultra-faint dwarf galaxies from deep photometric surveys (e.g. Belokurov et al., 2007; Chiti et al., 2022; Drlica-Wagner et al., 2015), these data now allows us to perform statistical studies of dwarf galaxy populations alongside detailed case-by-case dynamical analyses. For all of these reasons, dwarf galaxies provide an important bridge between theoretical predictions and observational tests of galaxy formation and cosmology on the smallest galactic scales.

1.3.1 How small can galaxies be?

For much of the history of extragalactic astronomy, only a handful of dwarf galaxies were known. For centuries, the MW was believed to host just two satellite galaxies, the Large and Small Magellanic Clouds, visible to the naked eye and recognised as external stellar systems long before the nature of galaxies was fully understood (Von Humboldt, 1859). The first faint dwarf spheroidal galaxies were not identified until the early twentieth century, when photographic surveys led to the discoveries of Sculptor and Fornax (Shapley, 1938). By the late twentieth century, the census of MW satellites had grown slowly, reaching eleven known systems with the discovery of the Sagittarius dwarf galaxy (Ibata et al., 1994). Among them, Draco had the lowest integrated luminosity, with an absolute magnitude of $M_V \approx -8.8$ and a stellar mass of $M_\star \sim 5 \times 10^5$ $M_\odot$ (Mateo, 1998).

As observational capabilities improved, similar populations of dwarf galaxies were identified throughout the Local Group and nearby galaxy groups (McConnachie, 2012; Pace, 2025). Dwarf galaxies are now understood as the smallest and most numerous galactic systems, typically with stellar masses $M_\star \sim 10^3$–10^8 $M_\odot$ (Mateo, 1998; McConnachie, 2012; Simon, 2019), though new surveys and deeper instruments continue to uncover even fainter and lower-mass systems, pushing the boundaries of what we define as a galaxy.

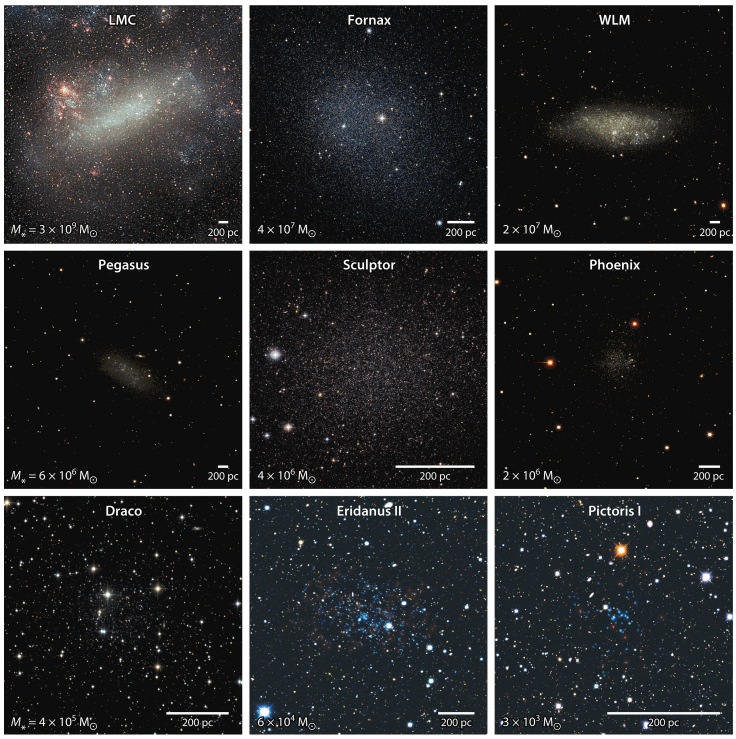


FIGURE 1.6: Dwarf galaxies spanning six orders of magnitude in stellar mass, from the Large Magellanic Cloud to ultra-faint systems, taken from Bullock & Boylan-Kolchin (2017). Gas-rich and star-forming dwarf irregulars (LMC, WLM and Pegasus) and gas-free dwarf spheroidals and ultra-faint dwarfs (the remaining six) illustrate the wide diversity of dwarf galaxy properties.

The past two decades have transformed this picture with the arrival of wide-field digital sky surveys. Beginning in 2005, analyses of the SDSS imaging revealed much fainter MW satellites, more than doubling the known population within just two years (Simon, 2019). Together with Pan-STARRS and DES, these surveys enabled systematic searches for low surface brightness stellar overdensities, leading to the discovery of dozens of new satellite galaxies around the MW and M31. These efforts revealed an entirely new population of ultra-faint dwarf galaxies (UFDs), defined as systems with $M_V \gtrsim -7.7$ (Simon, 2019), extending the galaxy luminosity function to very low luminosities. However, this definition is clearly dynamic: recent discoveries continue to push the limits to even fainter systems. The Ultraviolet Near-Infrared Optical Northern Survey (UNIONS) identified Ursa Major III/UNIONS 1, currently the faintest known MW satellite with $M_V \approx +2.2$ and a stellar mass of only $\sim 16\ M_\odot$ (Smith et al., 2024). Whether UMa3/U1 is a dark matter dominated dwarf galaxy or an extremely faint star cluster remains under investigation, illustrating that the boundary between galaxies and globular clusters continues to blur. These discoveries have increased the known population of MW satellites to ~ 60 systems.

Figure 1.7 shows this rapid increase in the number of known MW satellites, illustrating the impact of wide-field digital surveys on the discovery of faint galaxies. Regardless of this progress, the census remains incomplete, particularly at low surface brightness, large Galactocentric distances, and behind the obscuring Galactic disc. Despite their low luminosities, dwarf galaxies are extremely dark matter dominated, with mass-to-light ratios ranging from ~ 10 to several hundred $M_\odot/L_\odot$ (Walker et al., 2009b). Their compact sizes and large numbers make them ideal tracers of host galaxy potentials and of the small-scale structure predicted by ΛCDM.

The current census of dwarf galaxies is expected to expand dramatically in the near future. Upcoming surveys and instruments such as Legacy Survey of Space and Time (LSST), deeper *Gaia* data releases, and next-generation spectroscopic instruments will probe unprecedented volumes and surface-brightness limits, uncovering previously undetected UFDs and improving statistical constraints on the low-mass end of the galaxy population (Drlica-Wagner et al., 2020; Newton et al., 2018). Beyond the Local Group, the James Webb Space Telescope (JWST) and Euclid will allow resolved stellar population studies of faint galaxies at greater distances.

Together, these developments have transformed dwarf galaxies from previously sparsely known systems into a key component of near-field cosmology. Their abundance, extreme dark matter content, and sensitivity to both internal feedback and environmental effects place them at the boundary of galaxy formation, where the predictions of ΛCDM are most challenged by observations.

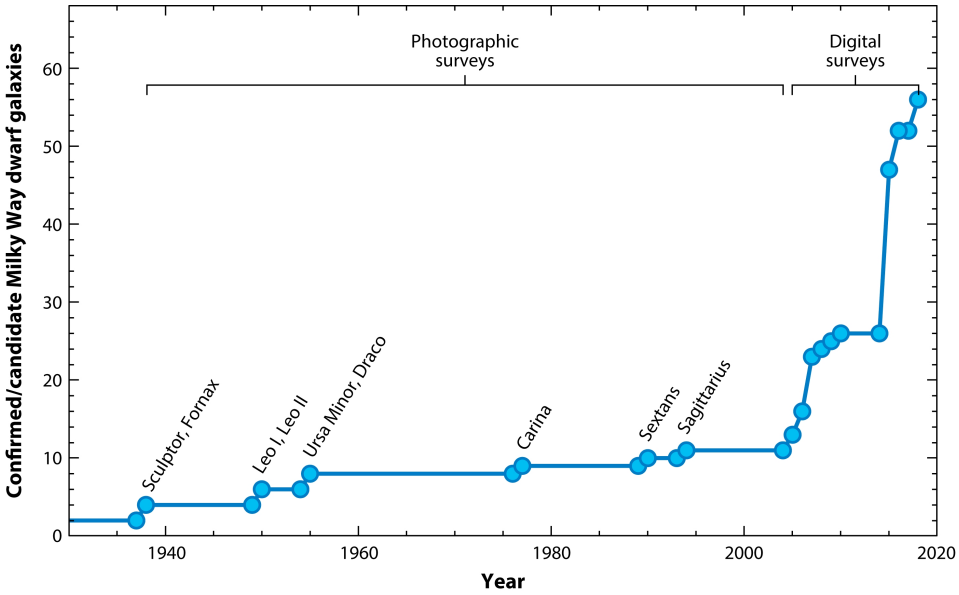


FIGURE 1.7: Census of MW satellite galaxies over time, taken from Simon (2019). The plot includes all spectroscopically confirmed dwarfs, as well as systems suspected to be dwarfs based on less conclusive spectroscopic or photometric evidence up to 2019. The contributions of wide-field digital sky surveys are highlighted here.

1.3.2 INSIGHTS FROM DWARF GALAXY DYNAMICS

From a dynamical perspective, two regimes are particularly informative. On larger scales, the orbits of dwarf galaxies within their host potential reflect their accretion histories, group infall, and exposure to environmental processes such as tides and ram pressure (e.g. Garavito-Camargo et al., 2021; Lynden-Bell, 1976; Pawlowski, 2018). On smaller scales, the internal motions of stars within dwarf galaxies probe the distribution and nature of dark matter in the lowest-mass haloes known (e.g. Fitts et al., 2019; Read et al., 2019; Walker et al., 2009b). Together, these two aspects allow us to connect the present-day properties of dwarf galaxies to their formation and evolution within ΛCDM.

The analysis of proper motions, orbital properties, and internal kinematics of dwarf galaxies provides multiple cosmological insights. By measuring the mass and density profiles of low-mass haloes, we can constrain the inner structure of dark matter haloes and test longstanding issues such as the core–cusp problem (Read et al., 2019; Walker et al., 2009b). The phase-space distributions of satellites, including evidence for group infall, constrain models of hierarchical accretion and the formation of planar satellite configurations (Lynden-Bell, 1976; Pawlowski, 2018). Scaling relations, such as those connecting stellar mass and velocity dispersion or luminosity and metallicity, probe the efficiency of galaxy formation in low-mass haloes (Kirby et al., 2013). In addition, environmental effects including ram-pressure stripping, tidal heating, and disruption shape the evolution of satellites and the spatial distribution of their stellar content (Fillingham et al., 2016; Simon, 2019). Dwarf galaxy dynamics therefore play a central role in determining whether observed discrepancies arise from baryonic processes, environmental effects, or more fundamental shortcomings in the underlying cosmological model (e.g, Bullock & Boylan-Kolchin, 2017; Sales et al., 2022; Sawala et al., 2016).

In the following subsections, we first discuss how proper motions allow the reconstruction of dwarf galaxy orbits and their interaction histories. We then turn to the internal dynamics of dwarf galaxies, introducing the methods used to infer their dark matter content.

PROPER MOTIONS AND ORBITAL DYNAMICS

The arrival of high-precision astrometric data, particularly from the spaced-based telescopes HST and *Gaia*, has enabled the measurement of proper motions for numerous dwarf galaxies in the Local Group (Fritz et al., 2018; Gaia Collaboration et al., 2018). Proper motions, combined with line-of-sight velocities $v_{\rm los}$ and distances D, allow the reconstruction of the full three-dimensional velocity

vector of a galaxy. The tangential velocity components in km s^{-1} along right ascension (RA) and declination (Dec) are given by

$$v_\alpha = 4.74047\, \mu_\alpha\, cos\, \delta\, D, \quad v_\delta = 4.74047\, \mu_\delta\, D, \tag{1.4}$$

where μ_α and μ_δ are the proper motions (PMs) in mas yr^{-1}, D is the distance in kpc, and velocities are in km s^{-1} (Johnson & Soderblom, 1987). Combined with the line-of-sight (LOS) velocity, these components define the velocity vector in the local equatorial frame. Once the full velocity vector $\mathbf{v}$ is known, the orbit of a satellite in a host galaxy's gravitational potential $\Phi(\mathbf{r})$ can be integrated:

$$\frac{d^2\mathbf{r}}{dt^2} = -\nabla\Phi(\mathbf{r}), \tag{1.5}$$

where $\Phi(\mathbf{r})$ typically includes contributions from multiple components of the host galaxy, such as a dark matter halo, a stellar disc, and a bulge (e.g. Binney & Tremaine, 2011; Watkins et al., 2010). Integrating this equation returns the satellite's orbit over time, allowing the determination of quantities such as pericentre, apocentre, orbital eccentricity, and inclination. These orbital parameters provide insight into a satellite's dynamical history (e.g. Fritz et al., 2018; Lux et al., 2010).

Before the space-based astrometry from HST and *Gaia*, only a limited number of proper motions for Local Group satellites were measurable from the ground. Early photographic plate studies provided absolute motions for the Magellanic Clouds (e.g., Jones et al., 1994), and long-baseline ground programs later measured proper motions for individual dwarf galaxies such as Fornax and Draco (e.g., Casetti-Dinescu & Girard, 2016; Méndez et al., 2010). However, most dynamical studies remained dependent on line-of-sight velocities alone, which probe only one component of motion and introduce strong degeneracies in mass and orbital anisotropy (Binney & Mamon, 1982). For the MW, PMs have allowed detailed studies of satellite orbits (Battaglia et al., 2022; Fritz et al., 2018; Simon, 2018), satellites of satellites scenarios (Kallivayalil et al., 2018; Patel et al., 2020) and improved constraints on the Galactic potential and total mass (Fritz et al., 2020; Posti & Helmi, 2019). Recent HST studies have also measured internal PMs of stars in nearby dwarfs, providing the first direct constraints on internal velocity anisotropies and departures from equilibrium (e.g. Vitral et al., 2024, 2026). Although currently limited to nearby systems and the brightest stars, these measurements demonstrate the feasibility of fully three-dimensional modelling (discussed in more detail below). Beyond the MW, HST PMs of M31 satellites (Casetti-Dinescu et al., 2024, 2025; Sohn et al., 2012, 2020) are extending these analyses to an external galaxy, opening the door to comparative studies of satellite dynamics and group infall in a different environment.

Future *Gaia* data releases and next-generation facilities such as JWST, LSST and the Nancy Grace Roman Space Telescope, will extend high-precision astrometry to fainter stars and more distant satellites, allowing increasingly robust tests of dark matter halo structure, environmental effects, and the small-scale predictions of ΛCDM.

Internal dynamics and dark matter content

The internal dynamics of dwarf galaxies provide some of the strongest constraints on the nature and distribution of dark matter on small scales. Due to their extreme dark matter content, the gravitational potentials of dwarf galaxies are only weakly affected by baryonic components, making them particularly unique laboratories for dynamical studies of dark matter haloes. As a result, the structure of their dark matter haloes, including the inner density profile, is expected to be largely determined by the fundamental properties of dark matter.

The motions of stars in dwarf galaxies are governed by collisionless dynamics. As demonstrated by Binney & Tremaine (2011), the mean free path between stellar encounters in galaxies exceeds the age of the Universe by many orders of magnitude. As a result, stellar systems can be accurately described by the collisionless Boltzmann equation, which fully specifies the evolution of the stellar distribution function $f(\mathbf{x}, \mathbf{v}, t)$ in a gravitational potential $\Phi(\mathbf{x}, t)$:

$$\frac{\mathrm{d}f}{\mathrm{d}t} = \frac{\partial f}{\partial t} + \nabla_{\mathbf{x}} f \cdot \mathbf{v} - \nabla_{\mathbf{v}} f \cdot \nabla_{\mathbf{x}} \Phi = 0. \tag{1.6}$$

For systems in dynamical equilibrium, the explicit time dependence vanishes, $\partial f / \partial t = 0$. In principle, if the full six-dimensional phase-space coordinates of the stellar component were known, Equation 1.6 would provide a complete description of the system. In practice, however, the distribution function is six-dimensional and cannot be directly recovered from observations, because full 6D phase-space information is available for only a small subset of nearby systems. To make progress, simplified moment-based approaches are commonly adopted.

By integrating Equation 1.6 over velocities and assuming spherical symmetry and negligible rotation, one arrives at the Jeans equation (Jeans, 1922),

$$\frac{1}{\nu}\frac{\partial}{\partial r}\left(\nu\sigma_r^2\right) + \frac{2\beta(r)\sigma_r^2}{r} = -\frac{GM(<r)}{r^2}, \tag{1.7}$$

which relates the total enclosed mass $M(<r)$ to the radial velocity dispersion $\sigma_r(r)$, the tracer density profile $\nu(r)$, and the velocity anisotropy $\beta(r)$. Here,

$$\sigma_r^2 = \langle v_r^2 \rangle - \langle v_r \rangle^2, \tag{1.8}$$

with moments defined as $\langle v_r^n \rangle = \int v_r^n f \, \mathrm{d}^3\mathbf{v}$, while the tracer density is given by

$$\nu(r) = \int f \, \mathrm{d}^3\mathbf{v}. \tag{1.9}$$

The velocity anisotropy parameter,

$$\beta(r) \equiv 1 - \frac{\sigma_t^2(r)}{\sigma_r^2(r)}, \tag{1.10}$$

describes whether there is a preferred direction in the kinematics, with $\beta = 0$ corresponding to isotropy, $\beta > 0$ to radially biased orbits, and $\beta < 0$ to tangentially biased motion. Solving Equation 1.7 yields the radial velocity dispersion profile

$$\sigma_r^2(r) = \frac{1}{\nu(r)g(r)}\int_r^\infty \frac{GM(\tilde{r})\nu(\tilde{r})}{\tilde{r}^2} g(\tilde{r}) \, \mathrm{d}\tilde{r}, \tag{1.11}$$

where

$$g(r) = exp\left(2\int \frac{\beta(r)}{r}\mathrm{d}r\right). \tag{1.12}$$

In most observational studies of dwarf galaxies, however, only LOS velocities are available for individual stars. Consequently, the Jeans equation must be projected along the line of sight, leading to an expression for the observable velocity dispersion profile,

$$\sigma_{\mathrm{LOS}}^2(R) = \frac{2}{\Sigma_\star(R)}\int_R^\infty \left(1 - \beta\frac{R^2}{r^2}\right)\frac{\nu(r)\sigma_r^2(r)r}{\sqrt{r^2 - R^2}}\mathrm{d}r, \tag{1.13}$$

where $\Sigma_\star(R)$ is the projected surface density of the tracer population.

While LOS velocity measurements have enabled precise dynamical mass estimates for dwarf galaxies, they suffer from a fundamental degeneracy between the mass profile $M(<r)$ and the velocity anisotropy $\beta(r)$ (Binney & Mamon, 1982; Wolf et al., 2010). This mass–anisotropy degeneracy limits the ability to distinguish between cuspy and cored dark matter distributions, contributing to uncertainties in the interpretation of small-scale discrepancies such as the core–cusp and too-big-to-fail problems (Evans et al., 2009; Read et al., 2019; Walker & Peñarrubia, 2011). In addition, unresolved departures from equilibrium, such as tidal heating or streaming motions, can further bias inferences based solely on projected kinematics (Klimentowski et al., 2007; Muñoz et al., 2008; Read et al., 2006). An additional complication arises from the presence of unresolved binary stars, whose internal orbital motions can broaden the observed LOS velocity distribution and thus inflate measured velocity dispersions if not properly accounted for (e.g. Hargreaves et al., 1996; Mateo, 1998; Minor et al., 2010). This effect can be particularly significant in low-mass, low-dispersion systems such as ultra-faint dwarf galaxies (e.g. McConnachie & Côté, 2010; Spencer et al., 2018, 2017b).

The increasing availability of proper motion measurements for individual stars in nearby dwarf

galaxies is a powerful tool to overcome these limitations. By directly constraining the tangential components of stellar velocities, proper motions provide access to the full three-dimensional kinematics of the stellar population. This additional information breaks long-standing degeneracies in Jeans-based modelling, allows for direct tests of equilibrium assumptions, and for more robust constraints on the inner structure of dwarf galaxy dark matter haloes (Read & Steger, 2017; van der Marel, 1994). As such, proper motions mark a fundamental shift in the study of dwarf galaxy internal dynamics.

1.3.3 Stellar populations and evolutionary histories

Despite their low masses, dwarf galaxies exhibit a remarkable diversity of stellar populations and star formation histories (e.g. Tolstoy et al., 2009). In the Local Group, resolved stellar photometry allows detailed reconstructions of these histories, revealing systems that formed most of their stars early, others with extended or episodic star formation, and some that retain gas and continue forming stars to the present day (Skillman et al., 2017; Weisz et al., 2014a,b). Their chemical abundance patterns further trace the impact of feedback, enrichment, and gas loss over cosmic time (Kirby et al., 2011; Revaz & Jablonka, 2018; Venn et al., 2004).

Stellar population studies show that these evolutionary pathways are shaped by a combination of internal processes and environmental influences. Some dwarf galaxies appear to have been quenched shortly after reionisation (e.g. Brown et al., 2014), while others sustained star formation over several gigayears before being affected by tides, ram-pressure stripping, or satellite infall (e.g. Fillingham et al., 2016; Mayer et al., 2006). This diversity highlights the sensitivity of dwarf galaxies to both their formation history and subsequent interactions with their surroundings.

By linking star formation histories and chemical abundances to orbital properties and internal mass distributions, stellar populations provide essential context for interpreting dwarf galaxy dynamics. In particular, they allow tests of whether observed structural and kinematic features are consistent with feedback-driven evolution or instead require additional environmental or dynamical explanations.

1.3.4 Dwarf galaxies as ideal laboratories for small-scale tests

Taken together, their abundance, extreme dark matter content, and sensitivity to both internal and external processes make dwarf galaxies ideal laboratories for testing the predictions of ΛCDM on the smallest accessible scales (Bullock & Boylan-Kolchin, 2017; Simon, 2019). In the Local Group, where distances, proper motions, and individual stellar properties can now be measured with unprecedented precision. As a result, dwarf galaxies provide some of the strongest empirical constraints on models of structure formation, making this an especially timely opportunity to test ΛCDM on small scales (see e.g. Strigari, 2018, for a review).

By studying their numbers, dynamics, scaling relations, spatial organisation, and even stellar formations histories, it becomes possible to understand whether the observed small-scale tensions arise from incomplete astrophysical modelling, observational limitations, or more fundamental limitations of the standard cosmological paradigm (Bullock & Boylan-Kolchin, 2017).

As new observational facilities continue to expand the census of dwarf galaxies and improve the precision of existing measurements, the Local Group is transitioning from a small sample into a more complete and statistically robust laboratory. Moreover, the first dynamical and proper motion measurements for dwarf galaxies beyond the Local Group are now becoming available. This transformation opens the door to systematic tests of ΛCDM predictions in regimes that were previously inaccessible.

In the following chapters, the dynamical information available for dwarf galaxies to investigate these questions in detail is explored.

1.4 Scope and structure of this thesis

Dwarf galaxies in the Local Group occupy a privileged position in the current studies of galaxy formation and cosmology. As the most dark matter dominated systems known, and as remnants of the earliest stages of structure formation, they provide a uniquely powerful laboratory for testing both the internal predictions of ΛCDM and its predictions for the hierarchical assembly and orbital structure of satellite systems. Many of the small-scale tensions between theory and observations — including

the spatial and kinematic organisation of satellite systems and the internal dynamical behaviour of low-mass galaxies — are manifested in dwarfs, and, particularly, in satellite galaxies.

This thesis presents three first-author studies on the dynamical and structural properties of Local Group satellite dwarf galaxies, carried out in collaboration with co-authors. Together, they investigate two classes of small-scale challenges that remain particularly persistent within ΛCDM, even after accounting for baryonic physics. The first covers the orbital coherence and spatial correlations of satellite galaxies, which we call satellite planes. I look at group infall and the incidence of close satellite pairs as possible explanations, which test the hierarchical assembly and accretion history of MW–like haloes. The second has to do with the internal dynamics of dwarf galaxies, specifically the relation between their baryonic content and total gravitational potential, which provides a powerful probe of dark matter on the smallest galactic scales and a critical test of alternative theories of gravity.

By combining precise proper motion measurements, orbital modelling, statistical comparisons with cosmological simulations, and resolved dynamical analyses of individual dwarf galaxies, this work aims to investigate whether the observed properties of dwarfs can be reconciled with ΛCDM once baryonic physics and environmental effects are taken into account, or whether they instead point to limitations of existing theoretical models.

The following Chapters are structured around different small-scale challenges to ΛCDM. Together, they examine the external and internal dynamics of dwarf galaxies, from satellite pairs and group infall to radially resolved measurements of the radial acceleration within faint and ultra-faint systems.

Chapter 2 is based on **Júlio et al.** (2024) and presents a detailed dynamical study of a proposed satellite group infall event into the Milky Way, focusing on the Crater-Leo objects. Using new HST proper motions in combination with *Gaia* data, this chapter tests whether the observed phase-space coherence of these objects is consistent with a cosmologically expected group accretion scenario, offering new insight into the possible origins of satellite planes.

Chapter 3 broadens the environmental perspective by revisiting the incidence and properties of satellite galaxy pairs in the Local Group. By combining updated observational catalogues with mock observations of high-resolution constrained cosmological simulations, this chapter explores whether the observed frequency and characteristics of close satellite associations are consistent with ΛCDM expectations, and explores the role of environment and satellite-satellite interactions in shaping satellite populations.

Chapter 4 is based on **Júlio et al.** (2025b) and shifts the focus to the internal dynamics of dwarf galaxies, investigating the validity of the RAR at the lowest galaxy masses. Using resolved stellar kinematics and Jeans modelling to infer mass distributions in nearby dwarf galaxies, this chapter tests whether the tight coupling between baryons and dynamics observed in more massive systems extends to the edge of galaxy formation, and analyses the implications for dark matter and alternative gravity theories.

Together, these studies provide a coherent investigation of how dwarf galaxies challenge, constrain, and ultimately shed light on our understanding of ΛCDM on the smallest galactic scales. The final chapter summarises the main conclusions of the thesis and discusses prospects for future observational and theoretical work.

Part I: External dynamics

2

Satellite group infall into the Milky Way: exploring the Crater-Leo case with new HST proper motions

Context. Within Λ cold dark matter (ΛCDM) simulations, Milky Way-like galaxies accrete some of their satellite galaxies in groups of 3-5 members rather than individually, and this has been suggested as a possible mechanism driving the formation of satellite planes. Objects accreted in groups are expected to share similar specific total energy and angular momentum, and to also have identical orbital planes and directions.
Aims. Looking at observations of Milky Way satellites, the dwarf galaxies Leo II, IV, V, and Crater II, and the star cluster Crater 1 were proposed to be a vestige of group infall. The suggested 'Crater-Leo group' shows a coherent distance gradient and all these objects align along a great circle on the sky. We used proper motion data to investigate whether the phase-space distribution of the members of the proposed group are indeed consistent with group infall.
Methods. To further investigate this possibility, we used *Gaia* Data Release 3 (DR3) and new *Hubble* Space Telescope (HST) proper motions — namely, $(\mu_{\alpha*}, \mu_\delta) = (-0.1921 \pm 0.0514, -0.0686 \pm 0.0523)$ mas yr^{-1} for Leo IV and $(\mu_{\alpha*}, \mu_\delta) = (0.1186 \pm 0.1943, -0.1183 \pm 0.1704)$ mas yr^{-1} for Leo V — to derive accurate orbital properties for the proposed group objects. In addition, we explored other possible members of this putative association.
Results. Leo II, Leo IV, Leo V, and Crater 1 show orbital properties consistent with those we predict from assuming group infall. However, our results suggest that Crater II was not accreted with the rest of the objects. If confirmed with increasingly accurate proper motions in the future, the Crater-Leo objects would appear to constitute the first identified case of a cosmologically expected, typical group infall event, as opposed to the highly hierarchical Magellanic Cloud system.

M. P. Júlio, M. S. Pawlowski, S. Tony Sohn, S. Taibi, R. P. van der Marel, & S. S. McGaugh (July 2024). "Satellite group infall into the Milky Way: Exploring the Crater-Leo case with new HST proper motions". In: *A&A* 687, A212. DOI: 10.1051/0004-6361/202449985.

2.1 Introduction

The standard model of cosmology known as Λ-cold dark matter (ΛCDM) predicts that structure grows hierarchically. This means that small objects are formed first and eventually collapse under the influence of their own gravity, merging with each other to form more massive and larger objects (e.g. Blumenthal et al., 1984; White & Rees, 1978). In this scenario, the small objects — satellites — can orbit their host halo, but will ultimately merge with it or be tidally disrupted by it (e.g. Gao et al., 2004). Looking at the formation and evolution of galaxies in ΛCDM simulations, a large number of these satellites were found to survive to the present day (e.g. Springel et al., 2008) and it was shown that many of them were accreted in groups onto Milky Way-like haloes, a scenario Lynden-Bell (1976) proposed before the advent of ΛCDM.

Indeed Li & Helmi (2008) find in simulations[1] that at least one-third of the present-day satellites fell in groups and typically that these groups consist of three to five satellites of similar masses, contrary to the Magellanic Cloud (MC) system. Wheeler et al. (2015) used high-resolution hydrodynamical simulations to show that low-luminosity galaxies are expected to host luminous galaxies of their own. Wetzel et al. (2015) estimate significant group infall fractions (30% – 60%). This would suggest that 18-36 of the known $\approx$ 60 satellite galaxies of the Milky Way (MW) are likely to have been part of some group before being accreted onto its halo. If we also consider the globular clusters and assume a similar fraction, this number increases to 60-120 of the total objects ($\approx$ 210). Shao et al. (2018) used two different types of hydrodynamical simulations to study group and filamentary dwarf galaxy accretion into MW mass haloes. These authors find that only 14% of the present-day 11 most massive satellites were accreted in pairs, 14% in triplets, and that higher groups were extremely unlikely. However, these numbers increase for fainter satellites, with 12% being accreted in pairs, and 28% in richer groups. Bakels et al. (2021) use high-resolution dark-matter-only simulations and find that 20% of all the accreted systems were accreted in groups.

This process is often suggested as an important mechanism to produce spatial and kinematic coherence between satellite galaxies, such as the so-called planes of satellites (see e.g. D'Onghia & Lake, 2008; Li & Helmi, 2008). Kunkel & Demers (1976) & Lynden-Bell (1976) first discovered that the satellite galaxies align along a polar great circle around the MW. More recently, it was found that the anisotropic distribution of these satellites, now called the Vast Polar Structure (VPOS; Pawlowski et al., 2012), also shows coherent motion, which is inconsistent with the predictions of ΛCDM (Pawlowski et al., 2012; Pawlowski & Kroupa, 2020). Similar anisotropic structures have also been discovered around Andromeda (M31), the Great Plane of Andromeda (GPoA; Ibata et al., 2013; Koch & Grebel, 2006; McConnachie & Irwin, 2006), and around Centaurus A (Müller et al., 2016, 2018; Tully et al., 2015).

Lynden-Bell (1982) first proposed associations between satellite galaxies and globular clusters in the Local Group. In their seminal paper, Lynden-Bell & Lynden-Bell (1995) show that satellites accreted together leave signatures of group infall in their phase-space distribution. It is expected that objects that were accreted together share similar specific angular momentum and total energy. Using this argument and assuming a spherical potential for the MW, these latter authors are able to identify several possible associations between the known satellites at the time and predict their proper motions.

Li & Helmi (2008) find that infalling groups can remain coherent and share orbital planes for up to 8 Gyr, the typical time that satellites have been within the MW/M31 halo, making this argument more compelling. The simulations performed by Wetzel et al. (2015) support this finding. Group infall could also explain the high incidence of satellite galaxy pairs in the Local Group (see e.g. Fattahi et al., 2013).

In the ΛCDM paradigm, it is expected that haloes of $\sim 10^{11}\mathrm{M}_{\odot}$ contain subhaloes that have sufficient gravitational potential to host their own subhaloes (satellites of satellite galaxies, Patel et al., 2020). In the MW, the Large Magellanic Cloud (LMC) is the only galaxy in the $\sim 10^{11}\mathrm{M}_{\odot}$ range. D'Onghia & Lake (2008) & Sales et al. (2011) suggested that the Magellanic Clouds (MCs) were the largest members of a group of dwarf galaxies that fell onto the MW halo, originating the majority of the brighter satellites of the MW. Later studies found that the LMC should host $\approx 5 - 10$ ultra-faint dwarf galaxies with $M_{\star} \approx 10^2 - 10^5\mathrm{M}_{\odot}$ (e.g. Dooley et al., 2017; Jahn et al., 2019). Recently, the proper motions of the lowest-mass satellite galaxies were measured for the first time (Fritz et al.,

1. Since they use dark matter only simulations, their results are not strongly limited by resolution.

2018; Pace & Li, 2019), allowing the determination of which galaxies are dynamically associated with the MC (Kallivayalil et al., 2018). Patel et al. (2020) identified between three and six galaxies as MC satellites, which is consistent with the low end of the cosmological expectations. There is also observational evidence of low-mass groups existing in isolated environments (Stierwalt et al., 2017).

However, Li & Helmi (2008) & Wang et al. (2013) find that the typical group infall events in simulations consist of objects of similar mass. We therefore expect other group associations among the satellites of the MW, but observational evidence for past associations has, until now, been absent. Several other associations were proposed based on their positions and velocities, such as Fornax, Leo I, Leo II, and Sculptor (Lynden-Bell, 1982), with additional members being proposed later: Sextans, and Phoenix (Majewski, 1994); Pisces II and Pegasus III (Garofalo et al., 2021; Kim et al., 2015; Richstein et al., 2022); and NGC 147, NGC 185, and Cassiopeia II in the M31 galaxy (Arias et al., 2016). Tully et al. (2006, 2002) proposed several bound associations of dwarfs in the Local Group and beyond, with strong spatial and kinematic correlations, although they are of larger scales than the ones suggested between satellite galaxies. Fattahi et al. (2013) found that ~ 30% of Local Group satellites brighter than $M_V = -8$ are likely in pairs, such as And I/And III and NGC 147/NGC 185 in the M31 galaxy, although cosmological simulations predict that less than 4% of satellites are part of pairs in this range of luminosities. The suggestion that NGC 147 and NGC 185 were likely associated was first proposed by van den Bergh (1998) due to their proximity in position, distance, and velocity, but Sohn et al. (2020), using HST proper motions, find it to be very unlikely that these galaxies were ever gravitationally bound. Bell et al. (2022) argue that the extremely asymmetric satellite distribution of M81 indicates that many of the satellites were recently accreted as a group. However, apart from the MC system, none of these suggestions were ever confirmed through proper motion measurements. Furthermore, group infall on MW-like systems has been studied almost exclusively in cosmological simulations, but not observationally.

Jong et al. (2010) first proposed the association between Leo IV (Belokurov et al., 2007) and Leo V (Belokurov et al., 2008) to explain their proximity in distance and radial velocity. Although these authors find that these galaxies do not share the same orbit when a spherical potential is assumed, they conclude that they most likely fell into the MW halo together. When Crater 1 was discovered (Belokurov et al., 2014), it was proposed as an additional possible member of the association. This possible association was further discussed by Torrealba et al. (2016), with the discovery of Crater II. Leo II was then additionally included (Harrington & Wilson, 1950), as all five objects lie close to the great circle with the pole at $(\alpha, \delta) = (83.2°, -11.8°)$.

With measured proper motions we can properly explore the suggested association between the objects in the Leo-Crater group. Therefore, in order to further investigate the proposed group, here we present accurate proper motions of Leo IV and V using new data from the *Hubble* Space Telescope (HST), and combine these with existing *Gaia* and HST measurements for the other objects in the group. If these satellites are conclusively identified to have been accreted together, not only will they be the first confirmed case of group accretion in addition to the MC system, but they can also start to provide constraints on the environmental influences on dwarf galaxy formation and evolution in general, and the assembly history of the MW satellite system in particular.

In Sect. 2.2 we describe the data and observations of the objects proposed as a group. This is followed in Sect. 2.3 by the methods that we used to decipher whether or not these objects were accreted together and by our approach to find other possible associations in Sect. 2.3.1. We continue in Sect. 2.4 with our results on the predicted proper motions of the discussed objects (Sect. 2.4.2), and their corresponding orbital properties (Sect. 2.4.5). We show how we checked for previously unconsidered additional members of the group in Sect. 2.4.4 and whether or not the infall of the LMC had any effect on the measured direction of the angular momentum of the objects in Sect. 2.4.6. We end with a discussion and our conclusions in Sect. 2.5. In Appendices 2.A, 2.B, 2.C, 2.D, and 2.E, we provide supplementary material in support of the results that we discuss in the main text. Throughout the paper, the data from *Gaia* DR3 are always represented in shades of blue and green, and the data from HST are always represented in shades of yellow, orange, and red to facilitate recognition and association.

2.2 The proposed Crater-Leo group

The proposed Crater-Leo group, represented in Figure 2.1, consists of Leo II, a classical dwarf spheroidal galaxy, Leo IV and Leo V, both ultra-faint satellite galaxies, Crater 1, a globular cluster, and Crater II, a distant diffuse satellite galaxy.

2.2.1 Properties

Leo IV and Leo V were first proposed as a pair to explain both their spatial proximity ($< 3°$) and small differences in their line-of-sight distances (< 20 kpc) and velocities (< 40 kms^{-1}) (Jong et al., 2010). Their closeness is especially unusual since the outer halo of the MW is mostly empty, with only ~ 20% of all currently known dwarfs inside a 400 kpc radius located beyond 150 kpc from the Galactic centre (Torrealba et al., 2016). Following the discoveries of Crater 1 (Belokurov et al., 2014) and Crater II (Torrealba et al., 2016), the possible association between these objects was further explored. Together with Leo II, these objects align along a common great circle (see left panel of Figure 2.1), which is highly unlikely. Torrealba et al., 2016 estimated the probability of this happening randomly - without sharing a common group origin - using random Monte Carlo realisations of satellite distributions on the sky and determining the largest group of satellites that are strongly aligned for each realisation. They find that having apparent aligned groups with five or more members by random chance has a probability of only ~ 0.0045.

In addition, the objects show a monotonic distance gradient (see middle panel of Figure 2.1), moving up in declination from Crater II ($D_h = 116.6 \pm 6.6$ kpc) to Leo II ($D_h = 216.8 \pm 11.0$ kpc). To make this argument even more compelling, the line-of-sight velocities of these objects seem to prefer a common value of about zero in the Galactic rest frame[2] (see right panel of Figure 2.1), with Crater II being the most offset in velocity.

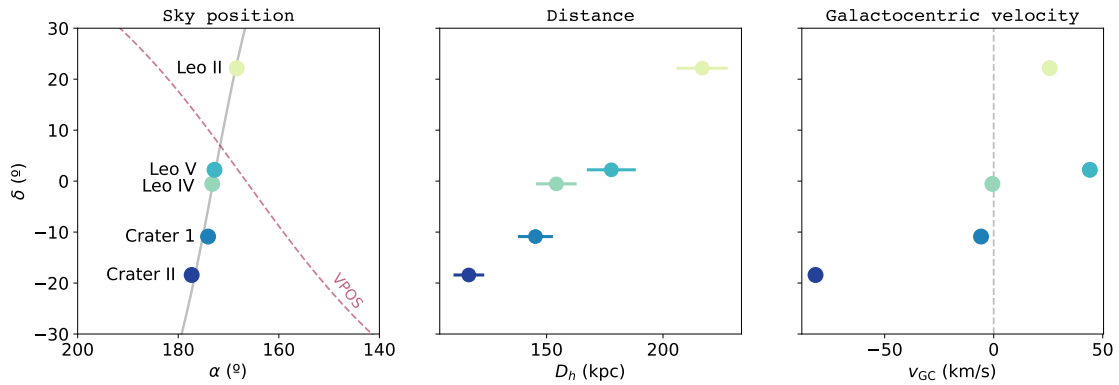


Figure 2.1: Crater-Leo objects. The left-hand panel shows the positions of Leo II, Leo IV, Leo V, Crater 1, and Crater II in the sky. The solid grey line represents the great circle with the pole at $(\alpha, \delta) = (263.01°, 10.78°)$ that passes close to all five satellites. The red dashed line represents the best-fit orbital plane of the VPOS at $(\alpha, \delta) = (76.53°, 36.24°)$ estimated by Fritz et al. (2018). The middle panel represents the declination versus the heliocentric distance of the satellites. The right-hand panel shows the declination versus line-of-sight velocity of the satellites, with $v_{GC} = 0$ km s^{-1} represented by the dashed line.

Furthermore, Fattahi et al. (2013) show that satellite galaxies close in position and velocity preferentially form pairs of comparable luminosity. When we look at the luminosity of these objects, Crater 1, Leo IV, and Leo V have comparable luminosities ($M_V = -5.3$, $M_V = -5.8$ and $M_V = -5.2$, respectively), as well as Leo II and Crater II ($M_V = -9.8$ and $M_V = -8.2$, respectively). These values are described in Table 2.1.

Finally, some of these objects also seem to share similar star formation histories (SFHs). The SFHs of Leo II and Leo IV indicate that these objects ended their star formation around 5-6 Gyr ago (Weisz et al., 2014a). Crater 1's stellar content appears to be metal-poor and old, with an age between 7 and

2. The root mean square (RMS) scatter is ~ 40 km s^{-1}, which can be compared to the larger one-dimensional velocity dispersion of ~ 100 km s^{-1} for the MW satellite population as a whole (Riley et al., 2019). When we exclude Crater II, this RMS scatter becomes ~ 25 km s^{-1}.

TABLE 2.1: Properties of the Crater-Leo objects.

Object	RA (°)	DEC (°)	M_V	dm	$\langle v_{los} \rangle$ (km s^{-1})	$\langle$[Fe/H]$\rangle$	$M^{(*)}$ ($10^6 M_\odot$)	References
Leo II	168.3627	22.1529	-9.8 ± 0.3	21.68 ± 0.11	$78.30^{+0.60}_{-0.60}$	$-1.63^{+0.01}_{-0.01}$	4.6	1, 2, 3, 4, 5, 6
Leo IV	173.2405	−0.5453	-5.8 ± 0.4	20.94 ± 0.07	$131.40^{+1.20}_{-1.10}$	$-2.47^{+0.14}_{-0.14}$	1.3	1, 7, 8, 9, 6
Leo V	172.7857	2.2194	-5.2 ± 0.4	21.25 ± 0.08	$173.00^{+1.00}_{-0.80}$	$-2.28^{+0.15}_{-0.16}$	1.1	1, 7, 10, 9, 6
Crater 1	174.0660	−10.8778	-5.3 ± 0.1	20.81 ± 0.05	$149.30^{+1.20}_{-1.20}$	$-1.68^{+0.05}_{-0.05}$	0.01	11, 12, 13
Crater II	177.3280	−18.4180	-8.2 ± 0.1	20.33 ± 0.07	$87.60^{+0.40}_{-0.40}$	$-1.95^{+0.06}_{-0.05}$	4.4	14, 15, 16, 17

Notes. Coordinates of the optical centre (RA and DEC) in degrees, absolute magnitude in the V-band (M_V), the distance modulus (dm), heliocentric systemic line-of-sight velocity ($\langle v_{los} \rangle$) in km s^{-1}, mean stellar metallicity ($\langle$[Fe/H]$\rangle$), dynamical/stellar mass (M) in solar masses, and the corresponding references.
References. (1) Muñoz et al. (2018); (2) Irwin & Hatzidimitriou (1995); (3) Gullieuszik et al. (2008); (4) Spencer et al. (2017b); (5) Kirby et al. (2013); (6) McConnachie (2012); (7) Jong et al. (2010); (8) Moretti et al. (2009); (9) Jenkins et al. (2021); (10) Mutlu-Pakdil et al. (2019); (11) Belokurov et al. (2014); (12) Weisz et al. (2016); (13) Kirby et al. (2015); (14) Vivas et al. (2020); (15) Torrealba et al. (2016); (16) Caldwell et al. (2017); (17) Fu et al. (2019).
(*)For the dwarf galaxies (Leo II, Leo IV, Leo V and Crater II), M corresponds to the dynamical mass inside the half-light radius. For the globular cluster (Crater 1), due to its lack of dark matter, M corresponds to its stellar mass.

10 Gyr, with three stars younger than 1 Gyr (Belokurov et al., 2014). It has been argued before that the globular clusters (GCs) on the outskirts of the MW were accreted together with their parent dwarf galaxies (see e.g. Huang & Koposov, 2021; Mackey & Gilmore, 2004). van den Bergh (2006) shows that the specific frequency of globular clusters fainter than $M_V \sim -7.5$ is particularly high in dwarf galaxies and that dwarfs with luminosity distributions similar to Leo II (with $M_V = -9.8 \pm 0.3$), can host globular clusters with luminosity distributions similar to Crater 1 (with $M_V = -5.3 \pm 0.1$)[3]. Weisz et al. (2016) argues that Crater 1 joined the MW halo less than 8 Gyr ago. This makes plausible the idea that Crater 1 originated from Leo II since these objects share similar metallicities (see Table 2.1). Leo II formed the second half of its stellar mass from 6 to 9 Gyr, which matches Crater 1's probable age. The SFH of Leo V is not well determined; however, Mutlu-Pakdil et al. (2019) argues that it should be similar to the SFH of Leo IV, since they have very similar colour-magnitude diagrams. The common end of star formation of the objects is consistent with an infall into the MW halo within the last 6 Gyr, with Crater 1 originating from one of them. Crater II, however, only shows signs of star formation events at 10.5 Gyr and 12.5 Gyr ago, with no presence of intermediate-age or younger stars (Walker et al., 2019). It was found that this dwarf galaxy shows strong signals of tidal disruption, affecting its kinematics (see e.g. Fu et al., 2019; Ji et al., 2021). However, this does not affect the infered age of its stellar content.

Li & Helmi (2008) found in cosmological simulations that accreted groups typically have between three and five satellites, which is consistent with the proposed group. However, when this group was first proposed, no proper motion measurements were available. With the measurements provided by *Gaia* DR3, we can investigate the tentative group once again to confirm or disregard their association.

Fritz et al. (2018) explored this possibility by determining the possible orbital poles for the five objects with *Gaia* DR2 proper motions. However, they found the association unlikely, since the orbital poles do not overlap well and had large uncertainties. They acknowledged the possibility of having two different groups (Crater 1 and Crater II as one of them, and Leo IV and Leo V as the other) instead of only one. However, they found that the orbital properties of Crater 1 and Leo II are consistent with each other, and Leo II also has orbital poles consistent with it being part of the other group, so they require better proper motions to confirm or exclude this possibility.

We used the metric defined by Geha et al. (2010) to test whether the Crater-Leo objects are currently bound to each other, as was done by Geha et al. (2015) & Sohn et al. (2020) for NGC 147 and NGC 185, and in Richstein et al. (2022) for Pisces II and Pegasus III. Specifically, for two point masses to be gravitationally bound, their gravitational potential energy has to exceed their kinetic energy (Davis et al., 1995), leading to the criterion $b \equiv 2GM_{sys}/\Delta r \Delta v^2$, where Δr is the total physical separation

3. For example, BKN 3N, with $M_V = -9.53$ has a globular cluster with $M_V = -5.23$ (van den Bergh, 2006).

between the objects and Δv the radial velocity difference between them. When $b > 1$, the system is considered bound. If our objects are indeed bound, we can assume they are associated. However, if they are not, this is not sufficient to disregard the possibility of them having been accreted together, since they might have just dispersed along their orbits. We determined this metric for every pair in our group using the values described in Table 2.1 and the masses described in Table 2.1, and we always get $b < 1$, meaning that none of the satellites are bound at the present time. For our satellites to be bound, taking into account their physical separation and the radial velocity difference, the mass of each pair would have to be $> 10^9 M_\odot$. We then need to perform an extensive analysis with up-to-date data, in particular recent and new proper motion measurements, to try to understand if these objects were accreted as a group.

2.2.2 Proper motions

With up-to-date data, described in Tables 2.1 and 2.2, we can expand upon this preliminary analysis again to test if the Crater-Leo objects are consistent with their expected dynamics if they were once part of a common group of satellites. We estimated the expected angular momentum of the group and its direction. With this, we can predict their proper motions and compare them with the current observations. This, combined with their orbital history, allows us to better assess the possibility of these objects being accreted together.

The large uncertainties of the proper motions of Leo IV and Leo V, however, make this analysis more difficult. For this reason, we started and executed an observational project to determine improved proper motions from HST, which we present and discuss below.

Table 2.2: Proper motions ($\mu_{\alpha*}$ and μ_δ) in mas yr^{-1} using *Gaia* DR3 from Battaglia et al. (2022).

Object	$\mu_{\alpha*}$ (mas yr^{-1})	μ_δ (mas yr^{-1})
Leo II	$-0.11^{+0.03}_{-0.03}$	$-0.14^{+0.03}_{-0.03}$
Leo IV	$-0.03^{+0.14}_{-0.14}$	$-0.28^{+0.11}_{-0.12}$
Leo V	$0.10^{+0.21}_{-0.21}$	$-0.41^{+0.15}_{-0.15}$
Crater 1	$-0.04^{+0.12}_{-0.12}$	$-0.12^{+0.10}_{-0.10}$
Crater II	$-0.07^{+0.02}_{-0.02}$	$-0.11^{+0.01}_{-0.01}$

2.2.3 New HST proper motions of Leo IV and Leo V

Imaging data used for measuring proper motions of Leo IV and Leo V were obtained with HST in two separate epochs. For Leo IV, the first-epoch data were obtained on January 2012 through HST program GO-12549 (PI: T. Brown) in F606W and F814W for studying the star formation histories of Ultra-Faint Dwarf galaxies (Brown et al., 2014), and the second-epoch data were obtained on November 2016 through HST program GO-14236 (PI: S. T. Sohn) in F606W for measuring proper motions of Leo IV along with other UFDs in the original Brown et al. (2014) sample. For Leo V, the first- and second-epoch data were obtained on March 2017 (in F606W and F814W) and March 2020 (in F606W), respectively, through the multi-cycle HST program GO-14770 (PI: S. T. Sohn).

To measure the PMs of both galaxies, we followed the methods used in our previous work on M31, and its two dwarf satellite galaxies NGC 147 and NGC 185 (Sohn et al., 2012, 2020). We downloaded the _flc.fits images from the Mikulski Archive for Space Telescopes (MAST). For each star in each galaxy, we measured its position and flux from the _flc.fits images using the hst1pass code (Anderson, 2022). We corrected the positions for geometric distortion using the solutions by Kozhurina-Platais et al. (2015). For each dwarf galaxy, we then created high-resolution stacked images using images from the first-epoch data.

As the next step, we constructed colour–magnitude diagrams (CMDs) for both Leo IV and Leo V using multi-band images obtained during the first epoch. The CMDs were used for identifying stars

associated with each dwarf galaxy. We also identified background galaxies to be used as astrometric reference sources from the stacked images, first through an objective selection based on the quality-of-fit parameter output from the hst1pass code, and then by visually inspecting each source. We then constructed a template for each star or background galaxy by supersampling the scene extracted from the high-resolution stack. Templates constructed this way take into account the point-spread functions (PSFs), the galaxy morphologies, and the pixel binning. We fitted these templates to stars and galaxies in each individual _flc.fits image for measuring their positions. For the first epoch, we fitted the templates directly onto the stars and galaxies in the individual images. For the second epoch, we derived convolution kernels by comparing PSFs of numerous bright and isolated stars between the first and second epochs, and applied these kernels when fitting templates to allow for differences in PSF between different epochs. Once the template-fitting process was complete, we were left with the positions of all stars and background galaxies in each individual image in each epoch.

The reference frames were defined by averaging the positions of stars from repeated first-epoch exposures. We used the positions of stars in each exposure of the second epoch to transform the positions of the galaxies into the reference frames. We then measured the positional difference for each background galaxy between the first and second epochs relative to the stars associated with Leo IV and Leo V. During this process, we applied "local correction" by making measurements only relative to stars with similar brightness in the local vicinity on the image to correct for residual CTE and any remaining geometric distortion systematics. We took the error-weighted average of all displacements of background galaxies with respect to Leo IV and Leo V stars for each individual second-epoch exposure to obtain an independent PM estimate. We then obtained the final PMs of Leo IV and Leo V by computing the error-weighted mean of these individual PM estimates, multiplying -1 by this value to account for the fact that what we measure is the reflex motion of background galaxies, and dividing by the time baseline in years. The final PMs and associated uncertainties derived as described in this subsection are listed in Table 2.3.

TABLE 2.3: Proper motions ($\mu_{\alpha*}$ and μ_δ) in mas yr^{-1} of Leo IV and Leo V from new HST measurements.

Object	$\mu_{\alpha*}$ (mas yr^{-1})	μ_δ (mas yr^{-1})
Leo IV	-0.1921 ± 0.0514	-0.0686 ± 0.0523
Leo V	0.1186 ± 0.1943	-0.1183 ± 0.1704

For completeness, we also use the available HST proper motion for Leo II. Piatek et al. (2016) measured this proper motion based on imaging with HST and Wide Field Camera 3 and got $(\mu_\alpha, \mu_\delta) = (-0.069 \pm 0.037, -0.087 \pm 0.039)$ mas yr^{-1}. With this result, they confirmed that the Leo II proper motion was aligned with the great circle that passes through Leo IV, Leo V, Crater 1 and Crater II, as first suggested by Torrealba et al. (2016). They also estimate the pericentre of Leo II, since if they are orbiting in coplanar orbits with a range of energies (possibly acquired during the disruption of the group), this value should be at least as small as the smallest current Galactocentric distance of the members of the group (120 kpc for Crater II). With their measured proper motion, they find that Leo II has a 31% chance of having its pericentre at 120 kpc or less. Their results then support the hypothesis that Leo II, Leo IV, Leo V, Crater 1 and Crater II fell into the Milky Way as a group, with the direction of motion indicating that Leo II would be leading this group.

Figure 2.2 shows *Gaia* DR3 proper motions represented by the blue arrows and the HST proper motions represented by the orange arrows, after being transformed into the Galactocentric frame. The arcs indicate $1-2\sigma$ intervals in the direction of motion. One can see that when we consider our HST proper motions for Leo IV and Leo V, their directions better align with the rest. However, as we do not know which one is closer to the true value, we use both measurements in this study and discuss their implications for our results. Crater II's proper motion is well-constrained, thanks to the abundance of member stars measured by *Gaia*, and does not seem to align with the great circle that passes close to all five satellites. The other objects, however, seem to be consistent with this great circle within 2σ, with almost all of them pointing in the same direction.

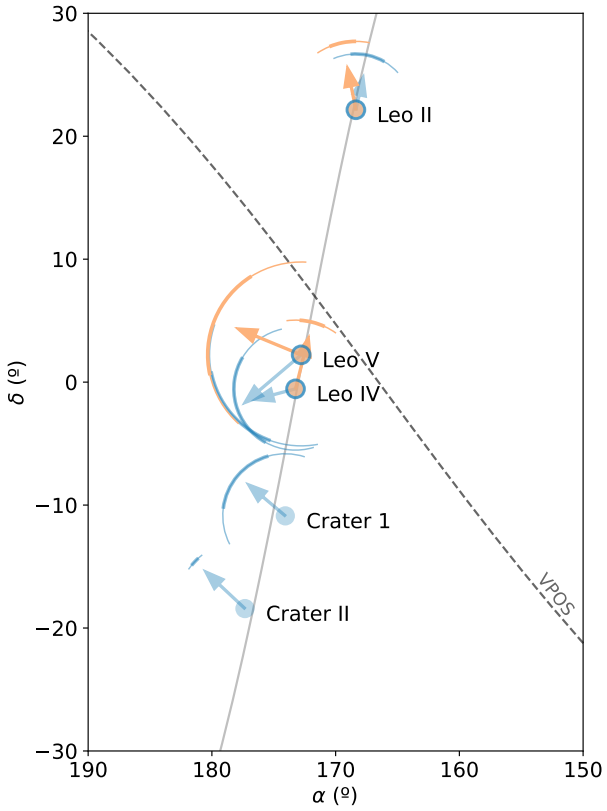


FIGURE 2.2: Positions of Leo II, Leo IV, Leo V, Crater 1, and Crater II in the sky. The solid grey line represents the great circle with the pole at $(\alpha, \delta) = (263.01°, 10.78°)$ that passes close to all five satellites. The black dashed line represents the best-fit orbital plane of the VPOS at $(\alpha, \delta) = (76.53°, 36.24°)$ estimated by Fritz et al. (2018). The arrows indicate the most likely direction of motion based on current proper motion estimates (the fainter ones, in blue, represent the *Gaia* measurements, and the solid ones, in orange, the HST proper motions) and the circle segments indicate the 1 and 2σ uncertainties in the velocity directions of the satellites.

2.3 Methods

We start by describing how we estimated the orbital poles of the Crater-Leo objects. This is followed by the explanation of the method that we use to determine if these objects were accreted together in Sect. 2.3.1. In Sect. 2.3.2 we explain how we accounted for intrinsic scatter within the group. Finally, in Sect. 2.3.3, we describe how we determine possible additional members to the initially proposed group.

As previously mentioned, if satellites are accreted together, we expect them to share similar specific angular momentum. Hence, they need to share orbital poles, that is, the directions of the angular momentum vectors. To determine the uncertainties in the derived orbital poles, we used Monte Carlo realisations, and incorporated the uncertainties of the proper motion measurements, of the distance, position, and line-of-sight velocity of the satellites (described in Table 2.1), of the distance of the Sun from the Galactic centre, $D_\odot = 8.178 \pm 0.022$ (GRAVITY Collaboration et al., 2019), of the circular velocity of the local standard of rest (LSR), $v_{\rm circ} = 234.7 \pm 1.7$ (Nitschai et al., 2021), and of the peculiar motion with respect to the LSR, $\boldsymbol{v}_{\rm LSR} = (11.10 \pm 0.72, 12.24 \pm 0.47, 7.25 \pm 0.37)$ (Schönrich et al., 2010).

2.3.1 Lynden-Bell method

Lynden-Bell & Lynden-Bell (1995) show that satellites that were accreted as a group share similar specific angular momentum h and total energy E and they use this argument to identify possible associations between the satellites of the MW at the time. By assuming a spherical and static potential of the form $\psi = -V_0^2 \ln r$, they are able to predict the proper motions of the objects they consider associated. A detailed explanation of its implementation can be found in their paper which we briefly summarise here for the reader's convenience.

The total specific energy of a satellite's motion around the Milky Way at Galactocentric position $r = (x, y, z)$ and velocity $v = (v_x, v_y, v_z)$ can be written as

$$E(r, v) = \frac{1}{2} v^2 + \Phi_{\rm MW}(r), \tag{2.1}$$

where $\Phi_{\rm MW}$ is the Galactic potential at the position of the satellite, and v^2 the total velocity of a satellite, given by $v^2 = v_{\rm r}^2 + v_{\rm tan}^2$. Since the objects under study are at large distances, the vector pointing from the Galactic Centre to the position of the object is similar to their line-of-sight, so we can approximate the radial velocity that would be seen from the Galactic Centre $v_{\rm r}$ to the line-of-sight velocity $v_{\rm los}$. The tangential velocity $v_{\rm tan}$ relative to the Galactic Centre is unknown; however, we can introduce the specific angular momentum $h = |r \times v| = |r| \cdot |v_{\rm tan}|$ and rewrite Equation 2.1 as

$$E \approx \frac{1}{2} v_{\rm los}^2 + \frac{1}{2} h^2 r^{-2} + \Phi_{\rm MW}(r). \tag{2.2}$$

We can then write the radial Energy, E_r, as

$$E_{\rm r} = \frac{1}{2} v_{\rm r}^2 + \Phi_{\rm MW}(r) = E - \frac{1}{2} h^2 r^{-2}. \tag{2.3}$$

Since objects that are associated should share the same E and h once both quantities are conserved, when we plot E_r against r^{-2}, they will lie on a line of gradient $-g = -h^2/2$ and intercept E (Lynden-Bell & Lynden-Bell, 1995).

If we consider $\boldsymbol{s}$ the vector along the line-of-sight, $\boldsymbol{r}$ the Galactocentric position and $\boldsymbol{r}_\odot$ the position of the Sun, we have

$$\boldsymbol{s} = \boldsymbol{r} - \boldsymbol{r}_\odot. \tag{2.4}$$

The velocity of the object in the Galactocentric system of rest is then

$$\boldsymbol{v} = v_r \hat{r} + \boldsymbol{h} \times \hat{r}/r. \tag{2.5}$$

The radial velocity becomes

$$v_r = (v_l - \boldsymbol{h} \cdot \hat{r} \times \hat{s}/r) = (v_l - h r^{-1} \Delta)/\hat{r} \cdot \hat{s}, \tag{2.6}$$

where v_l is the line-of-sight velocity corrected by the velocity of the Sun, $\boldsymbol{h} = h\hat{p}$ and $\Delta = \hat{p} \cdot (\hat{r} \times \hat{s})$. To determine the magnitude and sign of h, we start by using an approximated value h_0 estimated by fitting Equation 2.3 to our data. The true value of the specific angular momentum is then given by $h_\pm = \delta h \pm h_0$. Using Equation 2.6 in Equation 2.3, we get

$$E_r = \frac{1}{2}[v_l - (\delta h \pm h_0) r^{-1} \Delta]^2/(\hat{r} \cdot \hat{s})^2 - \Phi_{\rm MW} = E - \frac{1}{2} h^2 r^{-2}. \tag{2.7}$$

To find a better value for the specific angular momentum, we iteratively redetermine $-\frac{1}{2}h^2$ from the best-fitting line. This converges rapidly to give consistent values of $\pm h$. After five iterations, this value changes by less than $\approx 10^{-5}\%$, but we use 10 iterations just to be safe. For each possible association, we have two possible signs, however, the sign must be the same for all the members of a group, since it determines the direction of the orbit's circulation.

Using Equations 2.5 and 2.6, the total velocity relative to the Galactic centre is given by

$$\boldsymbol{v} = (v_l - h r^{-1} \Delta)\hat{r}/\hat{r} \cdot \hat{s} + \boldsymbol{h} \times \hat{r}/r. \tag{2.8}$$

Having the expected 3D velocity determined, we are able to calculate the corresponding proper motions of the associated objects for each direction of h.

Here, we use their method to predict the proper motions that the Crater-Leo objects would have if they were associated. However, instead of using the spherical potential that they adopted, we use the gravitational potential described by Bovy (2015) (MWPotential2014), hereafter MW-only potential, which was fitted to a large variety of data on the MW, serving both as a simple and accurate model for our galaxy's potential. This potential contains three components consisting of a stellar bulge, a disc, and a dark matter halo, with a total mass of $0.8 \times 10^{12} M_\odot$. In Appendix 2.B we check how our predictions are affected when we consider a MW mass of $1.6 \times 10^{12} M_\odot$. We considered scenarios

with and without the inclusion of the LMC potential, whereas, for the latter case, we used the potential defined by Vasiliev et al. (2021), using AGAMA (Vasiliev, 2019), with a MW mass of $0.88 \times 10^{12} M_\odot$ and a LMC mass of $1.5 \times 10^{11} M_\odot$.

If the Crater-Leo objects were accreted in one common group, then the predicted proper motions should match the measurements of the proper motions we have available today.

2.3.2 Intrinsic scatter

To account for the intrinsic scatter in the specific energy E and angular momentum h of the group that are is considered in the Lynden-Bell method, we adopted a Markov Chain Monte Carlo (MCMC) approach. Assuming that the uncertainties are Gaussian and that the measurements are independent, the likelihood of a model $y = y(x)$ is given, generically, by

$$\mathscr{L} = \prod_i \frac{1}{\sqrt{2\pi\sigma^2}} exp\left[-\frac{(y_i - y(x_i))^2}{2\sigma^2}\right]. \tag{2.9}$$

Taking into account our model, given by Eq. 2.3, and assuming that our uncertainties are underestimated by an intrinsic scatter, $\sigma_{\rm is}$, the uncertainty for each measurement n becomes

$$\epsilon_n^2 = \sigma_{\rm obs}^2 + \sigma_{\rm is}^2. \tag{2.10}$$

Our likelihood function will then be

$$ln\,\mathscr{L}(y|x,\sigma,h,E,f) = -\frac{1}{2}\sum_n \left[\frac{(y_n - [E - \frac{1}{2}h^2 x_n^{-2}])^2}{\epsilon_n^2} + ln\,(2\pi\epsilon_n^2)\right]. \tag{2.11}$$

To determine the posterior probability function of E and h given by

$$p(h,E,f|x,y,\sigma) \propto p(h,E,f)\ \mathscr{L}, \tag{2.12}$$

with $\mathscr{L}$ being our likelihood function, we need the prior function $p(h,E,f)$. For this, we use $0.5h_0 < h < 1.5h_0$, $0.5E_0 < E < 1.5E_0$ and $0.5\sigma_{\rm is_o} < \sigma_{\rm is} < 1.5\sigma_{\rm is_o}$, with the h_0, E_0 being determined by the fit described in Sect. 2.3.1, and $\sigma_{\rm is_o}$ being determined by the maximum likelihood result of this model. These are the range of values that allow us to include intrinsic scatter consistent with how far in specific energy the objects are from the best fit, while still making sure that the objects belong to the same group.

After this setup, we sample this distribution using emcee (Foreman-Mackey et al., 2013). We start by initialising the walkers ($n = 250$) around the maximum likelihood result and then run 10^4 steps of MCMC so they can explore the full posterior distribution. The first half of the steps generated were discarded as a conservative burn-in criterion.

2.3.3 Looking for additional members

In addition to the already considered group members, other dwarf galaxies or globular clusters around the Milky Way could in principle be associated to the group as well. To further explore other possible members of this association, we once again build upon the Lynden-Bell method. At the time, Lynden-Bell & Lynden-Bell (1995) did not have 3D positions and velocities available and, for that reason, it was not possible to determine the orbital poles of the objects. To overcome this, they used the Galactocentric vectors of every object and assumed that if two of them (with $\boldsymbol{a}$ and $\boldsymbol{b}$, respectively) were part of the same group, their common orbital pole would lie along $P = \pm\boldsymbol{a} \times \boldsymbol{b}$. The same would happen if several objects (with, for example, $\boldsymbol{c}$ and $\boldsymbol{d}$) are members of the same group: $\pm\boldsymbol{a} \times \boldsymbol{d}$, $\pm\boldsymbol{b} \times \boldsymbol{d}$ and $\pm\boldsymbol{c} \times \boldsymbol{d}$ would have directions close to P. Instead of determining orbital poles, they determine putative pole positions by pairing every object with every other.

To find additional members, we take the proposed group and follow the method previously described. We start by checking which objects in our data set have putative pole positions closer than 5° to the ones of our group, that is, which objects can lie along the great circle that passes close to

the group. This is a generous value since all objects of the putative group are closer than 1°. We keep the objects that pass this first criterion since we consider that they can share similar specific angular momentum with the rest of the members.

Following the discovery that satellites are usually accreted in 3-5 members by Li & Helmi (2008), we create new groups with the proposed Crater-Leo group plus an additional member that passed the first criterion. We then apply a second criterion to check whether these new objects are likely to share a specific angular momentum and specific energy with our original group or if their orbital poles are just close, without being related. To do this, we use the fitting method previously described and discard the groups that have relative errors in E_r and $h_0 > 10\%$ since objects accreted together should lie on a line. The new groups that pass this test are considered likely groups and their proper motions are predicted.

As a result of *Gaia* DR3 and HST, we currently have proper motions not only for the most massive dwarfs of the Milky Way but also for some of its faintest satellites (see e.g. Fritz et al., 2018). Thus, in the last step, the predicted proper motions are compared with the measured proper motions, and if the predictions match the observations within 2σ, the group of objects deserves further inspection.

2.4 Results

Using the Monte Carlo realisations described in Sect. 2.3, we estimated the orbital poles for the Crater-Leo objects individually and were able to get an idea of whether or not the objects are likely to share specific angular momentum. In Sect. 2.4.1, we present these orbital poles and discuss their implications. Using the Lynden-Bell method, discussed in Sect. 2.3.1, we predict the proper motions of the Crater-Leo objects. To do this, we used the properties of Crater 1, Crater II, Leo II, Leo IV, and Leo V discussed in Sect. 2.2. Here, in Sect. 2.4.2, we present the predictions that we obtain for the proposed group. Due to lack of agreement between the measurements and the predictions for Crater II, and the fact that this object does not share a common orbital pole with the others as discussed in Sect. 2.4.1, we repeat the analysis without this object in Sect. 2.4.3. We also check in Sect. 2.4.4 if any other satellites can be part of this putative group. Next, we determine the orbital properties of the objects, described in Table 2.4, and analyse their orbital histories in Sect. 2.4.5. Finally, we check if the LMC infall had an impact on the current measured orbital poles in Sect. 2.4.6. We predict the proper motions of the objects taking into account the shift in velocities and positions that they would have had if the dark matter halo of the MW was not affected by the nearby LMC.

2.4.1 Orbital poles

The orbital poles that we derive for the Crater-Leo objects using their measured proper motions and for the proposed group are shown in Figure 2.3. It is possible to see that all objects are consistent with co-orbiting the VPOS.

From this figure, one can directly identify that Crater II possibly does not belong to a common group of satellite galaxies. However, the other four objects seem to intercept within their uncertainties. We also find that when using the new measurements from HST of the proper motions of Leo IV and Leo V, a common orbital pole between the possible associated objects becomes more likely. These new HST proper motions also position the most likely orbital pole closer to the VPOS of the MW, as can be seen in this figure.

2.4.2 Predicted proper motions

Adopting the method previously discussed in Sect. 2.3.1, we can determine the specific angular momentum and energy for the group. Objects that were accreted together should share these quantities, and, consequently, align in a straight line when we plot E_r against r^{-2}, allowing us to determine their values for the group. This plot is represented in Figure 2.4, for both potentials. As one can see, all the objects lie close to the fitted line. Using the Lynden-Bell method, we get a specific angular momentum of $h_0 = 2.37 \times 10^4$ kpc km s^{-1} and specific energy of $E_0 = -0.99 \times 10^4$ km^{2}s^{-2} for the considered group. When we perform the MCMC method described in Sect. 2.3.2 we get a specific angular momentum of $h_0 = 2.32^{+0.29}_{-0.32} \times 10^4$ kpc km s^{-1} and specific energy of $E_0 = -1.05^{+0.32}_{-0.29} \times 10^4$ km^{2}s^{-2}

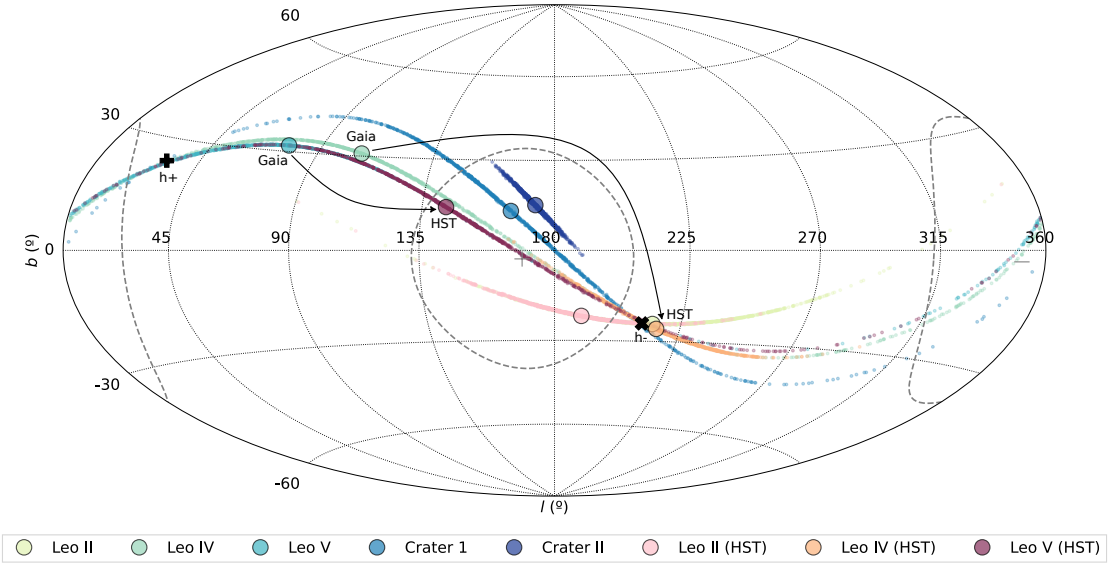


FIGURE 2.3: Most likely orbital poles (directions of angular momenta) represented by the large circles and their uncertainties represented by small circles in the corresponding colours for the proposed Crater-Leo objects, based on the proper motions discussed in Sect. 2.2.2. The uncertainties in orbital pole directions are obtained by Monte Carlo sampling of the proper motion and distance uncertainties (1000 realisations). The assumed VPOS pole is represented by the grey plus symbol and the opposite normal direction by the minus symbol, with the black circles containing 10% of the sky around them. The proposed group poles are represented by the bold black 'x' for the negative circulation, $h-$, and by the plus symbol for the positive circulation $h+$.

for the considered group. Including the influence of the LMC, these values change to $h_0 = 2.41 \times 10^4$ kpc km s^{-1} and $E_0 = -0.64 \times 10^4$ km^{2}s^{-2}. The MCMC method gives $h_0 = 2.38^{+0.25}_{-0.27} \times 10^4$ kpc km s^{-1} and $E_0 = -0.66^{+0.22}_{-0.20} \times 10^4$ km^{2}s^{-2} for this potential. The values that we get for the group for both the specific angular momentum and the specific energy are similar for both potentials, so it is expected that the proper motions that we predict from here are similar as well. The corner plots of the posterior distributions for the energy and angular momentum for both potentials can be seen in Figure 2.A.1 of the Appendix 2.A.

The predicted proper motions that we get for these objects are represented in Figure 2.5. The predictions remain nearly identical when we include the influence of the LMC in the potential of the MW. For that reason, they are not shown in the plot. To determine the parameter space of possible values that the measured proper motions can take within their uncertainties, we once again perform Monte Carlo realisations. We also take into account the systematic errors associated with the *Gaia* DR3 proper motion measurements, described in Battaglia et al. (2022).

The predicted proper motions seem to better match the measured ones for Leo II and Crater 1 when we consider negative $h-$ circulation. When we look at Leo IV and Leo V, we also note that those predictions are closer to the proper motions measured by HST. That is expected since their orbital poles lie close to the rest of the group when we consider the HST measurements. However, the predictions for Crater II do not match the measurements at all and the measured proper motions are well constrained. The possible orbital poles of this satellite suggest that this object cannot share the same angular momentum with the rest of the potential group, and this mismatch of predicted and measured proper motions is another indicator that this galaxy is not associated with it.

2.4.3 Removing Crater II

By looking at the orbital poles of the proposed group, Crater II does not seem to share a similar direction of angular momentum with the other objects. Furthermore, when we look at the line-of-sight velocities of these satellites, Crater II is the most offset one from the common value shared by the other objects (right panel of Figure 2.1). Additionally, as previously mentioned, this object only shows signs of star formation events at 10.5 Gyr and 12.5 Gyr ago, with no presence of intermediate-age or younger stars (Walker et al., 2019), contrary to the rest of the group. This suggests that this dwarf

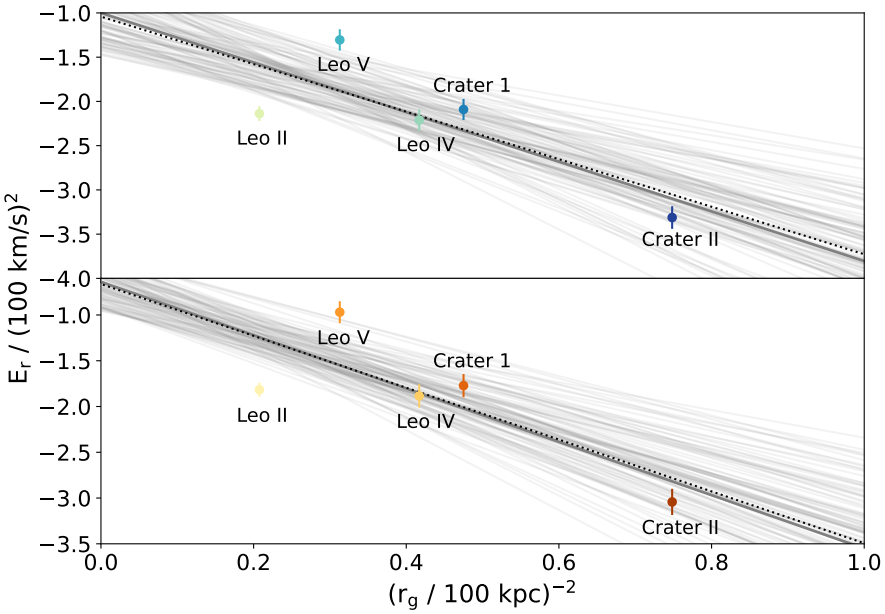


FIGURE 2.4: E_r plotted against r^{-2} for the proposed group. The coloured points represent the measured quantities and the associated uncertainties for each object. The grey solid line shows the fit that we get from the Lynden-Bell method by assuming that the objects under study share E and h. The dashed lines represent the mean fit obtained from the MCMC method, with the thin solid lines representing 100 random realisations of it. **Top:** Fit using MW-only potential. **Bottom:** Fit using the MW+LMC potential.

galaxy is unlikely to have been accreted with the other satellites. Since the predictions are based on the properties of the full ensemble of considered group members, the predicted proper motions will differ if one object is excluded. In order to see if the predicted proper motions better match the measured ones when this object is removed, we repeat the analysis previously described without Crater II.

In this case, we get a specific angular momentum of $h_0 = 1.25 \times 10^4$ kpc km s^{-1} and specific energy of $E_0 = -1.66 \times 10^4$ km^{2}s^{-2} for the Crater-Leo objects after removing Crater II from the putative group. The MCMC methods gives $h_0 = 1.24^{+0.42}_{-0.42} \times 10^4$ kpc km s^{-1} and $E_0 = -1.65^{+0.26}_{-0.24} \times 10^4$ km^{2}s^{-2}. When we use the potential that includes the influence of the LMC, these values change to $h_0 = 1.25 \times 10^4$ kpc km s^{-1} and $E_0 = -1.33 \times 10^4$ km^{2}s^{-2}. Considering the MCMC method, we get $h_0 = 1.23^{+0.42}_{-0.41} \times 10^4$ kpc km s^{-1} and $E_0 = -1.33^{+0.26}_{-0.24} \times 10^4$ km^{2}s^{-2}. Both the specific angular momentum and specific energy decrease for the group when we remove this satellite. These fits are represented in Figure 2.6 and the posterior distributions in Figure 2.A.2 of the Appendix 2.A. As one can see, the specific angular momentum is not well constrained for this case.

The proper motions that we get when we remove Crater II can be seen in Figure 2.7. The negative $h-$ circulation seems to predict the proper motion of the remaining objects relatively well, which is a strong indicator that these objects were accreted together. When we consider the new HST proper motions for Leo IV and Leo V, all the predictions fall within 1σ confidence level of the measured uncertainties. For Leo II, the prediction falls within the 0.5σ confidence level. For these reasons, we performed the rest of the analysis without Crater II.

2.4.4 Additional members

To determine which other MW halo objects could be possible additional members of the proposed group, we used a combination of the 3D positions and velocities of dwarf galaxies from Battaglia et al. (2022) and globular clusters from Baumgardt et al. (2019). We start by estimating the orbital poles of all the objects with distances $r > 20$ kpc, where our potential is well approximated by a spherical one. We use the method described in Sect. 2.3.3 and try to find groups with the previously discussed objects (Leo II, Leo IV, Leo V, and Crater 1) and possible additions.

We find five satellite galaxies that match our two first criteria (putative pole positions closer than 5° to the rest of the group and relative errors smaller than 10% in E_r and h_0 when we use the fitting

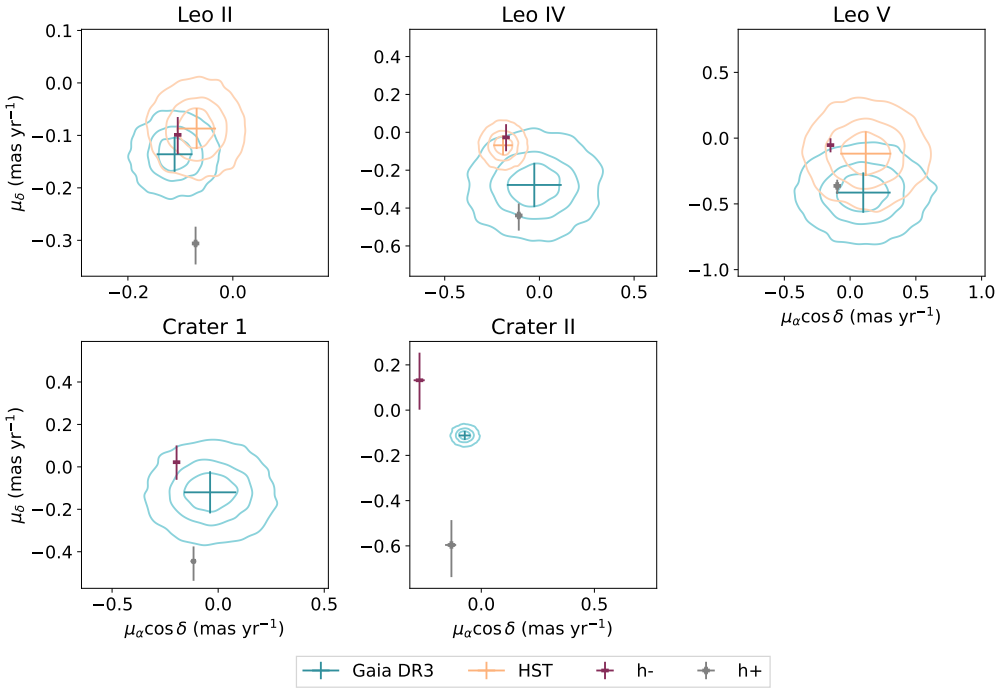


FIGURE 2.5: Predicted proper motions of the Crater-Leo objects. The grey plus symbol and magenta minus symbol represent the predictions obtained with the positive $h+$ and negative $h-$ circulation about the northern pole, respectively. The blue crosses represent the measured proper motions from *Gaia* DR3 with their uncertainties and the orange crosses represent the proper motion measurements from HST. The corresponding contours correspond to the 34%, 68%, and 95% confidence levels for the 2D distribution of the proper motion parameter space.

method for the group): Phoenix II, Tucana II (Koposov et al., 2015), Tucana IV, Tucana V (Drlica-Wagner et al., 2015), and Ursa Major II (Zucker et al., 2006). This means that these objects can share similar specific angular momenta and energy with the rest of the proposed group. However, when we compare the predicted proper motions of the possible additional objects with the observed ones from *Gaia* DR3 (Battaglia et al., 2022), they do not match within 1.5σ. Even increasing this value to $> 3\sigma$, the proper motions do not match, so it is very unlikely that they were accreted with the initially proposed group. The predicted proper motions of these objects can be seen in Figure 2.C.1 of the Appendix. As noticeable from this figure, the proper motions for these objects are not well constrained.

2.4.5 Orbital dynamics

For given proper motions (either measured or predicted), we can derive the orbital histories for each object to assess whether they could have been a bound group. We do this by integrating their orbits in the potentials discussed before for the measured proper motions (described in Tables 2.2 and 2.3), both in relation to the centre of the MW (in Figure 2.8) and for the mutual separation in relation to the most massive object, Leo II (in Figure 2.9).

Figure 2.8 shows the orbital evolution of the Crater-Leo objects for both the MW-only potential and the MW+LMC potential. We include the possible errors within the observational uncertainties, drawn from Monte Carlo realisations. We also plot in black the orbits derived from the predicted proper motions. It is possible to see that all objects reached their apocentre at the present time. For the MW-only potential, all objects except Leo V reached their pericentre around the same time (~ 2 Gyr ago) and with similar values (~ 60 kpc). When we consider the HST measurement for Leo IV, its orbit becomes almost circular, so its pericentre is further away from the MW centre. For Leo II and Crater 1, the predicted orbit is similar to the most likely orbit from the measurements. For the remaining objects, even though the most likely and the predicted orbits do not match, the predicted orbit is still consistent within the uncertainties. When we look only at the bound orbits of Leo IV and Leo V, this consistency is even larger, suggesting that with future proper motions we may get

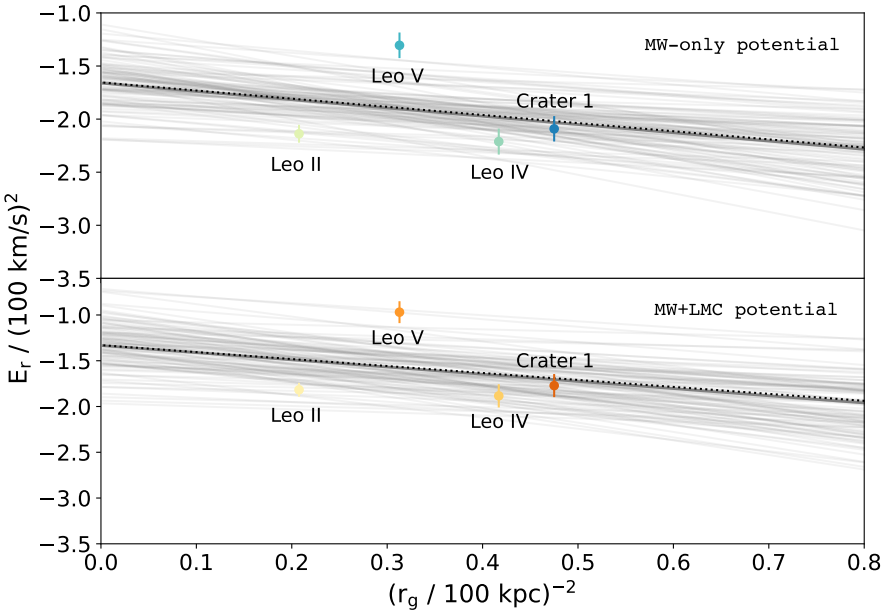


FIGURE 2.6: E_r plotted against r^{-2} after removing Crater II from the group. The coloured points represent the measured quantities and the associated uncertainties for each object. The grey solid line shows the fit that we get from the Lynden-Bell method by assuming that the objects under study share E and h. The dashed lines represent the mean fit obtained from the MCMC method, with the thin solid lines representing 100 random realisations of it. **Top:** Fit using MW-only potential potential. **Bottom:** Fit using the MW+LMC potential.

measured orbits closer to the predicted ones. Figure 2.D.1 of the Appendix shows the same thing but for the face-on view of the orbits.

When we include the LMC in the potential, the pericentres of the satellites no longer happen at the same time, but rather one at a time, with an increased time with decreasing distance to the MW. The proper motion of Leo V is still too unconstrained to reach such conclusions since this object appears to be on first infall into the MW throughout its orbit history when we consider the most likely PM. If this was the real orbit of this dwarf galaxy, then it would mean that this object is just passing close to the MW at the present time, and by chance, ended up close to the other objects. The orbital parameters that we get for this galaxy also show this, since we get unreasonable values for the parameters and extremely large errors. However, when we look at the possible orbits within the observational errors, some orbits are bound, for both the *Gaia* and the HST proper motions. Considering only those, Leo V is also at its apocentre at the present time. When we look back in time, its pericentre matches the time when the other objects also reached their pericentres.

Figure 2.9 shows the separation of Leo IV, Leo V and Crater 1 with respect to Leo II, for the MW-only potential and the MW+LMC potential. We use the *Gaia* DR3 proper motion to get the orbit of Leo II since it is the closest to the prediction. This helps us to understand how close the other objects have been to Leo II during their orbital history. In the MW-potential, if we consider the HST proper motion for Leo IV, this object gets as close as $\approx$ 20 kpc to Leo II $\sim$ 3 Gyr ago. However, if we consider the *Gaia* proper motion, both Leo IV and Crater 1 are closer to Leo II $\sim$ 2 Gyr ago for the MW-only potential, and $\sim$ 2 Gyr ago for the MW+LMC potential. However, all of them are close to Leo II at the present time. This time, the predicted orbit is quite similar for Crater 1 when we consider the MW-only potential. Looking at Leo IV, the prediction follows the behaviour obtained with both potentials. But, for Leo V, once again, most orbits are unbound due to the high uncertainties of the proper motions. Yet, looking only at the bound orbits, they also follow the same behaviour as the prediction, especially for the MW+LMC potential, which is another indicator that these objects were indeed accreted as a group. Our preferred orbits, indicated by the black lines, have the galaxies at comparable distances from each other some $\sim$ 3 Gyr ago as they are today. This is consistent with our finding that there is a physical association between these galaxies, and that they are not just a chance alignment at the present time. Further back in time, our orbit calculations show a trend of increasing distances. This is opposite to what may be expected (namely that the galaxies were closer together

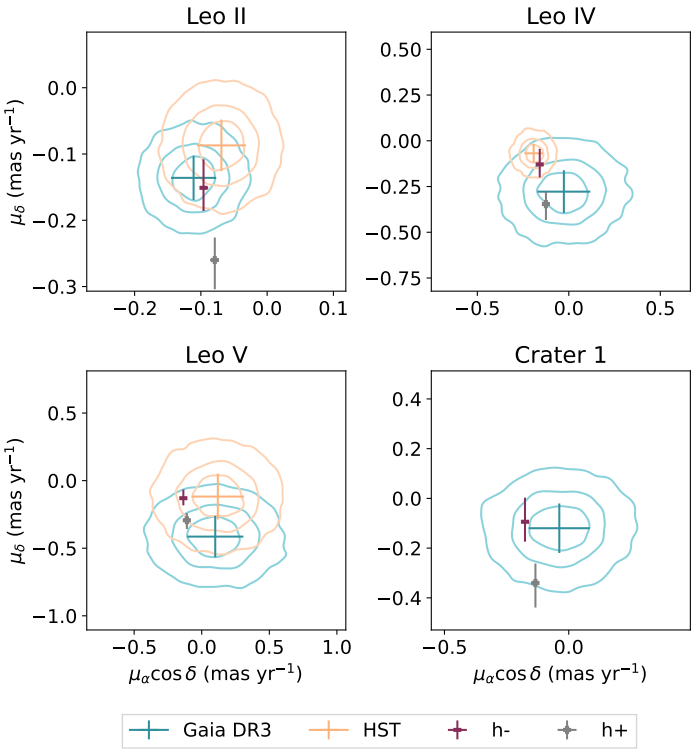


FIGURE 2.7: Predicted proper motions of the Crater-Leo objects without Crater II. The grey plus symbol and magenta minus symbol represent the predictions obtained with the positive $h+$ and negative $h-$ circulation about the northern pole, respectively. The blue crosses represent the measured proper motions from *Gaia* DR3 with their uncertainties and the orange crosses represent the proper motion measurements from HST. The corresponding contours correspond to the 34%, 68%, and 95% confidence levels for the 2D distribution of the proper motion parameter space.

in the past, and have suffered subsequent diffusion and phase mixing). However, this could easily be due to shortcomings in our orbit calculations, which, e.g. do not account for dynamical friction from the MW, or to hierarchical growth of the MW mass over cosmological timescales. Furthermore, the mutual gravity of the objects was not considered, and since Leo II is more massive than the rest of the objects, it can have an effect on their proximity when we look at their mutual separation.

In both plots 2.8 and 2.9, it is possible to see that for all objects, there are orbits within the observational uncertainties that make no physical sense for bound satellites, for the same reasons previously stated for Leo V. Evidently, the subset of allowed orbits is smaller for the objects with larger errors. When we compare only the bound orbits with the orbits derived from the predicted PMs, they are similar. This means that the physically allowed orbits for our objects are consistent with the ones that we get when we assume that they share similar specific angular energy and angular momentum. Besides being consistent with the observations, our predictions also provide a physical explanation for the coherence among the Crater-Leo objects.

We can now look at the derived orbital parameters (namely pericentre, $r_{\rm peri}$, apocentre, $r_{\rm apo}$, eccentricity, e, and time since the last pericentre, $t_{\rm peri}$) of the Crater-Leo objects. To determine the errors in the parameters, we draw 10^4 Monte Carlo samples as before. We use the coordinates, distances and velocities described in Table 2.1 and their corresponding errors for this purpose. The results that we get are summarised in Table 2.4. For Leo IV and Leo V, we also compare the derived properties that we get using our HST proper motions. Since some orbits that we get within the uncertainties are unbound (as can be seen in Figure 2.8), we only consider the bound orbits to perform this calculation. The unbound orbits are likely not physical, but instead due to the very uncertain nature of the proper motion measurements of the objects. Furthermore, since the most likely orbit of Leo V – for both the HST and *Gaia* measurements – is unbound, we consider the mean value of the MC realisations as the central value instead. For consistency, we do this for all objects. Once again, we only derive the orbital properties using the predicted proper motions assuming $h-$ since a common group accretion requires a common orbiting direction and the objects prefer this one. For the latter, the errors were estimated taking into account the error in all parameters except the proper motions.

As anticipated, taking into account that the predicted PMs for both potentials are nearly identical, the orbital properties obtained using these values are quite similar.

We can compare these values with the ones derived by Fritz et al. (2018) since they use the same MW-only potential. However, they use *Gaia* DR2 to obtain them, and the proper motions of the

TABLE 2.4: Derived orbital parameters of Crater-Leo objects: the pericentre ($r_{\rm peri}$), apocentre ($r_{\rm apo}$), and eccentricity (e).

MW-only	$r_{\rm peri}$ (kpc)			$r_{\rm apo}$ (kpc)			e			$t_{\rm peri}$ (Gyr)			Bound orbits (%)	
Object	*Gaia*	HST	Predicted	*Gaia*	HST	Predicted	*Gaia*	HST	Predicted	*Gaia*	HST	Predicted	*Gaia*	HST
Leo II	71^{+26}_{-18}	-	48^{+16}_{-10}	226^{+9}_{-9}	-	225^{+7}_{-7}	$0.55^{+0.11}_{-0.10}$	-	$0.66^{+0.07}_{-0.08}$	$-2.1^{+0.1}_{-0.1}$	-	$-1.9^{+0.1}_{-0.1}$	83%	-
Leo IV	87^{+24}_{-24}	110^{+14}_{-25}	56^{+16}_{-10}	176^{+60}_{-10}	185^{+54}_{-10}	156^{+6}_{-5}	$0.39^{+0.16}_{-0.11}$	$0.27^{+0.13}_{-0.06}$	$0.48^{+0.08}_{-0.09}$	$-1.3^{+0.5}_{-0.4}$	$-1.2^{+0.3}_{-0.2}$	$-1.6^{+0.1}_{-0.1}$	70%	91%
Leo V	93^{+17}_{-24}	87^{+18}_{-23}	40^{+13}_{-8}	236^{+33}_{-16}	234^{+34}_{-15}	207^{+10}_{-8}	$0.47^{+0.13}_{-0.04}$	$0.49^{+0.13}_{-0.05}$	$0.62^{+0.06}_{-0.06}$	$-1.2^{+0.2}_{-0.1}$	$-1.2^{+0.2}_{-0.1}$	$-1.3^{+0.1}_{-0.1}$	14%	19%
Crater 1	76^{+24}_{-20}	-	59^{+15}_{-9}	154^{+53}_{-7}	-	145^{+5}_{-4}	$0.39^{+0.16}_{-0.11}$	-	$0.43^{+0.07}_{-0.08}$	$-1.8^{+0.5}_{-1.3}$	-	$-1.6^{+0.1}_{-0.1}$	70%	-
MW+LMC														
Leo II	111^{+11}_{-20}	-	48^{+18}_{-10}	217^{+23}_{-10}	-	225^{+7}_{-7}	$0.41^{+0.13}_{-0.09}$	-	$0.66^{+0.07}_{-0.08}$	$-1.8^{+0.1}_{-0.3}$	-	$-2.0^{+0.1}_{-0.1}$	77%	-
Leo IV	81^{+27}_{-18}	94^{+8}_{-16}	56^{+16}_{-10}	163^{+56}_{-10}	163^{+50}_{-10}	156^{+6}_{-5}	$0.42^{+0.14}_{-0.16}$	$0.34^{+0.14}_{-0.09}$	$0.48^{+0.08}_{-0.09}$	$-1.6^{+0.6}_{-1.2}$	$-1.2^{+0.1}_{-0.3}$	$-1.6^{+0.1}_{-0.1}$	65%	97%
Leo V	111^{+18}_{-30}	100^{+23}_{-27}	50^{+13}_{-9}	198^{+54}_{-14}	184^{+51}_{-12}	207^{+10}_{-8}	$0.32^{+0.18}_{-0.09}$	$0.35^{+0.17}_{-0.10}$	$0.62^{+0.06}_{-0.06}$	$-1.3^{+0.3}_{-0.5}$	$-1.5^{+0.4}_{-0.4}$	$-1.3^{+0.1}_{-0.1}$	17%	26%
Crater 1	52^{+27}_{-14}	-	59^{+15}_{-9}	154^{+26}_{-6}	-	145^{+5}_{-4}	$0.54^{+0.12}_{-0.13}$	-	$0.43^{+0.07}_{-0.08}$	$-2.3^{+0.5}_{-1.0}$	-	$-1.6^{+0.1}_{-0.1}$	78%	-

Notes. We compare the derived orbital parameters using the proper motions described in Table 2.2 (*Gaia* DR3) with the ones derived using the predicted proper motions with the Lynden-Bell method described in Sect. 2.4.2 (Predicted). For Leo IV and Leo V, we also derive the orbital parameters using our new HST proper motions (HST). For all the derived orbital parameters, the properties described in Table 2.1 were used. We also mention the percentage of bound orbits that we get for each object. We do this for both the MW-only potential and the MW+LMC potential.

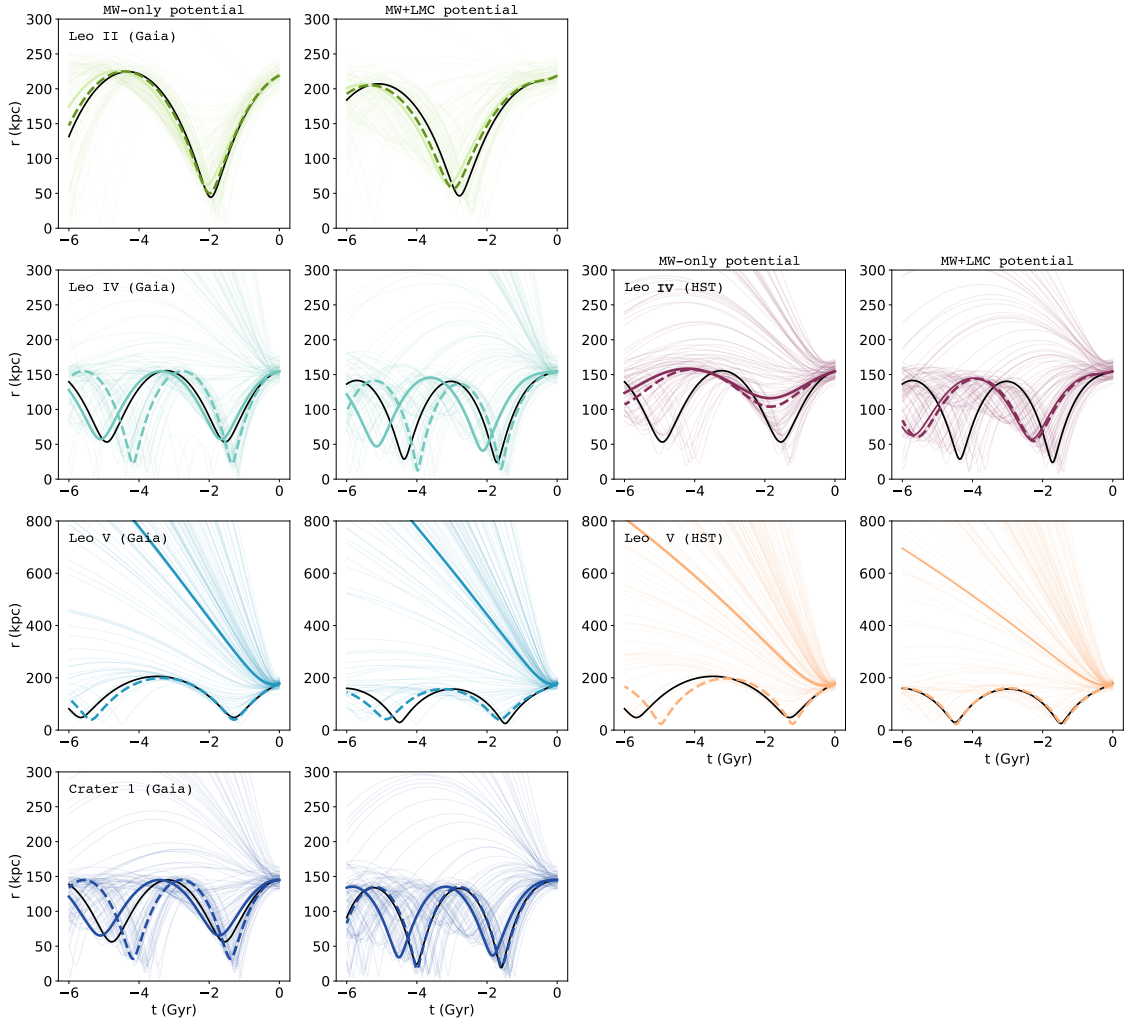


FIGURE 2.8: Orbital evolution for the proposed group integrating backwards in time for 6 Gyr using both the MW-only potential and the MW+LMC potential. The thick lines indicate their most likely orbit from the measured proper motions and the thinner lines represent 100 Monte-Carlo realisations within their uncertainties. The black solid lines represent the orbital evolution obtained using the predicted proper motions for each object. The dashed lines represent the mean orbital evolution obtained using only the bound orbits.

objects under consideration have larger errors in their data. Their derived parameters are described in Table 2.5. Our derived values for both the predicted proper motions and the measured ones match their values within the errors. The proper motions of Leo V, even when considering our new HST ones, are too unconstrained. This biases the derived orbital properties to higher values when we consider the MW-only potential. We can also compare our derived orbital parameters with Battaglia et al. (2022), since we use their *Gaia* DR3 PMs. However, we assume a slightly different MW mass and we remove the unbound orbits and that leads to slightly different results. They use a light ($M_{\rm MW} = 0.9 \times 10^{12} {\rm M}_{\odot}$) and a heavy potential ($M_{\rm MW} = 1.6 \times 10^{12} {\rm M}_{\odot}$) for the MW, and our results are closer to the ones obtained by assuming a lighter potential, since our assumed mass is closer to that one ($M_{\rm MW} = 0.8 \times 10^{12} {\rm M}_{\odot}$).

2.4.6 Effect of the LMC on the orbital poles

It was argued in Garavito-Camargo et al. (2021) that the infall of a massive LMC can perturb the MW halo, affecting the orbital poles of its satellites. This happens because, as described in Gómez et al. (2015), as the LMC passes through its pericentre, the orbital barycentre of the MW-LMC system shifts away from the centre of the MW's disc. Consequently, the resulting reflex motion of the disc

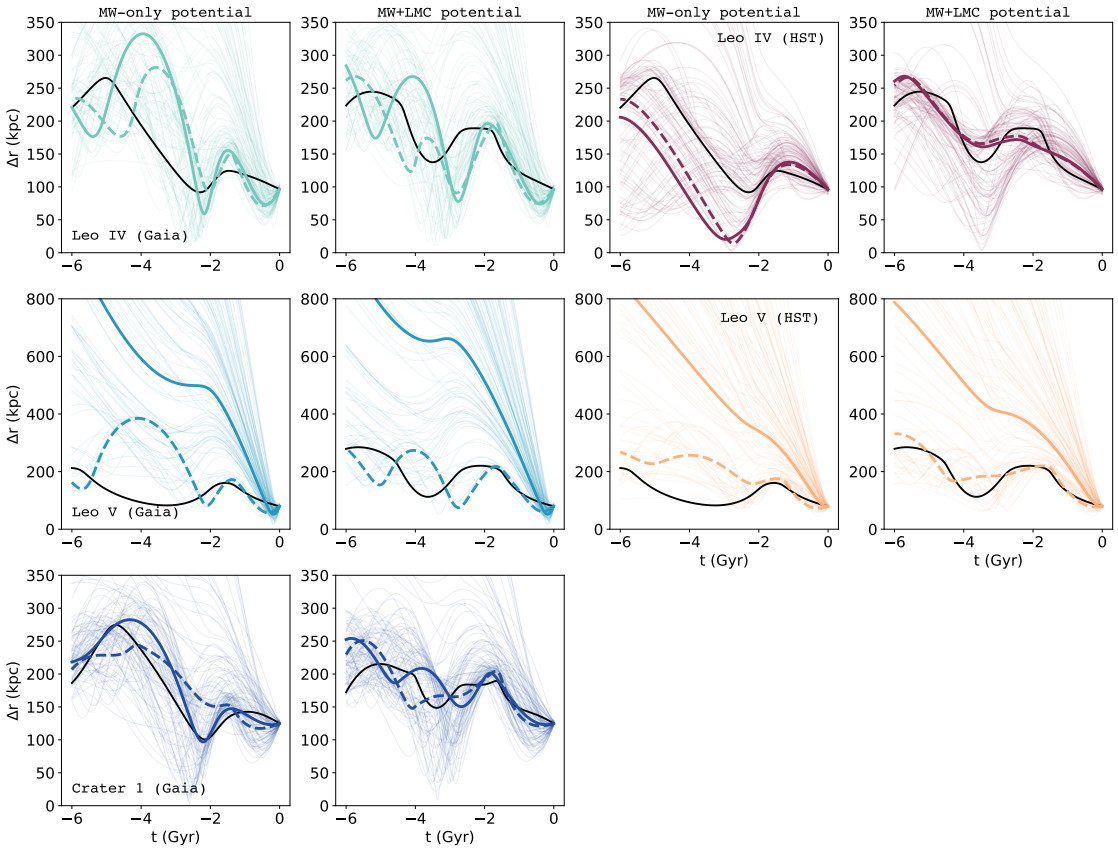


FIGURE 2.9: Orbital evolution for the proposed group integrating backwards in time for 6 Gyr for the mutual separation of the objects in relation to Leo II using both the MW-only potential and the MW+LMC potential. The thick lines indicate their most likely orbit from the measured proper motions and the thinner lines represent 100 Monte-Carlo realisations within their uncertainties. The black solid lines represent the orbital evolution obtained using the predicted proper motions for each object. The dashed lines represent the mean orbital evolution obtained using only the bound orbits.

is represented by an all-sky dipole pattern in radial velocities (e.g. Garavito-Camargo et al., 2019; Gómez et al., 2015; Petersen & Peñarrubia, 2020).

In Garavito-Camargo et al. (2021), they reproduce this behaviour by adopting different reference centres of mass for different radial shells, consequently changing the positions and velocities of the satellites. Similarly to Pawlowski et al. (2022), we invert the approach of Garavito-Camargo et al. (2021) and subtract the shifts from the observed MW dwarf galaxies created by the LMC influence. Following the method described in Pawlowski et al. (2022), we reproduce the centres of mass shifts from plots 4 and 6 of Garavito-Camargo et al. (2021) and subtract the respective distance-dependent values from the Cartesian positions and velocities of the observed MW satellites (previously described in Table 2.1). This allows us to determine the positions and velocities that the satellites would have had relative to the centre of the MW dark matter halo if the MW at the centre was not affected by the nearby LMC. These new values are described in Table 2.E.1 of the Appendix, as well as a Figure 2.E.1 that shows these shifts.

Here, we repeat the previous analysis to get proper motion predictions taking into account this shift, but this time only with the MW-only potential, since we are hypothesising that our group fell onto the MW halo before the LMC.

Figure 2.10 shows the new fits that give us $h_0 = 1.43 \times 10^4$kpc km s^{-1} and specific energy of $E_0 = -2.54 \times 10^4$km^{2}s^{-2} when we include Crater II, and $h_0 = 2.11 \times 10^4$kpc km s^{-1} and specific energy of $E_0 = -2.07 \times 10^4$km^{2}s^{-2} when we remove it. Again, applying the MCMC method described in Sect. 2.3.2, gives $h_0 = 1.44^{+0.27}_{-0.32} \times 10^4$ kpc km s^{-1}, $E_0 = -2.53^{+0.22}_{-0.22} \times 10^4$ km^{2}s^{-2} and $h_0 = 2.12^{+0.19}_{-0.21} \times 10^4$ kpc km s^{-1}, $E_0 = -2.06^{+0.18}_{-0.18} \times 10^4$ km^{2}s^{-2}, with and without Crater II, respectively. Contrary to what happened before when we removed this object, this time the specific angular momentum and energy increase after removing it. From this figure, it is possible to see that the alignment with a

TABLE 2.5: Pericentre (r_{peri}), apocentre (r_{apo}), and eccentricity (e) derived from *Gaia* DR2 proper motions from Fritz et al. (2018).

Object	r_{peri} (kpc)	r_{apo} (kpc)	e
Leo II	67^{+154}_{-52}	248^{+613}_{-26}	$0.67^{+0.26}_{-0.39}$
Leo IV	153^{+8}_{-87}	26071^{+46619}_{-25908}	$0.989^{+0.007}_{-0.56}$
Leo V	168^{+12}_{-104}	27704^{+45671}_{-27495}	$0.988^{+0.007}_{-0.46}$
Crater 1	81^{+65}_{-70}	159^{+7932}_{-16}	$0.68^{+0.3}_{-0.43}$

linear fit becomes much better (see plots 2.4 and 2.6) when we include this effect. The corner plots of the posterior distributions for the energy and angular momentum for both potentials can be seen in Figure 2.E.2 of the Appendix 2.E.

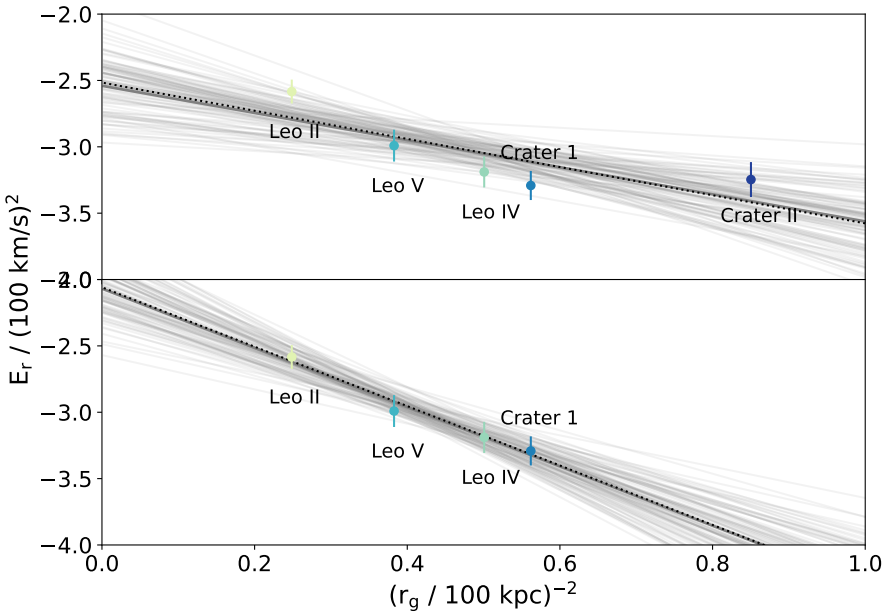


FIGURE 2.10: E_r plotted against r^{-2} after applying the shifts to the positions and velocities from Garavito-Camargo et al. (2021). The coloured points represent the shifted quantities and the associated uncertainties for each object. The grey solid line shows the fit that we get from the Lynden-Bell method by assuming that the objects under study share E and h. The dashed lines represent the mean fit obtained from the MCMC method, with the thin solid lines representing 100 random realisations of it. **Top:** Fit considering the original proposed group. **Bottom:** Fit after removing Crater II.

To compare our predictions with the measured proper motions, we shift them back to the reference frame of the MW centre. As before, the prediction for Crater II is far from the measured one, so we can continue to assume that this object was not accreted with the rest of the group, even if the group was indeed accreted before the LMC. The predictions that we get when we include and exclude this dwarf are both represented in Figure 2.11. Interestingly, this time, when we consider Crater II as a member, the predicted proper motions that we get in both orbital directions are identical. When we look only at the *Gaia* DR3 measurements, it even looks like Leo II and Leo V might prefer the positive circulation in this scenario. However, their proper motions are so unconstrained that the negative circulation is consistent with $1-2\sigma$ errors. Furthermore, when we remove Crater II, the closest prediction to all the remaining objects is the one that we get when we consider a negative circulation. Since group infall requires a common orbital direction, once again the results lean towards a negative circulation about the northern pole.

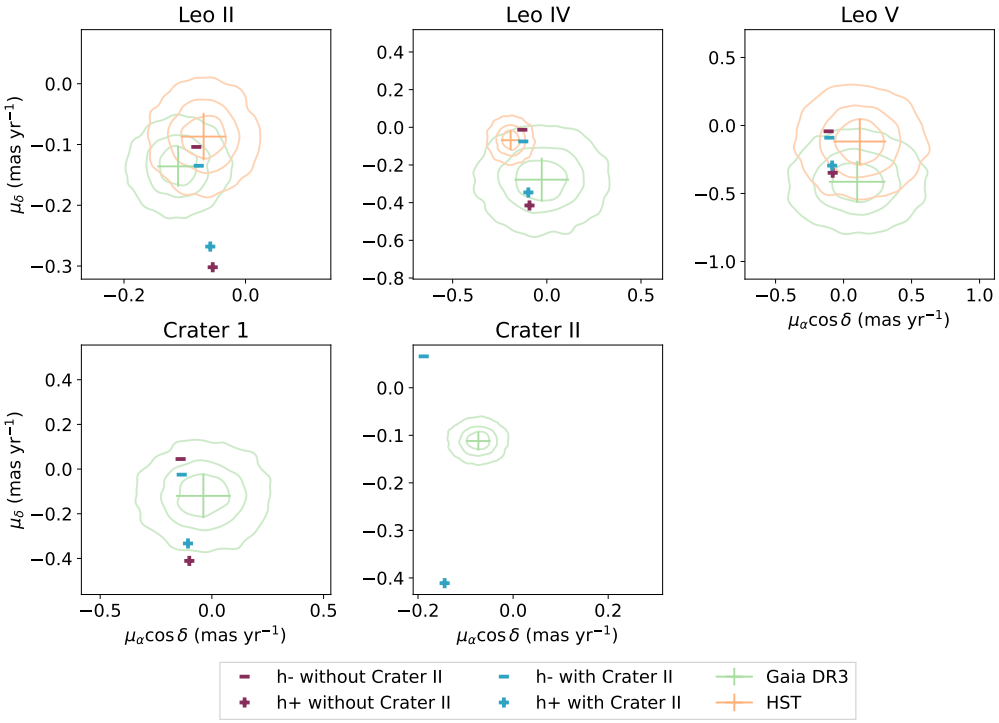


FIGURE 2.11: Predicted proper motions of the Crater-Leo objects that we get when we consider the shifts from Garavito-Camargo et al. (2021), after shifting them back to the current centre of mass of the MW. The magenta plus and minus symbols represent the predictions obtained with the positive $h+$ and negative $h-$ circulation about the northern pole, respectively, when we consider Crater II as part of the group. The light-blue plus and minus symbols represent the predictions obtained with the negative $h-$ and positive $h+$ circulation about the northern pole, respectively, when we exclude Crater II. The green crosses represent the measured proper motions from *Gaia* DR3 with their uncertainties and the orange crosses represent the proper motion measurements from HST. The corresponding contours correspond to the 34%, 68%, and 95% confidence levels for the 2D distribution of the proper motion parameter space.

2.5 Discussion and Conclusions

We used up-to-date data to infer whether or not the dwarfs Leo II, IV, V, and Crater II as well as the star cluster Crater 1 were accreted as a group onto the MW halo, as suggested by Torrealba et al. (2016). We present new measurements for the proper motions of Leo IV and Leo V dwarf galaxies using multi-epoch HST imaging data. Our final results for the PMs are $(\mu_{\alpha*}, \mu_\delta) = (-0.1921 \pm 0.0514, -0.0686 \pm 0.0523)$ mas yr^{-1} for Leo IV and $(\mu_{\alpha*}, \mu_\delta) = (0.1186 \pm 0.1943, -0.1183 \pm 0.1704)$ mas yr^{-1} for Leo V.

We start by determining the orbital poles of the putative group with the proper motions available from *Gaia* DR3, and the new HST proper motions presented in this paper. The possible orbital poles suggest that these objects can share a common value for their specific angular momentum within their uncertainties. When we take into account the new HST proper motion measurements, a common orbital pole becomes even more likely.

We used the method proposed by Lynden-Bell & Lynden-Bell (1995) to predict the proper motions of the considered satellites, assuming that they share a common group origin. Our proper motion predictions are consistent with the measured proper motions within the errors for most of the proposed members. Based on *Gaia* DR3 measurements alone, the predictions of the proper motions for Leo IV and Leo V seem to prefer the positive circulation about the northern pole. In contrast, Leo II and Crater 1 predictions clearly favour the negative circulation. However, a common group accretion requires a common orbiting direction. When we consider our new HST measurements, this changes and all four objects prefer the one co-orbiting direction ($h-$). Better proper motion measurements with lower uncertainties are required to confirm this association with higher confidence.

Crater II, however, has a well-constrained proper motion and does not share a similar orbital pole with the rest of the objects, nor does it match our proper motion predictions. Furthermore, Crater II

is the object with the highest offset from the common value of the line-of-sight velocity shared by the group. We can therefore rule out an association with the other members.

Other objects were identified as possible additional members of the Crater-Leo group due to their orbital poles. Nevertheless, their proper motion predictions are far from the measured ones, suggesting that they were not part of it.

Based on HST and *Gaia* DR3 proper motions, we performed orbital analyses for the four satellites that we consider as possibly associated, namely Leo II, Leo IV, Leo V, and Crater 1, in order to try to understand whether or not they have a shared orbital history and to look for possible evidence that the objects were bound in the past. For both considered potentials, all objects are near their apocentre at the present time. All objects are consistent with having reached their pericentre around the same time, within their uncertainties. When we look at the separation of Leo IV, Leo V, and Crater 1 with respect to Leo II, they were all at comparable distances from each other ~ 3 Gyr ago, suggesting that there is a physical association between these objects and not just a chance alignment at the present time. The derived orbital properties are consistent – within their observational uncertainties — with those we predict from assuming group infall, especially when we compare with the properties obtained with our new HST proper motions.

We show that the bound orbits derived from the observational uncertainties match the orbits derived from the predicted PMs. These are the orbits that not only have PMs consistent with observations, but that also have similar specific energy and angular momentum. Our assumptions can therefore explain why these align along a great circle at the present time.

When we consider the effect that the infall of the LMC might have had on the orbital properties of our putative group, we find that the probability of the objects sharing the same specific angular momentum and specific energy increases. Once again, it seems that Crater II was not accreted with the other satellites. When we shift our predicted proper motions back to the centre of mass of the current MW halo to compare with the current measurements, we get similar results to the previous ones, suggesting that the infall of the LMC did not have a strong effect on the orbital poles of the considered objects, which is not surprising, as they largely reside on the opposite side of the MW. The predictions that the proper motions seem to prefer the negative circulation about the northern pole are strengthened when we consider the new proper motion measurements.

Leo II, Leo IV, Leo V, and Crater 1 show orbital properties that are consistent with those we predict from assuming group infall; however, the uncertainties on the current proper motion measurements with both *Gaia* and HST are too high to conclusively confirm their dynamical associations. The next data releases for *Gaia* will likely reduce both the systematic and random uncertainties for these objects. Furthermore, with an increased time baseline, proper motion measurements using future HST or JWST observations will provide a definitive answer as to whether or not (some of) the Crater-Leo objects constitute the first identified case of a cosmologically expected, typical group infall event. Time is on our side.

Acknowledgements

MPJ and MSP acknowledge funding via a Leibniz-Junior Research Group (project number J94/2020). MPJ thanks Gurtina Besla for the helpful advice. MPJ thanks Nuno Humberto for the valuable discussions and suggestions. MPJ thanks the "Summer School for Astrostatistics in Crete" for providing training on the statistical methods adopted in this work. This research has made use of agama (Vasiliev, 2019), Astropy (Astropy Collaboration et al., 2022), corner.py (Foreman-Mackey, 2016), galpy (Bovy, 2015), matplotlib (Hunter, 2007), NASA's Astrophysics Data System Bibliographic Services, NumPy (Harris et al., 2020) and SciPy (Virtanen et al., 2020). Based on observations made with the NASA/ESA *Hubble* Space Telescope, obtained from the Data Archive at the Space Telescope Science Institute (STScI). Support for this work was provided by NASA through grants for programs GO-14770 and 15507 from STScI, which is operated by the Association of Universities for Research in Astronomy (AURA), Inc., under NASA contract NAS5-26555. These projects are part of the HSTPROMO (High resolution Space Telescope PROper MOtion) Collaboration, a set of projects aimed at improving our dynamical understanding of stars, clusters, and galaxies in the nearby Universe through measurement and interpretation of proper motions from HST, *Gaia*, and other space observatories. We thank the collaboration members for sharing their ideas and software.

Appendix

2.A Intrinsic scatter

The intrinsic scatter of the putative group was determined by the method described in Sect. 2.3.2. Here, the posterior distributions of h_0, E_0 and σ_{is_0} are represented for both potentials (MW-only, in blue and MW+LMC, in orange), for both the cases with (Fig. 2.A.1) and without Crater II (Fig. 2.A.2).

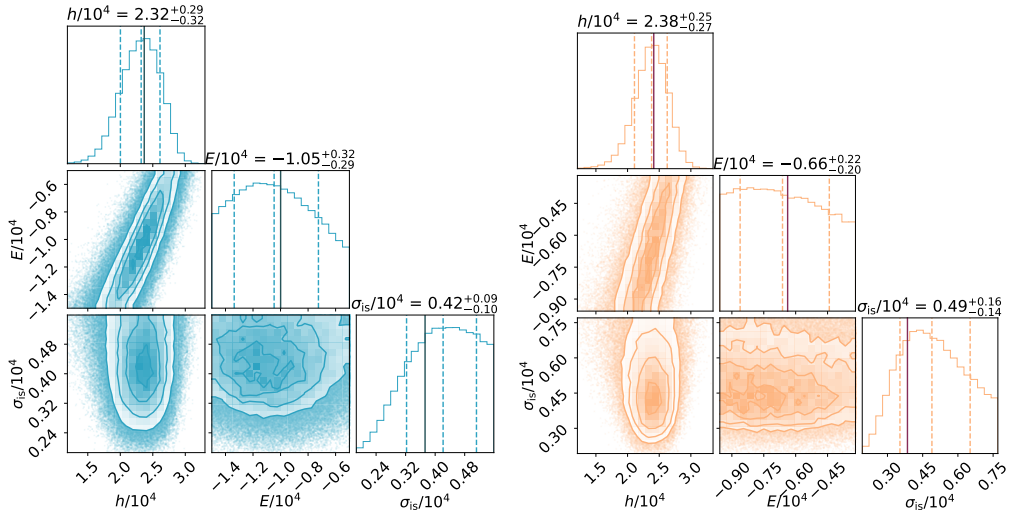


Figure 2.A.1: Posterior distributions for h_0, E_0 and σ_{is_0} for the putative group after removing Crater II. The histograms along the diagonal represent the posterior distribution for each parameter. Their units are omitted for clarity. The vertical dashed lines indicate the median and 68% confidence interval. The bottom left panel represents the 2D posterior distribution of these parameters, with the contours corresponding to the 0.5σ, 1σ, 1.5σ, and 2σ confidence levels, where σ is the standard deviation of the 2D distribution. The solid lines represent the values for h_0 and E_0 that we get from the fit of the Lynden-Bell method. **Top:** Results considering the MW-only potential. **Bottom:** Results considering the MW+LMC potential.

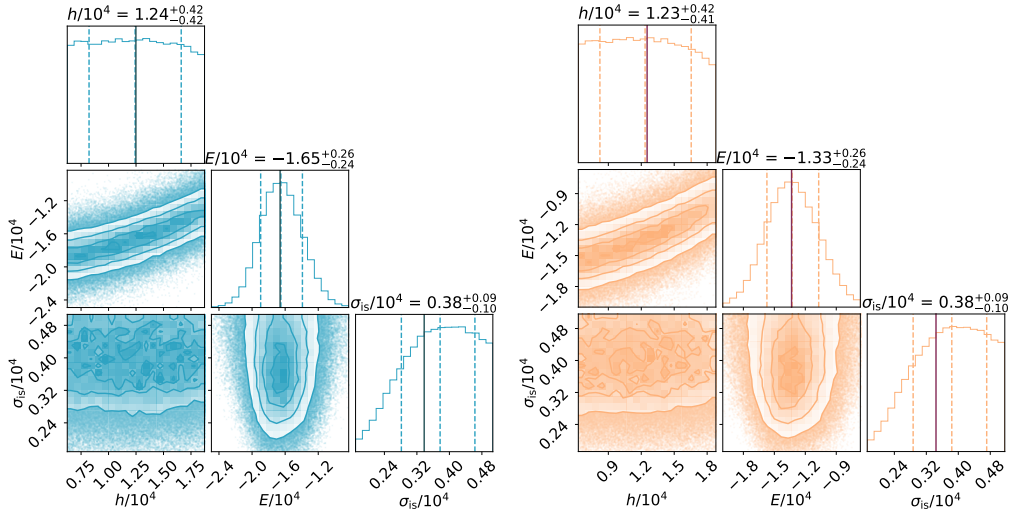


Figure 2.A.2: Posterior distributions for h_0, E_0 and σ_{is_0} for the putative group after removing Crater II. The histograms along the diagonal represent the posterior distribution for each parameter. Their units are omitted for clarity. The vertical dashed lines indicate the median and 68% confidence interval. The bottom left panel represents the 2D posterior distribution of these parameters, with the contours corresponding to the 0.5σ, 1σ, 1.5σ, and 2σ confidence levels, where σ is the standard deviation of the 2D distribution. The solid lines represent the values for h_0 and E_0 that we get from the fit of the Lynden-Bell method. **Top:** Results considering the MW-only potential. **Bottom:** Results considering the MW+LMC potential.

2.B Effect of the MW mass

Since the mass of the MW is still unconstrained, here, we check what happens to the predicted proper motions when we increase its mass. As can be seen in Figure 2.B.1, the predictions slightly change but the conclusions remain the same. We decided to plot only the proper motions obtained with the negative $h-$ direction since our whole analyses show that this is the preferred direction of the group.

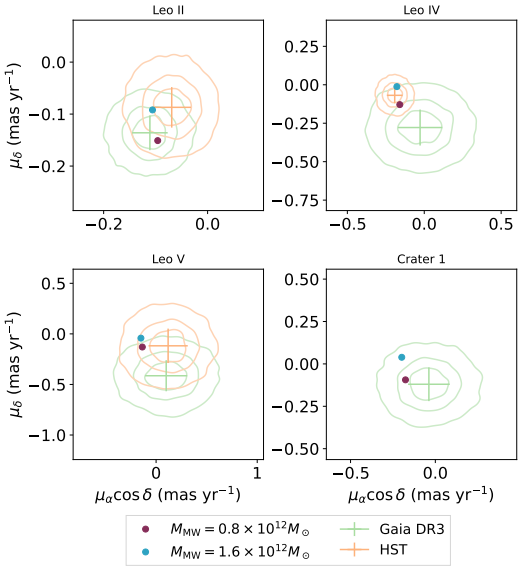


FIGURE 2.B.1: Predicted proper motions of the Crater-Leo objects for different masses of the MW. The magenta and blue dots represent the predictions obtained with $M_{MW} = 0.8 \times 10^{12} M_\odot$ and $M_{MW} = 1.6 \times 10^{12} M_\odot$, respectively. For both we assume the negative $h-$ circulation about the northern pole. The green crosses represent the measured proper motions from *Gaia* DR3 with their uncertainties and the orange crosses represent the measured proper motions from HST. The contours correspond to the 34%, 68% and 95% confidence levels for the 2D distribution of the proper motion parameter space.

2.C Additional members

The possible additional members of the group were determined by the previously described method, in Sect. 2.3.3, taking into account their orbital pole positions. Here, we can find the comparison between the predictions that we get for each object, assuming a group with Crater 1, Leo II, Leo IV and Leo V, plus one of the possible additional members. For simplicity, only the predictions for the additional members are displayed.

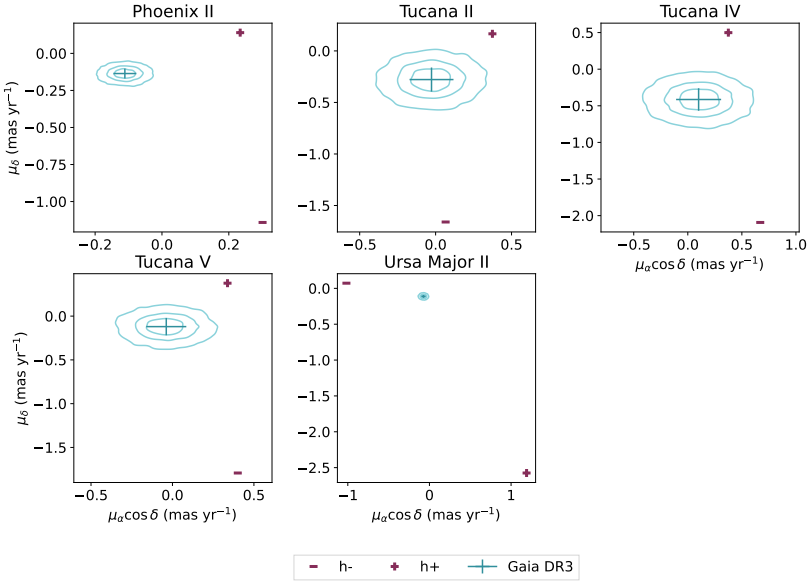


FIGURE 2.C.1: Predicted proper motions of the possible additional members of the Crater-Leo group. The magenta "-" and "+" symbols represent the predictions obtained with the negative $h-$ and positive $h+$ circulation about the northern pole, respectively. The green crosses represent the measured proper motions from *Gaia* DR3 with their uncertainties. The contours correspond to the 34%, 68% and 95% confidence levels for the 2D distribution of the proper motion parameter space.

2.D Orbital histories

In Sect. 2.4.5 we discussed the orbital histories of the Crater-Leo objects for both the MW-only and the MW-LMC potential. Here, we show supplementary plots to support the results discussed in the main text.

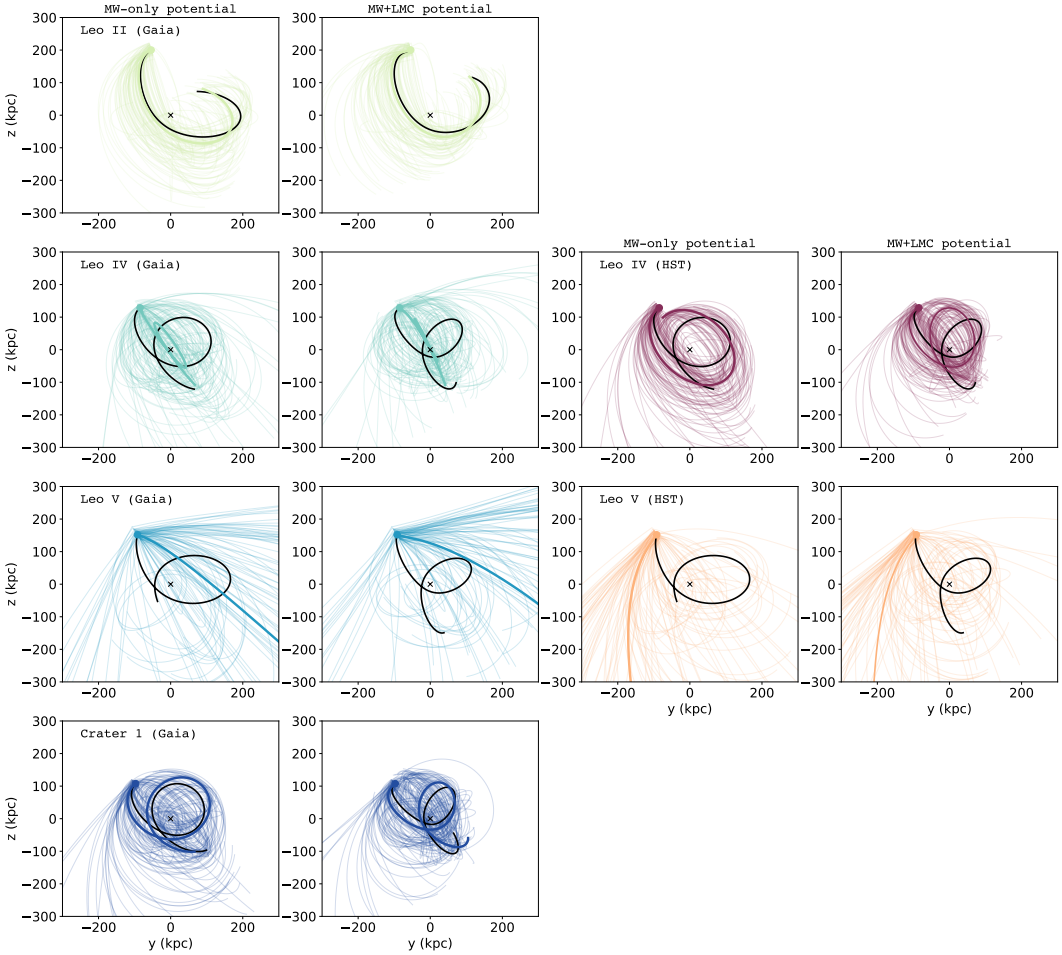


Figure 2.D.1: Orbital evolution for the proposed group up to 6 Gyr in the Galactocentric Cartesian $Y - Z$ plane using both the MW-only potential and the MW+LMC potential. The thick lines indicate their most likely orbit and the thinner lines represent 100 Monte-Carlo realisations. The black solid line represents the orbital evolution obtained using the predicted proper motions for each object.

2.E Effect of the LMC

Table 2.E.1: New positions in Galactocentric coordinates and velocities of the Crater-Leo objects after applying the shifts from Garavito-Camargo et al. (2021).

Object	x	y	z	v_x	v_y	v_z
		(kpc)			(kms^{-1})	
Leo II	−68.4	−35.3	185.2	−48.3	67.4	−22.5
Leo IV	−13.2	−78.7	116.6	92.6	16.5	−24.0
Leo V	−18.8	−81.7	138.2	246.0	−76.8	9.9
Crater 1	1.5	−92.3	96.3	42.6	83.4	20.8
Crater II	12.2	−82.7	69.1	23.6	127.8	−22.5

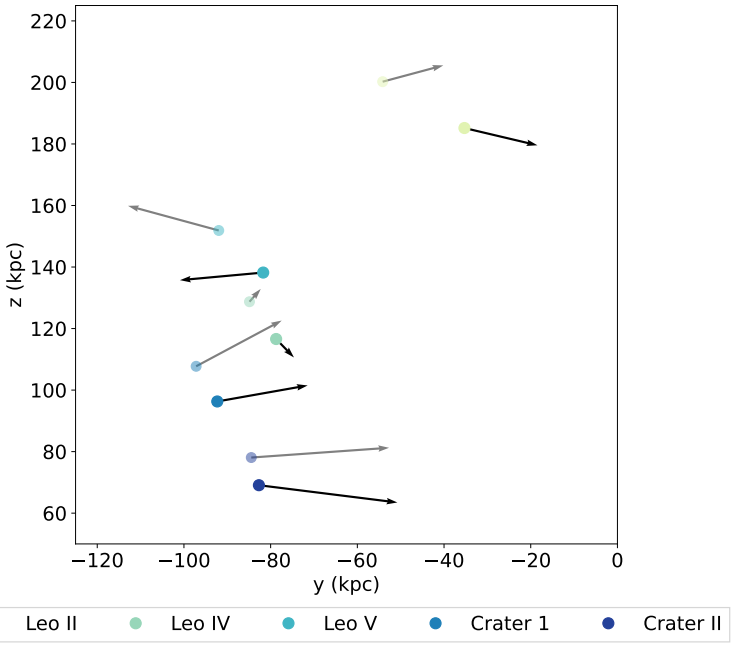


FIGURE 2.E.1: Positions and velocities (as vectors) of the Crater-Leo objects. The bigger markers correspond to the position/velocity after applying the shifts from Garavito-Camargo et al. (2021) and the smaller and fainter markers indicate the current measurements.

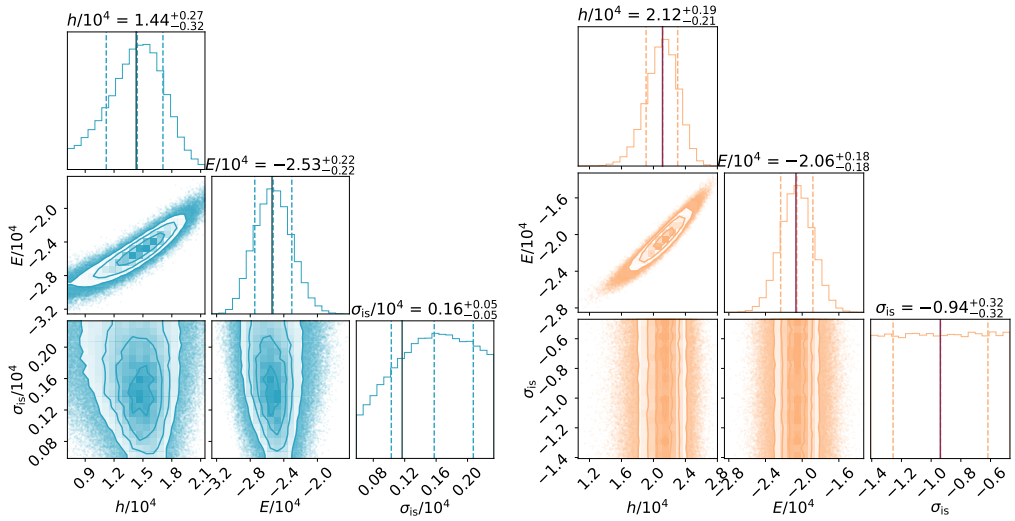


FIGURE 2.E.2: Posterior distributions for h_0, E_0 and σ_{is_0} for the putative group considering the LMC effect. The histograms along the diagonal represent the posterior distribution for each parameter. Their units are omitted for clarity. The vertical dashed lines indicate the median and 68% confidence interval. The bottom left panel represents the 2D posterior distribution of these parameters, with the contours corresponding to the 0.5σ, 1σ, 1.5σ, and 2σ confidence levels, where σ is the standard deviation of the 2D distribution. The solid lines represent the values for h_0 and E_0 that we get from the fit of the Lynden-Bell method. **Top:** Results considering Crater II as part of the group. **Bottom:** Results excluding Crater II from the group.

3

Spatial and kinematic signatures of satellite pairs in the Local Group

Context. The satellite galaxies of the Local Group provide key insights into galaxy formation, evolution, and cosmology. The frequency of close satellite pairs, in particular, serves as a probe of group accretion and subhalo clustering, and previous studies have suggested potential tensions between observed pair frequencies and cosmological simulations.
Aims. We investigate the incidence and physical nature of satellite galaxy pairs in the Local Group using updated observational data for the Milky Way (MW) and Andromeda (M31), together with analogues from the HESTIA constrained cosmological simulations.
Methods. We identify nearest-neighbour pairs and assess their significance relative to the expected nearest-neighbour distribution from random isotropic populations that reproduce the radial distributions of each system. We complement this spatial selection with kinematic and dynamical diagnostics, including line-of-sight velocity differences, proper motion alignment (when available), and gravitational binding estimates.
Results. We find that the MW satellite system exhibits a significant excess of close associations relative to isotropic expectations, with a pairing efficiency of $\sim$ 53%, nearly a factor of two higher than in the HESTIA analogues ($\sim$ 17–27%). This excess remains when applying a stellar mass cut ($M_\star > 10^4 \mathrm{M}_\odot$) to match the resolution limits of the simulations. In contrast, the M31 satellite system shows no comparable clustering signal and remains broadly consistent with isotropy, with a pairing efficiency of $\sim$ 28%. Kinematic diagnostics indicate that only a subset of spatially selected pairs exhibit small line-of-sight velocity differences or aligned proper motions, and an even smaller fraction are consistent with being gravitationally bound. This demonstrates that many statistically significant nearest-neighbour associations correspond to transient configurations or remnants of disrupted groups rather than long-lived binaries.
Conclusions. These results suggest that the excess of satellite pairs in the MW reflects the presence of phase-space correlated structures associated with recent or ongoing group accretion (e.g. the Magellanic system), while M31 appears more consistent with typical ΛCDM expectations. The contrasting behaviour of the two hosts highlights the role of stochastic accretion histories, observational limitations, and mass completeness in shaping the apparent clustering of satellite galaxies.

M. P. Júlio, M. S. Pawlowski & N. I. Libeskind (to be submitted)

3.1 Introduction

Satellite galaxies are the low-mass companions that orbit more massive host galaxies such as the Milky Way (MW) and Andromeda (M31). In the hierarchical framework of Λ Cold Dark Matter (ΛCDM) cosmology, these systems are understood as the surviving remnants of smaller dark matter haloes accreted during the assembly of their hosts (Blumenthal et al., 1984; White & Rees, 1978). In this scenario, satellite galaxies are not necessarily accreted individually. Cosmological simulations predict that they can instead enter host haloes as members of larger satellite associations (Li & Helmi, 2008; Wetzel et al., 2015). Although tidal interactions with the host and dynamical processes such as phase mixing gradually disperse these associations into the general satellite population (Deason et al., 2014), remnants of their original configuration may persist as spatially or kinematically correlated pairs (Lynden-Bell & Lynden-Bell, 1995).

The presence of satellite pairs may also be connected to the larger-scale organisation of satellite systems in the Local Group. Observations of both the MW and M31 have revealed that their satellite populations are not distributed isotropically; instead, many satellites appear to reside in thin, spatially extended, and kinematically coherent structures known as planes of satellites (see Pawlowski, 2018, 2021b, for a review). The origin of the Vast Polar Structure (VPOS; Pawlowski et al., 2012; Pawlowski & Kroupa, 2014) around the MW and the Giant Plane of Andromeda (GPoA; Conn et al., 2013; Ibata et al., 2013) remains a subject of active debate, as such strong spatial and orbital alignments are rare in standard ΛCDM simulations (Pawlowski & McGaugh, 2014a). Group infall provides a potential mechanism for producing these correlated structures. If a significant fraction of satellites are accreted together as part of a pre-existing group, they may naturally share similar orbital planes and angular momentum vectors (Li & Helmi, 2008; Lynden-Bell & Lynden-Bell, 1995; Wang et al., 2013). Recent kinematic studies of the MW's satellite system further support this scenario, suggesting that a substantial fraction of the VPOS may have originated from a few major accretion events of dwarf galaxies (Taibi et al., 2024). A striking example is the first-passage of the Large Magellanic Cloud (LMC), as dynamical modelling suggests that the LMC likely brought with it a significant number of smaller satellites, many of which remain spatially and kinematically associated today (Vasiliev, 2023). In this context, satellite pairs may represent the most compact surviving remnants of these larger accretion events.

While galaxy pairs have long been used as a diagnostic of hierarchical growth for massive galaxies ($M_\star \gtrsim 10^{10}\mathrm{M}_\odot$; e.g. Duncan et al., 2019; Patton et al., 2002), the low-mass regime of satellite galaxy pairs have been less studied. In the literature, definitions of a "satellite pair" vary, ranging from simple distance–velocity thresholds (e.g. Besla et al., 2018; Stierwalt et al., 2017) to strict gravitational binding criteria (Sales et al., 2013). Regardless of the specific definition adopted, ΛCDM simulations predict that subhaloes are frequently accreted as groups (Wetzel et al., 2015), and cosmological simulations show non-zero fractions of surviving satellite pairs at the present day (Callingham & Helmi, 2025; Fattahi et al., 2013).

In the Local Group, several candidate satellite associations have been proposed over the past decades, mostly based on spatial proximity and line-of-sight velocities. Early examples include the Fornax–Leo–Sculptor system (Lynden-Bell, 1982), which was later expanded to include Sextans and Phoenix (Majewski, 1994). Perhaps the most prominent example of an interacting satellite pair in the Local Group is the Large and Small Magellanic Clouds, which are widely believed to have been accreted together as part of a common system (Besla et al., 2007; D'Onghia & Lake, 2008; Patel et al., 2020; Vasiliev, 2023). Beyond the Magellanic Clouds, several other possible associations have been discussed in the literature. More recent candidates include Pisces II and Pegasus III (Garofalo et al., 2021; Kim et al., 2015; Richstein et al., 2022), as well as the trio NGC 147, NGC 185, and Cassiopeia II around M31 (Arias et al., 2016; van den Bergh, 1998). A particularly intriguing association in the MW halo involves the Crater-Leo system. Initially proposed to include Leo IV and Leo V, whose proximity in space and velocity was noted by Jong et al. (2010), this group was later expanded to include Crater 1, Crater II, and possibly Leo II (Torrealba et al., 2016). Recent work has used *Gaia* and HST proper motions to assess this configuration, finding dynamical support for the group infall scenario for a subset of its members (**Júlio et al.**, 2024).

Outside of the Local Group, another striking candidate for a recent group accretion is the asymmetric satellite distribution of the M81 system, which Bell et al. (2022) interpret as evidence for the infall of a satellite group. A likely satellite pair was recently found around the NGC 4490 system, marking

a rare case of such an association identified beyond the Local Group (Pawlowski et al., 2024). On larger scales, Tully et al. (2006, 2002) identified spatial and kinematic associations of dwarf galaxies in the Local Volume, though these systems are generally more extended than typical satellite pairs.

However, establishing whether such systems represent real physical associations remains challenging. Many early suggestions were based primarily on projected spatial proximity and line-of-sight velocities, which provide only partial information about the true orbital configuration of satellites. As more precise proper motion measurements have become available, some proposed systems have been re-evaluated. For example, the long-suspected binary nature of the M31 satellites NGC 147 and NGC 185 has been recently re-evaluated. While their close projected proximity once suggested a bound state (Geha et al., 2010), recent Hubble Space Telescope (HST) proper motions and high-precision distance measurements revealed that they only recently reached their minimum separation and likely entered the M31 halo independently (Savino et al., 2022; Sohn et al., 2020). These developments illustrate the difficulty of distinguishing true physical pairs from chance alignments within the satellite population.

Despite these uncertainties, previous studies have suggested that satellite pairs may be relatively common in the Local Group. Fattahi et al. (2013), for instance, found that a substantial fraction (30%) of satellites brighter than $M_V < -8$ appear to have unusually close neighbours compared to expectations from isotropic distributions. However, by applying the same method to a semi-analytic model of the satellite population in the six simulated haloes of the Aquarius Project (Springel et al., 2008), they found that fewer than 4% of such satellites were paired. This difference of one order of magnitude highlights a significant tension between observed satellite distributions and theoretical expectations and suggests that the standard cosmological model fails to capture the frequency of group-infall events or the survival rate of satellite associations.

In this work, we revisit the incidence of satellite pairs in the Local Group by combining updated observational data with full phase-space information (when available). We characterise satellite associations using both their spatial proximity and kinematic coherence, and assess their significance by comparison to mock satellite populations drawn from cosmological simulations. This allows us to place the observed pair population in a statistically robust cosmological context and to evaluate whether the apparent excess of close associations from previous works can be reconciled with expectations from hierarchical galaxy formation.

In Sect. 3.2 we describe the data of the dwarf galaxies that we used for this study, both for the observations (Sect. 3.2.1) and for the simulations (Sect. 3.2.2). This is followed in Sect. 3.3 by the methods that we used to understand how many of these objects can be found in pairs. We continue in Sect. 3.4 with our results. We end with a discussion and our conclusions in Sect. 3.5. In Appendices 3.A, 3.B and 3.C, we provide supplementary material in support of the results that we discuss in the main text.

3.2 Data

3.2.1 Observations

For our analysis, we rely on the up-to-date Local Volume Database (Pace, 2025)[1] as the source of the positions, distances, proper motions, line-of-sight velocities and stellar masses of Local Group dwarfs. We exclude unconfirmed dwarf candidates and satellites with no distance measurements. In addition, we exclude dwarfs that have $d_{\rm host} > 350$ kpc. This approximately corresponds to the outer regions of the virial volumes of both the MW and M31, beyond which satellites are likely to be weakly bound or part of the surrounding Local Group environment rather than the host halo itself. Furthermore, given their extreme isolation, including them would disproportionately skew the radial distribution and introduce statistical noise into our nearest-neighbour analysis (described in the next Sect.), where no physical associates are expected at such large distances. After this, our sample consists of 51 satellites of the MW and 40 satellites of M31.

To ensure a fair comparison with the finite resolution of the HESTIA simulations (described below), we also consider a subsample of the observed satellites selected by imposing a lower limit on their stellar mass ($M_\star > 10^4\,{\rm M}_\odot$). This cut approximately matches the stellar mass completeness of the simulated satellite populations, in an attempt to alleviate possible biases introduced by the inclusion

1. Last accessed on 12-03-2026.

of ultra-faint systems that are unresolved in the simulations. We perform our analysis on both the full observational sample and this mass-limited subsample, allowing us to assess how the results are affected when limited to the mass range resolved by the simulations. On the observational side, we do not have galaxies with masses as low as this among the known M31 satellites, so we retain all 40 satellites. For the MW satellites, 26 satellites have masses lower than this number. In this case, we end up with 25 MW satellites. These numbers are summarised in Table 3.1.

3.2.2 Simulations

The 'High-resolutions Environmental Simulations of The Immediate Area' (HESTIA) project is described in detail in Libeskind et al., 2020. We briefly summarise the key features of the simulations here for the reader's convenience.

HESTIA (Libeskind et al., 2020) is a suite of high-resolution cosmological magneto-hydrodynamical simulations of the Local Group in a ΛCDM cosmology ($\Omega_\mathrm{m} = 0.270$, $\Omega_\Lambda = 0.682$, $\Omega_\mathrm{b} = 0.048$, and $\mathrm{H}_0 = 100h$ kms^{-1}Mpc^{-1}, where $h = 0.677$; Planck Collaboration et al. 2014). It uses the code AREPO (Springel, 2010) and the galaxy formation model from AURIGA (Grand et al., 2017). These simulations successfully reproduce the large-scale environment of the Local Group, and also the masses of the MW and M31, their relative distance and velocity.

In this work, we use the resulting 3 high-resolution LGs, corresponding to 8192^3 particles within the region composed of two overlapping spheres around the two main $z = 0$ LG members with a radius of 3.7 Mpc (2.5 Mpch^{-1}) each. The mass and spatial resolution achieved is $\mathrm{m_{dm}} = 1.5 \times 10^5\,\mathrm{M_\odot}$, $\mathrm{m_{gas}} = 2.2 \times 10^4\,\mathrm{M_\odot}$ and $\epsilon = 220$ pc. In this set of simulations, dwarf galaxies are resolved and have similar stellar mass distributions and radial concentration as observed (Libeskind et al., 2020). The use of these constrained simulations is particularly motivated by their ability to reproduce the Local Group's unique dynamical environment. By reproducing the large-scale structure and density field of the local Universe, HESTIA provides a realistic cosmographic environment in which the assembly and accretion of satellite systems can be studied, including processes such as group infall that are expected in ΛCDM.

To construct our satellite sample, we keep only the luminous subhaloes. After this first selection, we then remove leftover baryon-dominated substructures associated with the central galactic discs. These objects are identified as subhaloes for which the baryonic mass fraction, defined as $f_b = (M_\star + M_\mathrm{gas})/M_\mathrm{vir}$, exceeds 0.5, indicating that they are not dark matter dominated and are therefore unlikely to represent satellite galaxies.

As shown in Figure 3.1, the distribution of f_b for all luminous subhaloes across the HESTIA runs reveals a distinct bimodality. The majority of subhaloes have $f_b \lesssim 0.2$, consistent with dark-matter-dominated satellite galaxies. A separate population is found at extremely high baryonic fractions ($f_b \gtrsim 0.9$). These objects lack a significant dark matter component and are located in close proximity to the host's central regions, so we consider them as fragments of the galactic disc rather than authentic dwarf galaxies. The vertical dashed line at $f_b = 0.5$ effectively separates these two populations across all HESTIA realisations. After applying this cleaning step, we get a final sample of ~20–60 satellites per host (see Table 3.1), which is broadly comparable to the number of confirmed satellites in the observational sample.

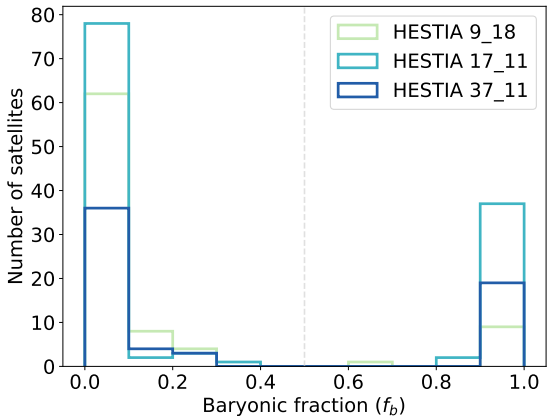


FIGURE 3.1: Distribution of baryonic fractions f_b for all luminous satellites ($N_\star > 0$) in the HESTIA simulations. MW-like and M31-like host satellites are combined for each of the three simulation realisations (shown in different colours). The vertical dashed line indicates the baryon fraction where we performed the cut to remove disc fragments from the final sample.

TABLE 3.1: Number of satellite galaxies per host after sample selection.

Dataset	MW	M31
Observations	51	40
Observations ($M_\star > 10^4\,\mathrm{M}_\odot$)	25	40
HESTIA 9_18	45	29
HESTIA 17_11	26	58
HESTIA 37_11	24	19

3.3 METHODS

Similarly to Fattahi et al., 2013, we start by finding which objects have nearest neighbours (NN) closer than those expected from a random isotropic population of satellites around their host. To do this, we use Monte Carlo sampling to generate an isotropic population with the same number of satellites and the same radial distribution as the observed sample.

The radial distribution is modelled directly from the data by constructing the cumulative distribution function (CDF) of the satellites' Galactocentric distances. For each realisation, radial distances are then drawn by sampling from this empirical CDF using either a spline interpolation or a kernel density estimate (KDE), ensuring that the synthetic populations follow the same radial profile as the observed system. Angular positions are assigned isotropically by drawing random directions uniformly over the sphere. For the MW satellites, we additionally impose an obscuration region of 15° around the Galactic plane to mimic observational incompleteness.

As illustrated in Figure 3.2, the observed radial distribution of satellites is shown by the solid blue line, with the surrounding blue shaded region representing the variation in the cumulative profile when accounting for satellite distance uncertainties. We compare these observations against the 10^5 isotropic realisations. The median of these realisations is represented by the solid dark grey line, while the shaded grey envelopes indicate the 1σ (68%), 2σ (95%), and 3σ (99.7%) confidence intervals of the generated populations. This way, it is possible to see that by generating this amount of isotropic populations, we are able to reproduce the radial distribution of the observed ones, even when the distance uncertainties are taken into account. The same analysis for the HESTIA simulated analogues can be found in Figure 3.A.1 of the Appendix.

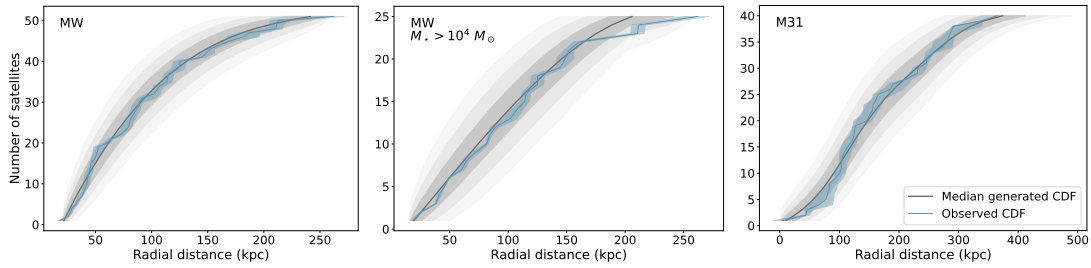


FIGURE 3.2: Cumulative radial distributions of satellites around the MW (left and centre panels) and M31 (right panel). The solid blue line shows the cumulative number of satellites as a function of host-centric distance. The surrounding blue shaded region illustrates the variation in the cumulative profile obtained using the lower and upper bounds of the 1σ distance uncertainties. The solid dark-grey line shows the median cumulative distribution obtained from 10^5 isotropic realisations. The grey shaded regions represent the 1σ (68%), 2σ (95%), and 3σ (99.7%) ranges of the generated isotropic populations. This comparison illustrates that the observed radial concentration of satellites is consistent with a random spatial distribution.

We generate 10^5 isotropic realisations for each dataset: the full MW sample, the stellar mass-limited MW sample, the M31 sample, and each of the individual HESTIA host analogues. In each iteration, we estimate, for every observed satellite, the distance to its NN within the synthetic isotropic population. The resulting distribution of NN distances provides the expectation for the separation of a satellite

from its closest companion under isotropy. By comparing this distribution with the observed NN separation, we estimate the probability P of that pair being that close by random chance.

To assess the impact of distance uncertainties on the significance of the identified associations, we propagate the observational errors on the heliocentric distances of both satellites in each pair. For each Monte Carlo realisation, we assign a perturbed distance

$$d' = d + \mathcal{N}(0,\, \sigma_d), \tag{3.1}$$

where $\mathcal{N}(0,\, \sigma_d)$ represents a normal distribution with mean zero and standard deviation σ_d, defined as the average of the upper and lower reported distance uncertainties.

Using these perturbed distances while keeping the sky positions fixed, we recompute the three-dimensional separation between the satellite under study and its observed nearest neighbour. Repeating this 10^5 times produces a distribution of possible pair separations consistent with the distance uncertainties. The minimum and maximum separations obtained from this distribution are then compared to the isotropic NN-distance distribution to derive a corresponding range of probabilities, $P_{\rm min}$–$P_{\rm max}$.

For a fair comparison, we also assign mock distance uncertainties to the HESTIA satellites. We assign each simulated satellite a distance-dependent uncertainty $f(d)$ calibrated to match the errors of the observed sample. The lower and upper heliocentric distance bounds are then defined as

$$d_{\pm} = d \pm \sigma_d, \tag{3.2}$$

where d is the mock heliocentric distance and $\sigma_d = f(d)\, d$. These bounds are projected along the same line of sight and transformed into the corresponding host-centric distances.

The distinction between a significant pair and a random association, as well as the impact of including distance uncertainties, is illustrated in Figure 3.3. This figure shows two representative cases: one where the pair classification is robust to the inclusion of distance uncertainties, and another where the inferred significance changes once the uncertainties are taken into account.

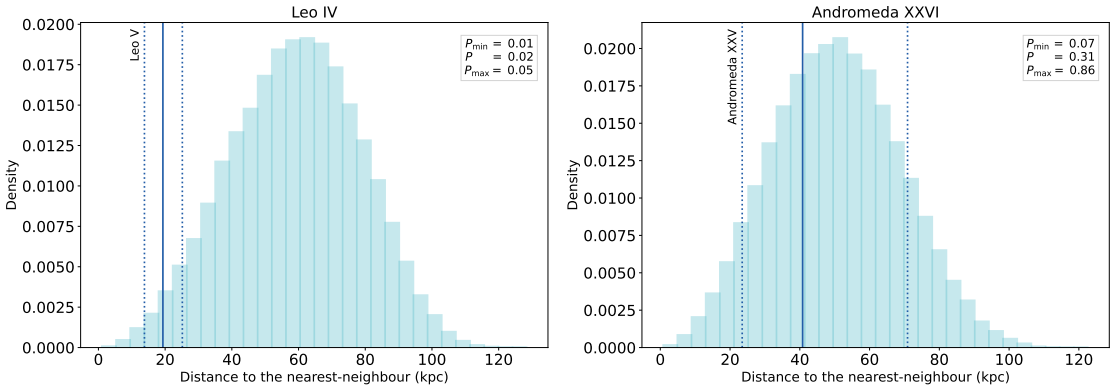


FIGURE 3.3: Examples of NN distance distributions obtained from 10^5 isotropic realisations. The vertical solid line marks the observed NN separation. The dashed vertical lines show the minimum and maximum separations obtained by resampling the heliocentric distances within their uncertainties, corresponding to the range of allowed NN probabilities (P_{min}–P_{max}). Left: Leo IV, identified as a highly significant pair candidate with its observed NN (Leo V), whose classification remains robust when distance uncertainties are considered. Right: Andromeda XXVI, and its observed NN (Andromeda XXV), for which the inferred probability spans both sides of the $P = 0.25$ threshold, illustrating how distance uncertainties can change whether a pair is classified as significant.

We consider satellites to be pair candidates if they have $P < 0.25$. This statistical selection identifies associations that are spatially significant, but spatial proximity alone does not guarantee a physical association. For these candidates, we further investigate their physical properties for signs of common accretion. Theoretically, pairs that were accreted together should exhibit similar line-of-sight velocities and consistent directions of motion. While such kinematic data are often unavailable in observations, we can also look at their internal properties, such as the stellar mass.

To assess the dynamical state of the identified satellite associations, we use the gravitational binding

criterion defined by Geha et al. (2010). For a pair of satellites to be considered gravitationally bound, their mutual gravitational potential energy must exceed their relative kinetic energy (Davis et al., 1995). This relationship is expressed through the dimensionless parameter b:

$$b \equiv \frac{2GM_{\rm pair}}{\Delta r \Delta v^2}, \tag{3.3}$$

where Δr represents the total 3D physical separation between the two objects and Δv is their relative velocity. In a perfectly bound system, $b > 1$. However, the application of this metric requires different approaches depending on whether it is applied to the simulated or observational datasets, primarily due to the availability of phase-space information and mass constraints.

For the HESTIA simulation suite, we have access to the full 6D phase-space information (3D positions and 3D velocities) and the total halo masses ($M_{\rm vir}$) for every subhalo. In this case, we calculate b using the true 3D relative velocity, $\Delta v_{\rm 3D} = \sqrt{\Delta v_x^2 + \Delta v_y^2 + \Delta v_z^2}$. With this, we are able to verify the binding state, allowing us to confirm whether the pairs identified by our P-value metric are indeed gravitationally trapped or are merely transient associations.

Conversely, for the majority of the observational sample, 3D velocity information is unavailable as proper motions remain sparse or carry significant uncertainties. For these systems, we must rely on the line-of-sight velocity difference ($\Delta v_{\rm los}$). Because $\Delta v_{\rm los}$ captures only one component of the full velocity vector, it represents a lower limit of the true relative motion ($\Delta v_{\rm los} \leq \Delta v_{\rm 3D}$). Consequently, the calculated b factor for observations serves as an upper limit on the degree of binding. Furthermore, because the total dynamical masses of the observed satellites are not well-determined, we treat $M_{\rm pair}$ as an unknown. We invert the binding criterion to solve for the minimum binding mass ($M_{\rm bound}$) required to satisfy $b \geq 1$:

$$M_{\rm bound} = \frac{\Delta r \Delta v_{\rm los}^2}{2G}. \tag{3.4}$$

This $M_{\rm bound}$ value represents the lower limit of the total system mass necessary for the pair to constitute a bound system.

3.4 Results and discussion

3.4.1 Statistical analysis

We first evaluate the spatial clustering of the satellite populations by examining the distribution of P-values derived from our NN analysis. We assign a P-value to every individual satellite in the sample, which is defined as the probability of a satellite's NN being at the observed distance (or closer) if the satellite population were distributed isotropically. Figure 3.4 shows the CDF of these P-values for both the observational sample, with and without the stellar mass cut discussed above, and the HESTIA simulated suites.

In a perfectly isotropic system, the P-value distribution is expected to be uniform, and therefore the CDF should follow the 1:1 diagonal line. Under this null hypothesis, 25% of satellites are expected to have $P < 0.25$ by chance. An excess above the 1:1 line at low P therefore indicates an excess of unusually close nearest neighbours relative to isotropic expectations.

To assess the effect of distance uncertainties, we Monte Carlo sample the heliocentric distances of each satellite and its observed NN, keeping their sky positions fixed, and recompute their 3D separation. From the resulting distribution, we adopt the lower bound on the separation (corresponding to the smallest plausible distances within the uncertainties) to recompute the NN probability with respect to the isotropic distribution. This gives an optimistic estimate of the probability, $P_{\rm min}$, corresponding to the maximum number of close associations allowed by the data. These uncertainty ranges are shown as shaded bands around the CDFs in Figure 3.4.

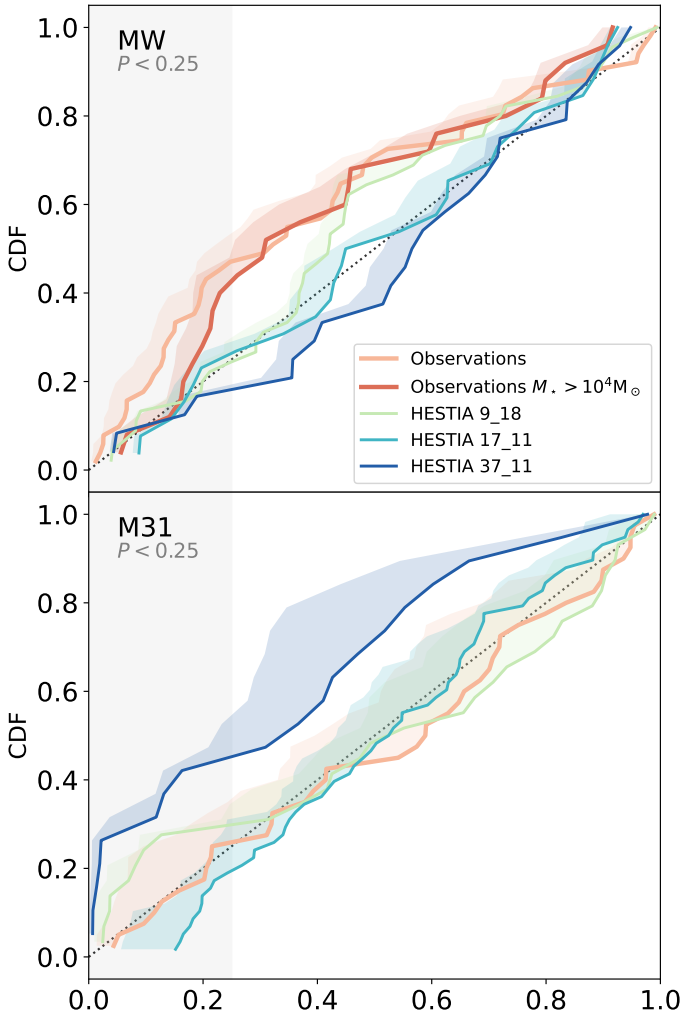


FIGURE 3.4: CDF of p-values for the nearest-neighbour (NN) distances in the MW (top) and M31 (bottom) satellite systems. The solid orange lines represent the full observational samples, while the red lines indicate the resolution-matched samples ($M_\star > 10^4\,M_\odot$). Results from HESTIA simulated analogues are shown in shades of blue and green. Shaded regions indicate the most optimistic P-value distributions obtained by propagating distance uncertainties and adopting the minimum allowed separations, maximising the number of potential close associations. The black dotted 1:1 line represents the expectation for a perfectly isotropic distribution. The grey shaded region indicates the regime of statistically significant clustering ($P < 0.25$).

In the MW system (top panel), both the full observational sample and the resolution-matched sample ($M_\star > 10^4\,M_\odot$) lie significantly above the 1:1 line. When we account for distance uncertainties, our results closely track the CDF that we get without uncertainties, suggesting that current observational errors are not large enough to artificially impact the clustering significance. This indicates that the MW satellite system looks more clustered than expected from an isotropic distribution across all mass scales.

Applying the stellar cut to match the simulation resolution limits shifts the observed distribution slightly towards higher P-values, reducing the fraction of highly significant close associations. This suggests that the ultra-faint dwarf population increases the number of close associations. We note, however, that this signal may be partially driven by observational selection effects. Current surveys of ultra-faint dwarfs are limited to specific sky footprints, resulting in uneven coverage. These spatial biases can artificially inflate the apparent angular clustering of faint satellites, even when they are widely separated along the line-of-sight (e.g. Cameron & Driver, 2007; Metz et al., 2009a; Pawlowski, 2016; Yan et al., 2025). Consequently, the increased clustering seen in the full MW sample might partly reflect survey incompleteness rather than intrinsic physical associations.

Compared with the simulations, the observational MW curves lie well above all three HESTIA analogues. This implies that the real MW contains a higher incidence of close satellite associations than predicted by the simulations, a scenario also seen in Fattahi et al. (2013). The fact that the full sample is the most clustered suggests that the presence of ultra-faint dwarfs creates a level of small-scale "clumpiness" that current simulations may not fully replicate due to resolution limits. Alternatively, it may point to differences in the accretion history or the survival of low-mass groups in the real MW halo, such as the LMC and its associated satellites (Patel et al., 2020), or the Crater-Leo group (**Júlio et al.**, 2024).

In contrast, the M31 system (bottom panel) remains broadly consistent with isotropy, showing no

significant excess of close pairs. When distance uncertainties are propagated, the shaded band extends toward lower P-values, reflecting the larger distance errors of M31 satellites. In the most favourable case, the number of satellites satisfying $P < 0.25$ could increase from 10 to 14. Thus, while additional close associations cannot be excluded, the overall P-value distribution of M31 remains much closer to isotropic expectations than the MW.

However, this behaviour is not reproduced by all the HESTIA M31 analogues. Two of the simulated M31 systems show substantially stronger clustering, with P-value distributions lying well above both the observational curve and the isotropic expectation. This suggests that, in these cases, the simulations overpredict the degree of small-scale "clumpiness" around M31.

Interestingly, the 37_11 realisation, which contains the least massive hosts in our sample, shows the most extreme behaviour. In this case, the M31 analogue is less massive than the MW-like hosts in the other HESTIA runs, resulting in a smaller satellite population. Its P-value distribution instead closely resembles that of the observed MW system, even more so than the simulated MW analogues themselves. This behaviour is illustrated explicitly in Fig. 3.B.1 of Appendix 3.B, where we overplot the simulated CDFs against both observed hosts.

This suggests that the apparent tension in clustering significance may be partially driven by the total mass of the host halo and the resulting number of satellites ($N_{\rm sats}$), since systems with fewer satellites are statistically less likely to produce extremely small nearest-neighbour separations by chance. At the same time, stochastic variations in the accretion history, group infall, and the local environment of each simulated halo are also expected to contribute to the diversity in clustering signals. A larger suite of simulations spanning a broader range of host masses and assembly histories will therefore be required to robustly assess whether the observed MW–M31 contrast is statistically significant within ΛCDM.

We also note that the HESTIA satellite populations are generally more radially concentrated than the observed samples, with most simulated satellites lying within $d_{\rm host} \lesssim 200$ kpc. In principle, a more compact satellite distribution would naturally increase the probability of finding small physical separations and could therefore bias NN statistics toward stronger clustering signals. However, this effect is largely accounted for in our methodology, since the isotropic realisations are constructed to reproduce the radial distribution of each individual host separately. The resulting P-value distributions therefore measure deviations from isotropy at fixed radial profile, rather than being directly driven by differences in the overall radial extent of the satellite populations.

Taken together, these results highlight a tension in opposite directions for the MW and M31. This divergence might result from differences in observational perspective and selection effects. While the MW satellite census is susceptible to the footprint limitations of deep surveys, the M31 satellite system is observed from the outside, resulting in a more uniform (though luminosity-limited) spatial distribution. Interestingly, M31 is known to have its own form of spatial anisotropy, a "lopsided" distribution where the majority of satellites are located on the side of M31 facing the MW (Conn et al., 2013; Kanehisa et al., 2025; Savino et al., 2022). The fact that M31 appears consistent with isotropy in our NN analysis, despite this known lopsidedness, suggests that spatial asymmetries do not necessarily manifest as small-scale clustering or an excess of close pairs.

3.4.2 Pair candidates

While the CDF analysis may identify a statistical departure from isotropy in some cases, it cannot alone distinguish between physical associations and chance spatial proximity. To investigate the nature of these clustering signals, we now focus on the individual satellite associations that fall below our significance threshold of $P < 0.25$.

Based on this threshold of $P < 0.25$, we identify a set of initial satellite pair candidates for both the observational and simulated samples. To avoid overcounting, we remove duplicate entries where both satellites in a pair were each other's NN, resulting in a census of unique candidate associations. However, it is important to note that these associations are not always two-sided pairs. It is common that several satellites share the same NN. For example, in the full observation MW sample, Tucana II, Tucana IV and the SMC are identified as being associated with Tucana V. This does not change the resulting number of pair candidates, which are summarised in Table 3.2. It is also possible for an association to be asymmetrically significant: for example, Canes Venatici II is a significant neighbour

to Canes Venaciti I ($P < 0.25$), but Canes Venaciti I is not a significant neighbour to Canes Venatici II ($P > 0.25$) due to differing local density expectations. In our census, we include any association where at least one member of the pair meets the significance threshold.

In the MW, we find 16 pair candidates in the full observational sample. However, this number drops to 7 when applying the $M_\star > 10^4\,\mathrm{M}_\odot$ resolution cut, suggesting that many of the MW pairs are composed of at least one ultra-faint dwarf. The M31 sample remains unchanged at 6 candidates, since applying the stellar mass cut does not change the number of satellites associated with this host. This stability is a direct consequence of current observational limits: due to the distance to M31 ($\sim$ 780 kpc), its population of ultra-faint dwarfs is undetectable, so the known satellite census of this galaxy is limited to the classical dwarf regime.

Within the HESTIA suites, the number of pair candidates varies across realisations, ranging from 3 to 7 for MW-like hosts and 5 to 8 for M31-like hosts.

To quantify the degree of phase-space clustering, we calculate the pairing efficiency as the fraction of all considered satellites (N_{sats}) involved in at least one identified association (N_{assoc}). The expected number of associations ($N_{\mathrm{exp,sat}}$) is defined as the number of satellites expected to identify a significant nearest neighbour ($P < 0.25$) under the null hypothesis of isotropy. While a single physical association (e.g., a reciprocal pair) involves two satellites, $N_{\mathrm{exp,sat}}$ represents the frequency of significant directed associations. The comparison between N_{assoc} and $N_{\mathrm{exp,sat}}$ therefore tests whether the total number of satellites with unusually close nearest neighbours exceeds random expectations, regardless of the clustering configuration (reciprocal or otherwise).

As shown in Table 3.2, and as already seen in Figure 3.4, this metric reveals a significant difference between the observational MW and its simulated analogues. In the full MW observational sample, 27 out of 51 satellites are part of at least one association, corresponding to a pairing efficiency of $\sim$ 53%. Even when applying the stellar mass cut, the efficiency remains similarly high at 52% (13 out of 25 satellites).

By contrast, the HESTIA MW-like hosts exhibit significantly lower efficiencies, ranging from $\sim$ 17% to $\sim$ 27%. This level of clustering is consistent with expectations from a random isotropic distribution: given our threshold of $P < 0.25$, one would statistically expect approximately one-quarter of any satellites to be identified as "associated" by chance. The fact that the simulated hosts generally lie close to this 25% expectation suggests they contain very few, if any, real satellite pairs. By contrast, the elevated pairing efficiency in the MW points to a real excess of close associations beyond random expectations. This indicates that the real MW is almost twice as "clustered" as its simulated counterparts, even when the absolute number of pairs (N_{pairs}) is identical.

Once again, as previously noticed in Figure 3.4, M31 appears more "typical" of the HESTIA environment. Its observational pairing efficiency of 27.5% is broadly consistent with the simulated M31-like hosts (which range from $\sim$ 24% to $\sim$ 42%). This suggests that the high clustering signal in the LG is primarily driven by the MW's satellite system.

The number of unique pairs should be interpreted together with both $N_{P<0.25}$ and N_{assoc}, since $N_{\mathrm{exp,sat}}$ refers to individual satellites rather than pair counts. In the full MW sample, 24 satellites satisfy the $P < 0.25$ criterion, compared to $N_{\mathrm{exp,sat}} = 12.8$ expected under isotropy, while 27 unique satellites participate in at least one identified association. This confirms that the MW contains an excess of satellites with unusually close nearest neighbours. In contrast, the M31 sample contains 10 satellites satisfying the $P < 0.25$ threshold, fully consistent with the isotropic expectation of $N_{\mathrm{exp,sat}} = 10$ for a sample of 40 satellites. Although six unique M31 candidate pairs are identified, the overall incidence of significant nearest-neighbour associations is consistent with random expectations.

As discussed in the previous section, the comparatively large distance uncertainties of M31 satellites can could have washed out some genuine close associations. Using the minimum separations permitted by the distance uncertainties, the number of M31 satellites satisfying $P < 0.25$ could increase from 10 to 14. This represents the most favourable case for maximising the clustering signal. Even under this optimistic scenario, the inferred clustering of the M31 satellite system remains substantially weaker than that of the MW and broadly consistent with expectations from an isotropic distribution.

When considering the Local Group as a whole, the observational pairing efficiency ($\sim$ 42% for the full sample) consistently exceeds the values found across all HESTIA realisations ($\sim$ 24% to $\sim$ 28%). This may suggest that the observed LG is currently likely dominated by recent, coherent infall of satellite groups.

These numbers represent the maximum possible number of associations based purely on spatial

TABLE 3.2: Summary of satellite pair candidates and pairing efficiencies.

Dataset	$N_{\rm sats}$	$N_{\rm pairs}$	$N_{P<0.25}$	$N_{\rm exp,sat} \pm \sigma_{N_{\rm exp}}$	$N_{\rm assoc}$	Eff.%
MW						
Observations	51	16	24	12.8 ± 3.6	27	52.9
$M_\star > 10^4\,{\rm M}_\odot$	25	7	10	6.5 ± 2.5	13	52.0
HESTIA 9_18	45	7	11	11.3 ± 3.4	12	26.7
HESTIA 17_11	26	3	6	6.5 ± 2.5	6	23.1
HESTIA 37_11	24	3	6	6.0 ± 2.4	4	16.7
M31						
Observations	40	6	10	10.0 ± 3.2	11	27.5
HESTIA 9_18	29	5	8	7.3 ± 2.7	9	31.0
HESTIA 17_11	58	8	14	14.5 ± 3.8	14	24.1
HESTIA 37_11	19	5	5	4.8 ± 2.2	8	42.1
LG						
Observations	91	22	34	22.8 ± 4.8	38	41.8
$M_\star > 10^4\,{\rm M}_\odot$	65	13	20	16.3 ± 4.0	23	35.4
HESTIA 9_18	74	12	19	18.5 ± 4.3	21	28.4
HESTIA 17_11	84	11	20	21.0 ± 4.6	20	23.8
HESTIA 37_11	43	8	11	10.8 ± 3.3	12	27.9

Columns from left to right: (1) Dataset; (2) total number of satellites ($N_{\rm sats}$); (3) number of unique identified candidate associations after removing reciprocal duplicates ($N_{\rm pairs}$); (4) number of satellites satisfying the significance threshold $P < 0.25$; (5) expected number of satellites with $P < 0.25$ under isotropy, with Poisson uncertainty ($N_{\rm exp,sat}$); (6) number of unique satellites involved in at least one association ($N_{\rm assoc}$); and (7) pairing efficiency ($N_{\rm assoc}/N_{\rm sats}$).
We note that $N_{P<0.25}$ and $N_{\rm exp,sat}$ refer to individual satellites satisfying the significance threshold, whereas $N_{\rm pairs}$ counts unique associations after removing reciprocal duplicates. These quantities are therefore not directly equivalent when several satellites share the same nearest neighbour or when associations are not reciprocal.

clustering. In the following sections, we move beyond simple spatial proximity to examine other indicators of physical association for each of these candidates. A true joint accretion event should leave traces in the satellites' broader phase-space distribution (e.g. Lynden-Bell & Lynden-Bell, 1995). Fattahi et al. (2013) concluded that physically associated satellites should have small line-of-sight velocity differences and comparable luminosities. We follow the same logic, but use stellar mass rather than luminosity as the mass-similarity diagnostic, since this quantity is available consistently for both the observations and the HESTIA simulations.

Taking this into account, we evaluate these candidates based on:

- **Kinematic coherence:** physical pairs are expected to share similar line-of-sight velocities;
- **Mass similarity:** associations of satellites typically exhibit comparable masses;
- **Motion alignment:** when proper motions are available, we examine the alignment of the velocity vectors;
- **Gravitational binding:** we calculate the minimum dynamical mass required for a pair to be bound and compare it to the expected total mass of the system.

3.4.2.1 Kinematic coherence

The phase-space distribution of the identified satellite pairs is shown in Figure 3.5, where we compare the observational pair candidates of the MW (top panels) and M31 (bottom panels) against their respective analogues in the HESTIA simulations.

In the left-hand panels, which show the internal separation (ΔR) versus the line-of-sight velocity difference ($|\Delta v_{\rm los}|$), both systems exhibit pairs that are predominantly clustered at small separations ($\Delta R < 40$ kpc). In the MW, the higher-mass subset (red points) spans a broader region of the phase-space than the low-mass population. In contrast, the low-mass satellites (represented by the orange points without coloured edges) are predominantly found at smaller internal separations (< 50 kpc).

This concentration of low-mass satellites may again be influenced by observational selection effects. Ultra-faint dwarfs are increasingly difficult to detect at large Galactocentric distances, leading to a more radially concentrated observed sample. This higher spatial density in the inner halo increases the probability of finding satellites in close neighbours, which may artificially boost the clustering signal for the low-mass systems. Nevertheless, several observed pairs in both the MW and M31 occupy the region of small velocity differences. Following Fattahi et al. (2013), pairs with $|\Delta v_{\rm los}|$ below the velocity difference of the LMC–SMC system are considered strong candidates for a common dynamical association. In that work, this reference value was taken to be ~ 75 km s^{-1}. Using the systemic heliocentric velocities reported in the Local Volume Database (Pace, 2025), the present-day line-of-sight velocity difference between the LMC and SMC is $|\Delta v_{\rm los}| \sim 117$ km s^{-1}. Since all velocities in our analysis are taken from the same catalogue, we adopt this value as a consistent reference scale when evaluating kinematic similarity between satellite pairs.

Adopting this updated value as a less conservative threshold, we find that approximately 44% (7 out of 16) of the full MW sample and 43% (3 out of 7) of the resolution-matched sample exhibit velocity differences below this limit. In M31, 75% (3 out of 4) of the pairs with available velocity measurements satisfy this criterion. Therefore, these systems represent the most promising candidates for genuine dynamically associated pairs, although full phase-space information is required to confirm whether they are truly bound.

A similar fraction of low $|\Delta v_{\rm los}|$ pairs is found in the HESTIA simulations (20 out of 31 across hosts, corresponding to approximately 65%), indicating that small line-of-sight velocity differences can arise naturally in cosmological satellite populations. This reinforces the need to combine kinematic information with spatial clustering when identifying genuinely associated systems.

The right-hand panels show the pairs' average distance from the host ($\overline{d}_{\rm host}$) against their average line-of-sight velocity relative to the systemic motion of the host ($\overline{v}_{\rm los}$). For the MW, the observational pairs are mostly concentrated at small host-centric distances ($\overline{d}_{\rm host} \lesssim 100$ kpc). In M31, the pairs are distributed further from the host on average, both in the observations and simulations, with most pair candidates around $100 - 150$ kpc. We also note that two M31 satellites (Pegasus V and Pegasus VII) lack measurements of $v_{\rm los}$, which prevents a complete characterisation of all pairs. As a result, the trends identified here likely represent a conservative view of the true level of kinematic coherence within the satellite pair population.

For the observations, the MW velocities are corrected to the Galactic standard-of-rest frame, while the M31 velocities are measured relative to the systemic velocity of M31. In the simulations, we place a mock observer at the Solar position and measure the line-of-sight velocities in an equivalent way, ensuring a consistent comparison between the observations and the mock-observed simulated systems. We emphasise that these quantities do not correspond to true three-dimensional host-centric radial velocities, since only the line-of-sight component of the motion is considered.

3.4.2.2 Mass similarity

To visualise the members of the identified satellite pairs and their corresponding physical properties, we show their distribution in Figure 3.6. The Milky Way (MW) samples are presented in Galactic coordinates (l, b), while the M31 sample is shown in host-centric relative coordinates $(\Delta\alpha, \Delta\delta)$. Each connected symbol represents the two satellites belonging to a pair.

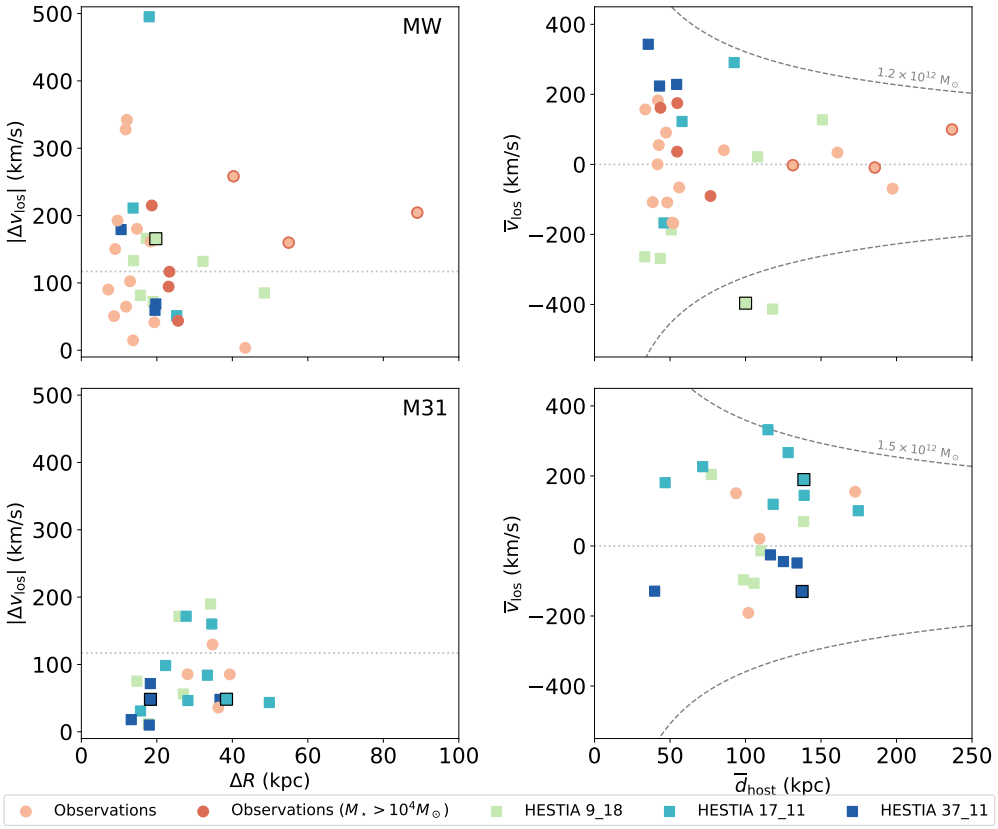


FIGURE 3.5: Phase-space diagnostics of satellite pairs candidates in the MW (top) and M31 (bottom) system, compared to HESTIA analogues. Observational candidates are shown as circles and simulated candidates from three HESTIA suites are shown as squares. The pairs that were found to be gravitationally bound are highlighted with black edges. Left: Internal pair dynamics showing 3D separation (ΔR) versus line-of-sight velocity difference ($|\Delta v_{\rm los}|$). The horizontal dashed line at 117 km s^{-1} represents the $|\Delta v_{\rm los}|$ of the LMC–SMC system, used as a threshold for potential dynamical association. Right: Distribution of pairs showing the average distance from the host ($\overline{d}_{\rm host}$) as a function of their average line-of-sight velocity relative to the host systemic motion ($\overline{v}_{\rm los}$). The grey dashed lines represent the escape velocity curves ($v_{\rm esc}$) for the assumed host masses (1.2×10^{12} M$_\odot$ for the MW and 1.5×10^{12} M$_\odot$ for M31, and are shown for reference only, as the velocities are not three-dimensional host-centric).

For the MW (top and centre panels), the pairs are broadly distributed across the sky, without an obvious large-scale clustering or alignment. Some pairs appear relatively isolated, while others lie in regions where multiple satellites are present, but there is no clear evidence that the identified associations are driven by a single event.

As seen in the previous section, several pairs show similar velocity values between their members. However, in a few cases, the velocity difference within a pair is relatively large, highlighting that spatial proximity alone does not guarantee kinematic coherence. Nevertheless, the presence of multiple pairs with comparable velocities strengthens the case that at least a subset of these systems may represent genuine physical associations.

Looking at the stellar mass ($log_{10} M_\star$) of the satellites, we can distinguish between "major" pairs (two dwarfs of similar mass, with mass ratios $M_{\star,1}/M_{\star,2} < 10$) and "hierarchical" pairs (a massive dwarf with an ultra-faint companion, with mass ratios $M_{\star,1}/M_{\star,2} > 10$). In the full MW sample, approximately 69% of our identified associations are major pairs, suggesting that our phase-space metric is highly effective at identifying satellites of comparable mass ($M_{\star,1}/M_{\star,2} \approx 1.0$ in Table 3.3). The remaining 31% are hierarchical associations, which include extreme cases such as the LMC–Pictor II and SMC–Tucana V systems, where the mass ratio exceeds 10^6. This is consistent with hierarchical structure formation: while some satellites seem to be accreted in pairs of similar mass, many seem to be part of larger groups dominated by a massive companion that has retained its own low-mass satellites (see e.g. D'Onghia & Lake, 2008).

When the stellar mass cut is applied, the pair distribution changes, but the population remains dominated by mass symmetry. As indicated by the bolded entries in Table 3.3, only a subset of the

original associations survive this threshold. These surviving systems are characterised by relatively low mass ratios (approximately 71% of associations qualify as "major" pairs), such as the Draco–Ursa Minor and LMC–SMC systems. In contrast, the "hierarchical" pairs that are present in the full sample (typically consisting of an ultra-faint satellite associated with a more massive companion) are largely removed by this cut, as it excludes the faintest systems, which are responsible for these extreme mass ratios.

The fact that these hierarchical pairs disappear once the stellar mass cut is applied highlights that the clustering signal is strongly mass-dependent, and may significantly influence comparisons with both simulations due to resolution limits and M31 since its observations are restricted to relatively bright systems due to its distance. As a result, both cases are naturally biased towards detecting only higher-mass, "major" pairs, potentially underestimating the true abundance of hierarchical associations present in the underlying satellite population.

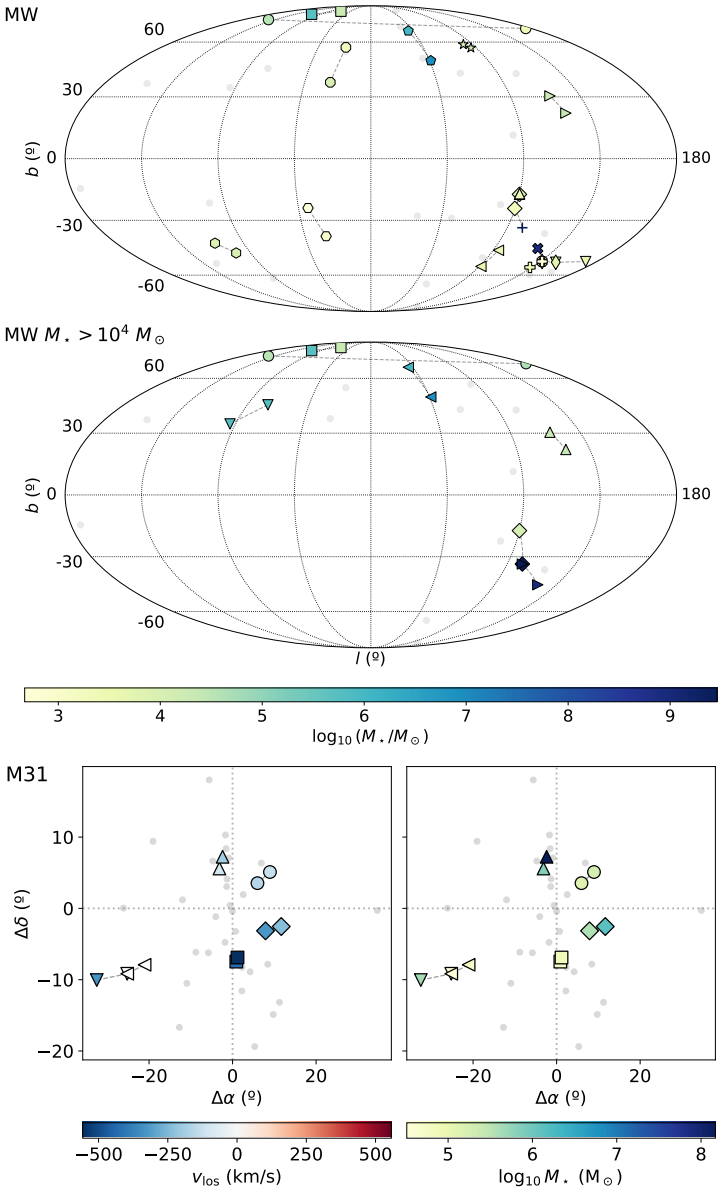


FIGURE 3.6: Comparative sky distribution and properties of satellite galaxy pairs in the MW and M31. The top panels show the distribution of MW satellites in Galactic coordinates (l, b) for the full sample (top) and the stellar-mass-cut sample ($M_\star > 10^4$ $M_\odot$, centre). The satellites in pairs are colour-coded by their stellar mass ($log_{10}(M_\star/M_\odot)$). The bottom panels display the M31 satellite distribution host-centric relative coordinates $(\Delta\alpha, \Delta\delta)$. In the left panel, M31 pairs are colour-coded to indicate their relative line-of-sight velocity (v_{los}), while in the right, they are colour-coded by stellar mass. In all panels, satellites identified as pairs are connected by dashed lines and shared marker shapes, while the remaining satellites are represented as faint grey dots. Markers with a white colour indicate satellites where the respective data is unavailable in the current dataset.

This interpretation is further supported by the spatial distribution of the identified pairs on the sky. In the full MW sample, a significant fraction of the low-mass associations are concentrated in the same region of the sky as the Magellanic Clouds (see Figure 3.6), forming a visually apparent clustering of satellites around the LMC–SMC system. Many of these associations disappear once the stellar mass cut is applied, indicating that the excess clustering signal is largely driven by ultra-faint dwarfs spatially associated with the Magellanic system. This behaviour is consistent with expectations from hierarchical accretion, in which a massive satellite such as the LMC brings its own population of low-mass companions into the MW halo (e.g. D'Onghia & Lake, 2008; Patel et al., 2020; Vasiliev, 2023). The observed excess of close associations in the MW may therefore partly reflect the recent accretion of the Magellanic group.

For M31 (bottom panels), the number of identified pairs is smaller, and they appear more spatially concentrated due to the limited angular extent of the system on the sky. Despite this, the same qualitative trends are present. The velocity-coloured panel (bottom-left) suggests that some pairs have comparable line-of-sight velocities, although the small sample size limits any strong conclusions. The stellar mass distribution (bottom-right), similar to the MW, indicates a preference for "major" associations, with $\approx$ 67% (4 out of 6) of the pairs exhibiting mass ratios $M_{\star,1}/M_{\star,2} < 10$. However, as current observational data for M31 are largely restricted to relatively bright systems, the lack of hierarchical pairs in the M31 sample is expected.

3.4.2.3 Motion alignment

While the line-of-sight velocities and 3D separations provide a statistical basis for identifying pairs, a more robust test of physical association lies in their three-dimensional velocity. However, proper motion measurements remain sparse in the Local Group and are often subject to high uncertainties. In the M31 system, PMs have been successfully derived for only a handful of the brightest satellites (e.g. Casetti-Dinescu et al., 2024, 2025; Sohn et al., 2020). For the M31 pair candidates identified in this work, we currently lack PM data for both members of the pair. This prevents a direct comparison of their orbital paths, which would be required to confirm a common infall origin or a gravitational bond. Consequently, our kinematic assessment for the M31 system remains limited to the line-of-sight component.

In Figures 3.7 and 3.8, we show the spatial distribution and direction of motion for pairs identified in both observational samples of the MW with high clustering significance ($P < 0.25$). Figures 3.9 and 3.10 show, respectively, the kinematics for the MW and M31 analogues in the HESTIA simulations. A qualitative classification of the motion alignment for each pair is provided in Appendix 3.C.

These figures illustrate the most likely direction of motion in the (α, δ) plane. For the observational MW samples, arrows indicate the most likely proper motion direction inferred from the measured PMs after correcting for the Solar reflex motion. The associated dashed curves show the great-circle tracks on the sky defined by these velocity directions, corresponding to the orbital planes of the satellites. The arcs centred on each satellite illustrate the 1σ and 2σ uncertainties in the inferred velocity directions.

Several pairs show velocity vectors that become consistent once their uncertainties are taken into account. When we consider the full MW sample (Figure 3.7), we find that $\sim$ 44% of the identified pair candidates exhibit velocity vectors that are statistically consistent within their 2σ uncertainties. For example, systems such as Canes Venatici I–Canes Venatici II, Leo IV–Leo V, and Pegasus III–Pisces II exhibit possible overlapping directions, indicating that their motions on the plane of the sky are compatible with a common trajectory within the current uncertainties. The association of Leo IV and Leo V is of particular interest, as their physical connection has been previously suggested based on their extreme spatial and kinematic proximity (Belokurov et al., 2007; Jong et al., 2010), and was recently confirmed as a highly significant group in the dynamical analysis of **Júlio et al.** (2024). Similarly, the kinematic alignment of Pegasus III and Pisces II reinforces previous suggestions that these two ultra-faint dwarfs form a physically bound pair accreted together (Kim et al., 2015; Richstein et al., 2022). In contrast, other pairs (e.g. Carina II–Pictor II) have really tight constraints on their proper motions and show less overlap, suggesting that not all spatially close systems are kinematically coherent.

When the $M_\star > 10^4\,\mathrm{M}_\odot$ cut is applied (Figure 3.8), some of the most significant pairs based on 3D distance and $v_{\rm los}$ appear to show divergent directions of motion in the (α, δ) plane. In particular, the LMC–SMC and Draco–Ursa Minor systems appear to be moving in different directions when con-

sidering only the projected proper motion vectors. However, this apparent misalignment arises from projecting curved trajectories on the celestial sphere onto the (α, δ) plane. Proper motion vectors represent only the local tangent to the orbit, while the true motion of a satellite follows a great circle corresponding to its orbital plane. When these great-circle trajectories are considered, both the LMC–SMC and Draco–Ursa Minor pairs are found to be consistent with coherent orbital motion, despite their apparently divergent projected velocity vectors. For this subset sample of the MW, approximately 70% of the pair candidates show velocity vectors that are statistically consistent within their 2σ uncertainties.

A case of high-confidence association is found in Carina II–LMC pair, which shows near-perfect alignment in our analysis. This provides strong kinematic evidence that Carina II is a member of the Magellanic satellite system, a conclusion supported by several recent studies characterising LMC satellites brought in during the system's first infall (Battaglia et al., 2022; Fritz et al., 2018; Kallivayalil et al., 2018; Pace et al., 2022; Patel et al., 2020). We also identify Carina II–Carina III as pair candidates with significant kinematic overlap with the LMC system in our full sample, further illustrating the "clumpliness" of the Magellanic accretion event.

A similar behaviour is observed in the simulated host analogues (Figures 3.9 and 3.10). In these figures, arrows indicate the proper motion direction of the satellites as seen by the mock observer defined in the simulation, while the dashed curves again show the corresponding great-circle tracks. Unlike the observational case, these directions are derived directly from the simulated velocities and are therefore shown without uncertainties. A subset of pairs (14 of 31 candidates across all hosts, corresponding to $\approx 45\%$) exhibit a clear alignment in their projected velocity vectors, indicating that coherent satellite motions arise naturally in cosmological simulations.

The presence of directional coherence in both the observations and simulations suggests that at least a fraction of the identified pairs are not chance projections or transient encounters, but instead trace satellites sharing a common orbital motion. When combined with the small line-of-sight velocity differences and spatial proximity identified in previous sections, this suggests that some of these systems are likely represent genuine physical associations, rather than chance alignments or fly-by events.

3.4.2.4 Gravitational binding

To move beyond the statistical likelihood of association, we now check the physical nature of the identified pairs using the dimensionless binding parameter b (Equation 3.3) for the simulations where we have the 3D velocity vectors and the minimum binding mass, $M_{\rm bound}$ (Equation 3.4), for the observations. $M_{\rm bound}$ represents the lower limit of the total system mass required for the pair to be gravitationally bound at present, given its current phase-space configuration. These results are presented in the last column of Table 3.3 and 3.4 for the observations and simulations, respectively.

When we apply the 3D binding criterion ($b > 1$) to the full HESTIA sample, we find that only a small fraction of the identified phase-space associations are currently gravitationally bound. Out of the numerous associations identified by our P-value metric (31 across hosts and runs), only three systems satisfy the requirement for gravitational binding: one in the MW 9_18 analogue, and two in the M31 analogues (17_11 and 37_11). Our results indicate that approximately 10% of statistically significant phase-space associations correspond to bound pairs at the present day.

This result is consistent with the expectation that $\sim$ 25% of phase-space associations arise from chance alignments rather than physical proximity. Furthermore, it is possible that some pairs were bound prior to infall and were disrupted by the host's tidal forces. Most "true" pairs likely enter the host as part of a bound group but are rapidly transformed into "association" objects that share a common orbital trajectory and phase-space signature but are no longer formally bound to one another.

For the observational sample, we evaluate the feasibility of binding by comparing $M_{\rm bound}$ to typical dwarf galaxy mass scales. In the full MW sample, we find that approximately 38% (6 out of 16) of associations have $M_{\rm bound} \lesssim 10^{10}\,{\rm M}_\odot$, a threshold consistent with the expected total halo masses of classical and bright ultra-faint dwarfs. Among these, Pegasus III–Pisces II ($M_{\rm bound} \approx 0.07 \times 10^9\,{\rm M}_\odot$) and Grus II–Tucana II ($\approx 0.34 \times 10^9\,{\rm M}_\odot$) stand out as the most likely candidates for physically bound systems. Conversely, pairs such as Leo I–Leo II require a total system mass exceeding $4 \times 10^{11}\,{\rm M}_\odot$ to be gravitationally bound. This extreme requirement reinforces the conclusion that their current proximity is a transient alignment within the Galactic halo rather than a physical association. This interpretation is further supported by recent dynamical studies, which suggest that Leo II is likely

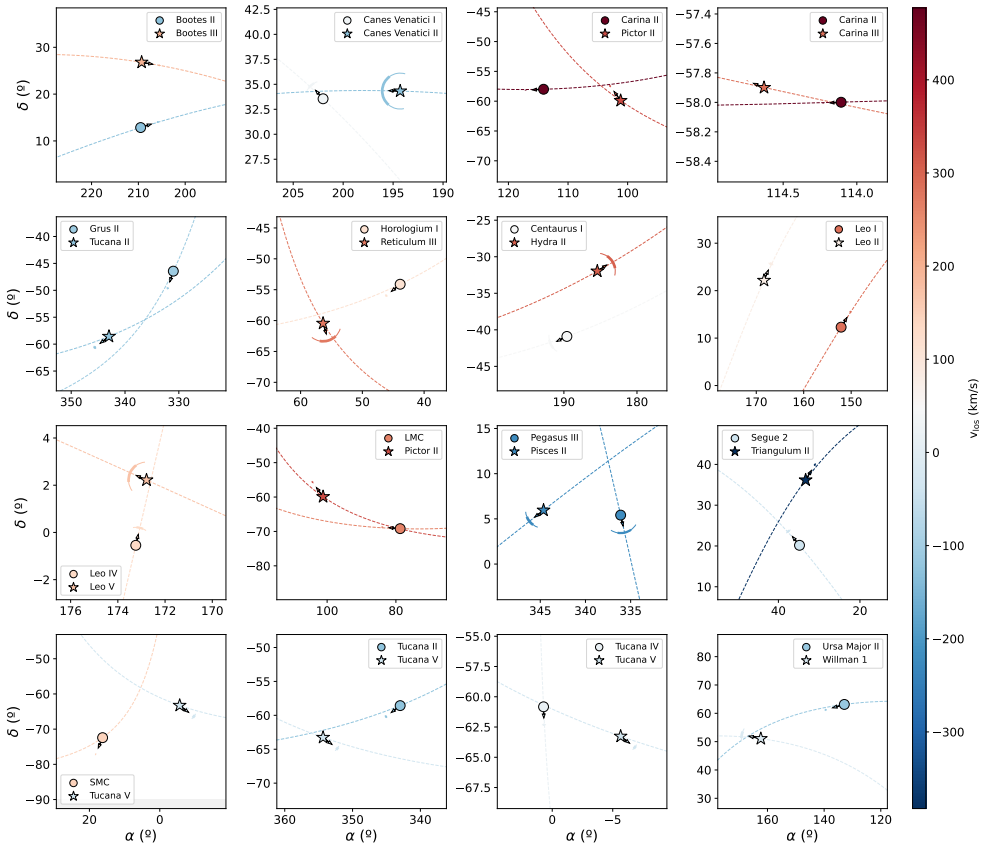


FIGURE 3.7: Spatial distribution and direction of motion of candidate satellite pairs with clustering significance $P < 0.25$ for the full observational sample of MW satellites. Each panel shows a pair where the markers are coloured by their $v_{\rm los}$. The circular marker represents the first satellite in the identified pair, while the star represents its nearest neighbour. Arrows indicate the most likely proper motion direction inferred from the measured proper motions after correcting for the Solar reflex motion. The dashed curves show the corresponding great circles on the sky defined by these velocity directions. The arcs centred on each satellite illustrate the 1σ and 2σ uncertainties in the velocity directions. Areas with $|\delta| > 90^\circ$ are shaded in grey to denote regions beyond the physical limits of the equatorial coordinate system.

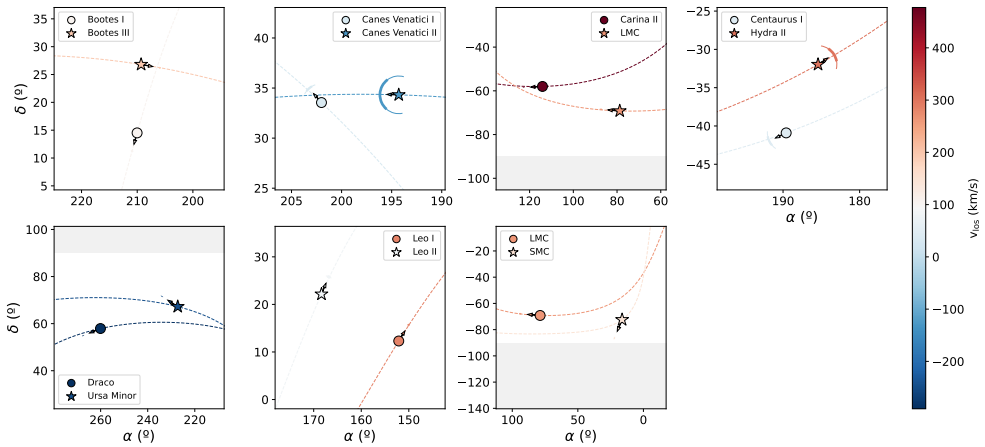


FIGURE 3.8: Spatial distribution and direction of motion of candidate satellite pairs with clustering significance $P < 0.25$ for the resolution-matched sample of MW satellites. Each panel shows a pair where the markers are coloured by their $v_{\rm los}$. The circular marker represents the first satellite in the identified pair, while the star represents its nearest neighbour. Arrows indicate the most likely proper motion direction inferred from the measured proper motions after correcting for the Solar reflex motion. The dashed curves show the corresponding great circles on the sky defined by these velocity directions. The arcs centred on each satellite illustrate the 1σ and 2σ uncertainties in the velocity directions. Areas with $|\delta| > 90^\circ$ are shaded in grey to denote regions beyond the physical limits of the equatorial coordinate system.

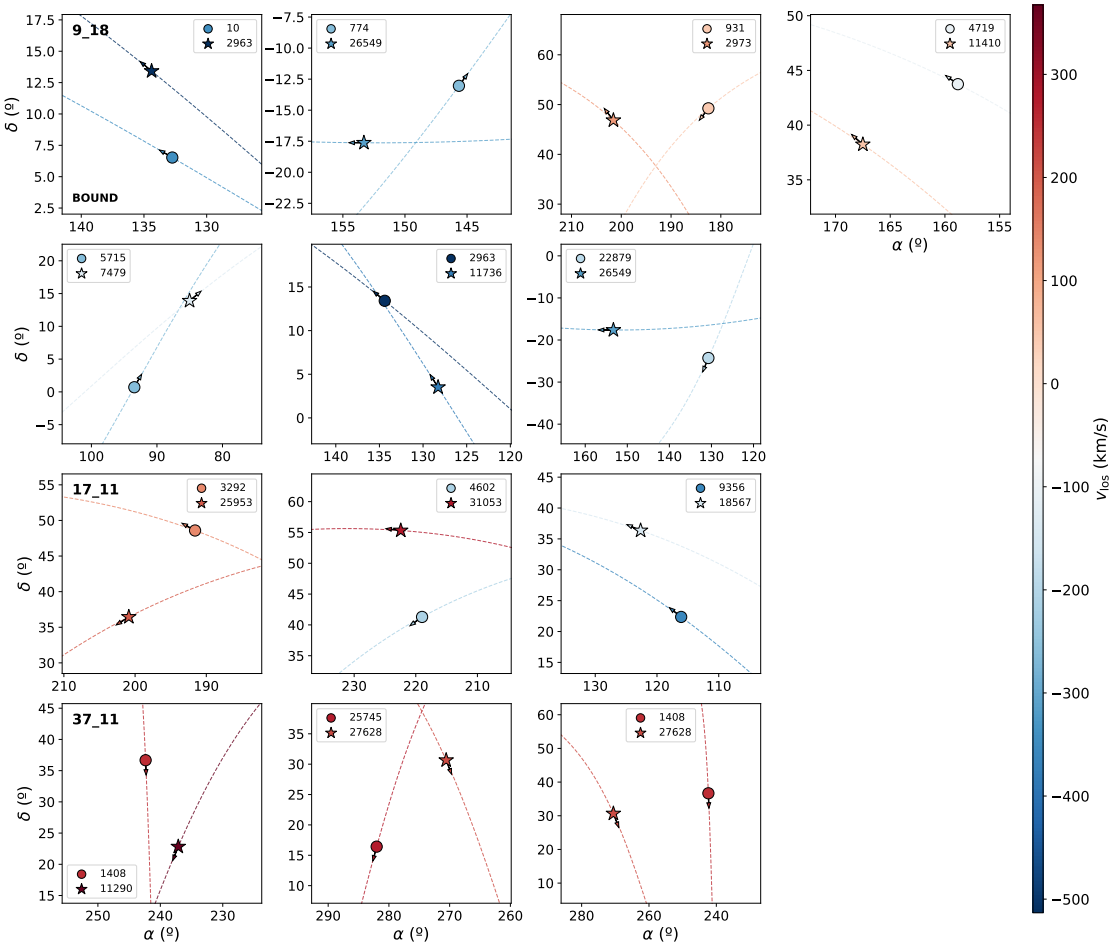


FIGURE 3.9: Spatial distribution and direction of motion of candidate satellite pairs with clustering significance $P < 0.25$ for the HESTIA MW analogues. Each panel shows a pair where the markers are coloured by their v_{los}. The circular marker represents the first satellite in the identified pair, while the star represents its nearest neighbour. Arrows indicate the proper motion direction as seen by a mock observer placed at the Solar position in the simulated MW analogue. The dashed curves show the great circles in the sky defined by these velocity directions. Pairs labelled "BOUND" correspond to systems that are gravitationally bound according to their full three-dimensional phase-space information in the simulation.

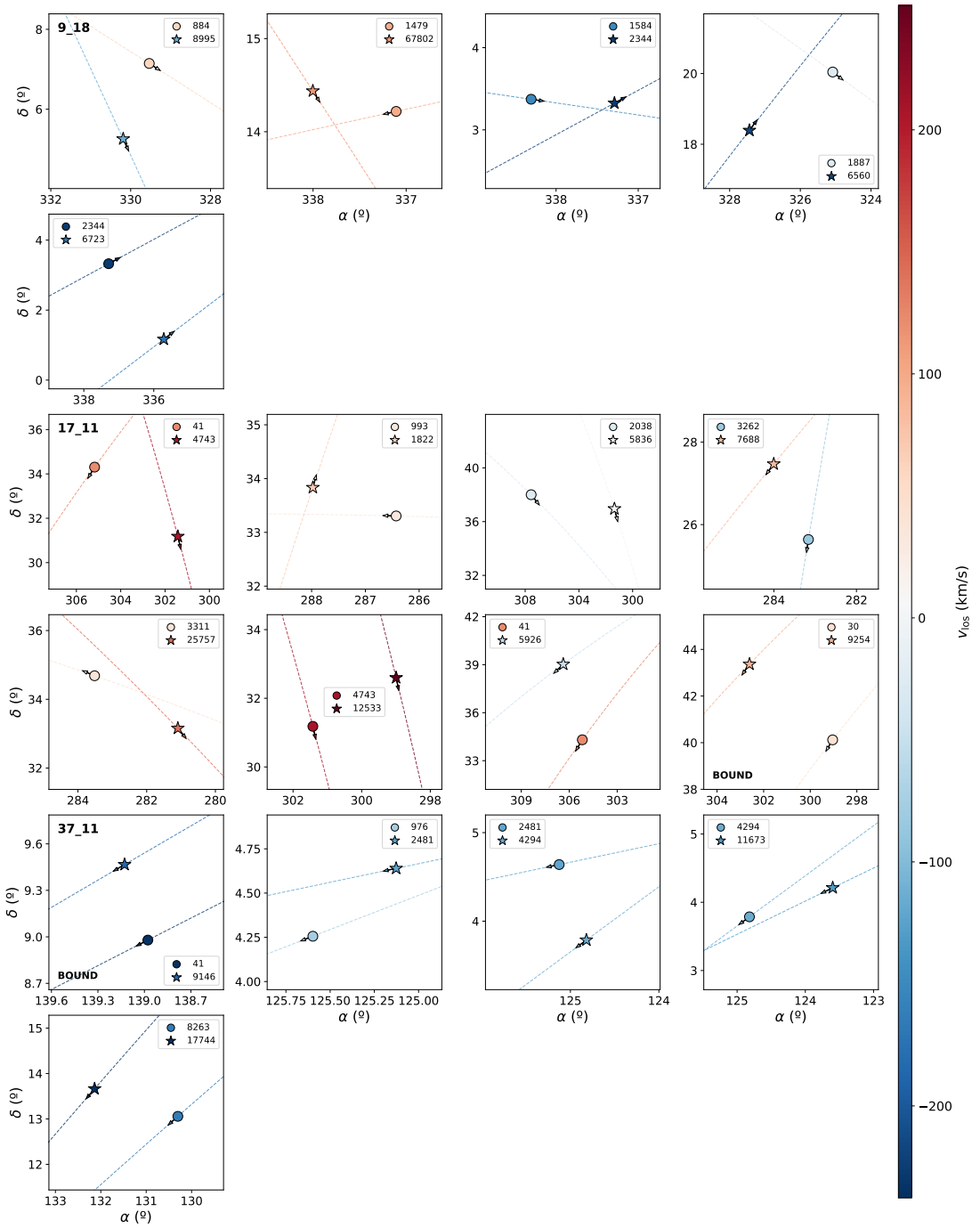


FIGURE 3.10: Spatial distribution and direction of motion of candidate satellite pairs with clustering significance $P < 0.25$ for the HESTIA M31 analogues. Each panel shows a pair where the markers are coloured by their v_{los}. The circular marker represents the first satellite in the identified pair, while the star represents its nearest neighbour. Arrows indicate the proper motion direction as seen by a mock observer located at the position of the simulated MW analogue relative to the M31. The dashed curves show the great circles on the sky defined by these velocity directions. Pairs labelled "BOUND" correspond to systems that are gravitationally bound according to their full three-dimensional phase-space information in the simulation.

associated with the Leo IV and Leo V group (**Júlio et al.**, 2024), rather than Leo I. The $M_{\rm bound}$ we find for the Leo IV–Leo V pair ($\sim 4 \times 10^9\,\mathrm{M}_\odot$) is orders of magnitude lower than that of the Leo I–II alignment, falling well within the expected mass range for such dwarfs. The fact that Leo II appears kinematically and spatially closer to the Leo IV–Leo V association in higher-dimensional phase-space further reinforces that this object is likely a more distant member of this infalling group that is only coincidentally passing near the much more distant Leo I.

In the resolution-matched sample, approximately 43% (3 out of 7) of the associations are physically plausible candidates. Specifically, Draco–Ursa Minor ($\sim 6 \times 10^9\,\mathrm{M}_\odot$) and the LMC–SMC ($\sim 37 \times 10^9\,\mathrm{M}_\odot$) require higher masses than the ultra-faint pairs, but these values remain well within (and in the case of the Magellanic Clouds, significantly below) the expected total masses for such systems. Given that the LMC's total mass is estimated to be $\sim 10^{11}\,\mathrm{M}_\odot$ (e.g. Erkal et al., 2019), the required $M_{\rm bound}$ is easily satisfied, confirming their status as a bound pair. Similarly, the value for Draco–Ursa Minor is consistent with recent mass estimates for their respective dark matter haloes (e.g. **Júlio et al.**, 2025b; Read et al., 2019), supporting the idea that they were accreted together.

For the M31 system, 75% (3 out of 4 with data) of the identified pairs are physically plausible based on their $M_{\rm bound}$ values. We find that Andromeda X–Andromeda XXIV ($\sim 5 \times 10^9\,\mathrm{M}_\odot$) stands out as a highly promising candidate. The low $M_{\rm bound}$ for this pair suggests that even with a moderate tangential velocity component, the system would remain gravitationally bound within the expected mass range of M31's dwarf population. Similarly, Andromeda XXV–NGC 147 ($\sim 24 \times 10^9\,\mathrm{M}_\odot$) exhibits a threshold easily satisfied by the presence of a massive dwarf like NGC 147.

3.5 Conclusion

In this work, we have revisited the incidence and nature of satellite galaxy pairs in the Local Group by combining updated observational data with HESTIA cosmological simulations within a consistent statistical framework.

We first identify candidate associations using nearest-neighbour statistics and quantify their significance through P-values relative to isotropic expectations. The Milky Way satellite system exhibits a clear excess of close associations compared to both isotropic realisations and ΛCDM simulations. This is reflected in its high pairing efficiency ($\sim$ 53%), which remains high even when applying the stellar mass cut motivated by the simulation's resolution ($\sim$ 52%). In contrast, the M31 satellite system shows no comparable excess and remains broadly consistent with an isotropic spatial distribution.

While spatial proximity provides an effective method to search for pair candidates, additional phase-space information is required to understand their physical nature. Using a revised reference scale based on the present-day LMC–SMC line-of-sight velocity difference ($|\Delta v_{\rm los}| \sim 117\,\mathrm{km\,s^{-1}}$), we find that approximately $\sim$ 44% (7 out of 16) of MW pairs in the full sample, and $\sim$ 43% (3 out of 7) in the resolution-matched sample, exhibit small velocity differences consistent with potential dynamical association. For M31, $\sim$ 75% (3 out of 4) of the pairs with available velocity measurements satisfy this criterion, although this estimate is based on a small sample.

Proper motion information filters this picture further. Among the MW pairs with available measurements, we find that $\sim$ 44% (7 out of 16) exhibit velocity vectors that are consistent within their uncertainties, indicating that a non-negligible subset of pairs is compatible with coherent orbital motion. Several of these systems also satisfy the line-of-sight velocity criterion, demonstrating that the two diagnostics identify overlapping subsets of candidate associations. However, the overlap is not complete, highlighting that line-of-sight velocities and projected proper motion alignments probe complementary aspects of phase-space coherence. For the more massive satellites ($M_\star > 10^4\,\mathrm{M}_\odot$), this fraction increases to $\sim$ 70% (5 out of 7). The lack of proper motion measurements for M31 satellites prevents a comparable analysis for that system.

In the simulations, where full phase-space information is available, a comparable analysis shows that only a subset of spatially selected pairs exhibit coherent kinematics. We find that $\sim$ 65% of simulated pairs satisfy the line-of-sight velocity criterion. A visual inspection of the proper motion directions indicates that a significant fraction of these systems ($\sim$ 45%) show aligned motions in projection. Together, these results confirm that many statistically significant nearest-neighbour associations do not correspond to long-lived bound binaries, but instead arise from transient configurations or remnants of disrupted groups.

TABLE 3.3: Properties of the pair candidates.

Pair	ΔR_{3D} (kpc)	ΔR_{los} (kpc)	Δv_{3D} (km s^{-1})	Δv_{los} (km s^{-1})	$\overline{d}_{host}$ (kpc)	$\overline{v}_{host}$ (km s^{-1})	$\Delta\theta$ (°)	$\frac{M_{\star,1}}{M_{\star,2}}$	M_{bound} (10^9 M$_\odot$)
MW									
Bootes II – Bootes III	11.8	6.1	432.9	327.9	42.6	55.2	13.9	13.2	147
Canes Ven. I – Canes Ven. II	54.9	50.1	182.3	159.8	185.6	-8.9	6.5	26.9	163
Carina II – Pictor II	9.0	7.4	333.2	150.3	41.9	182.8	6.9	5.9	24
Carina II – Carina III	9.6	9.3	262.1	192.6	33.6	157.0	0.3	7.4	41
Grus II – Tucana II	13.7	1.8	138.8	14.7	51.6	-166.3	14.1	1.3	0.3
Horologium I – Reticulum III	18.4	11.9	254.7	161.4	85.7	40.6	9.2	1.1	56
Centaurus I – Hydra II	40.3	34.4	354.7	258.3	131.3	-2.29	9.5	1.3	313
Leo I – Leo II	89.0	50.6	167.8	204.4	236.8	99.6	18.4	8.5	432
Leo IV – Leo V	19.3	17.9	239.0	41.5	160.9	34.0	2.8	1.7	4
LMC – Pictor II	11.9	3.4	153.8	64.7	47.4	90.9	13.2	1.5×10^6	6
Pegasus III – Pisces II	43.4	30.9	596.5	3.6	197.4	-69.2	8.5	1.1	0.1
Segue II – Triangulum II	12.1	7.7	369.8	342.1	38.5	-107.8	16.1	1.8	164
SMC – Tucana V	14.7	8.4	223.2	180.3	56.1	-65.9	12.2	1.9×10^6	56
Tucana II – Tucana V	7.1	0.6	346.8	90.0	52.2	-167.8	7.2	11.5	7
Tucana IV – Tucana V	8.7	7.4	156.8	50.6	48.2	-108.8	3.9	5.8	3
Ursa Major II – Willman I	12.9	1.9	237.3	102.4	41.8	-65.3	19.8	5.6	16
MW ($M_\star > 10^4$ M$_\odot$)									
Bootes I – Bootes III	23.1	18.4	267.5	94.5	54.8	175.1	12.3	1.3	24
Carina II – LMC	18.7	10.8	202.5	215.0	43.7	161.5	18.9	2.5×10^5	100
Draco – Ursa Minor	25.6	9.5	73.0	43.7	76.8	-90.3	17.4	1.0	6
LMC – SMC	23.3	11.2	95.8	116.6	54.7	36.5	19.8	3.2	37
M31									
And. X – And. XXIV	36.3	22.6		35.9	172.6	154.9	2.6	1.4	5
And. XI – And. XII	34.8	33.8		129.6	101.9	-191.3	0.6	1.2	68
And. XV – And. XXIII	39.3	3.1		85.3	109.2	20.7	3.0	3.6	33
And. XXV – NGC 147	28.2	17.0		85.4	93.7	150.6	1.7	199.5	24
And. XXVIII – Pegasus VII	82.0	7.7			328.4		6.3	13.5	
Pegasus V – Pegasus VII	75.9	59.3			268.9		3.7	1.7	

Columns from left to right: (1) Names of the satellites part of a pair candidate; (2) 3D physical separation; (3) line-of-sight separation; (4) 3D velocity difference; (5) line-of-sight velocity difference; (6) mean distance from the host; (7) mean pair velocity relative to the host; (8) angular separation; (9) stellar mass ratio defined as $max(M_{\star,1}, M_{\star,2}) / min(M_{\star,1}, M_{\star,2})$; and (10) the total mass that the system would have to have in order to be bound. The pairs highlighted in bold are identified in both the full observational sample and the stellar mass limited sample.

TABLE 3.4: Properties of the pair candidates found in the simulations.

Pair	Sim. number	ΔR_{3D} (kpc)	ΔR_{los} (kpc)	Δv_{3D} (km s^{-1})	Δv_{los} (km s^{-1})	$\overline{d}_{host}$ (kpc)	$\overline{v}_{host}$ (km s^{-1})	$\Delta\theta$ (º)	$M_{\star,1}/M_{\star,2}$	b
MW analogues										
10–2963	9_18	19.7	14.8	192.2	165.6	100.0	-396.3	6.8	853.7	2.1822
774–26549	9_18	19.0	17.8	315.9	72.3	43.5	-268.3	7.0	214.3	0.0052
931–2973	9_18	48.5	33.4	347.1	85.1	150.9	127.3	12.6	3.0	0.0023
4719–11410	9_18	17.2	2.1	196.1	166.1	108.0	21.7	8.6	1.30	0.0033
5715–7479	9_18	13.8	3.7	111.6	133.1	50.8	-187.0	14.5	9.6	0.0110
2963–11736	9_18	32.2	21.1	265.1	131.9	118.0	-413.2	11.6	26.3	0.0008
22879–26549	9_18	15.7	2.6	350.2	81.5	33.3	-263.7	22.1	3.5	0.0002
3292–25953	17_11	25.3	7.8	137.8	51.3	92.5	290.8	14.3	18.5	0.0042
4602–31053	17_11	18.0	8.1	518.2	495.2	57.9	122.6	15.2	8.9	0.0003
9356–18567	17_11	13.7	5.0	185.0	211.2	46.0	-167.2	13.8	8.1	0.0017
1408–11290	37_11	10.5	5.1	142.4	179.2	35.6	343.1	18.9	167.7	0.0151
25745–27628	37_11	19.7	12.8	233.7	68.7	54.4	228.5	15.2	1.1	0.0003
1408–27628	37_11	19.5	9.9	111.0	39.3	59.4	223.8	24.8	1377.4	0.0122
M31 analogues										
884-8995	9_18	25.9	9.04	257.4	171.5	138.5	69.7	2.0	343.3	0.0041
1479-67802	9_18	17.7	15.8	278.0	11.9	77.3	204.1	0.9	1.5	0.0045
1584-2344	9_18	14.7	10.9	254.2	75.3	98.7	-96.9	1.0	83.0	0.0078
1887-6560	9_18	34.2	16.6	283.7	189.8	110.2	-13.8	2.8	397.8	0.0015
2344-6723	9_18	27.0	8.3	84.4	56.2	105.6	-106.5	2.7	8.8	0.0240
41–4743	17_11	33.4	8.5	206.9	84.1	128.2	266.6	4.5	26191.9	0.1160
993–1822	17_11	15.7	11.8	408.0	31.0	46.8	180.7	1.4	19.2	0.0038
2038–5836	17_11	49.8	9.1	187.3	43.5	174.7	100.6	5.0	25.6	0.0022
3262–7688	17_11	27.7	20.6	242.0	171.6	118.3	119.1	2.0	7.0	0.0016
3311–25757	17_11	22.3	14.1	225.4	98.5	71.6	226.4	2.6	23.9	0.0018
4743–12533	17_11	28.2	22.2	171.2	46.5	114.9	331.9	2.5	1.8	0.0020
41–5926	17_11	34.6	2.2	188.5	160.7	138.8	144.5	4.8	151349.7	0.1344
30–9254	17_11	38.5	0.7	66.7	48.4	138.6	189.6	4.2	5675.6	1.6527
41–9146	37_11	18.3	17.3	53.6	48.2	137.5	-130.	0.5	1065.3	4.0451
976–2481	37_11	36.7	36.2	90.0	48.2	116.5	-25.5	0.6	2.3	0.0315
2481–4294	37_11	18.0	15.9	108.5	10.0	125.1	-44.6	0.9	1.1	0.0188
4294–11673	37_11	13.2	6.1	57.4	18.1	134.1	-48.6	1.3	34.4	0.0427
8263–17744	37_11	18.3	3.9	87.8	71.6	39.8	-129.1	1.9	43.4	0.0059

Columns from left to right: (1) Names of the satellites part of a pair candidate; (2) Number of the simulation; (3) 3D physical separation; (4) line-of-sight separation; (5) 3D velocity difference; (6) line-of-sight velocity difference; (7) mean distance from the host; (8) mean pair velocity relative to the host; (9) angular separation; (10) stellar mass ratio defined as $max(M_{\star,1}, M_{\star,2})/\,min(M_{\star,1}, M_{\star,2})$; and (11) the binding criteria b.

The properties of the identified pairs also reveal a dependence on stellar mass, although the population is consistently dominated by "major" pairs. In the full MW sample, ~ 69% of the associations correspond to systems with comparable stellar masses ($M_{\star,1}/M_{\star,2} < 10$), while the remaining ~ 31% are "hierarchical" pairs involving an ultra-faint companion. After applying the stellar mass cut, the overall number of pairs decreases, but the relative contribution of major pairs remains similar (~ 71%), as most hierarchical associations are removed.

This indicates that, while the clustering signal includes a contribution from low-mass companions, it is not dominated by them. However, both simulations and M31 observations (limited by resolution and distance, respectively) primarily probe the major-pair regime since they lack low-mass satellites. As a result, comparisons across these samples may underestimate the true abundance of hierarchical associations in the underlying satellite population.

Our dynamical analysis further shows that only a fraction of pairs are consistent with being currently gravitationally bound. In the observations, we find that ≈ 38% of the MW pair candidates satisfy this criterion, increasing to ≈ 43% when applying the stellar mass cut. For M31, this fraction rises to ~ 75%, although this likely reflects a selection bias towards more massive and tightly bound systems. In the simulations, however, only ~ 10% of pairs are identified as bound, indicating that most pairs are not long-lived bound systems but rather transient configurations or remnants of disrupted groups. This is consistent with expectations from hierarchical structure formation, where satellites are accreted in groups but rapidly lose their mutual binding within the host halo.

Although nearest-neighbour statistics provide an efficient way to identify candidate satellite associations, combining all available diagnostics significantly reduces the number of systems consistent with genuine physical pairs. Requiring simultaneous spatial clustering, kinematic coherence, aligned motions, and compatibility with gravitational binding leaves only a small fraction of the original candidates. In the full MW observational sample, only ~ 19% (3 out of 16) of the spatially selected candidates satisfy all three criteria simultaneously, increasing to ~ 29% (2 out of 7) in the resolution-matched sample. In the HESTIA simulations, the fraction is even smaller, with only ~ 8% (1 out of 13) of the MW analogue candidates and ~ 11% (2 out of 18) of the M31 analogue candidates satisfying all criteria simultaneously. This demonstrates that most statistically significant nearest-neighbour associations do not correspond to long-lived physical binaries, but instead trace transient configurations, tidal remnants, or satellites that were accreted together but are no longer gravitationally bound today.

Taken together, these results suggest that the excess of satellite pairs in the MW is not primarily due to an abundance of bound binaries, but instead reflects the presence of correlated phase-space structures associated with recent or ongoing group infall. The Magellanic system provides a clear example of this process.

Finally, the contrasting behaviour of the MW and M31 highlights the importance of individual accretion histories, as well as observational and numerical limitations, in shaping the inferred clustering properties of satellite systems. While the MW exhibits an excess of close associations, M31 remains consistent with isotropic expectations even when accounting for distance uncertainties. At the same time, some simulated M31 analogues display stronger clustering than observed, suggesting that environmental factors and stochastic assembly histories can produce a wide range of outcomes.

Future progress will require improved completeness for faint satellites, particularly around M31, together with more accurate distance measurements and precise proper motion to better constrain the full 6D phase-space information of candidate associations. On the theoretical side, a larger suite of high-resolution cosmological simulations spanning a broader range of host masses and assembly histories will be essential to robustly assess the statistical significance of the observed MW–M31 differences within the ΛCDM framework.

Acknowledgements

MPJ and MSP acknowledge funding via a Leibniz-Junior Research Group (project number J94/2020). This research has made use of Astropy (Astropy Collaboration et al., 2018), galpy (Bovy, 2015), matplotlib (Hunter, 2007), NASA's Astrophysics Data System Bibliographic Services, NumPy (Harris et al., 2020) and SciPy (Virtanen et al., 2020).

Appendices

3.A Cumulative radial distribution of simulations

Following the methodology applied to the observed satellite systems described in Sect. 3.3, we show here the radial distributions of the HESTIA simulated analogues. Figure 3.A.1 presents the cumulative radial distributions of satellites around each MW- and M31-like host in three simulation runs, compared against 10^5 isotropic realisations constructed from the same radial profiles.

In all cases, the simulated satellite distributions fall within the 1σ to 3σ confidence intervals of the isotropic populations, confirming that the radial profiles of the simulated analogues are statistically consistent with the isotropic realisations used to generate the nearest-neighbour reference distributions in our analysis.

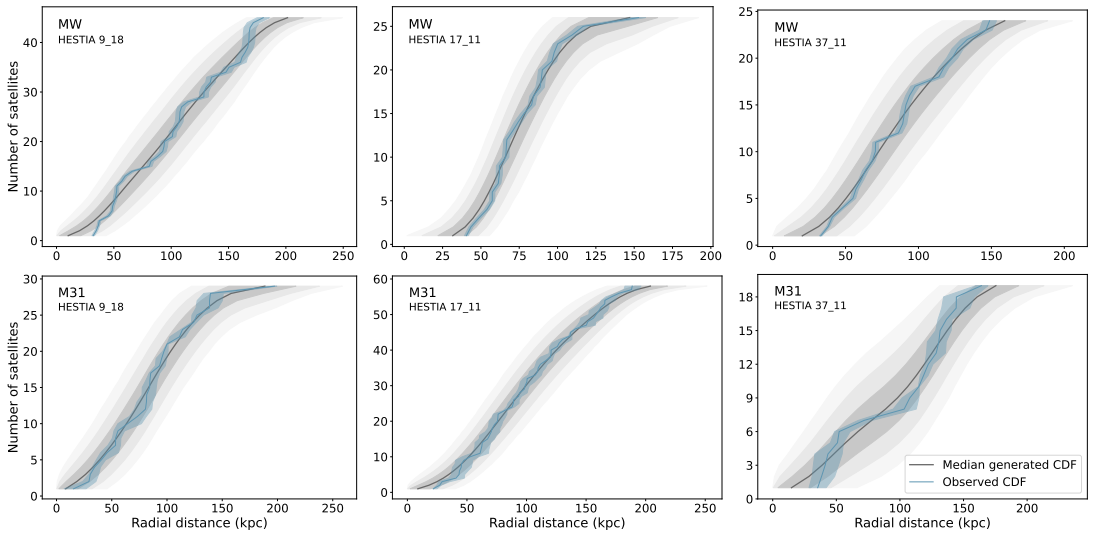


Figure 3.A.1: Cumulative radial distributions of satellites for the simulated HESTIA MW and M31 analogues satellite systems. The solid blue line represents the cumulative number of satellites as a function of host-centric distance, with the surrounding blue shaded region indicating the range obtained when the satellite distances are shifted by their reported upper and lower uncertainties. The median distribution of 10^5 isotropic realisations is shown as a solid dark grey line. The grey shaded regions represent the 1σ (68%), 2σ (95%) and 3σ (99%) confidence intervals, respectively, for the generated isotropic populations. This comparison illustrates whether the observed radial concentration of satellites is consistent with a random spatial distribution.

3.B *P*-value distributions of opposite host analogues

In Sect. 3.4.1 we noted that the level of apparent clustering depends partly on the total number of satellites in a system, which in turn correlates with the mass of the host halo. To illustrate this effect, we compare the *P*-value distributions of the simulated MW and M31 analogues across the same HESTIA realisations.

Figure 3.B.1 shows the same *P*-value CDFs as in Fig. 3.4, but now including the *P*-value distribution of the *opposite* host analogue from the same simulation run. In other words, when comparing to the observed MW we also plot the corresponding M31 analogue from that run, and vice versa.

In some cases, the *P*-value distribution of the opposite host analogue reproduces the observed system more closely than the nominal host counterpart. This behaviour is particularly evident in the 37_11 realisation, where the M31 analogue (despite belonging to the M31 side of the simulated pair) tracks the observed MW *P*-value distribution more closely than the MW analogue itself.

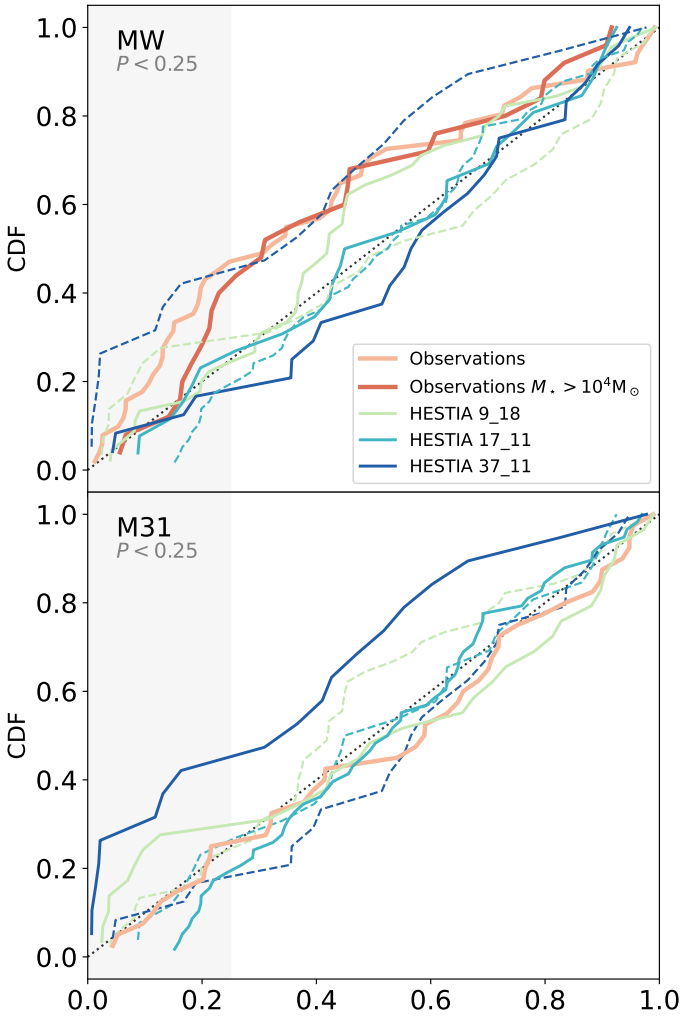


FIGURE 3.B.1: P-value distributions for the nearest-neighbour (NN) separations in the MW (top) and M31 (bottom) satellite systems. The solid orange lines represent the observational samples, while the red line indicates the resolution-matched MW sample ($M_\star > 10^4\,M_\odot$). Results from the HESTIA simulated analogues are shown in shades of blue and green. The dashed curves show the P-value distributions of the *opposite* host analogue from the same simulation run (M31 analogues in the top panel and MW analogues in the bottom panel). The black dotted line represents the expectation for a perfectly isotropic distribution. The grey shaded region marks the regime used to identify statistically significant close associations ($P < 0.25$).

3.C KINEMATIC COHERENCE OF PAIR CANDIDATES

The nearest-neighbour analysis presented in Sect. 3.4.2 identifies satellites that are unusually close in space compared to expectations from isotropy. However, spatial proximity alone does not guarantee a physical association. Satellites that were accreted together or belong to the same substructure are expected to exhibit additional signatures of coherence, such as similar line-of-sight velocities, aligned orbital motions, or the possibility of being gravitationally bound.

To qualitatively assess the likelihood that the identified candidate pairs correspond to genuine physical associations, we therefore examine several additional diagnostics: (i) kinematic coherence based on the difference in line-of-sight velocities, (ii) consistency of the orbital motions when proper motions are available, and (iii) whether the minimum dynamical mass required for the pair to be gravitationally bound is compatible with the expected halo masses of the satellites.

Tables 3.C.1 and 3.C.2 summarise these diagnostics for the observational and simulated candidate pairs, respectively. These indicators provide a qualitative assessment of whether the spatially identified pairs are consistent with a common origin or represent chance alignments. For two of the observed M31 pair candidates, there are no kinematic measurements, so none of the criteria can be qualified.

TABLE 3.C.1: Qualitative assessment of the physical coherence of the observed pair candidates.

Pair	Kinematics	Motions	Bound
MW			
Bootes II – Bootes III	no	no	no
Can.Ven. I – Can.Ven. II	no	yes	no
Carina II – Pictor II	no	no	no
Carina II – Carina III	no	yes	no
Grus II – Tucana II	yes	no	yes
Horo. I – Reti. III	yes	yes	no
Cent. I – Hydra II	no	no	no
Leo I – Leo II	no	yes	no
Leo IV – Leo V	yes	yes	yes
LMC – Pictor II	yes	yes	yes
Pegasus III – Pisces II	yes	yes	yes
Segue II – Trian. II	no	no	no
SMC – Tucana V	no	no	yes
Tucana II – Tucana V	yes	no	yes
Tucana IV – Tucana V	yes	no	yes
U. Major II – Willman I	yes	no	yes
MW ($M_\star > 10^4\,M_\odot$)			
Bootes I – Bootes III	yes	no	no
Carina II – LMC	no	yes	yes
Draco – Ursa Minor	yes	yes	yes
LMC – SMC	yes	yes	yes
M31			
And. X – And. XXIV	yes		yes
And. XI – And. XII	no		no
And. XV – And. XXIII	yes		no
And. XXV – NGC 147	yes		no

Columns from left to right: (1) Names of the satellites part of a pair candidate; (2) kinematic coherence based on the difference in line-of-sight velocity ($\Delta v_{\rm los} < 117\,{\rm km\,s^{-1}}$); (3) possible alignment of the orbital motions based on proper motions and great-circle trajectories when available; (4) whether the minimum dynamical mass required for the pair to be gravitationally bound is compatible with expected satellite halo masses.

TABLE 3.C.2: Qualitative assessment of the physical coherence of pair candidates identified in the HESTIA simulations.

Pair	Sim.	Kinematics	Motions	Bound
MW analogues				
10–2963	9_18	no	yes	yes
774–26549	9_18	yes	no	no
931–2973	9_18	yes	no	no
4719–11410	9_18	no	yes	no
5715–7479	9_18	no	yes	no
2963–11736	9_18	no	yes	no
22879–26549	9_18	yes	no	no
3292–25953	17_11	yes	no	no
4602–31053	17_11	no	no	no
9356–18567	17_11	no	yes	no
1408–11290	37_11	no	no	no
25745–27628	37_11	yes	no	no
1408–27628	37_11	yes	yes	no
M31 analogues				
884-8995	9_18	no	no	no
1479-67802	9_18	yes	no	no
1584-2344	9_18	yes	no	no
1887-6560	9_18	no	no	no
2344-6723	9_18	yes	yes	no
41–4743	17_11	yes	no	no
993–1822	17_11	yes	no	no
2038–5836	17_11	yes	no	no
3262–7688	17_11	no	no	no
3311–25757	17_11	yes	no	no
4743–12533	17_11	yes	yes	no
41–5926	17_11	no	yes	no
30–9254	17_11	yes	yes	yes
41–9146	37_11	yes	yes	yes
976–2481	37_11	yes	yes	no
2481–4294	37_11	yes	no	no
4294–11673	37_11	yes	yes	no
8263–17744	37_11	yes	yes	no

Columns from left to right: (1) Pair of satellites identified as a candidate association; (2) Simulation realisation; (3) kinematic coherence based on the difference in line-of-sight velocity ($\Delta v_{\rm los} < 117 {\rm km\,s^{-1}}$); (4) possible alignment of the orbital motions; (5) whether the pair is gravitationally bound.

Part II: Internal dynamics

The radial acceleration relation at the EDGE of galaxy formation: testing its universality in low-mass dwarf galaxies

4

Abstract. A tight correlation between the baryonic and observed acceleration of galaxies has been reported over a wide mass range ($10^8 < M_{\rm bar}/{\rm M}_\odot < 10^{11}$); this is known as the radial acceleration relation (RAR). This has been interpreted as evidence that dark matter is actually a manifestation of a modified, weak-field gravity theory. In this work, we studied the radially resolved RAR of 12 nearby dwarf galaxies, with baryonic masses in the $10^4 < M_{\rm bar}/{\rm M}_\odot < 10^{7.5}$ range, using a combination of literature data and data from the MUSE-Faint survey. We used stellar line-of-sight velocities and the Jeans modelling code GravSphere to infer the mass distributions of these galaxies, allowing us to compute the RAR. We compare the results with the EDGE simulations of isolated dwarf galaxies with similar stellar masses in a Λ cold dark matter cosmology. We find that most of the observed dwarf galaxies lie systematically above the low-mass extrapolation of the RAR. Each galaxy traces a locus in the RAR space that can have a multi-valued observed acceleration for a given baryonic acceleration, while there is significant scatter from galaxy to galaxy. Our results indicate that the RAR does not apply to low-mass dwarf galaxies, and that the inferred baryonic acceleration of these dwarfs does not contain enough information, on its own, to derive the observed acceleration. The simulated EDGE dwarfs behave similarly to the real data, with a higher observed acceleration at a fixed baryonic acceleration than the extrapolated RAR. We show that, in the context of modified, weak-field gravity theories, these results cannot be explained by differential tidal forces from the Milky Way or by the galaxies being far from dynamical equilibrium, since none of the galaxies in our sample seem to experience strong tides. As such, our results provide further evidence of the need for invisible dark matter in the smallest dwarf galaxies.

M. P. Júlio, J. I. Read, M. S. Pawlowski, P. Li, D. Vaz, J. Brinchmann, M. P. Rey, O. Agertz, & T. Holmes (Dec. 2025b). "The radial acceleration relation at the EDGE of galaxy formation: Testing its universality in low-mass dwarf galaxies". In: *A&A* 704, A330. DOI: 10.1051/0004-6361/202557106

4.1 Introduction

A key puzzle of galaxy formation in the standard Λ-cold dark matter (ΛCDM) cosmology is the apparently tight correlation between the distribution of baryonic matter in galaxies and their observed dynamics, even in systems where the dark matter dominates (see e.g. Bullock & Boylan-Kolchin, 2017, for a review). These correlations have been known since the 1970s and include the Tully-Fisher relation (Tully & Fisher, 1977), which links the luminosity to the peak rotation velocity for rotationally-supported galaxies, and the Faber-Jackson relation (Faber & Jackson, 1976), which links stellar mass and stellar velocity dispersion for pressure-supported systems. More recently, the mass-discrepancy acceleration relation, which relates the distribution of baryonic matter with the observed acceleration of a galaxy (McGaugh, 2004), and the radial acceleration relation (RAR; Lelli et al., 2017; McGaugh et al., 2016), which relates the observed dynamical radial acceleration with the acceleration expected from the visible baryons in galaxies, were discovered.

To establish the RAR, McGaugh et al. (2016) used the Spitzer Photometry and Accurate Rotation Curves (SPARC) database (Lelli et al., 2016) to determine the observed and the baryonic acceleration of over 150 late-type galaxies. These covered a wide range of morphological types (So to Irr), surface brightnesses ($\sim$ 4 dex), and luminosities ($\sim$ 5 dex), corresponding to baryonic masses over the $10^8 < M_{\rm bar}/{\rm M}_\odot < 10^{11}$ range. This relation is surprisingly tight, with an observed scatter of just 0.13 dex, which is mostly driven by observational errors. In Lelli et al. (2017), it was confirmed that early-type galaxies and classical dwarf spheroidals (dSphs) followed the same relation as the one in McGaugh et al. (2016), within the uncertainties at that time. Furthermore, the residuals are well described by a Gaussian with a width of 0.11 dex and did not show any correlation with galaxy properties, such as baryonic mass, gas fraction, or radius. Freundlich et al. (2022) showed that ultra-diffuse galaxies in the Coma cluster also follow the RAR. Mistele et al. (2024) used kinematic and gravitational-lensing data to derive the RAR over a wide dynamic range. They found that the RAR inferred from weak-lensing data smoothly continues the trend inferred from kinematic data towards lower accelerations by about 2.5 dex. They also found that early- and late-type galaxies lie on the same joint RAR when a sufficiently strict isolation criterion is adopted. Recently, Vărăşteanu et al. (2025) used resolved HI kinematics from the MIGHTEE-HI survey (Jarvis et al., 2018) to extend the RAR down to accelerations of $log(g_{\rm bar}/{\rm m\,s^{-2}}) \sim -12$ and found that gas-rich galaxies continue to follow the same relation over several orders of magnitude ($M_\star \sim 10^8 - 10^{10}{\rm M}_\odot$) up to $z = 0.08$. Taken together, these works suggested that the RAR could be a fundamental relation obeyed by all galaxies.

However, for very low- and high-mass systems, and when considering distinct radii within galaxies, cracks begin to show in the idea that the RAR is universal. At high masses, both the brightest galaxies in galaxy clusters, and galaxy clusters themselves, appear to obey an RAR, but one distinct from the galactic RAR (Li et al., 2023; Tian et al., 2024, 2020). At low masses, Lelli et al. (2017) showed preliminary evidence that dSph galaxies tend to scatter above the low-mass extrapolation of the RAR, with large galaxy-to-galaxy scatter (though within the quoted observational uncertainties at that time). Read et al. (2019) showed that two of the satellites of the Milky Way (MW), Draco and Carina, have similar baryonic mass distributions and similar orbits around their host, but distinct dynamical mass distributions, which is inconsistent with a universal RAR. Finally, individual galaxies can deviate from the RAR deep in the centre. For example, some galaxies at lower accelerations trace a curved locus in the RAR space, with two different observed accelerations for the same baryonic acceleration (Eriksen et al., 2021), but this is less frequent in observations than in simulations (Mercado et al., 2024). As such, it is yet unclear if the RAR is truly a one-to-one map from baryonic to observed accelerations.

Several theoretical studies have attempted to explain the RAR in a ΛCDM cosmology (e.g. Garaldi et al., 2018; Ludlow et al., 2017; Tenneti et al., 2018). These studies found that a correlation between the total and the baryonic accelerations can arise in ΛCDM as well, which is perhaps not surprising – more massive galaxies contain more gas and form more stars (e.g. Wang et al., 2015). However, matching the RAR in detail has proven more challenging. For instance, the relation found in Ludlow et al. (2017) using galaxies with stellar masses ranging from $10^5{\rm M}_\odot$ to $10^{12}{\rm M}_\odot$, has a significantly higher characteristic acceleration scale as compared to the measured RAR. Similarly, Tenneti et al. (2018) find, for galaxies with stellar masses of $> 10^{12}{\rm M}_\odot$, a linear correlation, without any trace of an acceleration scale. In fact, as pointed out by Li et al. (2022), comparing the intrinsic scatter of the observed RAR with that from simulated galaxies is not straightforward (see also Dutton et al., 2019; Garaldi et al., 2018; Keller & Wadsley, 2017), because it requires the modelling of observational errors,

rotation-curve sampling, and the covariance between the total and the baryonic acceleration. As such, it remains unclear whether the emergence of the RAR can be understood in the standard cosmology or not.

If galaxy-formation simulations in ΛCDM continue to struggle to reproduce the RAR in detail, then it could be that the RAR indicates a need for new physics. One such set of models that could explain the RAR is modified Newtonian dynamics (MOND, Milgrom, 1983). This is a modified, weak-field gravitational-force law hypothesised as an alternative to dark matter. In MOND, the classical laws of Newtonian dynamics are modified at low accelerations instead of by adding dark matter, directly coupling the observed baryonic mass distribution to the observed galaxy dynamics (e.g. Li et al., 2018). As such, MOND naturally reproduces the RAR with, formally, zero scatter (e.g. Lelli et al., 2017). However, it predicts deviations from the RAR for satellite galaxies, which is opposite to what is observed (Lelli et al., 2017). MOND does not follow the equivalence principle, so the internal dynamics of satellite galaxies orbiting in the tidal field of their host galaxy experience an 'external field effect' (EFE; e.g. Bekenstein & Milgrom, 1984; Famaey & McGaugh, 2012; Milgrom, 1983). This effectively lowers the MOND acceleration scale, causing the internal dynamics of the satellite to behave more like that of the Newtonian gravity case. This, in turn, causes satellites orbiting in strong tidal fields to scatter systematically *below* the RAR (Chae et al., 2021, 2020; Freundlich et al., 2022; McGaugh & Milgrom, 2013; McGaugh et al., 2016; Müller et al., 2019; Pawlowski & McGaugh, 2014b; Pawlowski et al., 2015b), which is opposite to what is observed for dSph satellites in the Local Group (Lelli et al., 2017). More modern relativistic alternative gravity theories show promise (e.g. Skordis & Złośnik, 2021) and have weak-field behaviour that is rich and distinct from MOND (e.g. Durakovic & Skordis, 2024). It remains to be seen if these more complete theories can explain the latest data.

Given that the deviations from the RAR lack a full explanation in both the standard-cosmology and modified-gravity theories, it is interesting to further explore its extremities with observational data. In this work, we used stellar line-of-sight velocities from the literature for the classical dSph satellite galaxies of the MW, combined with MUSE-Faint velocities of ultra-faint dwarfs, in order to study the radially resolved RAR at much lower accelerations than has previously been possible. Moving to a regime one-to-two orders of magnitude lower in baryonic mass than the SPARC sample, we probed the internal acceleration profiles of each dwarf galaxy and the scatter between them. We discuss how the EFE impacts our results, given that many galaxies in our sample orbit within the MW, and we compare our findings to the RAR calculated for simulated dwarf galaxies in ΛCDM taken from the 'Engineering Dwarfs at Galaxy Formation's Edge' (EDGE) project (Agertz et al., 2020). Our goal is to determine whether the RAR really is a one-to-one map from the baryonic-to-observed acceleration in galaxies. If so, the RAR could indicate the need for new physics at low accelerations. If not, the RAR is more likely to be an emergent phenomenon – a challenge for modern galaxy-formation theories to solve.

This paper is organised as follows. In Sect. 4.2, we describe the data we used to measure the RAR (4.2.1) and describe the EDGE simulations that we compare our results to (Sect. 4.2.2). In Sect. 4.3, we briefly describe the mass-modelling method we used in this work to compute the baryonic and observed accelerations of these galaxies (GravSphere; Sect. 4.3.2), and we tested its recovery of the RAR using mock data drawn from the EDGE simulations (Sect. 4.3.4). We present our results in Sect. 4.4, where we show the RAR for our galaxy sample (Sect. 4.4.1) and compare this to the EDGE simulations (Sect. 4.4.2). Finally, we discuss our results in Sect. 4.5 and present our conclusions in Sect. 4.6. For completeness, we provide supplementary material and relevant code modifications in support of the results that we discuss in the main text in Appendices 4.A, 4.B, 4.C, 4.D, and 4.E. Throughout this paper, all logarithms are base 10; i.e., $log \equiv log_{10}$.

4.2 Data

4.2.1 Observational data

Our data sample comprises 12 dwarf galaxies, with eight of them being the classical dSphs of the MW, and the other four being faint and ultra-faint dwarfs of the MW and beyond, taken from the MUSE-Faint survey (Zoutendijk et al., 2021a). Figure 4.1 shows their structural properties, described

in Table 4.1, and the structural properties of the EDGE simulated dwarfs for comparison, described in Table 4.2 of Sect. 4.2.2.

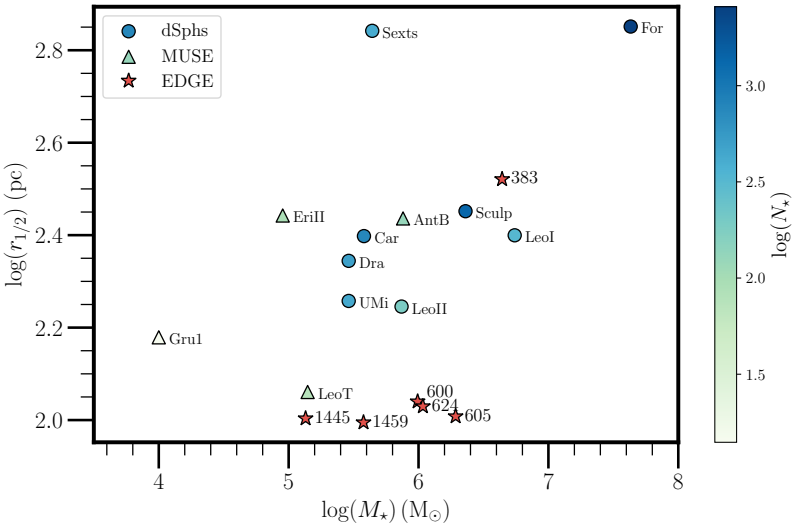


FIGURE 4.1: Stellar mass, $M_\star$, against the half-light radius, $r_{1/2}$, for our galaxy sample. The circles indicate the classical dSphs, and the triangles represent the dwarfs from MUSE-Faint. Objects are colour-coded by the number of stars with velocities available for each object. The red stars represent the EDGE simulated dwarfs.

4.2.1.1 Dwarf spheroidals

Our sample of dSphs is comprised of Carina (Car), Draco (Dra), Fornax (For), Leo I, Leo II, Sextans (Sexts), Sculptor (Sculp), and Ursa Minor (UMi). For all of these galaxies, we have kinematics for $\gtrsim$ 190 stars, and their photometric light profiles are well measured (see Read et al., 2019 for an extensive analysis).

For the photometric data, we used the Panoramic Survey Telescope and Rapid Response System (Pan-STARRS) DR1 catalogue (Flewelling et al., 2020) for Draco, Leo I, Leo II, Sextans, and Ursa Minor; the VLT/ATLAS DR1 catalogue (as re-processed by Koposov et al., 2014) for Fornax and Sculptor; and a catalogue derived from observations with the Dark Energy Camera by McMonigal et al. (2014) for Carina. For the kinematic data, we adopted spectroscopic data samples from Walker et al. (2009a) for Carina, Fornax, Sculptor and Sextans; from Mateo et al. (2008) for Leo I; from Spencer et al. (2017a) for Leo II; from Spencer et al. (2018) for Draco; and from Read et al. (2019) for Ursa Minor. For a comprehensive description of the selection of member stars for all dwarfs, see Read et al. (2019). All of the dwarfs have tidal radii today that are significantly larger than their stellar half-light radii (Pace et al., 2022; see also Sect. 4.5.3), though some could have experienced stronger tidal forces in the past (e.g. Genina et al., 2022).

4.2.1.2 MUSE-Faint dwarfs

Our sample of faint dwarfs comprises the ultra-faint dwarfs of the MW Eridanus II (EriII), Grus 1 and Leo T, and the faint dwarf Antlia B (AntB), which is associated with NGC 3109. We used mock photometry catalogues with 10,000 sample photometric positions drawn from the best-fit exponential profiles found for each dwarf (see Zoutendijk et al., 2021a for further details).

We used spectroscopic observations from the MUSE-Faint survey, a survey of ultra-faint dwarfs conducted using the Multi Unit Spectroscopic Explorer, for these objects. The extensive data reduction and analysis for these objects can be found in Zoutendijk et al. (2020) for Eridanus II, in Zoutendijk et al. (2021a) and Vaz et al. in prep for Grus 1, in **Júlio et al.** (2023) for Antlia B, and in Vaz et al. (2023) for Leo T. For these dwarfs, we have from 14 (for Grus 1) to 127 stars (for Antlia B). As with the classical dwarfs, our faint dwarfs also have tidal radii far larger than their stellar light profiles (Pace et al., 2022; see also Sect. 4.5.3).

TABLE 4.1: Parameters adopted from the literature.

Galaxy	D (kpc)	$r_{1/2}$ (pc)	r_t (pc)	M_V (mag)	$M_\star$ ($10^6 M_\odot$)	$M_{\rm gas}$ ($10^6 M_\odot$)	$N_\star$	References
Carina	106 ± 6	250 ± 39	2387	-9.1	0.38	-	767	1, 2
Fornax	138 ± 8	710 ± 77	6083	-13.4	43	-	2573	3, 2
Draco	76 ± 6	221 ± 19	2172	-8.8	0.29	-	504	4, 5
Leo I	254 ± 15	251 ± 27	5299	-12.0	5.5	-	328	6, 2
Leo II	233 ± 14	176 ± 42	3875	-9.8	0.74	-	186	7, 2
Sculptor	86 ± 6	283 ± 45	2502	-11.1	2.3	-	1351	8, 2
Sextans	86 ± 4	695 ± 44	2930	-9.3	0.44	-	417	9, 2
Ursa Minor	76 ± 3	181 ± 27	2279	-8.8	0.29	-	430	10, 2
Antlia B	1350 ± 60	273 ± 29	7777*	-9.7	0.76	0.28	127	11, 12, 13
Eridanus II	366 ± 17	277 ± 14	5154	-7.1	0.09	-	92	14, 15
Grus 1	125	151^{+21}_{-31}	1076	-4.1	0.01	-	14	16, 17, 13
Leo T	409 ± 28	115 ± 17	5639	-7.6	0.14	0.41	75	18, 19, 13

Notes. From left to right, the columns show the name of the galaxy and Galactocentric distance ($D_\odot$); half-light radius ($r_{1/2}$); tidal radius (r_t) estimated with the dynamical masses from Pace (2025); absolute V-band magnitude (M_V); stellar mass ($M_\star$); gas mass ($M_{\rm gas}$); and number of kinematic member stars ($N_\star$). The units for each column are marked in the second row.
*Obtained using the distance from Ant B to its host $D = 72$ kpc (Sand et al., 2015) and $M_{\rm NGC3109} = 1.1\times10^{10} M_\odot$ (Huchtmeier, 1973).
References. (1) Pietrzyński et al. (2009), (2) Irwin & Hatzidimitriou (1995), (3) de Boer et al. (2012), (4) Bonanos et al. (2004), (5) Martin et al. (2008), (6) Bellazzini et al. (2004), (7) Bellazzini et al. (2005), (8) Pietrzyński et al. (2009), (9) Lee et al. (2009), (10) Carrera et al. (2002), (11) Sand et al. (2015), (12) Hargis et al. (2020), (13) Zoutendijk et al. (2021b), (14) Crnojević et al. (2016), (15) Zoutendijk et al. (2021a), (16) Koposov et al. (2015), (17) Chiti et al. (2022), (18) Clementini et al. (2012), and (19) Wolf et al. (2010).

4.2.2 EDGE simulation data

The EDGE project is described in detail in Agertz et al. (2020). We briefly summarise the key features of the simulations here for the reader's convenience. The simulations we used were first published in Gray et al. (2025) & Orkney et al. (2021) and are summarised in Table 4.2.

The Engineering Dwarfs at Galaxy Formation's Edge is a suite of high-resolution cosmological zoom simulations of isolated dwarf galaxies in a ΛCDM cosmology ($\Omega_m = 0.309$, $\Omega_\Lambda = 0.691$, $\Omega_{\rm b} = 0.045$, and $\rm H_0 = 67.77 km\,s^{-1} Mpc^{-1}$; Planck Collaboration, 2020). It uses the adaptive mesh refinement hydrodynamics code RAMSES (Teyssier, 2002); a maximum spatial resolution of 3 pc; and a mass resolution of $\rm M_{gas}$=18 $\rm M_\odot$, $\rm M_\star$=300 $\rm M_\odot$, and $\rm M_{DM}$=117 $\rm M_\odot$ for the higher resolution simulations we present here (Orkney et al., 2021). We also compare these with lower resolution simulations that have $\rm M_{gas}$=161 $\rm M_\odot$, $\rm M_\star$=300 $\rm M_\odot$, and $\rm M_{DM}$=945 $\rm M_\odot$ to test numerical convergence (Rey et al., 2020, 2019). For Halo 383, there is no higher resolution version available, so we only used the lower resolution one (Gray et al., 2025). The galaxy formation model includes subgrid prescriptions for star formation, stellar feedback, cosmic reionisation, and gas cooling. Star formation occurs when the gas temperature falls below $T_{\rm SF} = 100$ K and the gas density rises above $\rho_{\rm SF} = 300$ atoms/cc. Stars are then formed stochastically at a rate of $\dot{\rho}_\star = \varepsilon_{\rm ff} \frac{\rho_{\rm g}}{t_{\rm ff}}$, where $\varepsilon_{\rm ff} = 0.1$ is the star formation efficiency and $t_{\rm ff}$ is the local gas free-fall time. Each star particle has a mass of $\sim 300\,M_\odot$ and represents a single stellar population that has a Kroupa (2001) initial stellar mass function. Energy from supernovae (Type Ia and Type II) is injected purely thermally and if the cooling radius is resolved (which

TABLE 4.2: Properties of simulated EDGE dwarf galaxies at redshift $z = 0$ used in this paper.

Name	Resolution	M_{200}	r_{200}	$M_\star$	M_V	$r_{1/2}$	[Fe/H]
	$(m_{DM},m_{gas},m_\star)/M_\odot$	$(10^9 M_\odot)$	(kpc)	$(10^6 M_\odot)$	(mag)	(pc)	(dex)
Halo383	[945,161,300]	5.7	38.00	4.4	−10.88	331.80	−2.00
Halo600	[117,18,300]	2.65	31.17	0.984	−9.19	109.65	−2.48
Halo605	[117,18,300]	3.20	31.08	1.930	−9.84	101.83	−1.96
Halo624	[117,18,300]	3.23	29.18	1.080	−9.44	107.04	−2.12
Halo1445	[117,18,300]	1.32	23.10	0.135	−6.93	100.79	−2.49
Halo1459	[117,18,300]	1.43	23.75	0.377	−8.03	98.80	−2.02

Notes. From left to right, the columns show the simulation label; mass resolution [dark matter, gas, stars]; halo virial mass (M_{200}); halo virial radius (r_{200}); stellar mass ($M_\star$); absolute V-band magnitude (M_V); projected half-light radius ($r_{1/2}$); and iron abundance ([Fe/H]). The units for each column are marked in the second row. All properties are reported for the higher resolution version of these simulations, except for Halo 383. To study numerical convergence, we also compare our results with lower resolution simulations that have a mass resolution of $[945, 161, 300]\,M_\odot$. All simulations were first presented in Orkney et al. (2021, 2023) and Gray et al. (2025) for Halo 383.

is the case > 90% of the time). If not, some additional momentum is also injected to compensate for gas over-cooling (see Agertz et al., 2020, for details). Stellar winds from massive stars ($> 5\,M_\odot$) continuously inject energy, mass, and metals into the interstellar medium, as in Agertz et al. (2013). These EDGE simulations do not include radiative-transfer (photo-ionisation or photo-heating) from young stars (such physics is included in EDGE2, without significant changes to stellar masses and sizes; Rey et al., 2025). Finally, reionisation is modelled as a uniform, time-dependent, heat source (Haardt & Madau, 1995; Rey et al., 2020).

4.3 METHODS

In this section, we describe our methodology. In Sect. 4.3.1, we explain how we estimated the baryonic and total, 'observed', acceleration for our sample of galaxies. In Sect. 4.3.2, we describe the mass modelling tool, GRAVSPHERE (Collins et al., 2021; Genina et al., 2020; Read & Steger, 2017; Read et al., 2018, 2019), which we used to determine the cumulative mass profiles of our sample of galaxies from their photometric and kinematic data.

4.3.1 THE RADIAL RELATION ACCELERATION

Throughout this paper, we assume that our sample of dwarf galaxies is in dynamical pseudo-equilibrium (meaning that while they may deviate from strict equilibrium due to tidal or internal processes, their overall kinematics are sufficiently stable for equilibrium methods to apply), which is a good assumption given that they all orbit in a weak tidal field[1] (Pace et al., 2022 and see Sect. 4.5.3). Furthermore, we assumed spherical symmetry. This is not likely to be valid for our sample of galaxies (e.g. Goater et al., 2024; Orkney et al., 2023). However, bias due to triaxiality, for the number of kinematic tracers we used in this work, is expected to be small. Read & Steger (2017) applied GRAVSPHERE to a triaxial mock with axis ratios 1:0.8:0.6, which is consistent with standard cosmology expectations (e.g. Orkney et al., 2023). They showed that the assumption of spherical symmetry in GRAVSPHERE leads to bias when applied to triaxial mock data, but, for ~ 1000 tracer stars, this is typically smaller than their quoted 95% confidence intervals. This conclusion is further supported by Genina et al. (2020) & Nguyen et al. (2025). They applied GRAVSPHERE to mock

1. The Small Magellanic Cloud is undergoing heavy tidal disruption (De Leo et al., 2020), much more extreme than any of the galaxies we studied here. Yet, it can still be successfully mass modelled (De Leo et al., 2024).

satellites drawn from cosmological simulations APOSTLE and FIRE, respectively. In both cases, GravSphere provides an excellent recovery of the truth within its quoted uncertainties. This demonstrates that our results will not be significantly biased by realistic departures from spherical symmetry or tidal forces from the MW.

Assuming spherical symmetry, the observed acceleration then follows as

$$g_{\rm obs}(r) = -\nabla \Phi_{\rm tot}(r) = \frac{GM_{\rm tot}(< r)}{r^2}, \tag{4.1}$$

where G is the gravitational constant and $M_{\rm tot}(< r)$ is the total cumulative mass at radius r. The baryonic acceleration follows similarly from the baryonic mass:

$$g_{\rm bar}(r) = \frac{GM_{\rm bar}(< r)}{r^2}. \tag{4.2}$$

where $M_{\rm bar}(< r) = M_\star(< r) + M_{\rm gas}(< r)$ is the cumulative baryonic mass (i.e. the sum of the cumulative stellar and gas masses).

Lelli et al. (2017) argued that one cannot estimate the gravitational field as a function of radius for dSph galaxies because of a well-known degeneracy between the projected stellar velocity dispersion, $\sigma_{\rm LOS}(R)$, and the velocity dispersion anisotropy, $\beta(r)$ — known as the mass-anisotropy degeneracy. However, we now have line-of-sight velocities for many individual stars in each dwarf we model in this paper, and we have a mass modelling method, GravSphere, that can break the mass-anisotropy degeneracy by using information about the shape of the velocity distribution function (Collins et al., 2021; Genina et al., 2020; Read & Steger, 2017; Read et al., 2018, 2019). We describe how we used GravSphere to estimate both $M_{\rm tot}(< r)$ and $M_\star(< r)$ at each radius, r, in the next section.

4.3.2 GravSphere

To measure the mass profiles of our sample, we used the updated version of the GravSphere Jeans modelling code[2]. A detailed explanation of the code can be found in Collins et al. (2021), Genina et al. (2020), Read & Steger (2017), & Read et al. (2018). We briefly summarise this here for the reader's convenience.

GravSphere solves the Jeans equation (Jeans, 1922) for our member stars while assuming that the stellar system is spherical, non-rotating, and in a steady state. It is given by

$$\frac{1}{\nu_\star}\frac{\partial}{\partial r}\left(\nu_\star \sigma_r^2\right) + \frac{2\beta(r)\sigma_r^2}{r} = -\frac{GM(< r)}{r^2}; \tag{4.3}$$

here, the velocity anisotropy profile $\beta(r)$ is defined as

$$\beta = 1 - \frac{\sigma_t^2}{\sigma_r^2}, \tag{4.4}$$

where σ_t and σ_r are the tangential and radial velocity dispersions respectively, and σ_r is given by (Mamon & Lokas, 2005; van der Marel, 1994)

$$\sigma_r^2 = \frac{1}{\nu_\star(r)g(r)}\int_r^\infty \frac{GM(\tilde{r})\nu_\star(\tilde{r})}{\tilde{r}^2} g(\tilde{r})\,{\rm d}\tilde{r}, \tag{4.5}$$

with

$$g(r) = exp\left(2\int \frac{\beta(r)}{r}\,{\rm d}r\right), \tag{4.6}$$

and $M(< r)$ is the total cumulative mass as a function of the radius, r. The tracer number density, $\nu_\star$, characterises the radial density profile of a population of massless tracers (in our case, stars moving in a galaxy) that move in the gravitational potential of its cumulative mass distribution, $M(< r)$, modelled

2. The newest version of this code is available to download at https://github.com/justinread/gravsphere (Collins et al., 2021).

either[3] with a sum of N_P Plummer spheres (Plummer, 1911)

$$\nu_\star(r) = \sum_j^{N_P} \frac{3M_j}{4\pi a_j^3}\left(1 + \frac{r^2}{a_j^2}\right)^{-5/2}, \tag{4.7}$$

where M_j and a_j are the mass and scale length of each individual component, or with the generic $\alpha\beta\gamma$ profile initially proposed by Zhao (1996) and parametrised by Bañares-Hernández et al. (2025); this is given by a double power-law model:

$$\nu_\star(r) = \frac{\rho_c}{(r/r_c)^\gamma(1 + (r/r_c)^\alpha)^{(\gamma-\beta)/\alpha}}, \tag{4.8}$$

where three exponent variables, α, β, γ, and the scale radius, r_c, and density, ρ_c, were introduced.

This allowed us to recover the density profile, $\rho(r)$, and the velocity anisotropy profile, $\beta(r)$, of the studied stellar systems (Read & Steger, 2017). These are modelled as

$$\beta(r) = \beta_0 + (\beta_\infty - \beta_0)\frac{1}{1 + (r_0/r)^\nu}, \tag{4.9}$$

where β_0 and β_∞ are the values of the anisotropy profile at $r = 0$ and $r = \infty$, r_0 is a transition radius, and ν is the steepness of the transition. To avoid infinities, GravSphere uses a symmetrised version of $\beta(r)$:

$$\tilde{\beta}(r) = \frac{\beta}{2 - \beta}, \tag{4.10}$$

where $\tilde{\beta} = -1$ and $\tilde{\beta} = 1$ correspond to a fully tangential and a fully radial distribution, respectively.

GravSphere harnesses higher order moments of the velocity distribution via the fourth-order virial shape parameters (VSPs; Merrifield & Kent, 1990; Read & Steger, 2017; Richardson & Fairbairn, 2014), given by

$$v_{s1} = \frac{2}{5}\int_\infty^0 GM(5 - 2\beta)\nu_\star\sigma_r^2 r\,\mathrm{d}r = \int_\infty^0 \Sigma\langle v_{\rm los}^4\rangle R\,\mathrm{d}R \tag{4.11}$$

and

$$v_{s2} = \frac{4}{35}\int_\infty^0 GM(7 - 6\beta)\nu_\star\sigma_r^2 r^3\,\mathrm{d}r = \int_\infty^0 \Sigma\langle v_{\rm los}^4\rangle R^3\,\mathrm{d}R \tag{4.12}$$

to break the mass-anisotropy degeneracy. The cumulative mass distribution, $M(< r)$, is modelled with a cNFWt profile (Read et al., 2018). This is based on the Navarro-Frenk-White profile (NFW; Navarro et al., 1996b) fitted to pure dark-matter simulations:

$$\rho_{\rm NFW}(r) = \frac{\rho_0}{(r/r_s)(1 + r/r_s)^2}. \tag{4.13}$$

To account for the possibility of cored profiles, as is observed in many dwarf galaxies (see e.g. Marchesini et al., 2002; McGaugh et al., 2001), and the possibility of mass loss beyond the tidal radius for satellite dwarfs (e.g. Read et al., 2006), the cNFWt modifies the NFW profile at both small and large radii. The density profile of this model is given by

$$\rho_{\rm cNFWt}(r) = \begin{cases} f^n\rho_{\rm NFW} + \frac{nf^n(1-f^2)}{4\pi r^2 r_c}M_{\rm NFW}, r < r_t \\ f^n\rho_{\rm NFW} + \frac{nf^n(1-f^2)}{4\pi r^2 r_c}M_{\rm NFW}\left(\frac{r}{r_t}\right)^{-\delta}, r > r_t \end{cases}, \tag{4.14}$$

where $M_{\rm NFW}$ is the mass profile of the NFW model and the function f^n determines how cuspy the halo is below a core-size parameter, r_c:

$$f^n = \left[tanh\left(\frac{r}{r_c}\right)\right]^n. \tag{4.15}$$

3. The estimate of the baryonic acceleration is highly sensitive to the accuracy of the fitted $\nu_\star(r)$, so we fitted both profiles for each galaxy and adopted the one that best reproduces the observed distribution. The impact of adopting these different profiles on the inferred RAR is illustrated in Appendix 4.D for the case of Grus I, the least well-sampled system, showing that our results are robust against the choice of tracer density profile.

The cumulative mass of the cNFWt model is then given by

$$M_{\rm cNFWt}(<r) = \begin{cases} M_{\rm NFW}(<r) f^n, r < r_t \\ M_{\rm NFW}(r_t) f^n + \\ 4\pi\,\rho_{\rm cNFWt}(r_t)\,\frac{r_t^3}{3-\delta}\left[\left(\frac{r}{r_t}\right)^{3-\delta} - 1\right], r > r_t \end{cases}, \tag{4.16}$$

where r_t and δ model the effect of tidal stripping beyond r_t, with r_t being the tidal stripping radius and δ the density slope beyond r_t.

To assign the data to bins of the projected radius, R, we used an algorithm called Binulator (Collins et al., 2021). After running the Binulator routine, we ran GravSphere to determine the cumulative mass profile. GravSphere solves the Jeans equation for the projected velocity dispersion. It also fits the two VSPs, as determined from the stellar kinematic data by the Binulator.

GravSphere uses the ensemble sampler Emcee (Foreman-Mackey et al., 2013) to fit the model to the data. Each Markov chain (walker) communicates with the other walkers at each step. We used the default number of walkers $N_{\rm walkers} = 250$ and steps $N_{\rm steps} = 50000$, since these values were sufficient to achieve convergence. The first half of the steps generated are always discarded as a conservative burn-in criterion.

4.3.3 Priors

We kept the GravSphere priors to their default values, which we summarise here for convenience. We used priors on the symmetrised velocity anisotropy of $-1 < \tilde{\beta}_0 < 1$, $-1 < \tilde{\beta}_\infty < 1$, $-1 < log_{10}(r_0/\mathrm{kpc}) < 0$, and $1 < \eta < 3$. We used a flat prior on the baryonic mass of $0.75M_\star < M_{\rm bar} < 1.25M_\star$, where $M_\star$ corresponds to the measured stellar mass described in Table 4.1. In cases where gas is also present, we added it to the stellar mass and used the total value as the prior for the baryonic mass.

For the cNFWt model, we fitted the following free parameters: the halo mass, $M_{200,}$ and concentration parameter before infall, c_{200}; the dark-matter core-size parameter, r_c; the tidal stripping radius, r_t, and the logarithmic density slope beyond r_t, δ. We assumed flat priors of $10^{7.5}\ \mathrm{M}_\odot < M_{200} < 10^{11.5}\mathrm{M}_\odot$ and $1 < c_{200} < 50$ (see **Júlio et al.**, 2023 for a discussion of these choices), $-2 < log_{10}(r_c/\mathrm{kpc}) < 0.5$, $0.3 < log_{10}(r_t/R_{1/2}) < 1$ and $3.5 < \delta < 5$ on these parameters. Our results are not sensitive to these choices (refer to **Júlio et al.**, 2023; Zoutendijk et al., 2021b for a comprehensive discussion on the robustness of the results obtained using GravSphere in MUSE-Faint data).

Finally, it is important to note that the Jeans equations, which GravSphere solves, assume only that weak-field gravity is described by a scalar field, and that the gravitational force follows from the gradients of this scalar field. The Poisson equation was not considered when deriving the observed accelerations. It would only be considered if we chose to interpret the observed acceleration as owing to some enclosed dark-matter mass. This is an important point because it means that we can directly compare our observed accelerations, derived using GravSphere, to alternative gravity models such as MOND.

4.3.4 Recovering the RAR from mock data

In this section, we test how well we can recover the RAR by applying GravSphere to mock data taken from the simulated EDGE dwarfs. For this test, we used all of the simulated star particles to fit the photometric light profile and a random 1000 stars to measure the line-of-sight velocity dispersion profile up to 1 kpc (broadly representative of our observed dwarfs; see Table 4.1). In addition, to reproduce the observational uncertainties in our mock data, we imposed velocity errors of 2 $\mathrm{km\,s^{-1}}$ on the individual stars. These data were passed to the Binulator and then to GravSphere, as described in Sect. 4.3.2. The results are shown in Figure 4.2. Based on an empirical rotation estimator applied to all galaxies, we find that the observed dwarfs are consistent with being non-rotating, while the EDGE dwarfs display significant rotation. To account for this behaviour in GravSphere, we

introduced a new rotation parameter, which is described in Appendix 4.A. We note that the true acceleration, directly determined from the simulations, matches within the 68% confidence bands determined by GravSphere.

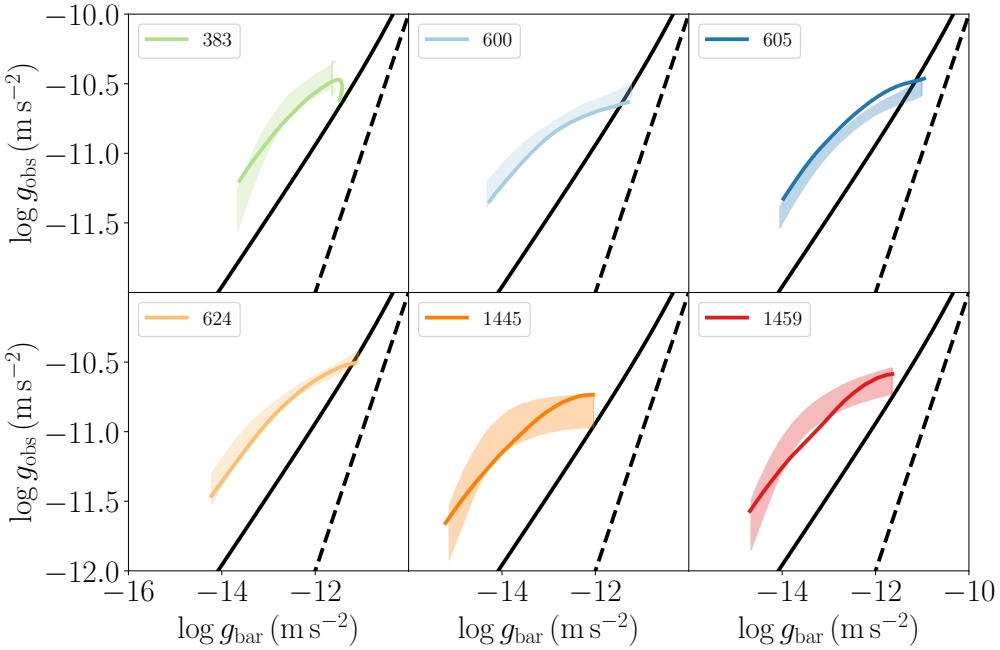


Figure 4.2: Test of our recovery of RAR by applying GravSphere to mock data drawn from simulated EDGE dwarfs. For this test, we used all of the simulated star particles to fit the photometric light profile and a random 1000 stars to measure the line-of-sight velocity dispersion profile (similar to our more poorly sampled observed dwarfs; see Table 4.1). The shaded band marks the 68% confidence intervals. The true answer (as determined directly from the simulations, using Equations 4.1 and 4.2, assuming spherical symmetry) is marked by the solid lines. The solid black line marks the RAR derived by McGaugh et al. (2016) for SPARC local spiral galaxies. The dashed black line marks $g_{\rm obs} = g_{\rm bar}$.

4.4 Results

By using GravSphere, described in Sect. 4.3.2, and the equations described in Sect. 4.3.1, in this section, we estimate the observed and baryonic accelerations for both our observed (Sect. 4.2.1) and simulated (Sect. 4.2.2) data. In Sect. 4.4.1, we present the resulting RAR of our observations. In Sect. 4.4.2, we present the same for the simulated EDGE dwarf galaxies.

4.4.1 RAR of the observations

Figure 4.3 shows the RAR we obtain for our sample of 12 dwarf galaxies. We plot the $g_{\rm obs}-g_{\rm bar}$ relation as a function of radius within each galaxy, where each colour corresponds to a different galaxy, the shaded bands mark the 68% confidence intervals, the lines show the median values, and the dotted lines show extrapolations outside the data range to larger radii. We compare this with the RAR derived by McGaugh et al. (2016) (solid black line). We highlight that, with the exception of Fornax (light green), all of the dwarf galaxies systematically lie above the low-mass extrapolation of the RAR from McGaugh et al. (2016). This deviation becomes stronger for the galaxies with lower baryonic masses (i.e. lower $g_{\rm bar}$). Fornax stands out as an outlier in our sample, lying below the classical RAR, in contrast to the other dwarfs. Its substantially higher stellar mass and extended star formation history (e.g. de Boer et al., 2012) distinguish it from both the other observed dwarfs and the EDGE galaxies. These properties make Fornax particularly susceptible to repeated gas cooling and stellar feedback, which is expected to produce a dark-matter core (e.g. Di Cintio et al., 2014; Pontzen & Governato, 2012; Read & Gilmore, 2005). Indeed, there is already dynamical evidence for such a core reported in the literature (e.g. Cole et al., 2012; Goerdt et al., 2006; Pascale et al., 2018; Read et al., 2019; however, see Genina et al., 2022). Cored dwarfs occupy a distinct locus in the RAR compared to

those with a central cusp, behaving more similarly to MOND predictions (Eriksen et al., 2021). If Fornax is uniquely cored amongst our sample, then this provides a natural explanation for its more MOND-like locus in the RAR. However, more detailed work, left for future studies, will be needed to fully understand this difference.

Furthermore, in some galaxies the radially resolved data exhibit upward or downward 'hooks' in the RAR plane. These features are similar to those described in Li et al. (2022) & Mercado et al. (2024): low-mass galaxies with cuspy dark-matter-halo profiles should have upward-bending hook features that deviate from the observed RAR; while, conversely, downward hooks arise due to the non-monotonic behaviour of the total acceleration profile in the presence of a feedback-induced core, leading to multiple observed accelerations, $g_{\rm obs}$, for a given baryonic acceleration, $g_{\rm bar}$. Given the uncertainties, several of our systems allow for both scenarios, or even for a more monotonic relation. However, for most of them, there is no one-to-one map from $g_{\rm bar}$ to $g_{\rm obs}$, neither within each dwarf nor between them as populations.

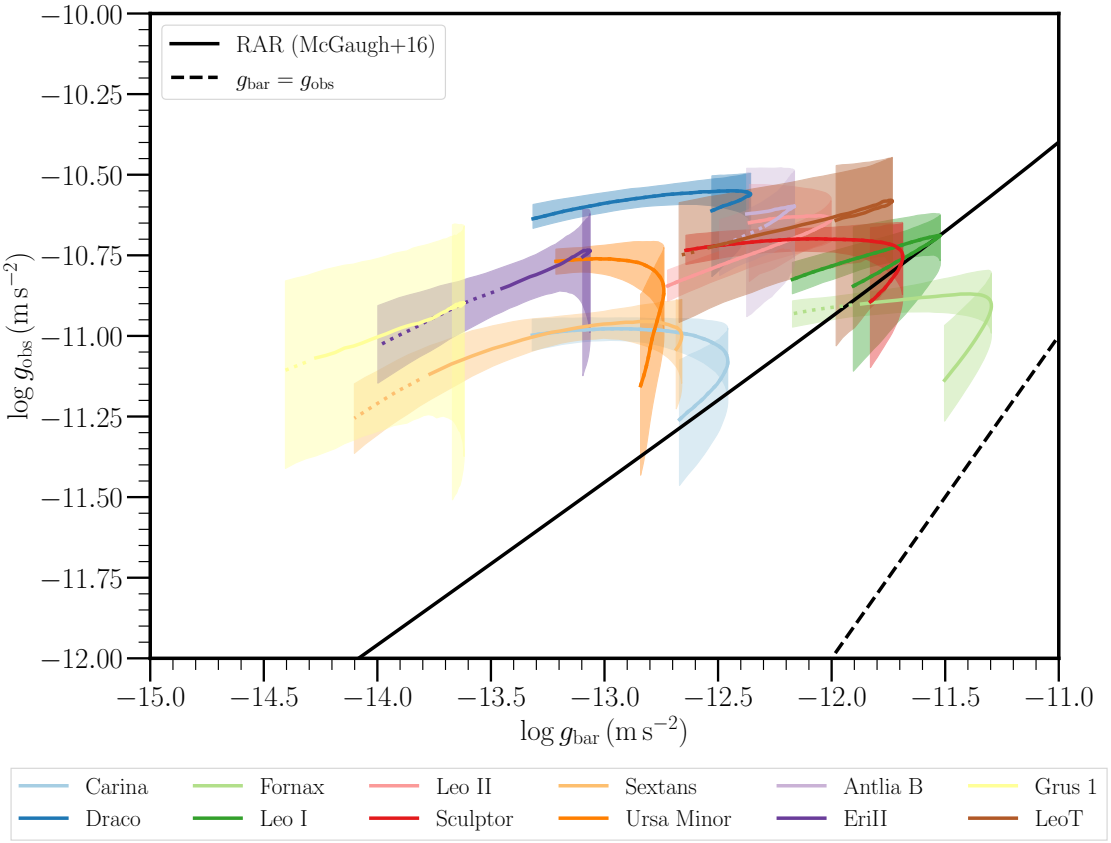


FIGURE 4.3: Radial acceleration relation (RAR) for our sample of dwarf galaxies. Each colour corresponds to a different galaxy, where the shaded area corresponds to the 68% confidence interval and the solid line marks the median value. The dotted lines correspond to extrapolations beyond the kinematic data range. The solid black line marks the RAR derived by McGaugh et al. (2016) for SPARC local spiral galaxies. The dashed black line marks $g_{\rm obs} = g_{\rm bar}$.

4.4.2 RAR OF THE EDGE SIMULATIONS

Figure 4.4 shows the for the EDGE simulated galaxies. The low- and high-resolution results are in good agreement for all of the simulated dwarfs, though the higher resolution simulations (right panel) slightly deviate from the lower resolution ones (left panel) at low and high $g_{\rm bar}$[4]. Furthermore, as most observed dwarfs, the EDGE dwarfs systematically lie above the RAR from McGaugh et al. (2016).

None of the EDGE dwarfs scatter below the McGaugh et al. (2016) RAR line, and so none look

4. When extending the radial range of the high-resolution haloes down to $r = 0.01$ kpc, the hooks in the RAR become visible. Their apparent absence in our fiducial plots is thus not physical, but a consequence of the adopted radial cut at $r > 0.1$ kpc (see Figure 4.B.1 of Appendix 4.B).

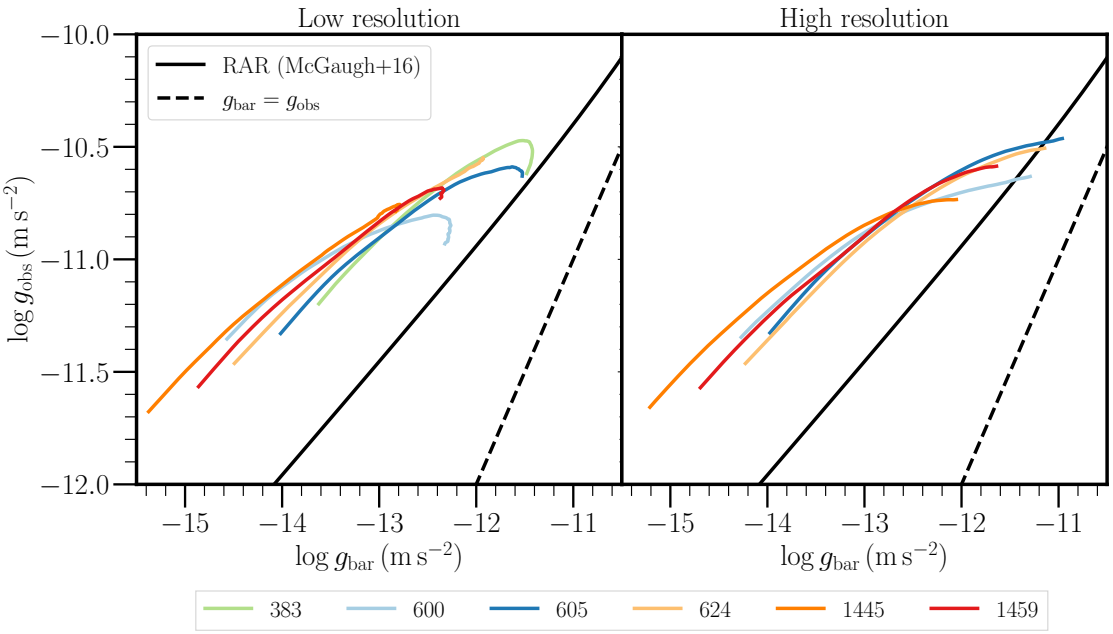


FIGURE 4.4: Radial acceleration relation for EDGE simulated dwarf galaxies. The colours show each simulation as marked in the legend. The solid black line corresponds to the RAR derived by McGaugh et al., 2016 for SPARC local spiral galaxies. The black dashed line marks $g_{\rm obs} = g_{\rm bar}$. Left: RAR of lower resolution simulations. Right: RAR of higher resolution simulations.

similar to the data for Fornax. However, notice that the EDGE dwarfs are ~ 10 times less massive than Fornax (see Figure 4.1), and so this does not (at least not yet) constitute a mismatch between theory and data.

In Figure 4.5, we quantitatively compare the EDGE simulated RAR with our observed dwarf galaxy sample. For this comparison, we only plot the higher resolution simulations (except for Halo 383, for which we only have the lower resolution version). The median and 68% scatter in the observed $g_{\rm obs} - g_{\rm bar}$ relations are marked by the solid grey lines and shaded regions, respectively. The relations estimated directly from the simulations are represented by solid red lines. Notice that the agreement between the two is remarkably good, both in terms of the median relation and its scatter. Also shown, in blue, is the RAR for classical dSphs derived at their half-light radii from Lelli et al. (2017). These measurements, although noisier and more sparsely sampled, are broadly consistent with both our results and the simulations, further reinforcing the conclusion that the standard ΛCDM cosmology reproduces the observed behaviour of galaxies in the RAR plane on the dwarf galaxy scale.

4.5 Discussion

4.5.1 The origin of scatter in the RAR of low-mass dwarf galaxies

One may reasonably ask what the origin of the scatter in the EDGE simulated RAR is. As stated in Kim et al. (2024) & Rey et al. (2019), the EDGE dwarfs show significant scatter in M_* at a given M_{200} (~0.5 dex (1σ) at a halo mass of ~10^9 $\mathrm{M}_\odot$). This owes to reionisation combined with scatter in dwarf galaxy assembly histories. At fixed M_{200}, dwarfs that form earlier form more stars before reionisation quenching, leading to a higher M_* today. As such, variations in the $M_* - M_{200}$ relation of low-mass dwarfs in ΛCDM naturally generate scatter in the $g_{\rm bar} - g_{\rm obs}$ plane.

To illustrate this explicitly, in Figure 4.B.1 of Appendix 4.B we show the 'genetically modified' versions of Halo 1459, in which only reionisation and early assembly history were varied. These runs (MX02 and MX03) share the same halo mass, but differ in their stellar mass, and exhibit $g_{\rm bar} - g_{\rm obs}$ tracks offset by an amount comparable to the scatter between distinct EDGE dwarfs.

That said, the scatter in EDGE is smaller than in the observational data (see Figure 4.5). Even after including observational uncertainties in the mock data (discussed in Sect. 4.3.4), the EDGE scatter

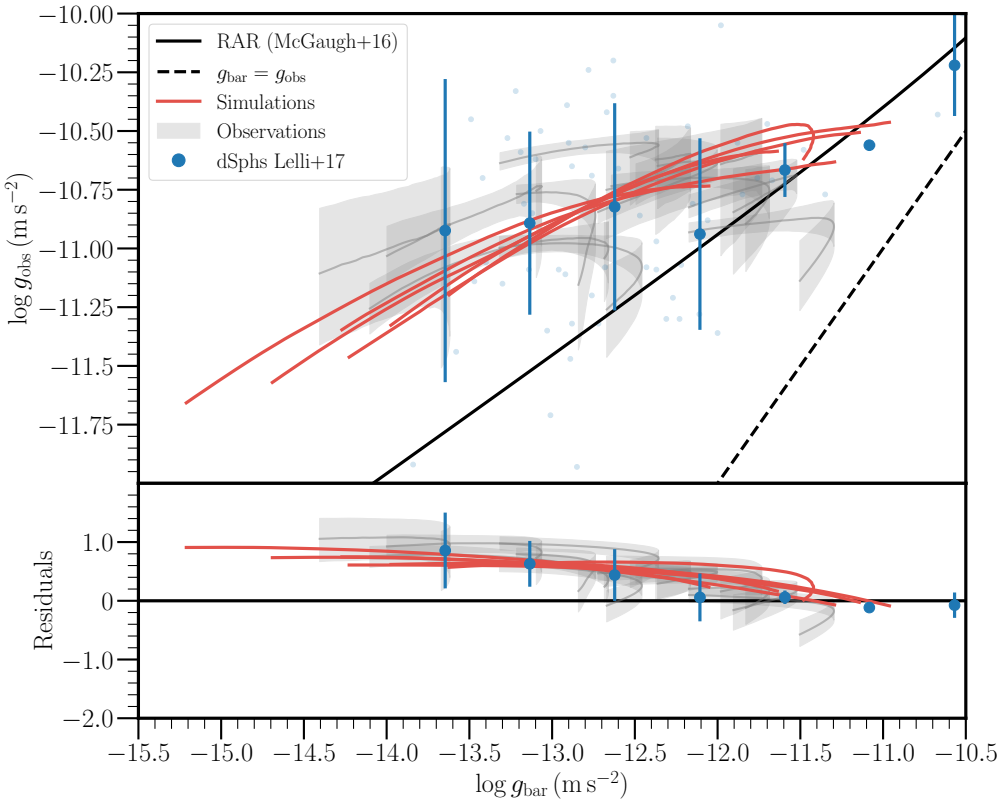


FIGURE 4.5: Quantitative comparison of the EDGE simulated RAR with our observed dwarf galaxy sample. The black solid line corresponds to the RAR derived by McGaugh et al. (2016) for SPARC local spiral galaxies. The median and 68% scatter in the observed $g_{obs} - g_{bar}$ relations are marked by the grey solid lines and shaded regions, respectively. The $g_{obs} - g_{bar}$ relations estimated directly from the simulations are represented by solid red lines. The blacked dashed line marks $g_{obs} = g_{bar}$. The small blue points mark the positions of the dSphs on this relation from Lelli et al. (2017), while the blue circles indicate the mean and 1σ scatter of the binned data. At the bottom, the residuals relative to the McGaugh et al. (2016) relation (black solid line) are represented for the observed, the simulated, and the Lelli et al. (2017) data.

does not reach the full amplitude seen in the Local Group dwarfs (see Figure 4.B.2 in Appendix 4.B). This does not necessarily indicate a problem for ΛCDM, since additional sources of scatter are expected in the observed sample. The Local Group dwarfs are satellites, whereas EDGE dwarfs are isolated galaxies, and quenching on infall (e.g. Read & Erkal, 2019) and tidal effects (e.g. Read et al., 2006) can both increase the scatter. Moreover, the observed dwarfs span a wider range of pre-infall halo masses than our EDGE comparison sample. This is particularly relevant for Fornax, which is among the most discrepant galaxies in the data and likely originates from a substantially more massive progenitor. While the EDGE scatter alone falls short of matching the data, the combination of reionisation, assembly history, observational uncertainties, satellite-specific processes, and a broader halo-mass range might explain the observed dispersion in the dwarf galaxy RAR within ΛCDM.

4.5.2 Comparing isolated EDGE dwarfs to observed satellite dwarfs

Our simulated EDGE dwarfs are *isolated*, whereas our sample of observed dwarfs all orbit in the tidal field of a larger host galaxy. As such, we may worry that the two populations may not be directly comparable. We selected our observed dwarf galaxies such that they orbit in a weak tidal field today, with a tidal radius that lies far beyond their stellar light profile (Pace et al., 2022; see Table 4.1 and Sect. 4.5.3). As such, the tidal field of the host galaxy is not likely to significantly influence the stellar light profiles of our sample of dwarfs (Goater et al., 2024; Read et al., 2006). However, it is likely that some of our observed dwarfs — particularly the more massive ones such as Fornax — had their star formation shut down by ram pressure from their host galaxy's hot gaseous corona (e.g. Gatto et al., 2013). This lowers their total stellar mass compared to a similar but isolated counterpart, lowering g_{bar} for a given g_{obs} and inducing more scatter in the RAR plane. As such, we can consider the scatter that

we see in the RAR plane for our EDGE dwarfs as a lower bound on the scatter expected for satellite dwarfs in a ΛCDM cosmology.

4.5.3 The external field effect

We show that our observed dwarf galaxies do not follow any simple RAR (see Figure 4.3). However, as discussed in Sect. 4.1, alternative weak-field gravity theories including MOND are typically non-linear, leading to an 'external field effect'. Since our sample of dwarfs all orbit in the tidal field of a larger host galaxy, we may worry that the scatter in the RAR is actually expected in MOND — a result of each dwarf experiencing a distinct EFE.

To test this idea, we followed the approach in McGaugh & Milgrom (2013) to estimate the relative size of the internal, $a_{\rm in}$, and external, $a_{\rm ex}$, acceleration (the EFE) for each dwarf in our observational sample. To determine the internal field, which depends only on the baryonic properties of the dwarf, we followed McGaugh & Milgrom (2013), which derived

$$a_{\rm in} \sim \frac{\left(\frac{4}{9} G M_{\rm bar} a_0\right)^{1/2}}{R_{1/2}}, \tag{4.17}$$

which is valid for MOND. We assume here that $a_0 = 1.2 \times 10^{-10} \mathrm{m\,s^{-2}}$ (McGaugh & Milgrom, 2013).

The EFE ($a_{\rm ex}$) depends on the total baryonic mass of the host galaxy and, similarly to Pawlowski et al. (2015b), we adopted the empirical MW model of McGaugh (2008) using $a_{\rm ex} = V_{\rm MW}^2/D$, where $V_{\rm MW}$ is the circular velocity of the MW and D is the Galactocentric distance of the object (this is reported in Table 4.1). Ant B is not a satellite galaxy of the MW, but is instead a satellite of NGC 3109. As such, for this specific case, we used a circular velocity of $52\,\mathrm{kms^{-1}}$ (Huchtmeier, 1973) and a distance of $D = 72$ kpc (Sand et al., 2015).

We report our values for $a_{\rm in}$ and $a_{\rm ex}$, derived as described above, in Table 4.3. A system is considered to be in the MOND regime if $a_{\rm ex} < a_{\rm in} \ll a_0$, and in the EFE regime if $a_{\rm ex} > a_{\rm in}$. As can be seen, five of our dwarfs are clearly in the MOND regime (Fornax, Leo I, Leo II, Ant B, Leo T), five are clearly in the EFE regime (Carina, Draco, Sextans, Ursa Minor, Grus I) and the remainder are at the boundary (Sculptor, Eri II). This means that we do indeed expect scatter in the RAR for these dwarf galaxies in MOND. However, galaxies in the EFE regime should scatter *below* the RAR, while the opposite is what we see. Furthermore, we see no systematic trend between galaxies in the MOND or EFE regimes. Draco and Carina are a particularly illustrative example, as was already pointed out by Read et al. (2019). Both galaxies are in the EFE regime on very similar orbits around the MW. Both have very similar baryonic mass distribution and, therefore, similar $g_{\rm bar}$. Yet, as can be seen in Figure 4.3, they have very different $g_{\rm obs}$ at high statistical significance. This difference might be due to their distinct evolutionary paths: Draco is a quenched system with a predominantly old stellar population and very slow chemical enrichment, consistent with a system that ceased star formation early, likely around the epoch of reionisation (Cohen & Huang, 2009; Weisz et al., 2014a). Its high dark-matter content makes it strongly dark-matter-dominated at all radii (Read et al., 2019). Carina, by contrast, experienced extended and bursty star formation episodes with multiple distinct episodes of enrichment (de Boer et al., 2014), which likely drove repeated gas outflows and feedback events. Such processes can reduce the central dark-matter density, producing a lower observed acceleration at fixed baryonic content (Read et al., 2019). These contrasting star formation and feedback histories naturally produce the observed offset in their RARs within ΛCDM. However, this suggests that the scatter in the RAR observed in our sample of dwarf galaxies poses a challenge for a MOND-like explanation, since galaxies with the same baryonic mass distribution and external field should fall on the same RAR. It remains to be seen if other alternative gravity theories that show different non-linear weak-field behaviour could explain these data.

4.5.4 Challenges to interpretation

During our analysis with Gravsphere, we assume that the systems under study have spherical symmetry. As previously pointed out, this might not be valid for our sample. Even though it was shown that the expected departures from spherical symmetry bias GravSphere mass models by less than

TABLE 4.3: MOND internal and external accelerations of our observed sample of dwarf galaxies.

Galaxy	$a_{\rm in}$	$a_{\rm ex}$
	$(10^{-12}\,{\rm m\,s^{-2}})$	
Carina	6.72	9.90
Fornax	25.17	7.61
Draco	6.64	13.81
Leo I	25.47	3.27
Leo II	13.32	3.56
Sculptor	14.61	12.21
Sextans	2.60	12.21
Ursa Minor	8.11	13.81
Antlia B	10.18*	1.22
Eridanus II	2.95	2.27
Grus 1	1.81	8.4
Leo T	17.58*	2.03

(*) The estimation of $a_{\rm in}$ requires the mass of the system; so, for these galaxies we considered both the stellar and the gas mass.

their quoted 95% confidence intervals for stellar kinematic samples of up to ~ 1000 stars, for some systems — namely for the MUSE-Faint dwarfs — we have fewer than 100 stars. Furthermore, for these particular dwarfs, the data are mostly concentrated inside their half-light radius, so the baryonic distribution is extrapolated from their surface brightness profile in the outskirts. As a result of the undersampling, both in the number of stars and the radius range in which they are concentrated, the RAR of these galaxies should be interpreted cautiously. However, within their error bars, they mostly agree with the dSphs for which we have a significant amount of data across a large range of radii. Moreover, our overall results remain unchanged even when these systems are excluded from the analysis — their inclusion simply amplifies the observed trends.

As shown in Table 4.1, Antlia B and Leo T have gas. We assumed, for simplicity, that the gas content of Antlia B and Leo T follows the same mass distribution as the stars, and this assumption underlies the results presented in Figure 4.3. We show in Appendix 4.E, in Figure 4.E.1, how the RAR of these two galaxies change when we exclude their gas content. As expected, since we assumed that the gas and stars follow the same mass distribution, omitting the gas leads to a uniform decrease in the baryonic acceleration at all radii, effectively shifting the RAR to the left. While this approach provides a useful first-order approximation, it is important to note that, in reality, the gas content of a galaxy can be significantly more extended than its stellar distribution. This would increase the baryonic content of the galaxy at large radii, resulting in increased baryonic and total accelerations in the outer regions. Nonetheless, this would not change our conclusions.

Another potential caveat is the impact of binary stars, which can artificially increase the observed stellar velocity dispersions, leading to overestimated dynamical masses and elevated $g_{\rm obs}$ at fixed $g_{\rm bar}$ (e.g. Gration et al., 2025; Pianta et al., 2022). In our analysis, we do not explicitly correct for binaries. However, the MUSE-Faint data were obtained over multiple epochs and combined into period-averaged velocities, which reduces the binary contamination (discussed for Leo T in Vaz et al., 2026; and for the remaining MUSE-Faint UFDs in Vaz et al., in prep.). For the classical dSphs, binaries have only a minor impact on the velocity dispersion at the current levels of precision (e.g. McConnachie

& Côté, 2010; Wang et al., 2023). In these cases, we rely on the published membership catalogues, which in many instances make use of multi-epoch data to identify and remove likely binaries (e.g. Walker et al., 2006). Furthermore, for the more massive dwarfs, the higher intrinsic dispersions further suppress the contribution from binaries. We therefore expect that while binaries may introduce some additional scatter, it is unlikely that their contamination alters our main results.

Finally, tidal interactions may have influenced the past evolution of some systems. Yet, since all of our galaxies orbit in relatively weak present-day tidal fields, we do not expect tides to significantly affect our main conclusions. Moreover, our estimates of the tidal radius are based on the dynamical masses from Pace (2025), which were derived within the 3D half-light radius using the dynamical mass estimator in Wolf et al. (2010). This likely underestimates the true masses of some dwarfs, and therefore also underestimates their tidal radii, making them appear more susceptible to tides than they actually are. In that sense, our assumption is conservative. Given that even heavily disrupted systems such as the Small Magellanic Cloud can still be reliably mass modelled (De Leo et al., 2020, 2024), we expect our main results to remain robust despite the possible influence of tides.

4.6 Conclusions

We used literature line-of-sight velocities for the classical dSphs of the MW, combined with MUSE-Faint velocities of ultra-faint dwarfs, to measure the radially resolved radial acceleration relation of galaxies down to baryonic accelerations $log(g_{\rm bar}/{\rm m\,s^{-2}}) \sim -14$, for the first time. We estimated the baryonic and observed accelerations, $g_{\rm bar}$ and $g_{\rm obs}$, using the Gravsphere Jeans mass-modelling code, assuming that our galaxies are spherical, non-rotating, and in a steady state. We tested these assumptions by applying GravSphere to mock data for simulated dwarf galaxies taken from the EDGE project, showing that we can successfully recover the RAR of these mock dwarfs within our quoted uncertainties.

We then applied our method to real data for 12 nearby dwarfs. Our dynamical analysis reinforced previous results that in the lowest mass galaxies, the $g_{\rm obs} - g_{\rm bar}$ relation does not follow the RAR calibrated on higher mass galaxies (McGaugh et al., 2016), but is systematically higher. Furthermore, we found significant scatter from galaxy to galaxy, while, when considering distinct radii within individual galaxies, we found that some galaxies can have two different values of $g_{\rm obs}$ at the same $g_{\rm bar}$.

We considered whether these results could be explained by the EFE that can occur in non-linear, weak-field gravity theories such as MOND. However, we show that the EFE has the wrong sign, causing galaxies to scatter below the RAR, which is opposite to what is observed. Furthermore, we found no correlation between galaxies in the EFE regime as compared to galaxies outside it. Moreover, we show that galaxy 'twins' exist, such as Carina and Draco, that have a similar EFE, similar orbits around the MW, and similar baryonic-mass distribution ($g_{\rm bar}$), yet statistically significantly distinct $g_{\rm obs}$. Our results demonstrate that the RAR for low-mass dwarf galaxies is not universal and that the baryonic acceleration does not contain enough information, on its own, to derive the observed acceleration for these objects.

Finally, we compared our results with the RAR predicted in high-resolution simulations of isolated dwarf galaxies in a ΛCDM cosmology, taken from the EDGE project. We show that the higher and lower resolution versions of these simulations agreed well with one another, demonstrating good numerical convergence. We then showed that the simulated dwarfs behave similarly to our observed sample in lying systematically above the low-mass extrapolation of the RAR from McGaugh et al. (2016). However, the scatter in EDGE, which is caused by a combination of reionisation and the scatter in dark-matter-halo assembly histories (Kim et al., 2024), is smaller than that seen in the Local Group dwarfs. While part of this difference can be attributed to additional dispersion introduced by GravSphere and observational uncertainties, further contributions are expected from the fact that the Local Group dwarfs are satellites rather than isolated dwarfs, and from their broader range of pre-infall halo masses. This makes the low-mass end of the RAR a powerful probe of both cosmology and the complex evolutionary paths of dwarf galaxies.

Acknowledgements

MPJ and MSP acknowledge funding via a Leibniz-Junior Research Group (project number J94/2020). OA acknowledges support from the Knut and Alice Wallenberg Foundation, the Swedish Research Council (grant 2019-04659), the Swedish

National Space Agency (SNSA Dnr 2023-00164), and the LMK Foundation. Based on observations made with ESO Telescopes at the La Silla Paranal Observatory under programme IDs 0100.D-0807, 0101.D-0300, 0102.D-0372 and 0103.D-0705. This research has made use of Astropy (Astropy Collaboration et al., 2022), corner.py (Foreman-Mackey, 2016), matplotlib (Hunter, 2007), NASA's Astrophysics Data System Bibliographic Services, NumPy (Harris et al., 2020), SciPy (Virtanen et al., 2020). Based on observations made with the NASA/ESA Hubble Space Telescope, and obtained from the Hubble Legacy Archive, which is a collaboration between the Space Telescope Science Institute (STScI/NASA), the Space Telescope European Coordinating Facility (ST-ECF/ESA) and the Canadian Astronomy Data Centre (CADC/NRC/CSA). JIR would like to acknowledge support from STFC grants ST/Y002865/1 and ST/Y002857/1.

Appendices

4.A Adding rotation to GravSphere

$$g(r)' = exp\left(-2\int_0^r \frac{\beta}{r'}\,dr'\right), \tag{4.18}$$

where

$$\beta' = 1 - \frac{\sigma_\theta^2 + \sigma_\phi^2 + \bar{v}_\phi^2}{2\sigma_r^2} \tag{4.19}$$

$$= \beta + \frac{\bar{v}_\phi^2}{2\sigma_r^2} \tag{4.20}$$

accounts for the mean streaming motion in the plane, $\bar{v}_\phi$. This, therefore, accounts for any unmodelled rotation.

We roughly parameterise the effect of β' using a dimensionless 'rotation parameter', $A_{\rm rot}$, such that the streaming motion rotation rises linearly with radius:

$$\frac{\bar{v}_\phi^2}{2\sigma_r^2} = A_{\rm rot}\left(\frac{r}{R_{1/2}}\right) \tag{4.21}$$

where $R_{1/2}$ is the projected half radius. This way, $A_{\rm rot} = 0$ corresponds to no rotation while $A_{\rm rot} = 1/2$ corresponds to an equal balance of rotation and 1D pressure support at $R_{1/2}$.

Using the above simplified model for $\bar{v}_\phi$, Equation 4.18 becomes:

$$g(r)' = g(r)\,exp\left(-2A_{\rm rot}\frac{r}{R_{1/2}}\right) \tag{4.22}$$

We note that this is just a lower limit of the rotation, since we do not account for the inclination of a galaxy.

4.B Additional sources of scatter

Here, we aim to clarify both the physical and observational contributions to scatter in the RAR.

Figure 4.B.1 shows results of the genetically modified (GM) versions of the EDGE Halo 1459 extended down to $r = 0.01$ kpc, which were designed to vary only the formation time relative to reionisation. This demonstrates that differences in assembly history at fixed halo mass can induce scatter in the $g_{\rm bar}$—$g_{\rm obs}$ relation comparable to that seen between different EDGE dwarfs. This supports the interpretation that the scatter in EDGE primarily arises from a combination of reionisation and assembly history effects.

Figure 4.B.2 illustrates the additional dispersion introduced by our mass-modelling pipeline GravSphere and observational uncertainties, quantified by re-running the modelling on mock data. This shows that observational effects can increase the apparent scatter in the RAR. Once accounting for observational uncertainties, the scatter in the EDGE simulations and the real data is comparable for lower baryonic accelerations ($g_{\rm bar} < -13.5$ m s^{-2}). At higher baryonic accelerations, however, the data show larger scatter than the simulations. This could be explained by the fact that the simulations are of isolated dwarfs while the data are for satellite dwarfs that span a wider range of pre-infall masses

than EDGE (Read & Erkal, 2019; Rey et al., 2025). We will explore this in more detail in future work.

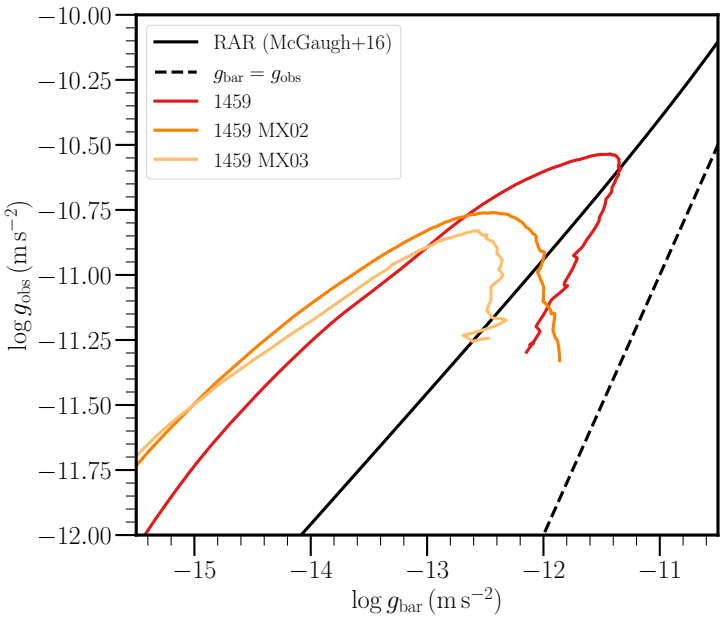


FIGURE 4.B.1: $g_{obs} - g_{bar}$ relations for genetically modified versions of Halo 1459 (MX02, MX03) extended down to $r = 0.01$ kpc. The black solid line marks the RAR derived by McGaugh et al. (2016) for SPARC local spiral galaxies. The blacked dashed line marks $g_{obs} = g_{bar}$.

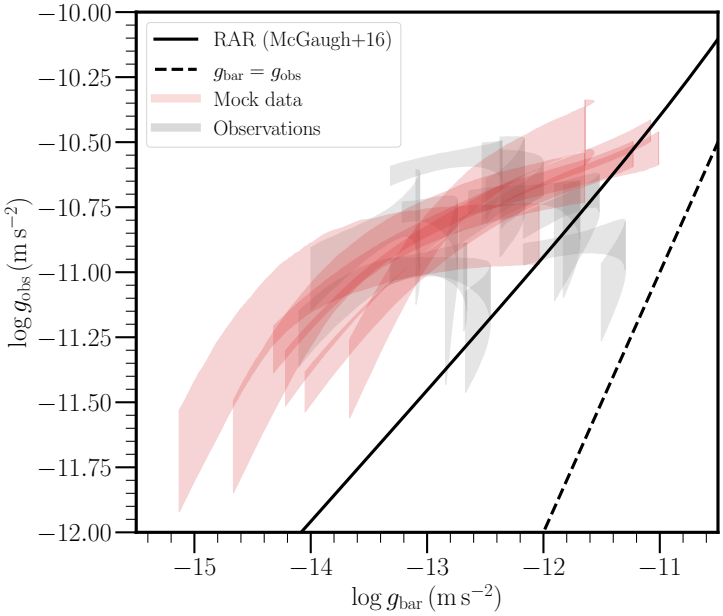


FIGURE 4.B.2: Effect of the mass-modelling pipeline and observational uncertainties on the RAR. The 68% scatter obtained for the observed and for the mocks from the simulated $g_{obs} - g_{bar}$ relations are marked by the grey and red shaded regions, respectively. The black solid line marks the RAR derived by McGaugh et al. (2016) for SPARC local spiral galaxies. The blacked dashed line marks $g_{obs} = g_{bar}$.

4.C GravSphere fits

This appendix presents the GravSphere model fits to our observational data, allowing an assessment of how well the models reproduce the key dynamical and photometric properties of the galaxies. Figures 4.C.1 and 4.C.2 show the results for each galaxy in our sample. For each object, we display the line-of-sight velocity dispersion profile (left column), the surface brightness profile (centre column), and the cumulative mass profile (right column).

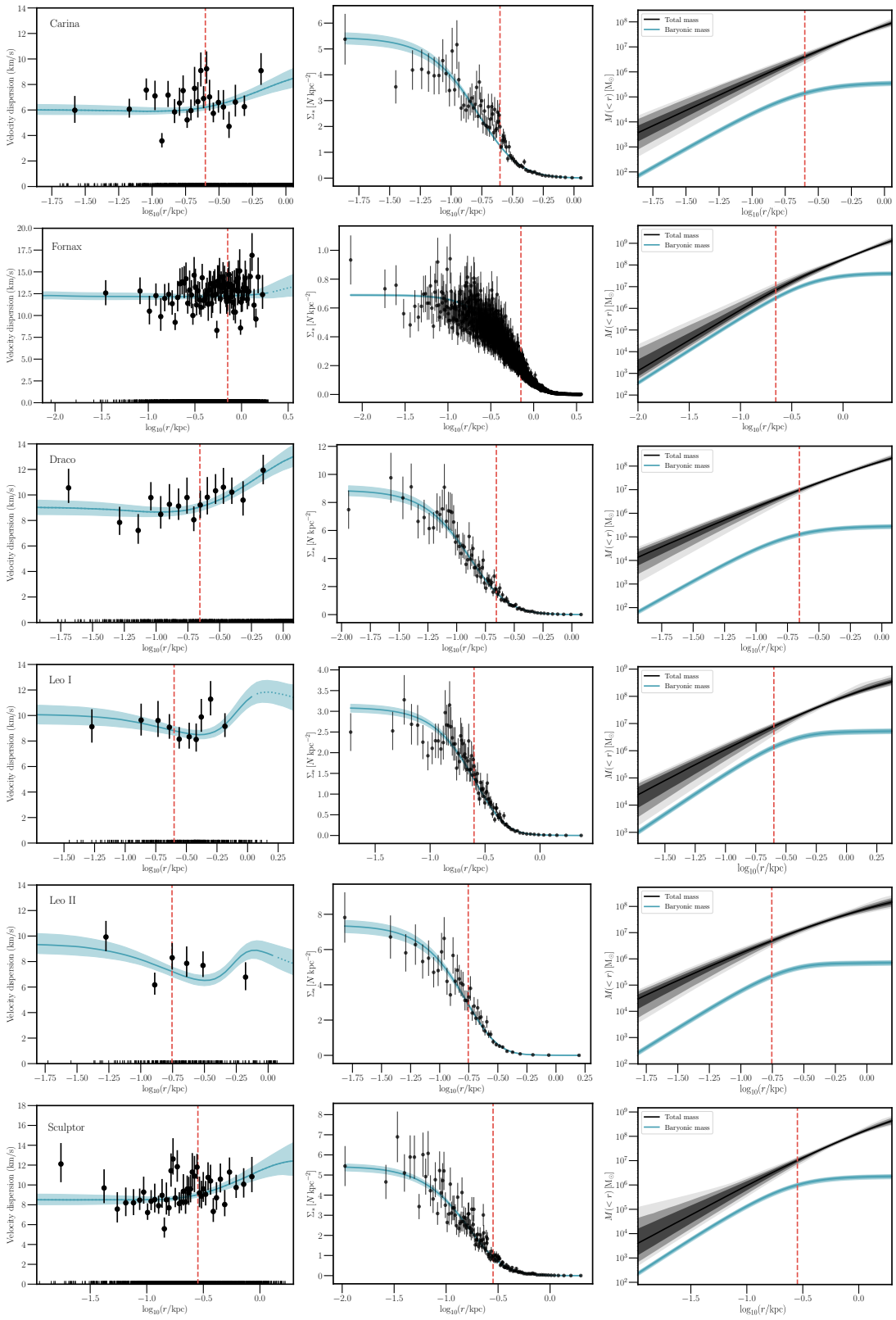


FIGURE 4.C.1: GRAVSPHERE fits for the velocity dispersion profile (left), surface brightness profile (centre), and mass profile (right) of the observed dwarf galaxies under study. The vertical red line in each plot represents the half-light radius.

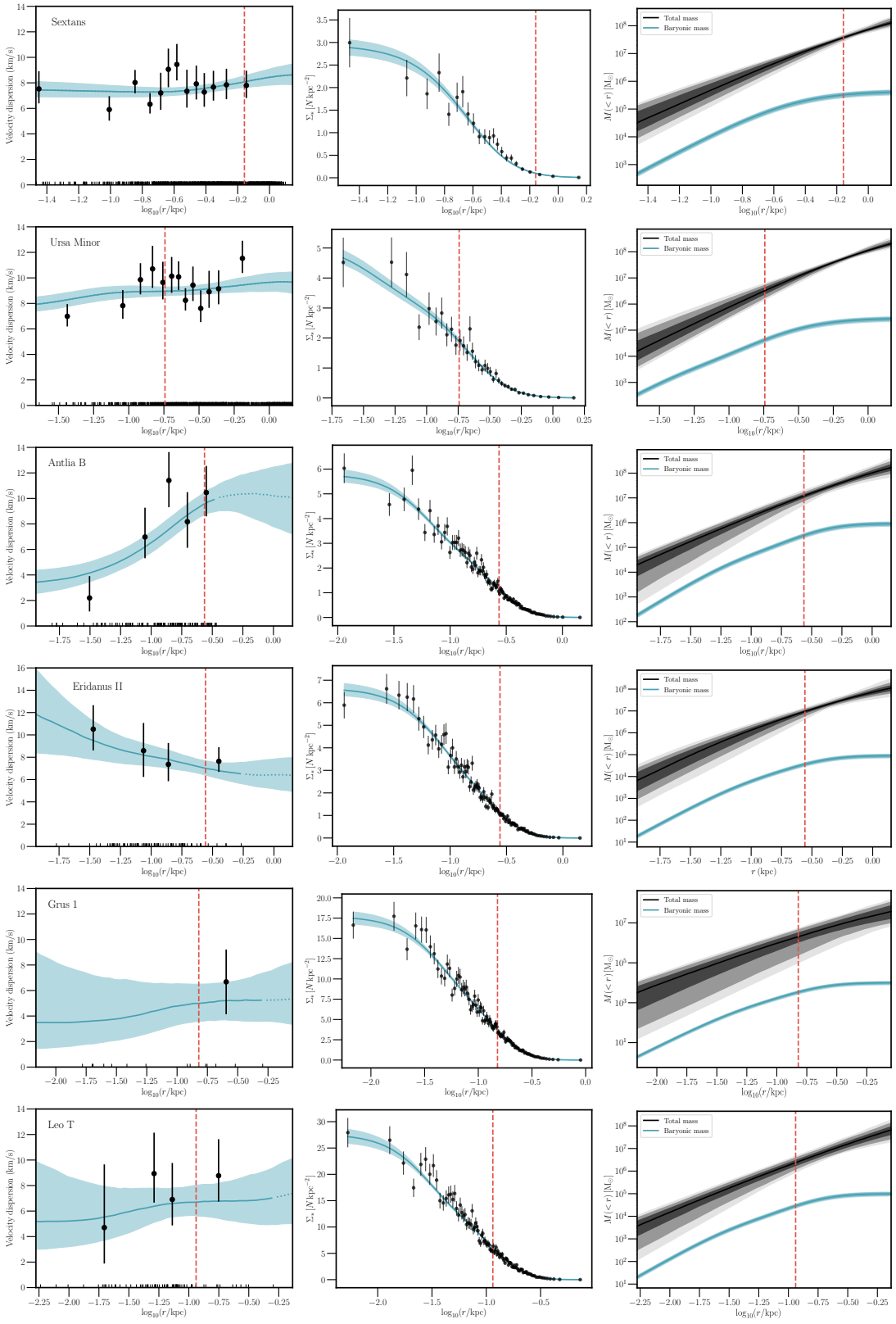


FIGURE 4.C.2: Continuation.

4.D TRACER DENSITY PROFILE

Figure 4.D.1 illustrates how the RAR of Grus I, the UFD with the fewest tracers (14 stars), is affected by changing the assumed tracer density profile $\nu_\star(r)$. The blue represents the case where a Plummer pro-

file (Equation 4.7) is adopted, while the green correspond to an alternative $\alpha\beta\gamma$ profile (Equation 4.8). Despite this change in parametrisation, the qualitative behaviour of the RAR remains consistent, and the results agree within the 68% confidence intervals. This shows that even for the least well-sampled systems, our conclusions are robust against the choice of tracer profile. For dwarfs with larger tracer samples, the sensitivity to the assumed functional form is expected to be even lower.

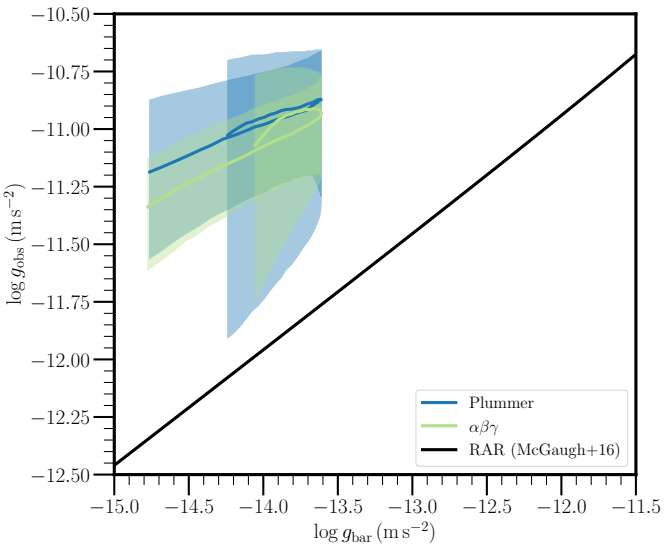


FIGURE 4.D.1: Comparison of the RAR of Grus I assuming two different tracer density profiles. The solid lines represent the estimated median RAR: the $\alpha\beta\gamma$ profile for the tracers in green, and a Plummer profile in blue. The shaded area corresponds to the 68% confidence interval.

4.E GALAXIES WITH GAS

Figure 4.E.1 illustrates how the RARs of Antlia B and Leo T are affected by the inclusion or exclusion of their gas content. The dashed lines represent the first case, in which the gas is assumed to follow the same mass distribution as the stars, while the solid lines correspond to the scenario where only the stellar component is considered. As expected under our simplifying assumption, removing the gas shifts the RAR horizontally toward lower baryonic accelerations, without altering the overall shape of the relation. This shift reflects the reduced baryonic content at all radii when the gas is omitted. Despite this change, the qualitative behaviour of the RAR remains consistent, and our conclusions are unaffected.

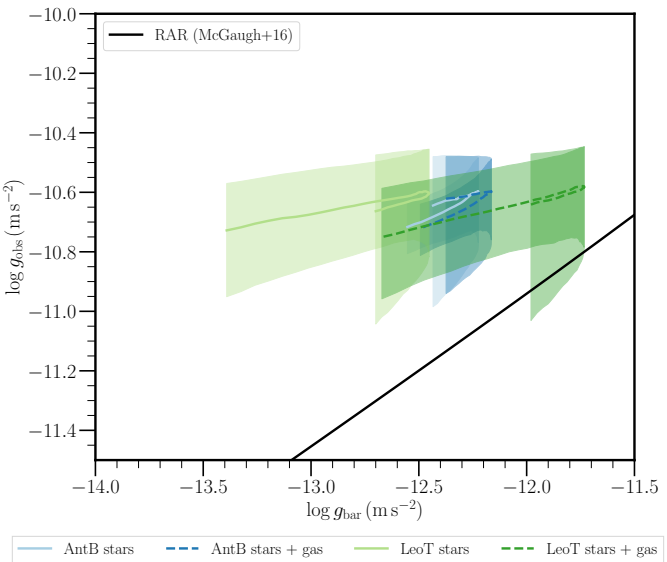


FIGURE 4.E.1: Comparison of the RAR of AntB and LeoT with and without their gas content. The solid lines represent their estimated median RAR considering only the mass of the stars and the dashed lines represent their estimated median RAR considering also their gas content. The shaded area corresponds to the 68% confidence interval. For this comparison, we used the gas and stellar mass described in Table 4.1.

5 Conclusions

Dwarf galaxies have long occupied a central role in discussions of the small-scale challenges faced by the Λ cold dark matter paradigm. Their extreme dark-matter content, shallow potential wells, and sensitivity to environmental effects make them both powerful probes of cosmology and complex systems to interpret. In this thesis, dwarf galaxies in the Local Group have been used as dynamical laboratories to investigate whether some of the most persistent tensions with ΛCDM can be understood within the standard framework once realistic physics and observational constraints are taken into account.

A recurring theme throughout this work is the importance of dynamics — both orbital and internal — in disentangling the physical origin of observed small-scale problems. On the scale of satellite systems, the spatial and kinematic organisation of dwarf galaxies provides direct insight into the assembly history of Milky Way–like haloes.

In Chapter 2, I presented a detailed dynamical test of the proposed Crater-Leo association as a possible example of cosmologically expected group infall (**Júlio et al.**, 2024). By combining *Gaia* DR3 astrometry with our new HST proper motion measurements for Leo IV and Leo V, I derived the orbital properties of the candidate members and performed a consistent phase-space analysis of the system. I found that Leo II, Leo IV, Leo V, and Crater 1 have orbital poles that are compatible within their uncertainties. These systems are also consistent with sharing similar specific angular momentum and energy, as expected for satellites accreted as a group. When applying the framework first introduced by Lynden-Bell & Lynden-Bell (1995), the predicted proper motions assuming a common origin agree with the observed values. This agreement becomes significantly stronger once the new HST measurements are included, favouring a single co-rotating solution for all four objects, which is required for a common infall scenario.

My orbital integrations further showed that these satellites are currently near apocentre and are consistent with having reached pericentre at similar times. Tracing their orbits back in time suggests that they were in close physical proximity $\sim$ 3 Gyr ago, supporting a genuine physical association rather than a chance alignment along a great circle. In contrast, Crater II is inconsistent with this scenario: it exhibits a distinct and well-constrained orbital pole, deviates from the predicted proper motions, and shows a significant offset from the common value of the line-of-sight velocity shared by the group, allowing it to be robustly excluded from the proposed association.

I also explored the impact of the Large Magellanic Cloud on the inferred orbital properties, motivated by the findings of Garavito-Camargo et al. (2021), and found that, while it can increase the likelihood of shared dynamical properties, it does not alter the overall conclusions. Taken together, these results provide strong evidence that a subset of the originally proposed Crater-Leo objects identified by Torrealba et al. (2016) were accreted together, offering one of the clearest observational indications to date that cosmologically expected group infall can be identified in the Local Group. However, current proper-motion uncertainties remain the main limiting factor. Future *Gaia* data releases, together with extended astrometric baselines from additional HST epochs or complementary JWST observations, will be required to definitively confirm the association.

In Chapter 3, I extended this perspective to the statistical analysis of satellite galaxy pairs in the Local Group. Previous studies suggested that the Milky Way and M31 may contain an unexpectedly high number of close satellite associations compared to ΛCDM expectations (Fattahi et al., 2013). By combining updated observational catalogues with the HESTIA cosmological simulations (Libeskind et al., 2020) and a consistent nearest-neighbour framework, I reassessed the incidence and nature of these associations while accounting for observational uncertainties.

I found that the Milky Way satellite population exhibits a clear excess of close associations relative to isotropic expectations and to ΛCDM simulations, with a pairing efficiency of $\sim$ 53% that remains high even after applying stellar-mass cuts matched to the resolution limits of the simulations ($\sim$ 52%). In contrast, the M31 satellite population shows no comparable excess and remains broadly consistent with a random spatial distribution, with a pairing efficiency of $\sim$ 28%.

I further showed that incorporating kinematic information is crucial for understanding the nature of these systems. Only a subset of spatially identified pairs exhibit small line-of-sight velocity differences

consistent with potential dynamical association, and among those with proper motion measurements, only a fraction show statistically compatible velocity vectors. A comparable analysis in the simulations, where full phase-space information is available, confirms that many statistically significant nearest-neighbour associations arise from chance alignments or transient configurations, reinforcing the need for dynamical constraints beyond spatial proximity alone.

The identified pairs are predominantly composed of satellites with comparable stellar masses, although systems involving ultra-faint companions also contribute to the clustering signal, particularly around the Magellanic Clouds. This behaviour is consistent with expectations from hierarchical accretion, in which massive satellites may bring their own populations of lower-mass companions into the host halo. However, both current simulations and the observed M31 satellite population remain limited to higher-mass satellites, implying that the abundance of low-mass hierarchical associations may still be underestimated.

I additionally showed that only a minority of pairs, for both observations and simulations, are consistent with being gravitationally bound at present time. This indicates that most close associations are not long-lived binary systems, but rather transient configurations or remnants of disrupted groups accreted together.

Requiring simultaneous spatial clustering, kinematic coherence, aligned motions, and compatibility with gravitational binding reduces the number of plausible physical associations even further. Taken together, these findings suggest that the excess of satellite pairs observed around the Milky Way is likely driven by correlated phase-space structures associated with recent group accretion events, such as the Magellanic system and the previously identified Crater–Leo group, rather than by an overabundance of bound binaries. The contrasting behaviour between the Milky Way and M31 further emphasises the role of stochastic assembly histories, as well as the need for improved completeness, accurate distances, and proper motions to fully characterise satellite clustering in the Local Group.

On smaller, internal scales, I demonstrated in Chapter 4 that the dynamical structure of low-mass dwarf galaxies departs significantly from a scaling relation established at higher masses (**Júlio et al.**, 2025b). By combining literature data for classical dwarf spheroidals with new measurements from the MUSE-Faint survey, I extended radially resolved measurements of the radial acceleration relation (RAR) down to baryonic accelerations as low as $log(g_{\rm bar}/{\rm m\,s^{-2}}) \sim -14$, reaching the lowest-acceleration regime explored with radially resolved measurements to date.

Using the Jeans modelling code GravSphere (Collins et al., 2021; Read & Steger, 2017), I first demonstrated through mock observations of simulated dwarf galaxies from the EDGE project (Agertz et al., 2020; Orkney et al., 2021) that the adopted methodology can robustly recover underlying mass profiles within the quoted uncertainties. Applying this framework to real galaxies, I found that low-mass dwarfs systematically lie above the extrapolation of the RAR calibrated on more massive galaxies (McGaugh et al., 2016), confirming and extending previous indications of deviations in this regime (Lelli et al., 2017).

In addition, I found substantial dwarf-to-dwarf scatter, together with multi-valued behaviour within individual systems, where different radii correspond to different observed accelerations at the same baryonic acceleration. These results demonstrate that the RAR is not universal in the low-mass regime and that the baryonic acceleration alone does not contain enough information, on its own, to derive the observed acceleration for these objects. This poses a significant challenge for MOND (McGaugh et al., 2016; Milgrom, 1983) in which the observed acceleration is expected to be uniquely determined by the baryonic distribution, except for well-defined effects such as the external field effect (EFE).

I therefore investigated whether the observed deviations could be explained by the EFE. However, I found that the predicted EFE acts in the opposite direction to the observed deviations and fails to reproduce the measured trends. Moreover, the existence of "twin" galaxies with similar baryonic structure and orbital properties but significantly different dynamical accelerations provides strong evidence against a purely baryon-driven relation.

I also explored several important systematic effects that could potentially bias these measurements, including the impact of unresolved binary stars and tidal perturbations from the host galaxy. While binaries can artificially inflate stellar velocity dispersions and tides can perturb dynamical equilibrium, multi-epoch spectroscopy together with conservative tidal estimates indicate that these effects are insufficient to explain the observed offsets and scatter, and thus these caveats do not alter the main interpretation of the results.

Finally, I compared the observations with high-resolution ΛCDM simulations from the EDGE pro-

ject and found that simulated dwarf galaxies naturally reproduce many of the observed features, including the systematic offset from the extrapolated RAR and the intrinsic scatter, although with somewhat reduced dispersion. This difference likely reflects a combination of observational uncertainties, modelling limitations, and the fact that Local Group dwarfs are satellites subject to environmental effects that are not fully captured in isolated simulations. Overall, these results establish the lowest-mass dwarf galaxies as a fundamental regime in which stochastic star formation, halo assembly, and environmental processes combined, produce intrinsically diverse dynamical behaviour.

Taken together, the results of this thesis illustrate that several of the most prominent small-scale challenges to ΛCDM are interconnected. Dwarf galaxies often exhibit multiple tensions simultaneously, and trying to understand any of them by itself risks missing the broader physical context. This work shows that to understand the formation and evolution of these systems, one needs to combine precise dynamical measurements with statistically meaningful samples and realistic comparisons to simulations such as those of the EDGE and HESTIA projects.

At the same time, important questions remain open. While group infall and environmental effects can explain part of the observed satellite structure, the full diversity of satellite configurations in the Local Group has yet to be reproduced in detail by simulations. Similarly, although the breakdown of the RAR in low-mass dwarfs appears consistent with ΛCDM expectations, the relative roles of feedback, tidal effects, and non-equilibrium dynamics remain to be fully quantified. Upcoming astrometric, spectroscopic, and photometric surveys will significantly expand the census of dwarf galaxies and improve the precision of their dynamical measurements, offering new opportunities to test these ideas.

In conclusion, this thesis shows that dwarf galaxies are not only problematic outliers at the edge of galaxy formation, but also essential tracers of cosmology on the smallest galactic scales. By probing both their orbital histories and their internal dynamics, dwarf galaxies provide some of the strongest and most informative tests of the ΛCDM paradigm. Continued progress in this field will require treating these systems not as isolated curiosities, but as powerful laboratories for testing cosmology, galaxy formation, and the complex physics that links the two.

Outlook

The coming decade promises a significant change in our ability to test small-scale predictions of the ΛCDM paradigm using dwarf galaxies. Fast advances in astrometry, spectroscopy, and deep imaging are transforming dwarf galaxy studies from analyses of small, heterogeneous samples into a statistically driven field with access to full six-dimensional phase-space information for an increasing number of systems. This progress will be particularly impactful for the dynamical questions addressed in this thesis, where orbital coherence, satellite associations, and internal mass distributions are fundamental.

On the scale of satellite systems, improved proper-motion measurements will allow a more robust identification of physically associated satellites and group infall events. Future *Gaia* data releases (DR4 and DR5) will substantially improve the orbital constraints for Milky Way satellites, while targeted HST and JWST programmes will continue to expand the number of satellites with well-constrained proper motions around both the Milky Way and M31. Together, these datasets will allow orbital coherence, angular momentum alignment, and common infall histories to be quantified systematically rather than inferred from individual case studies. At the same time, wide-field surveys such as SAGA, ELVES, and UNIONS, and forthcoming spectroscopic programmes such as 4MOST and the Wide Spectroscopic Telescope (WST) will rapidly expand the known satellite population around Milky Way-like hosts and improve spectroscopic characterisation of faint systems.

Building on this progress, I aim to extend the analysis of satellite associations presented in this thesis to other satellite groups, quantifying orbital coherence and dynamical alignment whenever the data allow. The combination of growing satellite samples, improved proper motions, and increasingly complete spectroscopic data will make robust phase-space identification of satellite associations across multiple host systems possible. While full proper-motion measurements will remain limited to the Local Group for the foreseeable future, deeper photometric and spectroscopic surveys beyond the Local Group will allow comparative studies of satellite populations across different environments and assembly histories. We can then shift from studies of only a few well-observed and potentially exceptional systems to a fully statistical approach that can robustly test theoretical predictions.

At the level of internal dynamics, next-generation spectroscopic and imaging facilities will dramatically improve constraints on the dark matter content of the faintest galaxies. Deep integral-field spectroscopy from instruments such as MUSE, combined with the resolving power of the Extremely Large Telescope (ELT), will extend resolved stellar kinematic measurements to lower surface brightnesses and larger radii. Future facilities may even allow measurements of internal proper motions for nearby dwarf galaxies, complementing line-of-sight velocities and breaking long-standing degeneracies in dynamical modelling. Initial studies using HST have already demonstrated the feasibility of this approach for systems such as Draco and Sculptor (Vitral et al., 2024, 2026). These advances will allow stronger tests of dynamical equilibrium, velocity anisotropy, and mass-modelling assumptions, strengthening the interpretation of scaling relations such as the radial acceleration relation in the low-mass regime.

Space-based facilities will play a complementary role. JWST and Euclid are already allowing detailed studies of resolved stellar populations and structural properties of faint dwarfs, while the forthcoming Roman Space Telescope will provide deep, wide-field imaging and precise astrometry over unprecedented areas of the sky. As a member of the Roman Milky Way Dwarfs Science Team, I plan to contribute in characterising the stellar populations of dwarf galaxies, and link their internal properties to their dynamical and orbital histories.

Taken together, these developments will allow the field to move beyond small, potentially biased samples toward a unified, statistical view of dwarf galaxy formation and dynamics. By combining orbital information, internal kinematics, and environmental context across large samples and multiple hosts, it will become possible to understand whether the remaining small-scale tensions with ΛCDM are due to incomplete modelling of baryonic physics, environmental pre-processing, or more fundamental limitations of the standard cosmological paradigm. Dwarf galaxies will remain fundamental for this effort as probes of structure formation at the smallest galactic scales.

Bibliography

Agertz, O., A. V. Kravtsov, S. N. Leitner, & N. Y. Gnedin (2013). "Toward a Complete Accounting of Energy and Momentum from Stellar Feedback in Galaxy Formation Simulations". In: *ApJ* 770, 25. DOI: 10.1088/0004-637X/770/1/25.

Agertz, O., A. Pontzen, J. I. Read, et al. (2020). "EDGE: the mass-metallicity relation as a critical test of galaxy formation physics". In: *MNRAS* 491, 1656–1672. DOI: 10.1093/mnras/stz3053.

Anderson, J. (2022). *One-Pass HST Photometry with hst1pass*.

Arias, V., M. Guglielmo, N. Fernando, et al. (2016). "NGC 147, NGC 185 and CassII: a genetic approach to orbital properties, star formation and tidal debris". In: *MNRAS* 456, 1654–1665. DOI: 10.1093/mnras/stv2781.

Astropy Collaboration, A. M. Price-Whelan, B. M. Sipocz, et al. (2018). "The Astropy Project: Building an Open-science Project and Status of the v2.0 Core Package". In: *AJ* 156, 123. DOI: 10.3847/1538-3881/aabc4f.

Astropy Collaboration, A. M. Price-Whelan, P. L. Lim, et al. (2022). "The Astropy Project: Sustaining and Growing a Community-oriented Open-source Project and the Latest Major Release (v5.0) of the Core Package". In: *ApJ* 935, 167. DOI: 10.3847/1538-4357/ac7c74.

Bakels, L., A. D. Ludlow, & C. Power (2021). "Pre-processing, group accretion, and the orbital trajectories of associated subhaloes". In: *MNRAS* 501, 5948–5963. DOI: 10.1093/mnras/staa3979.

Bañares-Hernández, A., F. Calore, J. Martin Camalich, & J. I. Read (2025). "New constraints on the central mass contents of Omega Centauri from combined stellar kinematics and pulsar timing". In: *A&A* 693, A104. DOI: 10.1051/0004-6361/202451763.

Bañares-Hernández, A., J. I. Read, & **M. P. Júlio** (2026). "GravSphere2: A higher order Jeans method for mass modeling spherical stellar systems". In: *A&A* 705, A212. DOI: 10.1051/0004-6361/202557195.

Banik, I., I. Thies, R. Truelove, et al. (2022). "3D hydrodynamic simulations for the formation of the Local Group satellite planes". In: *MNRAS* 513, 129–158. DOI: 10.1093/mnras/stac722.

Battaglia, G., S. Taibi, G. F. Thomas, & T. K. Fritz (2022). "Gaia early DR3 systemic motions of Local Group dwarf galaxies and orbital properties with a massive Large Magellanic Cloud". In: *A&A* 657, A54. DOI: 10.1051/0004-6361/202141528.

Battaglia, G., A. Helmi, & M. Breddels (2013). "Internal kinematics and dynamical models of dwarf spheroidal galaxies around the Milky Way". In: *New Astronomy Reviews* 57, 52–79. DOI: 10.1016/j.newar.2013.05.003.

Baumgardt, H., M. Hilker, A. Sollima, & A. Bellini (2019). "Mean proper motions, space orbits, and velocity dispersion profiles of Galactic globular clusters derived from Gaia DR2 data". In: *MNRAS* 482, 5138–5155. DOI: 10.1093/mnras/sty2997.

Bekenstein, J. & M. Milgrom (1984). "Does the missing mass problem signal the breakdown of Newtonian gravity?" In: *ApJ* 286, 7–14. DOI: 10.1086/162570.

Bell, E. F., A. Smercina, P. A. Price, et al. (2022). "Ultrafaint Dwarf Galaxy Candidates in the M81 Group: Signatures of Group Accretion". In: *ApJ* 937, L3. DOI: 10.3847/2041-8213/ac8e5e.

Bellazzini, M., N. Gennari, & F. R. Ferraro (2005). "The red giant branch tip and bump of the Leo II dwarf spheroidal galaxy". In: *MNRAS* 360, 185–193. DOI: 10.1111/j.1365-2966.2005.09027.x.

Bellazzini, M., N. Gennari, F. R. Ferraro, & A. Sollima (2004). "The distance to the Leo I dwarf spheroidal galaxy from the red giant branch tip". In: *MNRAS* 354, 708–712. DOI: 10.1111/j.1365-2966.2004.08226.x.

Belokurov, V., M. J. Irwin, S. E. Koposov, et al. (2014). "ATLAS lifts the Cup: discovery of a new Milky Way satellite in Crater". In: *MNRAS* 441, 2124–2133. DOI: 10.1093/mnras/stu626.

Belokurov, V., M. G. Walker, N. W. Evans, et al. (2008). "Leo V: A Companion of a Companion of the Milky Way Galaxy?" In: *ApJ* 686, L83. DOI: 10.1086/592962.

Belokurov, V., D. B. Zucker, N. W. Evans, et al. (2007). "Cats and Dogs, Hair and A Hero: A Quintet of New Milky Way Companions". In: *ApJ* 654, 897–906. DOI: 10.1086/509718.

Bertone, G. & D. Hooper (2018). "History of dark matter". In: *Rev. Mod. Phys.* 90. DOI: 10.1103/revmodphys.90.045002.

Besla, G., N. Kallivayalil, L. Hernquist, et al. (2007). "Are the Magellanic Clouds on Their First Passage about the Milky Way?" In: *ApJ* 668, 949–967. DOI: 10.1086/521385.

Besla, G., D. R. Patton, S. Stierwalt, et al. (2018). "The frequency of dwarf galaxy multiples at low redshift in SDSS versus cosmological expectations". In: *MNRAS* 480, 3376–3396. DOI: 10.1093/mnras/sty2041.

Binney, J. & G. A. Mamon (1982). "M/L and velocity anisotropy from observations of spherical galaxies, or must M87 have a massive black hole ?" In: *MNRAS* 200, 361–375. DOI: 10.1093/mnras/200.2.361.

Binney, J. & S. Tremaine (2011). *Galactic Dynamics: Second Edition*. Princeton Series in Astrophysics. Princeton University Press. ISBN: 978-1-4008-2872-2.

Blumenthal, G. R., S. M. Faber, J. R. Primack, & M. J. Rees (1984). "Formation of galaxies and large-scale structure with cold dark matter." In: *Nature* 311, 517–525. DOI: 10.1038/311517a0.

Bonanos, A. Z., K. Z. Stanek, A. H. Szentgyorgyi, D. D. Sasselov, & G. A. Bakos (2004). "The RR Lyrae Distance to the Draco Dwarf Spheroidal Galaxy". In: *AJ* 127, 861. DOI: 10.1086/381073.

Bosma, A. (1981). "21-cm line studies of spiral galaxies. II. The distribution and kinematics of neutral hydrogen in spiral galaxies of various morphological types." In: *AJ* 86, 1825–1846. DOI: 10.1086/113063.

Bovy, J. (2015). "galpy: A python Library for Galactic Dynamics". In: *ApJS* 216, 29. DOI: 10.1088/0067-0049/216/2/29.

Boylan-Kolchin, M., J. S. Bullock, & M. Kaplinghat (2011). "Too big to fail? The puzzling darkness of massive Milky Way subhaloes". In: *MNRAS* 415, L40–L44. DOI: 10.1111/j.1745-3933.2011.01074.x.

Boylan-Kolchin, M., V. Springel, S. D. M. White, A. Jenkins, & G. Lemson (2009). "Resolving cosmic structure formation with the Millennium-II Simulation". In: *MNRAS* 398, 1150–1164. DOI: 10.1111/j.1365-2966.2009.15191.x.

Brown, T. M., J. Tumlinson, M. Geha, et al. (2014). "The Quenching of the Ultra-faint Dwarf Galaxies in the Reionization Era". In: *ApJ* 796, 91. DOI: 10.1088/0004-637X/796/2/91.

Bullock, J. S. & M. Boylan-Kolchin (2017). "Small-Scale Challenges to the ΛCDM Paradigm". In: *A&A Rev.* 55, 343–387. DOI: 10.1146/annurev-astro-091916-055313.

Bullock, J. S., A. V. Kravtsov, & D. H. Weinberg (2000). "Reionization and the Abundance of Galactic Satellites". In: *ApJ* 539, 517–521. DOI: 10.1086/309279.

Caldwell, N., M. G. Walker, M. Mateo, et al. (2017). "Crater 2: An Extremely Cold Dark Matter Halo". In: *ApJ* 839, 20. DOI: 10.3847/1538-4357/aa688e.

Callingham, T. M. & A. Helmi (2025). "Group accretion in Milky Way-like stellar haloes". In: *A&A* 700, A175. DOI: 10.1051/0004-6361/202554966.

Cameron, E. & S. P. Driver (2007). "The galaxy luminosity–size relation and selection biases in the Hubble Ultra Deep Field". In: *MNRAS* 377, 523–534. DOI: 10.1111/j.1365-2966.2007.11507.x.

Carrera, R., A. Aparicio, D. Martínez-Delgado, & J. Alonso-García (2002). "The Star Formation History and Spatial Distribution of StellarPopulations in the Ursa Minor Dwarf Spheroidal Galaxy". In: *AJ* 123, 3199. DOI: 10.1086/340702.

Casetti-Dinescu, D. I. & T. M. Girard (2016). "Proper motion of the Draco dwarf galaxy from Subaru Suprime-Cam data". In: *MNRAS* 461, 271–285. DOI: 10.1093/mnras/stw1337.

Casetti-Dinescu, D. I., M. S. Pawlowski, T. M. Girard, et al. (2024). "HST Proper Motion of Andromeda III. Another Satellite Coorbiting the M31 Satellite Plane". In: *AJ* 975, 138. DOI: 10.3847/1538-4357/ad7b10.

Casetti-Dinescu, D. I., M. S. Pawlowski, T. M. Girard, et al. (2025). "HST Proper Motions of Andromeda V and Andromeda VI". In: *ApJ* 992, 54. DOI: 10.3847/1538-4357/ae0479.

Chae, K.-H., H. Desmond, F. Lelli, S. S. McGaugh, & J. M. Schombert (2021). "Testing the Strong Equivalence Principle. II. Relating the External Field Effect in Galaxy Rotation Curves to the Large-scale Structure of the Universe". In: *ApJ* 921, 104. DOI: 10.3847/1538-4357/ac1bba.

Chae, K.-H., F. Lelli, H. Desmond, et al. (2020). "Testing the Strong Equivalence Principle: Detection of the External Field Effect in Rotationally Supported Galaxies". In: *ApJ* 904, 51. DOI: 10.3847/1538-4357/abbb96.

Chiti, A., J. D. Simon, A. Frebel, et al. (2022). "Magellan/IMACS Spectroscopy of Grus I: A Low Metallicity Ultra-faint Dwarf Galaxy". In: *ApJ* 939, 41. DOI: 10.3847/1538-4357/ac96ed.

Clementini, G., M. Cignoni, R. Contreras Ramos, et al. (2012). "Variability and Star Formation in Leo T, the Lowest Luminosity Star-forming Galaxy Known Today". In: *ApJ* 756, 108. DOI: 10.1088/0004-637X/756/2/108.

Clifton, T., P. G. Ferreira, A. Padilla, & C. Skordis (2012). "Modified gravity and cosmology". In: *Physics Reports* 513, 1–189. DOI: https://doi.org/10.1016/j.physrep.2012.01.001.

Cohen, J. G. & W. Huang (2009). "The chemical evolution of the Draco dwarf spheroidal galaxy". In: *ApJ* 701, 1053. DOI: 10.1088/0004-637X/701/2/1053.

Cole, D. R., W. Dehnen, J. I. Read, & M. I. Wilkinson (2012). "The mass distribution of the Fornax dSph: constraints from its globular cluster distribution". In: *MNRAS* 426, 601–613. DOI: 10.1111/j.1365-2966.2012.21885.x.

Collins, M. L. M., J. I. Read, R. A. Ibata, et al. (2021). "Andromeda XXI - a dwarf galaxy in a low-density dark matter halo". In: *MNRAS* 505, 5686–5701. DOI: 10.1093/mnras/stab1624.

Conn, A. R., G. F. Lewis, R. A. Ibata, et al. (2013). "The three-dimensional structure of the M31 satellite system; strong evidence for an inhomogeneous distribution of satellites". In: *ApJ* 766, 120. DOI: 10.1088/0004-637X/766/2/120.

Crnojević, D., D. J. Sand, D. Zaritsky, et al. (2016). "Deep Imaging of Eridanus II and Its Lone Star Cluster". In: *ApJ* 824, L14. DOI: 10.3847/2041-8205/824/1/L14.

D'Onghia, E. & G. Lake (2008). "Small dwarf galaxies within larger dwarfs: why some are luminous while most go dark". In: *ApJ* 686, L61. DOI: 10.1086/592995.

Davis, D. S., C. M. Bird, R. F. Mushotzky, & S. C. Odewahn (1995). "Abell 548: an X-Ray and Optical Analysis of Substructure". In: *ApJ* 440, 48. DOI: 10.1086/175246.

de Bernardis, P., P. A. R. Ade, J. J. Bock, et al. (2000). "A flat Universe from high-resolution maps of the cosmic microwave background radiation". In: *Nature* 404, 955–959. DOI: 10.1038/35010035.

de Blok, W. J. G. (2010). "The Core-Cusp Problem". In: *Adv. Astron.* 2010, 789293. DOI: 10.1155/2010/789293.

de Boer, T. J. L., E. Tolstoy, V. Hill, et al. (2012). "The star formation and chemical evolution history of the Fornax dwarf spheroidal galaxy". In: *A&A* 544, A73. DOI: 10.1051/0004-6361/201219547.

de Boer, T. J. L., E. Tolstoy, B. Lemasle, et al. (2014). "The episodic star formation history of the Carina dwarf spheroidal galaxy". In: *A&A* 572, A10. DOI: 10.1051/0004-6361/201424119.

De Leo, M., R. Carrera, N. E. D. Noël, et al. (2020). "Revealing the tidal scars of the Small Magellanic Cloud". In: *MNRAS* 495, 98–113. DOI: 10.1093/mnras/staa1122.

De Leo, M., J. I. Read, N. E. D. Noël, et al. (2024). "Surviving the waves: evidence for a dark matter cusp in the tidally disrupting Small Magellanic Cloud". In: *MNRAS* 535, 1015–1034. DOI: 10.1093/mnras/stae2428.

Deason, A., A. Wetzel, & S. Garrison-Kimmel (2014). "Satellite Dwarf Galaxies in a Hierarchical Universe: The Prevalence of Dwarf-Dwarf Major Mergers". In: *ApJ* 794, 115. DOI: 10.1088/0004-637X/794/2/115.

Di Cintio, A., C. B. Brook, A. V. Macciò, et al. (2014). "The dependence of dark matter profiles on the stellar-to-halo mass ratio: a prediction for cusps versus cores". In: *MNRAS* 437, 415–423. DOI: 10.1093/mnras/stt1891.

Dodelson, S. (2011). "The Real Problem with MOND". In: *Int. J. Mod. Phys. D* 20, 2749–2753. DOI: 10.1142/S0218271811020561.

Dooley, G. A., A. H. Peter, J. L. Carlin, et al. (2017). "The predicted luminous satellite populations around SMC- and LMC-mass galaxies - a missing satellite problem around the LMC?" In: *MNRAS* 472, 1060–1073. DOI: 10.1093/mnras/stx2001.

Drlica-Wagner, A., K. Bechtol, S. Mau, et al. (2020). "Milky Way Satellite Census. I. The Observational Selection Function for Milky Way Satellites in DES Y3 and Pan-STARRS DR1". In: *ApJ* 893, 47. DOI: 10.3847/1538-4357/ab7eb9.

Drlica-Wagner, A., K. Bechtol, E. S. Rykoff, et al. (2015). "Eight Ultra-faint Galaxy Candidates Discovered in Year Two of the Dark Energy Survey". In: *ApJ* 813, 109. DOI: 10.1088/0004-637X/813/2/109.

Duncan, K., C. J. Conselice, C. Mundy, et al. (2019). "Observational Constraints on the Merger History of Galaxies since z ≈ 6: Probabilistic Galaxy Pair Counts in the CANDELS Fields". In: *ApJ* 876, 110. DOI: 10.3847/1538-4357/ab148a.

Durakovic, A. & C. Skordis (2024). "Towards galaxy cluster models in Aether-Scalar-Tensor theory: isothermal spheres and curiosities". In: *J. Cosmology Astropart. Phys.* 2024, 040. DOI: 10.1088/1475-7516/2024/04/040.

Dutton, A. A., A. V. Macciò, A. Obreja, & T. Buck (2019). "NIHAO - XVIII. Origin of the MOND phenomenology of galactic rotation curves in a ΛCDM universe". In: *MNRAS* 485, 1886–1899. DOI: 10.1093/mnras/stz531.

Dutton, A. A., C. Conroy, F. C. van den Bosch, F. Prada, & S. More (2010). "The kinematic connection between galaxies and dark matter haloes". In: *MNRAS* 407, 2–16. DOI: 10.1111/j.1365-2966.2010.16911.x.

Dutton, A. A. & A. V. Macciò (2014). "Cold dark matter haloes in the Planck era: evolution of structural parameters for Einasto and NFW profiles". In: *MNRAS* 441, 3359–3374. DOI: 10.1093/mnras/stu742.

Elbert, O. D., J. S. Bullock, S. Garrison-Kimmel, et al. (2015). "Core formation in dwarf haloes with self-interacting dark matter: no fine-tuning necessary". In: *MNRAS* 453, 29–37. DOI: 10.1093/mnras/stv1470.

Eriksen, M. H., M. T. Frandsen, & M. H. From (2021). "A cusp-core-like challenge for modified Newtonian dynamics". In: *A&A* 656, A123. DOI: 10.1051/0004-6361/202040189.

Erkal, D., V. Belokurov, C. F. P. Laporte, et al. (2019). "The total mass of the Large Magellanic Cloud from its perturbation on the Orphan stream". In: *MNRAS* 487, 2685–2700. DOI: 10.1093/mnras/stz1371.

Evans, N. W., J. An, & M. G. Walker (2009). "Cores and cusps in the dwarf spheroidals". In: *MNRAS* 393, L50–L54. DOI: 10.1111/j.1745-3933.2008.00596.x.

Faber, S. M. & R. E. Jackson (1976). "Velocity dispersions and mass-to-light ratios for elliptical galaxies." In: *ApJ* 204, 668–683. DOI: 10.1086/154215.

Famaey, B. & S. McGaugh (2012). "Modified Newtonian Dynamics (MOND): Observational Phenomenology and Relativistic Extensions". In: *Living Rev. Relativ.* 15, 10. DOI: 10.12942/lrr-2012-10.

Fattahi, A., J. F. Navarro, E. Starkenburg, C. R. Barber, & A. W. McConnachie (2013). "Galaxy pairs in the local group." In: *MNRAS* 431, L73–L77. DOI: 10.1093/mnrasl/slt011.

Ferrero, I., M. G. Abadi, J. F. Navarro, L. V. Sales, & S. Gurovich (2012). "The dark matter haloes of dwarf galaxies: a challenge for the Λ cold dark matter paradigm?" In: *MNRAS* 425, 2817–2823. DOI: 10.1111/j.1365-2966.2012.21623.x.

Fillingham, S. P., M. C. Cooper, A. B. Pace, et al. (2016). "Under pressure: quenching star formation in low-mass satellite galaxies via stripping". In: *MNRAS* 463, 1916–1928. DOI: 10.1093/mnras/stw2131.

Fitts, A., M. Boylan-Kolchin, B. Bozek, et al. (2019). "Dwarf galaxies in CDM, WDM, and SIDM: disentangling baryons and dark matter physics". In: *MNRAS* 490, 962–977. DOI: 10.1093/mnras/stz2613.

Flewelling, H. A., E. A. Magnier, K. C. Chambers, et al. (2020). "The Pan-STARRS1 Database and Data Products". In: *ApJS* 251, 7. DOI: 10.3847/1538-4365/abb82d.

Foreman-Mackey, D. (2016). "corner.py: Scatterplot matrices in Python". In: *J. Open Source Softw.* 1, 24. DOI: 10.21105/joss.00024.

Foreman-Mackey, D., D. W. Hogg, D. Lang, & J. Goodman (2013). "emcee: The MCMC Hammer". In: *PASP* 125, 306–312. DOI: 10.1086/670067.

Forman, W. & C. Jones (1982). "X-ray-imaging observations of clusters of galaxies". In: *A&A Rev.* 20, 547–585. DOI: 10.1146/annurev.aa.20.090182.002555.

Fouquet, S., F. Hammer, Y. Yang, M. Puech, & H. Flores (2012). "Does the dwarf galaxy system of the Milky Way originate from Andromeda?" In: *MNRAS* 427, 1769–1783. DOI: 10.1111/j.1365-2966.2012.22067.x.

Freundlich, J., B. Famaey, P.-A. Oria, et al. (2022). "Probing the radial acceleration relation and the strong equivalence principle with the Coma cluster ultra-diffuse galaxies". In: *A&A* 658, A26. DOI: 10.1051/0004-6361/202142060.

Fritz, T. K., A. Di Cintio, G. Battaglia, C. Brook, & S. Taibi (2020). "The mass of our Galaxy from satellite proper motions in the Gaia era". In: *MNRAS* 494, 5178–5193. DOI: 10.1093/mnras/staa1040.

Fritz, T. K., G. Battaglia, M. S. Pawlowski, et al. (2018). "Gaia DR2 proper motions of dwarf galaxies within 420 kpc. Orbits, Milky Way mass, tidal influences, planar alignments, and group infall". In: *A&A* 619, A103. DOI: 10.1051/0004-6361/201833343.

Fu, S. W., J. D. Simon, & A. G. A. Jara (2019). "Dynamical Histories of the Crater II and Hercules Dwarf Galaxies". In: *ApJ* 883, 11. DOI: 10.3847/1538-4357/ab3658.

Gaia Collaboration, Katz, D., Antoja, T., et al. (2018). "Gaia Data Release 2 - Mapping the Milky Way disc kinematics". In: *A&A* 616, A11. DOI: 10.1051/0004-6361/201832865.

Gao, L., S. D. M. White, A. Jenkins, F. Stoehr, & V. Springel (2004). "The subhalo populations of ΛCDM dark haloes". In: *MNRAS* 355, 819–834. DOI: 10.1111/j.1365-2966.2004.08360.x.

Garaldi, E., E. Romano-Díaz, C. Porciani, & M. S. Pawlowski (2018). "Radial Acceleration Relation of ΛCDM Satellite Galaxies". In: *Phys. Rev. Lett.* 120, 261301. DOI: 10.1103/PhysRevLett.120.261301.

Garavito-Camargo, N., G. Besla, C. F. P. Laporte, et al. (2019). "Hunting for the Dark Matter Wake Induced by the Large Magellanic Cloud". In: *ApJ* 884, 51. DOI: 10.3847/1538-4357/ab32eb.

Garavito-Camargo, N., E. Patel, G. Besla, et al. (2021). "The Clustering of Orbital Poles Induced by the LMC: Hints for the Origin of Planes of Satellites". In: *ApJ* 923, 140. DOI: 10.3847/1538-4357/ac2c05.

Garofalo, A., M. Tantalo, F. Cusano, et al. (2021). "Born in a Pair (?): Pisces II and Pegasus III". In: *ApJ* 916, 10. DOI: 10.3847/1538-4357/ac0253.

Garrison-Kimmel, S., M. Boylan-Kolchin, J. S. Bullock, & K. Lee (2014). "ELVIS: Exploring the Local Volume in Simulations". In: *MNRAS* 438, 2578–2596. DOI: 10.1093/mnras/stt2377.

Gatto, A., F. Fraternali, J. I. Read, et al. (2013). "Unveiling the corona of the Milky Way via ram-pressure stripping of dwarf satellites". In: *MNRAS* 433, 2749–2763. DOI: 10.1093/mnras/stt896.

Geha, M., R. P. van der Marel, P. Guhathakurta, et al. (2010). "Local Group Dwarf Elliptical Galaxies. II. Stellar Kinematics to Large Radii in NGC 147 and NGC 185". In: *ApJ* 711, 361–373. DOI: 10.1088/0004-637X/711/1/361.

Geha, M., D. Weisz, A. Grocholski, et al. (2015). "HST/ACS Direct Ages of the Dwarf Elliptical Galaxies NGC 147 and NGC 185". In: *ApJ* 811, 114. DOI: 10.1088/0004-637X/811/2/114.

Genina, A., J. I. Read, C. S. Frenk, et al. (2020). "To β or not to β: can higher order Jeans analysis break the mass-anisotropy degeneracy in simulated dwarfs?" In: *MNRAS* 498, 144–163. DOI: 10.1093/mnras/staa2352.

Genina, A., A. Benítez-Llambay, C. S. Frenk, et al. (2018). "The core-cusp problem: a matter of perspective". In: *MNRAS* 474, 1398–1411. DOI: 10.1093/mnras/stx2855.

Genina, A., J. I. Read, A. Fattahi, & C. S. Frenk (2022). "Can tides explain the low dark matter density in Fornax?" In: *MNRAS* 510, 2186–2205. DOI: 10.1093/mnras/stab3526.

Goater, A., J. I. Read, N. E. D. Noël, et al. (2024). "EDGE: The direct link between mass growth history and the extended stellar haloes of the faintest dwarf galaxies". In: *MNRAS* 527, 2403–2412. DOI: 10.1093/mnras/stad3354.

Goerdt, T., B. Moore, J. I. Read, J. Stadel, & M. Zemp (2006). "Does the Fornax dwarf spheroidal have a central cusp or core?" In: *MNRAS* 368, 1073–1077. DOI: 10.1111/j.1365-2966.2006.10182.x.

Gómez, F. A., G. Besla, D. D. Carpintero, et al. (2015). "And yet it moves: the dangers of artificially fixing the Milky Way center of mass in the presence of a massive Large Magellanic Cloud". In: *ApJ* 802, 128. DOI: 10.1088/0004-637X/802/2/128.

Grand, R. J. J., F. A. Gómez, F. Marinacci, et al. (2017). "The Auriga Project: the properties and formation mechanisms of disc galaxies across cosmic time". In: *MNRAS* 467, 179–207. DOI: 10.1093/mnras/stx071.

Gration, A., D. D. Hendriks, P. Das, D. Heber, & R. G. Izzard (2025). "Stellar velocity distributions in binary-rich ultrafaint dwarf galaxies". In: *MNRAS* 543, 1120–1132. DOI: 10.1093/mnras/staf1481.

GRAVITY Collaboration, R. Abuter, A. Amorim, et al. (2019). "A geometric distance measurement to the Galactic center black hole with 0.3% uncertainty". In: *A&A* 625, L10. DOI: 10.1051/0004-6361/201935656.

Gray, E. I., J. I. Read, E. Taylor, et al. (2025). "EDGE: a new model for nuclear star cluster formation in dwarf galaxies". In: *MNRAS* 539, 1167–1179. DOI: 10.1093/mnras/staf521.

Gullieuszik, M., E. V. Held, L. Rizzi, et al. (2008). "The evolved stars of Leo II dSph galaxy from near-infrared UKIRT/WFCAM observations". In: *MNRAS* 388, 1185–1197. DOI: 10.1111/j.1365-2966.2008.13400.x.

Haardt, F. & P. Madau (1995). "Radiative transfer in a clumpy universe: Ii. the utraviolet extragalactic background". In: *ApJ* 461, 20. DOI: 10.1086/177035.

Hargis, J. R., S. Albers, D. Crnojević, et al. (2020). "Hubble Space Telescope Imaging of Antlia B: Star Formation History and a New Tip of the Red Giant Branch Distance". In: *ApJ* 888, 31. DOI: 10.3847/1538-4357/ab58d2.

Hargreaves, J. C., G. Gilmore, & J. D. Annan (1996). "The influence of binary stars on dwarf spheroidal galaxy kinematics". In: *MNRAS* 279, 108–120. DOI: 10.1093/mnras/279.1.108.

Harrington, R. G. & A. G. Wilson (1950). "Two New Stellar Systems in Leo". In: *PASP* 62, 118–120. DOI: 10.1086/126249.

Harris, C. R., K. J. Millman, S. J. v. d. Walt, et al. (2020). "Array programming with NumPy". In: *Nature* 585, 357–362. DOI: 10.1038/s41586-020-2649-2.

Hayashi, K. & M. Chiba (2012). "Probing Non-spherical Dark Halos in the Galactic Dwarf Galaxies". In: *ApJ* 755, 145. DOI: 10.1088/0004-637X/755/2/145.

Heesters, N., R. Habas, F. R. Marleau, et al. (2021). "Flattened structures of dwarf satellites around massive host galaxies in the MATLAS low-to-moderate density fields". In: *A&A* 654, A161. DOI: 10.1051/0004-6361/202141184.

Homma, D., M. Chiba, Y. Komiyama, et al. (2024). "Final results of the search for new Milky Way satellites in the Hyper Suprime-Cam Subaru Strategic Program survey: Discovery of two more candidates". In: *PASJ* 76, 733–752. DOI: 10.1093/pasj/psae044.

Huang, K.-W. & S. E. Koposov (2021). "Search for globular clusters associated with the Milky Way dwarf galaxies using Gaia DR2". In: *MNRAS* 500, 986–997. DOI: 10.1093/mnras/staa3297.

Huchtmeier, W. (1973). "The distribution of neutral hydrogen and the velocity field of the galaxy NGC 3109." In: *A&A* 22, 27–31.

Hunter, J. D. (2007). "Matplotlib: A 2D Graphics Environment". In: *Comput. Sci. Eng.* 9, 90–95. DOI: 10.1109/MCSE.2007.55.

Ibata, R., A. Sollima, C. Nipoti, et al. (2011). "The Globular Cluster NGC 2419: A Crucible for Theories of Gravity". In: *ApJ* 738, 186. DOI: 10.1088/0004-637X/738/2/186.

Ibata, R. A., G. Gilmore, & M. Irwin (1994). "A dwarf satellite galaxy in Sagittarius". In: *Nature* 370, 194–196. DOI: 10.1038/370194a0.

Ibata, R. A., G. F. Lewis, A. R. Conn, et al. (2013). "A vast, thin plane of corotating dwarf galaxies orbiting the Andromeda galaxy". In: *Nature* 493, 62–65. DOI: 10.1038/nature11717.

Ibata, R. A., N. G. Ibata, G. F. Lewis, et al. (2014). "A Thousand Shadows of Andromeda: Rotating Planes of Satellites in the Millennium-II Cosmological Simulation". In: *ApJ* 784, L6. DOI: 10.1088/2041-8205/784/1/L6.

Irwin, M. & D. Hatzidimitriou (1995). "Structural parameters for the Galactic dwarf spheroidals". In: *MNRAS* 277, 1354–1378. DOI: 10.1093/mnras/277.4.1354.

Jahn, E. D., L. V. Sales, A. Wetzel, et al. (2019). "Dark and luminous satellites of LMC-mass galaxies in the FIRE simulations". In: *MNRAS* 489, 5348–5364. DOI: 10.1093/mnras/stz2457.

Jarvis, M., R. Taylor, I. Agudo, et al. (2018). "The MeerKAT International GHz Tiered Extragalactic Exploration (MIGHTEE) Survey". In: *Proceedings of MeerKAT Science: On the Pathway to the SKA — PoS(MeerKAT2016)*. Vol. 277, 006. DOI: 10.22323/1.277.0006.

Jeans, J. H. (1922). "The Motions of Stars in a Kapteyn-Universe". In: *MNRAS* 82, 122–132. DOI: 10.1093/mnras/82.3.122.

Jenkins, S. A., T. S. Li, A. B. Pace, et al. (2021). "Very Large Telescope Spectroscopy of Ultra-faint Dwarf Galaxies. I. Boötes I, Leo IV, and Leo V". In: *ApJ* 920, 92. DOI: 10.3847/1538-4357/ac1353.

Ji, A. P., S. E. Koposov, T. S. Li, et al. (2021). "Kinematics of Antlia 2 and Crater 2 from the Southern Stellar Stream Spectroscopic Survey (S5)". In: *ApJ* 921, 32. DOI: 10.3847/1538-4357/ac1869.

Johnson, D. R. H. & D. R. Soderblom (1987). "Calculating galactic space velocities and their uncertainties, with an application to the Ursa Major group". In: *AJ* 93, 864. DOI: 10.1086/114370.

Jones, B. F., A. R. Klemola, & D. N. C. Lin (1994). "Proper Motion of The Large Magellanic Cloud And The Mass of The Galaxy. I. Observational Result". In: *AJ* 107, 1333. DOI: 10.1086/116947.

Jong, J. T. A. d., N. F. Martin, H.-W. Rix, et al. (2010). "The enigmatic pair of dwarf galaxies Leo IV and Leo V: coincidence or common origin?" In: *ApJ* 710, 1664. DOI: 10.1088/0004-637X/710/2/1664.

Júlio, M. P. (2023). "The Dark Matter Density Profiles of Antlia B". In: *EAS2023, European Astronomical Society Annual Meeting*, 1863.

Júlio, M. P., J. Brinchmann, J. I. Read, & M. Collaboration (2025a). "The Dark Matter Density Profiles of Antlia B". In: *Dynamical Masses of Local Group Galaxies*. Vol. 379. IAU Symposium, 147–153. DOI: 10.1017/S1743921323001473.

Júlio, M. P., J. Brinchmann, S. L. Zoutendijk, et al. (2023). "The MUSE-Faint survey. III. Constraining scalar field dark matter with Antlia B". In: *A&A* 678, A38. DOI: 10.1051/0004-6361/202346987.

Júlio, M. P. & M. S. Pawlowski (2023). "Exploring satellite group infall in the Milky Way: the case of the Crater-Leo objects". In: *EAS2023, European Astronomical Society Annual Meeting*, 2121.

Júlio, M. P., M. S. Pawlowski, S. Tony Sohn, et al. (2024). "Satellite group infall into the Milky Way: Exploring the Crater-Leo case with new HST proper motions". In: *A&A* 687, A212. DOI: 10.1051/0004-6361/202449985.

Júlio, M. P., J. I. Read, M. S. Pawlowski, et al. (2025b). "The radial acceleration relation at the EDGE of galaxy formation: Testing its universality in low-mass dwarf galaxies". In: *A&A* 704, A330. DOI: 10.1051/0004-6361/202557106.

Kahn, F. D. & L. Woltjer (1959). "Intergalactic Matter and the Galaxy." In: *ApJ* 130, 705. DOI: 10.1086/146762.

Kallivayalil, N., L. V. Sales, P. Zivick, et al. (2018). "The Missing Satellites of the Magellanic Clouds? Gaia Proper Motions of the Recently Discovered Ultra-faint Galaxies". In: *ApJ* 867, 19. DOI: 10.3847/1538-4357/aadfee.

Kanehisa, K. J., M. S. Pawlowski, N. Heesters, & O. Müller (2024). "A too-many dwarf satellite galaxies problem in the MATLAS low-to-moderate density fields". In: *A&A* 686, A280. DOI: 10.1051/0004-6361/202348242.

Kanehisa, K. J., M. S. Pawlowski, & N. Libeskind (2025). "Andromeda's asymmetric satellite system as a challenge to cold dark matter cosmology". In: *Nature Astronomy* 9, 692–701. DOI: 10.1038/s41550-025-02480-3.

Kanehisa, K. J., M. S. Pawlowski, & O. Müller (2023a). "The imprint of galaxy mergers on satellite planes in a cosmological context". In: *MNRAS* 524, 952–967. DOI: 10.1093/mnras/stad1861.

Kanehisa, K. J., M. S. Pawlowski, O. Müller, & S. T. Sohn (2023b). "Classifying the satellite plane membership of Centaurus A's dwarf galaxies using orbital alignment constraints". In: *MNRAS* 519, 6184–6198. DOI: 10.1093/mnras/stad061.

Kaplinghat, M., S. Tulin, & H.-B. Yu (2016). "Dark Matter Halos as Particle Colliders: Unified Solution to Small-Scale Structure Puzzles from Dwarfs to Clusters". In: *Phys. Rev. Lett.* 116, 041302. DOI: 10.1103/PhysRevLett.116.041302.

Karachentsev, I. D. & P. Kroupa (2024). "A co-rotating gas and satellite structure around the interacting galaxy pair NGC 4490/85". In: *MNRAS* 528, 2805–2811. DOI: 10.1093/mnras/stae184.

Keller, B. W. & J. W. Wadsley (2017). "ΛCDM is Consistent with SPARC Radial Acceleration Relation". In: *ApJ* 835, L17. DOI: 10.3847/2041-8213/835/1/L17.

Kelley, T., J. S. Bullock, S. Garrison-Kimmel, et al. (2019). "Phat ELVIS: The inevitable effect of the Milky Way's disc on its dark matter subhaloes". In: *MNRAS* 487, 4409–4423. DOI: 10.1093/mnras/stz1553.

Kim, D., H. Jerjen, D. Mackey, G. S. D. Costa, & A. P. Milone (2015). "A hero's dark horse: discovery of an ultra-faint Milky Way satellite in Pegasus". In: *ApJ* 804, L44. DOI: 10.1088/2041-8205/804/2/L44.

Kim, S. Y., J. I. Read, M. P. Rey, et al. (2024). "EDGE: Predictable Scatter in the Stellar Mass-Halo Mass Relation of Dwarf Galaxies". In: *arXiv e-prints*. DOI: 10.48550/arXiv.2408.15214.

Kirby, E. N., J. G. Cohen, P. Guhathakurta, et al. (2013). "The Universal Stellar Mass-Stellar Metallicity Relation for Dwarf Galaxies". In: *ApJ* 779, 102. DOI: 10.1088/0004-637X/779/2/102.

Kirby, E. N., G. A. Lanfranchi, J. D. Simon, J. G. Cohen, & P. Guhathakurta (2011). "Multi-element Abundance Measurements from Medium-resolution Spectra. III. Metallicity Distributions of Milky Way Dwarf Satellite Galaxies". In: *ApJ* 727, 78. DOI: 10.1088/0004-637X/727/2/78.

Kirby, E. N., J. D. Simon, & J. G. Cohen (2015). "Spectroscopic Confirmation of the Dwarf Galaxies Hydra II and Pisces II and the Globular Cluster Laevens 1". In: *ApJ* 810, 56. DOI: 10.1088/0004-637X/810/1/56.

Klimentowski, J., E. L. Łokas, S. Kazantzidis, et al. (2007). "Mass modelling of dwarf spheroidal galaxies: the effect of unbound stars from tidal tails and the Milky Way". In: *MNRAS* 378, 353–368. DOI: 10.1111/j.1365-2966.2007.11799.x.

Klypin, A., A. V. Kravtsov, O. Valenzuela, & F. Prada (1999). "Where Are the Missing Galactic Satellites?" In: *ApJ* 522, 82–92. DOI: 10.1086/307643.

Koch, A. & E. K. Grebel (2006). "The Anisotropic Distribution of M31 Satellite Galaxies: A Polar Great Plane of Early-type Companions". In: *AJ* 131, 1405–1415. DOI: 10.1086/499534.

Koposov, S., V. Belokurov, N. W. Evans, et al. (2008). "The Luminosity Function of the Milky Way Satellites". In: *ApJ* 686, 279–291. DOI: 10.1086/589911.

Koposov, S. E., M. Irwin, V. Belokurov, et al. (2014). "Discovery of a cold stellar stream in the ATLAS DR1 data". In: *MNRAS: Letters* 442, L85–L89. DOI: 10.1093/mnrasl/slu060.

Koposov, S. E., V. Belokurov, G. Torrealba, & N. W. Evans (2015). "Beasts of the Southern Wild: Discovery of Nine Ultra Faint Satellites in the Vicinity of the Magellanic Clouds." In: *ApJ* 805, 130. DOI: 10.1088/0004-637X/805/2/130.

Kozhurina-Platais, V., D. Borncamp, J. Anderson, N. Grogin, & M. Hack (2015). *ACS/WFC Revised Geometric Distortion for DrizzlePac*.

Kroupa, P. (2001). "On the variation of the initial mass function". In: *MNRAS* 322, 231–246. DOI: 10.1046/j.1365-8711.2001.04022.x.

Kumar, P., M. S. Pawlowski, K. J. Kanehisa, et al. (2025). "The effect of measurement uncertainties on the inferred stability of planes of satellite galaxies". In: *A&A* 699, A363. DOI: 10.1051/0004-6361/202453087.

Kunkel, W. & S. Demers (1976). "The Magellanic Plane". In: *Greenwich Obs. Bull.* 241, 182.

Lee, M. G., I.-S. Yuk, H. S. Park, J. Harris, & D. Zaritsky (2009). "Star formation history and chemical evolution of the Sextans dwarf spheroidal galaxy". In: *ApJ* 703, 692. DOI: 10.1088/0004-637X/703/1/692.

Lelli, F., S. S. McGaugh, & J. M. Schombert (2016). "SPARC: Mass Models for 175 Disk Galaxies with Spitzer Photometry and Accurate Rotation Curves". In: *AJ* 152, 157. DOI: 10.3847/0004-6256/152/6/157.

Lelli, F., S. S. McGaugh, J. M. Schombert, & M. S. Pawlowski (2017). "One Law to Rule Them All: The Radial Acceleration Relation of Galaxies". In: *ApJ* 836, 152. DOI: 10.3847/1538-4357/836/2/152.

Li, H., F. Hammer, C. Babusiaux, et al. (2021). "Gaia EDR3 proper motions of Milky Way dwarfs. I. 3D motions and orbits". In: *ApJ* 916, 8. DOI: 10.3847/1538-4357/ac0436.
Li, J., J. E. Greene, S. Danieli, S. G. Carlsten, & M. Geha (2026). "A Possible "Too-many-satellites" Problem in the Isolated Dwarf Galaxy DDO 161". In: *ApJ* 998, L24. DOI: 10.3847/2041-8213/ae3ddd.
Li, P., F. Lelli, S. McGaugh, & J. Schombert (2018). "Fitting the radial acceleration relation to individual SPARC galaxies". In: *A&A* 615, A3. DOI: 10.1051/0004-6361/201732547.
Li, P., A. Liu, M. Kluge, et al. (2024). "Gas thermodynamics meets galaxy kinematics: Joint mass measurements for eROSITA galaxy clusters". In: *A&A* 692, A253. DOI: 10.1051/0004-6361/202451266.
Li, P., S. S. McGaugh, F. Lelli, et al. (2022). "The Effect of Adiabatic Compression on Dark Matter Halos and the Radial Acceleration Relation". In: *ApJ* 927, 198. DOI: 10.3847/1538-4357/ac52aa.
Li, P., Y. Tian, **M. P. Júlio, et al.** (2023). "Measuring galaxy cluster mass profiles into the low-acceleration regime with galaxy kinematics". In: *A&A* 677, A24. DOI: 10.1051/0004-6361/202346431.
Li, Y.-S. & A. Helmi (2008). "Infall of substructures on to a Milky Way-like dark halo". In: *MNRAS* 385, 1365–1373. DOI: 10.1111/j.1365-2966.2008.12854.x.
Libeskind, N. I., E. Carlesi, R. J. J. Grand, et al. (2020). "The Hestia project: simulations of the Local Group". In: *MNRAS* 498, 2968–2983. DOI: 10.1093/mnras/staa2541.
Libeskind, N. I., A. Knebe, Y. Hoffman, et al. (2011). "The preferred direction of infalling satellite galaxies in the Local Group". In: *MNRAS* 411, 1525–1535. DOI: 10.1111/j.1365-2966.2010.17786.x.
López-Cano, D., R. E. Angulo, A. D. Ludlow, et al. (2022). "The cosmology dependence of the concentration–mass–redshift relation". In: *MNRAS* 517, 2000–2011. DOI: 10.1093/mnras/stac2785.
Lovell, M. R., V. R. Eke, C. S. Frenk, & A. Jenkins (2011). "The link between galactic satellite orbits and subhalo accretion". In: *MNRAS* 413, 3013–3021. DOI: 10.1111/j.1365-2966.2011.18377.x.
Lovell, M. R., C. S. Frenk, V. R. Eke, et al. (2014). "The properties of warm dark matter haloes". In: *MNRAS* 439, 300–317. DOI: 10.1093/mnras/stt2431.
Ludlow, A. D., A. Benítez-Llambay, M. Schaller, et al. (2017). "Mass-Discrepancy Acceleration Relation: A Natural Outcome of Galaxy Formation in Cold Dark Matter Halos". In: *Phys. Rev. Lett.* 118, 161103. DOI: 10.1103/PhysRevLett.118.161103.
Lux, H., J. I. Read, & G. Lake (2010). "Determining orbits for the Milky Way's dwarfs". In: *MNRAS* 406, 2312–2324. DOI: 10.1111/j.1365-2966.2010.16877.x.
Lynden-Bell, D. (1976). "Dwarf galaxies and globular clusters in high velocity hydrogen streams". In: *MNRAS* 174, 695–710. DOI: 10.1093/mnras/174.3.695.
– (1982). "The Fornax-Leo-Sculptor system". In: *The Observatory* 102, 202–208.
Lynden-Bell, D. & R. M. Lynden-Bell (1995). "Ghostly streams from the formation of the Galaxy's halo". In: *MNRAS* 275, 429–442. DOI: 10.1093/mnras/275.2.429.
Mackey, A. D. & G. F. Gilmore (2004). "Comparing the properties of local globular cluster systems: implications for the formation of the Galactic halo". In: *MNRAS* 355, 504–534. DOI: 10.1111/j.1365-2966.2004.08343.x.
Majewski, S. R. (1994). "The Fornax-Leo-Sculptor Stream Revisited". In: *ApJ* 431, L17. DOI: 10.1086/187462.
Mamon, G. A. & E. L. Lokas (2005). "Dark matter in elliptical galaxies - I. Is the total mass density profile of the NFW form or even steeper?" In: *MNRAS* 362, 95–109. DOI: 10.1111/j.1365-2966.2005.09225.x.
Marchesini, D., E. D'Onghia, G. Chincarini, et al. (2002). "Hα Rotation Curves: The Soft Core Question". In: *ApJ* 575, 801–813. DOI: 10.1086/341475.
Martin, N. F., J. T. A. d. Jong, & H.-W. Rix (2008). "A Comprehensive Maximum Likelihood Analysis of the Structural Properties of Faint Milky Way Satellites". In: *ApJ* 684, 1075. DOI: 10.1086/590336.
Mateo, M., E. W. Olszewski, & M. G. Walker (2008). "The Velocity Dispersion Profile of the Remote Dwarf Spheroidal Galaxy Leo I: A Tidal Hit and Run?" In: *ApJ* 675, 201–233. DOI: 10.1086/522326.
Mateo, M. L. (1998). "Dwarf Galaxies of the Local Group". In: *A&A Rev.* 36, 435–506. DOI: 10.1146/annurev.astro.36.1.435.
Mayer, L., C. Mastropietro, J. Wadsley, J. Stadel, & B. Moore (2006). "Simultaneous ram pressure and tidal stripping; how dwarf spheroidals lost their gas". In: *MNRAS* 369, 1021–1038. DOI: 10.1111/j.1365-2966.2006.10403.x.
McConnachie, A. W. & M. J. Irwin (2006). "The satellite distribution of M31". In: *MNRAS* 365, 902–914. DOI: 10.1111/j.1365-2966.2005.09771.x.
McConnachie, A. W. (2012). "The Observed Properties of Dwarf Galaxies in and around the Local Group". In: *AJ* 144, 4. DOI: 10.1088/0004-6256/144/1/4.
McConnachie, A. W. & P. Côté (2010). "Revisiting the Influence of Unidentified Binaries on Velocity Dispersion Measurements in Ultra-faint Stellar Systems". In: *ApJ* 722, L209–L214. DOI: 10.1088/2041-8205/722/2/L209.
McGaugh, S. & M. Milgrom (2013). "Andromeda Dwarfs in Light of Modified Newtonian Dynamics". In: *ApJ* 766, 22. DOI: 10.1088/0004-637X/766/1/22.
McGaugh, S. S. (2004). "The Mass Discrepancy-Acceleration Relation: Disk Mass and the Dark Matter Distribution". In: *ApJ* 609, 652–666. DOI: 10.1086/421338.
– (2008). "Milky Way Mass Models and MOND". In: *ApJ* 683, 137. DOI: 10.1086/589148.
McGaugh, S. S., F. Lelli, & J. M. Schombert (2016). "Radial Acceleration Relation in Rotationally Supported Galaxies". In: *Phys. Rev. Lett.* 117, 201101. DOI: 10.1103/PhysRevLett.117.201101.
McGaugh, S. S., V. C. Rubin, & W. J. G. de Blok (2001). "High-Resolution Rotation Curves of Low Surface Brightness Galaxies. I. Data". In: *AJ* 122, 2381–2395. DOI: 10.1086/323448.
McMonigal, B., N. F. Bate, G. F. Lewis, et al. (2014). "Sailing under the Magellanic Clouds: a DECam view of the Carina dwarf". In: *MNRAS* 444, 3139–3149. DOI: 10.1093/mnras/stu1659.
Méndez, R. A., E. Costa, M. H. Pedreros, et al. (2010). "Proper Motions of Local Group Dwarf Spheroidal Galaxies I: First Ground-Based Results for Fornax". In: *PASP* 122, 853. DOI: 10.1086/655149.
Mercado, F. J., J. S. Bullock, J. Moreno, et al. (2024). "Hooks & Bends in the radial acceleration relation: discriminatory tests for dark matter and MOND". In: *MNRAS* 530, 1349–1362. DOI: 10.1093/mnras/stae819.

Merrifield, M. R. & S. M. Kent (1990). "Fourth Moments and the Dynamics of Spherical Systems". In: *AJ* 99, 1548. DOI: 10.1086/115438.

Metz, M., P. Kroupa, & H. Jerjen (2009a). "Discs of Satellites: the new dwarf spheroidals". In: *MNRAS* 394, 2223–2228. DOI: 10.1111/j.1365-2966.2009.14489.x.

Metz, M., P. Kroupa, C. Theis, G. Hensler, & H. Jerjen (2009b). "Did the Milky Way dwarf satellites enter the halo as a group?" In: *ApJ* 697, 269. DOI: 10.1088/0004-637X/697/1/269.

Milgrom, M. (1983). "A modification of the Newtonian dynamics as a possible alternative to the hidden mass hypothesis." In: *ApJ* 270, 365–370. DOI: 10.1086/161130.

Minor, Q. E., G. Martinez, J. Bullock, M. Kaplinghat, & R. Trainor (2010). "Correcting Velocity Dispersions of Dwarf Spheroidal Galaxies for Binary Orbital Motion". In: *ApJ* 721, 1142–1157. DOI: 10.1088/0004-637X/721/2/1142.

Mistele, T., S. McGaugh, F. Lelli, J. Schombert, & P. Li (2024). "Radial acceleration relation of galaxies with joint kinematic and weak-lensing data". In: *JCAP* 2024, 020. DOI: 10.1088/1475-7516/2024/04/020.

Moore, B., S. Ghigna, F. Governato, et al. (1999). "Dark Matter Substructure within Galactic Halos". In: *ApJ* 524, L19–L22. DOI: 10.1086/312287.

Moretti, M. I., M. Dall'Ora, V. Ripepi, et al. (2009). "The Leo IV Dwarf Spheroidal Galaxy: Color-Magnitude Diagram and Pulsating Stars". In: *ApJ* 699, L125–L129. DOI: 10.1088/0004-637X/699/2/L125.

Müller, O., B. Famaey, & H. Zhao (2019). "Predicted MOND velocity dispersions for a catalog of ultra-diffuse galaxies in group environments". In: *A&A* 623, A36. DOI: 10.1051/0004-6361/201834914.

Müller, O., H. Jerjen, M. S. Pawlowski, & B. Binggeli (2016). "Testing the two planes of satellites in the Centaurus group". In: *A&A* 595, A119. DOI: 10.1051/0004-6361/201629298.

Müller, O., M. S. Pawlowski, F. Lelli, et al. (2021). "The coherent motion of Cen A dwarf satellite galaxies remains a challenge for ΛCDM cosmology". In: *A&A* 645, L5. DOI: 10.1051/0004-6361/202039973.

Müller, O., M. S. Pawlowski, H. Jerjen, & F. Lelli (2018). "A whirling plane of satellite galaxies around Centaurus A challenges cold dark matter cosmology". In: *Science* 359, 534–537. DOI: 10.1126/science.aao1858.

Müller, O., M. S. Pawlowski, Y. Revaz, et al. (2024). "A too-many-dwarf-galaxy-satellites problem in the M 83 group". In: *A&A* 684, L6. DOI: 10.1051/0004-6361/202348969.

Muñoz, R. R., P. Côté, F. A. Santana, et al. (2018). "A MegaCam Survey of Outer Halo Satellites. III. Photometric and Structural Parameters". In: *ApJ* 860, 66. DOI: 10.3847/1538-4357/aac16b.

Muñoz, R. R., S. R. Majewski, & K. V. Johnston (2008). "Modeling the Structure and Dynamics of Dwarf Spheroidal Galaxies with Dark Matter and Tides". In: *ApJ* 679, 346–372. DOI: 10.1086/587125.

Mutlu-Pakdil, B., D. J. Sand, M. G. Walker, et al. (2019). "Signatures of Tidal Disruption in Ultra-faint Dwarf Galaxies: A Combined HST, Gaia, and MMT/Hectochelle Study of Leo V". In: *ApJ* 885, 53. DOI: 10.3847/1538-4357/ab45ec.

Natarajan, P. & H. Zhao (2008). "MOND plus classical neutrinos are not enough for cluster lensing". In: *MNRAS* 389, 250–256. DOI: 10.1111/j.1365-2966.2008.13552.x.

Navarro, J. F., V. R. Eke, & C. S. Frenk (1996a). "The cores of dwarf galaxy haloes". In: *MNRAS* 283, L72–L78. DOI: 10.1093/mnras/283.3.L72.

Navarro, J. F., C. S. Frenk, & S. D. M. White (1996b). "The Structure of Cold Dark Matter Halos". In: *ApJ* 462, 563. DOI: 10.1086/177173.

Neto, A. F., L. Gao, P. Bett, et al. (2007). "The statistics of ΛCDM halo concentrations". In: *MNRAS* 381, 1450–1462. DOI: 10.1111/j.1365-2966.2007.12381.x.

Newton, O., M. Cautun, A. Jenkins, C. S. Frenk, & J. C. Helly (2018). "The total satellite population of the Milky Way". In: *MNRAS* 479, 2853–2870. DOI: 10.1093/mnras/sty1085.

Nguyen, T., J. Read, L. Necib, et al. (2025). "Trial by FIRE: Probing the dark matter density profile of dwarf galaxies with GraphNPE". In: *MNRAS*. DOI: 10.1093/mnras/staf1118.

Nitschai, M. S., A.-C. Eilers, N. Neumayer, M. Cappellari, & H.-W. Rix (2021). "Dynamical Model of the Milky Way Using APOGEE and Gaia Data". In: *ApJ* 916, 112. DOI: 10.3847/1538-4357/ac04b5.

Olive, K. A., G. Steigman, & T. P. Walker (2000). "Primordial nucleosynthesis: theory and observations". In: *Physics Reports* 333, 389–407. DOI: 10.1016/S0370-1573(00)00031-4.

Orkney, M. D. A., J. I. Read, M. P. Rey, et al. (2021). "EDGE: two routes to dark matter core formation in ultra-faint dwarfs". In: *MNRAS* 504, 3509–3522. DOI: 10.1093/mnras/stab1066.

Orkney, M. D. A., E. Taylor, J. I. Read, et al. (2023). "EDGE: the shape of dark matter haloes in the faintest galaxies". In: *MNRAS* 525, 3516–3532. DOI: 10.1093/mnras/stad2516.

Ostriker, J. P., P. J. E. Peebles, & A. Yahil (1974). "The Size and Mass of Galaxies, and the Mass of the Universe". In: *ApJ* 193, L1. DOI: 10.1086/181617.

Pace, A. B., D. Erkal, & T. S. Li (2022). "Proper Motions, Orbits, and Tidal Influences of Milky Way Dwarf Spheroidal Galaxies". In: *ApJ* 940, 136. DOI: 10.3847/1538-4357/ac997b.

Pace, A. B. (2025). "The Local Volume Database: a library of the observed properties of nearby dwarf galaxies and star clusters". In: *Open J. Astrophys.* 8. DOI: 10.33232/001c.144859.

Pace, A. B. & T. S. Li (2019). "Proper Motions of Milky Way Ultra-faint Satellites with Gaia DR2 ×DES DR1". In: *ApJ* 875, 77. DOI: 10.3847/1538-4357/ab0aee.

Pascale, R., L. Posti, C. Nipoti, & J. Binney (2018). "Action-based dynamical models of dwarf spheroidal galaxies: application to Fornax". In: *MNRAS* 480, 927–946. DOI: 10.1093/mnras/sty1860.

Patel, E., N. Kallivayalil, N. Garavito-Camargo, et al. (2020). "The Orbital Histories of Magellanic Satellites Using Gaia DR2 Proper Motions". In: *ApJ* 893, 121. DOI: 10.3847/1538-4357/ab7b75.

Patton, D. R., C. J. Pritchet, R. G. Carlberg, et al. (2002). "Dynamically Close Galaxy Pairs and Merger Rate Evolution in the CNOC2 Redshift Survey". In: *ApJ* 565, 208–222. DOI: 10.1086/324543.

Pawlowski, M. S., J. Pflamm-Altenburg, & P. Kroupa (2012). "The VPOS: a vast polar structure of satellite galaxies, globular clusters and streams around the Milky Way". In: *MNRAS* 423, 1109–1126. DOI: 10.1111/j.1365-2966.2012.20937.x.

Pawlowski, M. S., J. S. Bullock, T. Kelley, & B. Famaey (2019). "Do halos that form early, have high concentration, are part of a pair, or contain a central galaxy potential host more pronounced planes of satellite galaxies?" In: *ApJ* 875, 105. DOI: 10.3847/1538-4357/ab10e0.

Pawlowski, M. S., B. Famaey, D. Merritt, & P. Kroupa (2015a). "On the persistence of two small-scale problems in ΛCDM". In: *ApJ* 815, 19. DOI: 10.1088/0004-637X/815/1/19.

Pawlowski, M. S. (2016). "The alignment of SDSS satellites with the VPOS: effects of the survey footprint shape". In: *MNRAS* 456, 448–458. DOI: 10.1093/mnras/stv2673.

– (2018). "The planes of satellite galaxies problem, suggested solutions, and open questions". In: *Mod. Phys. Lett. A* 33, 1830004. DOI: 10.1142/S0217732318300045.

– (2021a). "It's time for some plane speaking". In: *Nature Astronomy* 5, 1185–1187. DOI: 10.1038/s41550-021-01452-7.

– (2021b). "Phase-Space Correlations among Systems of Satellite Galaxies". In: *Galaxies* 9, 66. DOI: 10.3390/galaxies9030066.

Pawlowski, M. S., **M. P. Júlio**, K. J. Kanehisa, & O. Müller (2025). "Testing a proposed planarity tool for studying satellite systems: The alleged consistency of Milky Way satellite galaxy planes with ΛCDM". In: *A&A* 694, L4. DOI: 10.1051/0004-6361/202453428.

Pawlowski, M. S. & P. Kroupa (2014). "The Vast Polar Structure of the Milky Way Attains New Members". In: *ApJ* 790, 74. DOI: 10.1088/0004-637X/790/1/74.

– (2020). "The Milky Way's disc of classical satellite galaxies in light of Gaia DR2". In: *MNRAS* 491, 3042–3059. DOI: 10.1093/mnras/stz3163.

Pawlowski, M. S. & S. S. McGaugh (2014a). "Co-orbiting planes of sub-halos are similarly unlikely around paired and isolated hosts". In: *ApJ* 789, L24. DOI: 10.1088/2041-8205/789/1/L24.

– (2014b). "Perseus I and the NGC 3109 association in the context of the Local Group dwarf galaxy structures". In: *MNRAS* 440, 908–919. DOI: 10.1093/mnras/stu321.

Pawlowski, M. S., S. S. McGaugh, & H. Jerjen (2015b). "The new Milky Way satellites: alignment with the VPOS and predictions for proper motions and velocity dispersions". In: *MNRAS* 453, 1047–1061. DOI: 10.1093/mnras/stv1588.

Pawlowski, M. S., O. Müller, S. Taibi, et al. (2024). "The satellite galaxy plane of NGC 4490 in light of ΛCDM. Sparsity of similarly extreme analogs and a possible role of satellite pairs". In: *A&A* 688, A153. DOI: 10.1051/0004-6361/202449954.

Pawlowski, M. S., P.-A. Oria, S. Taibi, B. Famaey, & R. Ibata (2022). "On the Effect of the Large Magellanic Cloud on the Orbital Poles of Milky Way Satellite Galaxies". In: *ApJ* 932, 70. DOI: 10.3847/1538-4357/ac6ce0.

Pawlowski, M. S. & S. Tony Sohn (2021). "On the Co-orbitation of Satellite Galaxies along the Great Plane of Andromeda: NGC 147, NGC 185, and Expectations from Cosmological Simulations". In: *ApJ* 923, 42. DOI: 10.3847/1538-4357/ac2aa9.

Peacock, J. A., S. Cole, P. Norberg, et al. (2001). "A measurement of the cosmological mass density from clustering in the 2dF Galaxy Redshift Survey". In: *Nature* 410, 169–173. DOI: 10.1038/35065528.

Peebles, P. J. & B. Ratra (2003). "The cosmological constant and dark energy". In: *Rev. Mod. Phys.* 75, 559–606. DOI: 10.1103/RevModPhys.75.559.

Peebles, P. J. E. (1982). "Large-scale background temperature and mass fluctuations due to scale-invariant primeval perturbations". In: *ApJ* 263, L1–L5. DOI: 10.1086/183911.

Peñarrubia, J., A. Pontzen, M. G. Walker, & S. E. Koposov (2012). "The coupling between the core/cusp and missing satellite problems". In: *ApJ* 759, L42. DOI: 10.1088/2041-8205/759/2/l42.

Perlmutter, S., G. Aldering, G. Goldhaber, et al. (1999). "Measurements of Ω and Λ from 42 High-Redshift Supernovae". In: *ApJ* 517, 565–586. DOI: 10.1086/307221.

Petersen, M. S. & J. Peñarrubia (2020). "Reflex motion in the Milky Way stellar halo resulting from the Large Magellanic Cloud infall". In: *MNRAS* 494, L11–L16. DOI: 10.1093/mnrasl/slaa029.

Pianta, C., R. Capuzzo-Dolcetta, & G. Carraro (2022). "The Impact of Binaries on the Dynamical Mass Estimate of Dwarf Galaxies". In: *ApJ* 939, 3. DOI: 10.3847/1538-4357/ac9303.

Piatek, S., C. Pryor, & E. W. Olszewski (2016). "Proper motion of the Leo II dwarf galaxy based on Hubble Space Telescope imaging". In: *AJ* 152, 166. DOI: 10.3847/0004-6256/152/6/166.

Pietrzyński, G., M. Górski, W. Gieren, et al. (2009). "The ARAUCARIA Project. Infrared tip of the red giant branch distances to the Carina and Fornax dwarf spheroidal galaxies". In: *AJ* 138, 459. DOI: 10.1088/0004-6256/138/2/459.

Planck Collaboration (2020). "Planck 2018 results-VI. Cosmological parameters". In: *A&A* 641, A6. DOI: 10.1051/0004-6361/201833910.

Planck Collaboration, P. A. R. Ade, N. Aghanim, et al. (2014). "Planck 2013 results. XVI. Cosmological parameters". In: *A&A* 571, A16. DOI: 10.1051/0004-6361/201321591.

Planck Collaboration, P. A. R. Ade, N. Aghanim, et al. (2016). "Planck 2015 results. XIII. Cosmological parameters". In: *A&A* 594, A13. DOI: 10.1051/0004-6361/201525830.

Plummer, H. C. (1911). "On the Problem of Distribution in Globular Star Clusters: (Plate 8.)" In: *MNRAS* 71, 460–470. DOI: 10.1093/mnras/71.5.460.

Pontzen, A. & F. Governato (2012). "How supernova feedback turns dark matter cusps into cores". In: *MNRAS* 421, 3464–3471. DOI: 10.1111/j.1365-2966.2012.20571.x.

Posti, L. & A. Helmi (2019). "Mass and shape of the Milky Way's dark matter halo with globular clusters from Gaia and Hubble". In: *A&A* 621, A56. DOI: 10.1051/0004-6361/201833355.

Read, J. I. & D. Erkal (2019). "Abundance matching with the mean star formation rate: there is no missing satellites problem in the Milky Way above $M_{200} \sim 10^9\ M_\odot$". In: *MNRAS* 487, 5799–5812. DOI: 10.1093/mnras/stz1320.

Read, J. I. & G. Gilmore (2005). "Mass loss from dwarf spheroidal galaxies: the origins of shallow dark matter cores and exponential surface brightness profiles". In: *MNRAS* 356, 107–124. DOI: 10.1111/j.1365-2966.2004.08424.x.

Read, J. I. & P. Steger (2017). "How to break the density-anisotropy degeneracy in spherical stellar systems". In: *MNRAS* 471, 4541–4558. DOI: 10.1093/mnras/stx1798.

Read, J. I., M. G. Walker, & P. Steger (2018). "The case for a cold dark matter cusp in Draco". In: *MNRAS* 481, 860–877. DOI: 10.1093/mnras/sty2286.

– (2019). “Dark matter heats up in dwarf galaxies”. In: *MNRAS* 484, 1401–1420. DOI: 10.1093/mnras/sty3404.
Read, J. I., M. I. Wilkinson, N. W. Evans, G. Gilmore, & J. T. Kleyna (2006). “The importance of tides for the Local Group dwarf spheroidals”. In: *MNRAS* 367, 387–399. DOI: 10.1111/j.1365-2966.2005.09959.x.
Reguitti, A., P. Ochner, H. Addison, et al. (2025). “Padova-Asiago Transient Classification Report for 2025-05-14”. In: *Transient Name Server Classification Report* 2025-1785, 1.
Revaz, Y. & P. Jablonka (2018). “Pushing back the limits: detailed properties of dwarf galaxies in a ΛCDM universe”. In: *A&A* 616, A96. DOI: 10.1051/0004-6361/201832669.
Rey, M. P., A. Pontzen, O. Agertz, et al. (2020). “EDGE: from quiescent to gas-rich to star-forming low-mass dwarf galaxies”. In: *MNRAS* 497, 1508–1520. DOI: 10.1093/mnras/staa1640.
Rey, M. P., A. Pontzen, O. Agertz, et al. (2019). “EDGE: The Origin of Scatter in Ultra-faint Dwarf Stellar Masses and Surface Brightnesses”. In: *ApJ* 886, L3. DOI: 10.3847/2041-8213/ab53dd.
Rey, M. P., E. Taylor, E. I. Gray, et al. (2025). “EDGE: the emergence of dwarf galaxy scaling relations from cosmological radiation-hydrodynamics simulations”. In: *MNRAS* 541, 1195–1217. DOI: 10.1093/mnras/staf1058.
Richardson, T. & M. Fairbairn (2014). “On the dark matter profile in Sculptor: breaking the β degeneracy with Virial shape parameters”. In: *MNRAS* 441, 1584–1600. DOI: 10.1093/mnras/stu691.
Richstein, H., E. Patel, N. Kallivayalil, et al. (2022). “Structural Parameters and Possible Association of the Ultra-faint Dwarfs Pegasus III and Pisces II from Deep Hubble Space Telescope Photometry”. In: *ApJ* 933, 217. DOI: 10.3847/1538-4357/ac7226.
Riess, A. G., A. V. Filippenko, P. Challis, et al. (1998). “Observational evidence from supernovae for an accelerating universe and a cosmological constant”. In: *AJ* 116, 1009. DOI: 10.1086/300499.
Riley, A. H., A. Fattahi, A. B. Pace, et al. (2019). “The velocity anisotropy of the Milky Way satellite system”. In: *MNRAS* 486, 2679–2694. DOI: 10.1093/mnras/stz973.
Rubin, V. C., J. Ford W. K., & N. Thonnard (1980). “Rotational properties of 21 SC galaxies with a large range of luminosities and radii, from NGC 4605 (R=4kpc) to UGC 2885 (R=122kpc).” In: *ApJ* 238, 471–487. DOI: 10.1086/158003.
Sales, L. V., J. F. Navarro, A. P. Cooper, et al. (2011). “Clues to the ’Magellanic Galaxy’ from cosmological simulations”. In: *MNRAS* 418, 648–658. DOI: 10.1111/j.1365-2966.2011.19514.x.
Sales, L. V., W. Wang, S. D. M. White, & J. F. Navarro (2013). “Satellites and haloes of dwarf galaxies”. In: *MNRAS* 428, 573–578. DOI: 10.1093/mnras/sts054.
Sales, L. V., A. Wetzel, & A. Fattahi (2022). “Baryonic solutions and challenges for cosmological models of dwarf galaxies”. In: *Nature Astronomy* 6, 897–910. DOI: 10.1038/s41550-022-01689-w.
Samuel, J., A. Wetzel, S. Chapman, et al. (2021). “Planes of satellites around Milky Way/M31-mass galaxies in the FIRE simulations and comparisons with the Local Group”. In: *MNRAS* 504, 1379–1397. DOI: 10.1093/mnras/stab955.
Sand, D. J., K. Spekkens, D. Crnojević, et al. (2015). “Antlia B: A faint dwarf galaxy member of the NGC 3109 association”. In: *Astrophys. J. Lett.* 812, L13. DOI: 10.1088/2041-8205/812/1/L13.
Sarazin, C. L. (1986). “X-ray emission from clusters of galaxies”. In: *Rev. Mod. Phys.* 58, 1–115. DOI: 10.1103/RevModPhys.58.1.
Savino, A., D. R. Weisz, E. D. Skillman, et al. (2022). “The Hubble Space Telescope Survey of M31 Satellite Galaxies. I. RR Lyrae-based Distances and Refined 3D Geometric Structure”. In: *AJ* 938, 101. DOI: 10.3847/1538-4357/ac91cb.
Sawala, T., C. S. Frenk, A. Fattahi, et al. (2016). “The chosen few: the low-mass haloes that host faint galaxies”. In: *MNRAS* 456, 85–97. DOI: 10.1093/mnras/stv2597.
Schönrich, R., J. Binney, & W. Dehnen (2010). “Local kinematics and the local standard of rest”. In: *MNRAS* 403, 1829–1833. DOI: 10.1111/j.1365-2966.2010.16253.x.
Shao, S., M. Cautun, C. S. Frenk, et al. (2018). “The multiplicity and anisotropy of galactic satellite accretion”. In: *MNRAS* 476, 1796–1810. DOI: 10.1093/mnras/sty343.
Shapley, H. (1938). “A Stellar System of a New Type”. In: *Harvard College Observatory Bulletin* 908, 1–11.
Simon, J. D. (2018). “Gaia Proper Motions and Orbits of the Ultra-faint Milky Way Satellites”. In: *ApJ* 863, 89. DOI: 10.3847/1538-4357/aacdfb.
– (2019). “The Faintest Dwarf Galaxies”. In: *A&A Rev.* 57, 375–415. DOI: 10.1146/annurev-astro-091918-104453.
Skillman, E. D., M. Monelli, D. R. Weisz, et al. (2017). “The ISLAndS Project. II. The Lifetime Star Formation Histories of Six Andomeda dSphS”. In: *ApJ* 837, 102. DOI: 10.3847/1538-4357/aa60c5.
Skordis, C. & T. Złośnik (2021). “New Relativistic Theory for Modified Newtonian Dynamics”. In: *Phys. Rev. Lett.* 127, 161302. DOI: 10.1103/PhysRevLett.127.161302.
Smith, R., P. A. Duc, F. Bournaud, & S. K. Yi (2016). “A Formation Scenario for the Disk of Satellites: Accretion of Satellites during Mergers”. In: *ApJ* 818, 11. DOI: 10.3847/0004-637X/818/1/11.
Smith, S. E. T., W. Cerny, C. R. Hayes, et al. (2024). “The Discovery of the Faintest Known Milky Way Satellite Using UNIONS”. In: *ApJ* 961, 92. DOI: 10.3847/1538-4357/ad0d9f.
Sohn, S. T., J. Anderson, & R. P. van der Marel (2012). “The M31 Velocity Vector. I. Hubble Space Telescope Proper-motion Measurements”. In: *ApJ* 753, 7. DOI: 10.1088/0004-637X/753/1/7.
Sohn, S. T., E. Patel, M. A. Fardal, et al. (2020). “HST Proper Motions of NGC 147 and NGC 185: Orbital Histories and Tests of a Dynamically Coherent Andromeda Satellite Plane”. In: *ApJ* 901, 43. DOI: 10.3847/1538-4357/abaf49.
Somerville, R. S. (2002). “Can Photoionization Squelching Resolve the Substructure Crisis?” In: *ApJ* 572, L23–L26. DOI: 10.1086/341444.
Spencer, M. E., M. Mateo, E. W. Olszewski, et al. (2018). “The Binary Fraction of Stars in Dwarf Galaxies: The Cases of Draco and Ursa Minor”. In: *AJ* 156, 257. DOI: 10.3847/1538-3881/aae3e4.
Spencer, M. E., M. Mateo, M. G. Walker, & E. W. Olszewski (2017a). “A Multi-epoch Kinematic Study of the Remote Dwarf Spheroidal Galaxy Leo II*”. In: *ApJ* 836, 202. DOI: 10.3847/1538-4357/836/2/202.
Spencer, M. E., M. Mateo, M. G. Walker, et al. (2017b). “The Binary Fraction of Stars in Dwarf Galaxies: The Case of Leo II”. In: *AJ* 153, 254. DOI: 10.3847/1538-3881/aa6d51.

Spergel, D. N., L. Verde, H. V. Peiris, et al. (2003). "First-year Wilkinson Microwave Anisotropy Probe (WMAP)* observations: determination of cosmological parameters". In: *ApJS* 148, 175. DOI: 10.1086/377226.
Springel, V., J. Wang, M. Vogelsberger, et al. (2008). "The Aquarius Project: the subhaloes of galactic haloes". In: *MNRAS* 391, 1685–1711. DOI: 10.1111/j.1365-2966.2008.14066.x.
Springel, V. (2010). "E pur si muove: Galilean-invariant cosmological hydrodynamical simulations on a moving mesh". In: *MNRAS* 401, 791–851. DOI: 10.1111/j.1365-2966.2009.15715.x.
Springel, V., C. S. Frenk, & S. D. M. White (2006). "The large-scale structure of the Universe". In: *Nature* 440, 1137–1144. DOI: 10.1038/nature04805.
Stierwalt, S., S. E. Liss, K. E. Johnson, et al. (2017). "Direct evidence of hierarchical assembly at low masses from isolated dwarf galaxy groups". In: *Nature Astronomy* 1, 0025. DOI: 10.1038/s41550-016-0025.
Strigari, L. E. (2018). "Dark matter in dwarf spheroidal galaxies and indirect detection: a review". In: *Rep. Prog. Phys.* 81, 056901. DOI: 10.1088/1361-6633/aaae16.
Taibi, S., M. S. Pawlowski, S. Khoperskov, M. Steinmetz, & N. I. Libeskind (2024). "A portrait of the vast polar structure as a young phenomenon: Hints from its member satellites". In: *A&A* 681, A73. DOI: 10.1051/0004-6361/202347473.
Taibi, S., M. S. Pawlowski, O. Müller, et al. (2025). "An LBT view of the co-rotating group of galaxies around NGC 2750: Deep imaging and new satellite candidates". In: *A&A* 699, A285. DOI: 10.1051/0004-6361/202554365.
Tegmark, M., M. R. Blanton, M. A. Strauss, et al. (2004). "The three-dimensional power spectrum of galaxies from the sloan digital sky survey". In: *ApJ* 606, 702. DOI: 10.1086/382125.
Tenneti, A., Y.-Y. Mao, R. A. C. Croft, et al. (2018). "The radial acceleration relation in disc galaxies in the MassiveBlack-II simulation". In: *MNRAS* 474, 3125–3132. DOI: 10.1093/mnras/stx3010.
Teyssier, R. (2002). "Cosmological hydrodynamics with adaptive mesh refinement-A new high resolution code called RAMSES". In: *A&A* 385, 337–364. DOI: 10.1051/0004-6361:20011817.
Tian, Y., C.-M. Ko, P. Li, S. McGaugh, & S. L. Poblete (2024). "A distinct radial acceleration relation across the brightest cluster galaxies and galaxy clusters". In: *A&A* 684, A180. DOI: 10.1051/0004-6361/202347868.
Tian, Y., K. Umetsu, C.-M. Ko, M. Donahue, & I.-N. Chiu (2020). "The Radial Acceleration Relation in CLASH Galaxy Clusters". In: *ApJ* 896, 70. DOI: 10.3847/1538-4357/ab8e3d.
Tolstoy, E., V. Hill, & M. Tosi (2009). "Star-Formation Histories, Abundances, and Kinematics of Dwarf Galaxies in the Local Group". In: *A&A Rev.* 47, 371–425. DOI: 10.1146/annurev-astro-082708-101650.
Torrealba, G., S. E. Koposov, V. Belokurov, & M. Irwin (2016). "The feeble giant. Discovery of a large and diffuse Milky Way dwarf galaxy in the constellation of Crater". In: *MNRAS* 459, 2370–2378. DOI: 10.1093/mnras/stw733.
Tully, R. B. & J. R. Fisher (1977). "A new method of determining distances to galaxies." In: *A&A* 54, 661–673.
Tully, R. B., N. I. Libeskind, I. D. Karachentsev, et al. (2015). "Two Planes of Satellites in the Centaurus A Group". In: *ApJ* 802, L25. DOI: 10.1088/2041-8205/802/2/L25.
Tully, R. B., L. Rizzi, A. E. Dolphin, et al. (2006). "Associations of Dwarf Galaxies". In: *AJ* 132, 729. DOI: 10.1086/505466.
Tully, R. B., R. S. Somerville, N. Trentham, & M. A. W. Verheijen (2002). "Squelched Galaxies and Dark Halos". In: *ApJ* 569, 573. DOI: 10.1086/339425.
Tyson, J. A., F. Valdes, & R. A. Wenk (1990). "Detection of Systematic Gravitational Lens Galaxy Image Alignments: Mapping Dark Matter in Galaxy Clusters". In: *ApJ* 349, L1. DOI: 10.1086/185636.
van den Bergh, S. (1998). "The Binary Galaxies NGC 147 and NGC 185". In: *AJ* 116, 1688–1689. DOI: 10.1086/300576.
– (2006). "Globular Clusters in Dwarf Galaxies". In: *AJ* 131, 304–311. DOI: 10.1086/498688.
van der Marel, R. P. (1994). "Velocity profiles of galaxies with claimed black holes - III. Observations and models for M87". In: *MNRAS* 270, 271–297. DOI: 10.1093/mnras/270.2.271.
Vărăşteanu, A. A., M. J. Jarvis, A. A. Ponomareva, et al. (2025). "MIGHTEE-HI: the radial acceleration relation with resolved stellar mass measurements". In: *MNRAS* 541, 2366–2392. DOI: 10.1093/mnras/staf1079.
Vasiliev, E. (2019). *Agama reference documentation*. DOI: 10.48550/arXiv.1802.08255.
– (2023). "The effect of the LMC on the Milky Way system". In: *Galaxies* 11, 59. DOI: 10.3390/galaxies11020059.
Vasiliev, E., V. Belokurov, & D. Erkal (2021). "Tango for three: Sagittarius, LMC, and the Milky Way". In: *MNRAS* 501, 2279–2304. DOI: 10.1093/mnras/staa3673.
Vaz, D., J. Brinchmann, S. Kamann, et al. (2026). "The MUSE-Faint survey - V. The binary fraction of Leo T". In: *A&A* 708, A101. DOI: 10.1051/0004-6361/202555752.
Vaz, D., J. Brinchmann, S. L. Zoutendijk, et al. (2023). "The MUSE-Faint survey. IV. Dissecting Leo T, a gas-rich relic with recent star formation". In: *A&A* 678, A59. DOI: 10.1051/0004-6361/202346453.
Venn, K. A., M. Irwin, M. D. Shetrone, et al. (2004). "Stellar Chemical Signatures and Hierarchical Galaxy Formation". In: *AJ* 128, 1177–1195. DOI: 10.1086/422734.
Virtanen, P., R. Gommers, T. E. Oliphant, et al. (2020). "SciPy 1.0: Fundamental Algorithms for Scientific Computing in Python". In: *Nature Methods* 17, 261–272. DOI: 10.1038/s41592-019-0686-2.
Vitral, E., R. P. van der Marel, S. T. Sohn, et al. (2024). "HSTPROMO Internal Proper-motion Kinematics of Dwarf Spheroidal Galaxies. I. Velocity Anisotropy and Dark Matter Cusp Slope of Draco". In: *ApJ* 970, 1. DOI: 10.3847/1538-4357/ad571c.
Vitral, E., R. P. van der Marel, S. T. Sohn, et al. (2026). "HSTPROMO Internal Proper-motion Kinematics of Dwarf Spheroidal Galaxies. II. Velocity Anisotropy and Dark Matter Cusp Slope of Sculptor". In: *ApJ* 998, 206. DOI: 10.3847/1538-4357/ae1f8a.
Vivas, A. K., A. R. Walker, C. E. Martínez-Vázquez, et al. (2020). "A DECam view of the diffuse dwarf galaxy Crater II - Variable stars". In: *MNRAS* 492, 1061–1077. DOI: 10.1093/mnras/stz3393.
Vogelsberger, M., J. Zavala, C. Simpson, & A. Jenkins (2014). "Dwarf galaxies in CDM and SIDM with baryons: observational probes of the nature of dark matter". In: *MNRAS* 444, 3684–3698. DOI: 10.1093/mnras/stu1713.
Von Humboldt, A. (1859). *Cosmos: a sketch of a physical description of the universe*. Vol. 5. Harper.
Wagoner, R. V., W. A. Fowler, & F. Hoyle (1967). "On the Synthesis of Elements at Very High Temperatures". In: *ApJ* 148, 3. DOI: 10.1086/149126.

Walker, A. R., C. E. Martínez-Vázquez, M. Monelli, et al. (2019). "A DECam view of the diffuse dwarf galaxy Crater II: the colour-magnitude diagram". In: *MNRAS* 490, 4121–4132. DOI: 10.1093/mnras/stz2826.

Walker, M. G., M. Mateo, & E. W. Olszewski (2009a). "Stellar Velocities in the Carina, Fornax, Sculptor, and Sextans dSph Galaxies: Data From the Magellan/MMFS Survey". In: *AJ* 137, 3100–3108. DOI: 10.1088/0004-6256/137/2/3100.

Walker, M. G., M. Mateo, E. W. Olszewski, et al. (2006). "Internal Kinematics of the Fornax Dwarf Spheroidal Galaxy". In: *AJ* 131, 2114–2139. DOI: 10.1086/500193.

Walker, M. G., M. Mateo, E. W. Olszewski, et al. (2009b). "A Universal Mass Profile for Dwarf Spheroidal Galaxies?" In: *ApJ* 704, 1274–1287. DOI: 10.1088/0004-637X/704/2/1274.

Walker, M. G. & J. Peñarrubia (2011). "A Method for Measuring (Slopes of) the Mass Profiles of Dwarf Spheroidal Galaxies". In: *ApJ* 742, 20. DOI: 10.1088/0004-637X/742/1/20.

Wang, J., C. S. Frenk, & A. P. Cooper (2013). "The spatial distribution of galactic satellites in the Λ cold dark matter cosmology". In: *MNRAS* 429, 1502–1513. DOI: 10.1093/mnras/sts442.

Wang, L., A. A. Dutton, G. S. Stinson, et al. (2015). "NIHAO project - I. Reproducing the inefficiency of galaxy formation across cosmic time with a large sample of cosmological hydrodynamical simulations". In: *MNRAS* 454, 83–94. DOI: 10.1093/mnras/stv1937.

Wang, W., L. Zhu, Y. Jing, et al. (2023). "Unraveling the Complexity of Dwarf Galaxy Dynamics: A Study of Binary Orbital Motions". In: *ApJ* 956, 91. DOI: 10.3847/1538-4357/acf314.

Watkins, L. L., N. W. Evans, & J. H. An (2010). "The masses of the Milky Way and Andromeda galaxies". In: *MNRAS* 406, 264–278. DOI: 10.1111/j.1365-2966.2010.16708.x.

Weinberg, S. (1989). "The cosmological constant problem". In: *Rev. Mod. Phys.* 61, 1–23. DOI: 10.1103/RevModPhys.61.1.

Weisz, D. R., A. E. Dolphin, E. D. Skillman, et al. (2014a). "The star formation histories of Local Group dwarf galaxies. I. Hubble Space Telescope/Wide Field Planetary Camera 2 observations*". In: *ApJ* 789, 147. DOI: 10.1088/0004-637X/789/2/147.

Weisz, D. R., S. E. Koposov, A. E. Dolphin, et al. (2016). "A Hubble Space Telescope Study of the Enigmatic Milky Way Halo Globular Cluster Crater*". In: *ApJ* 822, 32. DOI: 10.3847/0004-637X/822/1/32.

Weisz, D. R., E. D. Skillman, S. L. Hidalgo, et al. (2014b). "Comparing M31 and Milky Way Satellites: The Extended Star Formation Histories of Andromeda II and Andromeda XVI". In: *ApJ* 789, 24. DOI: 10.1088/0004-637X/789/1/24.

Wetzel, A. R., A. J. Deason, & S. Garrison-Kimmel (2015). "Satellite Dwarf Galaxies in a Hierarchical Universe: Infall Histories, Group Preprocessing, and Reionization". In: *ApJ* 807, 49. DOI: 10.1088/0004-637X/807/1/49.

Wheeler, C., J. O. orbe, J. S. Bullock, et al. (2015). "Sweating the small stuff: simulating dwarf galaxies, ultra-faint dwarf galaxies, and their own tiny satellites". In: *MNRAS* 453, 1305–1316. DOI: 10.1093/mnras/stv1691.

White, S. D. M. & M. J. Rees (1978). "Core condensation in heavy halos: a two-stage theory for galaxy formation and clustering." In: *MNRAS* 183, 341–358. DOI: 10.1093/mnras/183.3.341.

Willman, B., M. R. Blanton, A. A. West, et al. (2005). "A New Milky Way Companion: Unusual Globular Cluster or Extreme Dwarf Satellite?" In: *AJ* 129, 2692–2700. DOI: 10.1086/430214.

Wolf, J., G. D. Martinez, J. S. Bullock, et al. (2010). "Accurate masses for dispersion-supported galaxies". In: *MNRAS* 406, 1220–1237. DOI: 10.1111/j.1365-2966.2010.16753.x.

Yan, Z., A. H. Wright, N. E. Chisari, et al. (2025). "KiDS-Legacy: Angular galaxy clustering from deep surveys with complex selection effects". en. In: *A&A* 694, A259. DOI: 10.1051/0004-6361/202452808.

Zhao, H. (1996). "Analytical models for galactic nuclei". In: *MNRAS* 278, 488–496. DOI: 10.1093/mnras/278.2.488.

Zoutendijk, S. L., J. Brinchmann, L. A. Boogaard, et al. (2020). "The MUSE-Faint survey. I. Spectroscopic evidence for a star cluster in Eridanus 2 and constraints on MACHOs as a constituent of dark matter". In: *A&A* 635, A107. DOI: 10.1051/0004-6361/201936155.

Zoutendijk, S. L., J. Brinchmann, N. F. Bouché, et al. (2021a). "The MUSE-Faint survey. II. The dark-matter density profile of the ultra-faint dwarf galaxy Eridanus 2". In: *A&A* 651, A80. DOI: 10.1051/0004-6361/202040239.

Zoutendijk, S. L., **M. P. Júlio**, J. Brinchmann, et al. (2021b). "The MUSE-Faint survey. III. No large dark-matter cores and no significant tidal stripping in ultra-faint dwarf galaxies". In: *arXiv e-prints*. DOI: arXiv:2112.09374.

Zucker, D. B., V. Belokurov, N. W. Evans, et al. (2006). "A Curious Milky Way Satellite in Ursa Major". In: *ApJ* 650, L41–L44. DOI: 10.1086/508628.

Zwicky, F. (1933). "Die Rotverschiebung von extragalaktischen Nebeln". In: *Helvetica Physica Acta* 6, 110–127.

List of publications

Articles included in this dissertation:

1. **M. P. Júlio**, M. S. Pawlowski, S. Tony Sohn, S. Taibi, R. P. van der Marel, & S. S. McGaugh (July 2024). "Satellite group infall into the Milky Way: Exploring the Crater-Leo case with new HST proper motions". In: *A&A* 687, A212. DOI: 10.1051/0004-6361/202449985. (Chapter 2)

   Presents new HST proper motions for Leo IV and Leo V, uncovering kinematic evidence that the Crater–Leo objects were accreted as part of a common infalling group into the Milky Way halo.

2. **M. P. Júlio**, M. S. Pawlowski, & N. I. Libeskind. "Spatial and kinematic signatures of satellite pairs in the Local Group". To be submitted. (Chapter 3)

   Investigates the incidence and physical nature of satellite galaxy pairs in the Local Group, showing that the excess of close associations around the Milky Way is likely driven by recent group accretion, while the M31 satellite population remains broadly consistent with ΛCDM expectations from cosmological simulations.

3. **M. P. Júlio**, J. I. Read, M. S. Pawlowski, P. Li, D. Vaz, J. Brinchmann, M. P. Rey, O. Agertz, & T. Holmes (Dec. 2025b). "The radial acceleration relation at the EDGE of galaxy formation: Testing its universality in low-mass dwarf galaxies". In: *A&A* 704, A330. DOI: 10.1051/0004-6361/202557106. (Chapter 4)

   Provides the first radially resolved measurements of the radial acceleration relation in ultra-faint dwarf galaxies, demonstrating that its universality breaks down in the low-acceleration regime.

Letters and articles not included in this dissertation:

1. D. Vaz, J. Brinchmann, S. Kamann, S. Saracino, P. A. C. Cunha, & **M. P. Júlio** (Apr. 2026). "The MUSE-Faint survey - V. The binary fraction of Leo T". in: *A&A* 708, A101. DOI: 10.1051/0004-6361/202555752.

   Reviewed the draft and contributed to discussions of the results and presentation.

2. A. Bañares-Hernández, J. I. Read, & **M. P. Júlio** (Jan. 2026). "GravSphere2: A higher order Jeans method for mass modeling spherical stellar systems". In: *A&A* 705, A212. DOI: 10.1051/0004-6361/202557195.

   Co-developed GravSphere from its earliest versions, contributed to methodology and presentation of results; tested and validated the code prior to submission, and continue to provide improvements to the code.

3. P. Kumar, M. S. Pawlowski, K. J. Kanehisa, P. Li, **M. P. Júlio**, & S. Taibi (July 2025). "The effect of measurement uncertainties on the inferred stability of planes of satellite galaxies". In: *A&A* 699, A363. DOI: 10.1051/0004-6361/202453087.

   Contributed to discussions and conceptual development of the project and provided final feedback on the paper.

4. S. Taibi, M. S. Pawlowski, O. Müller, M. Bílek, **M. P. Júlio**, K. J. Kanehisa, M. Jovanović, A. Lalović, & S. Samurović (July 2025). "An LBT view of the co-rotating group of galaxies around NGC 2750: Deep imaging and new satellite candidates". In: *A&A* 699, A285. DOI: 10.1051/0004-6361/202554365.

   Reviewed the draft and contributed to discussions of the results and presentation.

5. M. S. Pawlowski, **M. P. Júlio**, K. J. Kanehisa, & O. Müller (Feb. 2025). "Testing a proposed planarity tool for studying satellite systems: The alleged consistency of Milky Way satellite galaxy planes with ΛCDM". in: *A&A* 694, L4. DOI: 10.1051/0004-6361/202453428.

   Performed the analysis in Appendix A, generated the associated figures, and co-authored the text.

6. P. Li, A. Liu, M. Kluge, J. Comparat, Y. Tian, **M. P. Júlio**, M. S. Pawlowski, J. Sanders, E. Bulbul, A. Schwope, V. Ghirardini, X. Zhang, Y. Emre Bahar, M. E. Ramos-Ceja, F. Balzer, & C. Garrel (Dec. 2024). "Gas thermodynamics meets galaxy kinematics: Joint mass measurements for eROSITA galaxy clusters". In: *A&A* 692, A253. DOI: 10.1051/0004-6361/202451266.

   Provided guidance on the mass modelling method GravSphere and its implementation.

7. M. S. Pawlowski, O. Müller, S. Taibi, **M. P. Júlio**, K. J. Kanehisa, & N. Heesters (Aug. 2024). "The satellite galaxy plane of NGC 4490 in light of ΛCDM. Sparsity of similarly extreme analogs and a possible role of satellite pairs". In: *A&A* 688, A153. DOI: 10.1051/0004-6361/202449954.

   Performed the calculations for Section 2.1, wrote the corresponding text, and provided final feedback on the paper.

8. **M. P. Júlio**, J. Brinchmann, S. L. Zoutendijk, J. I. Read, D. Vaz, S. Kamann, D. Krajnović, L. A. Boogaard, M. Steinmetz, & N. Bouché (Oct. 2023). "The MUSE-Faint survey. III. Constraining scalar field dark matter with Antlia B". in: *A&A* 678, A38. DOI: 10.1051/0004-6361/202346987.

Led the dynamical modelling and analysis, including modifications to the GravSphere code to implement alternative dark matter profiles, and wrote the manuscript. Combines MUSE-Faint spectroscopy of the dwarf galaxy Antlia B with dynamical modelling to place new constraints on the scalar-field dark matter model.

9. P. Li, Y. Tian, **M. P. Júlio**, M. S. Pawlowski, F. Lelli, S. S. McGaugh, J. M. Schombert, J. I. Read, P.-C. Yu, & C.-M. Ko (Sept. 2023). "Measuring galaxy cluster mass profiles into the low-acceleration regime with galaxy kinematics". In: *A&A* 677, A24. DOI: 10.1051/0004-6361/202346431.

   Trained the first author in the use and implementation of the mass-modelling method GravSphere.

10. S. L. Zoutendijk, **M. P. Júlio**, J. Brinchmann, J. I. Read, D. Vaz, L. A. Boogaard, N. F. Bouché, D. Krajnović, K. Kuijken, J. Schaye, & M. Steinmetz (Dec. 2021b). "The MUSE-Faint survey. III. No large dark-matter cores and no significant tidal stripping in ultra-faint dwarf galaxies". In: *arXiv e-prints*. DOI: arXiv:2112.09374.

    Conducted the analysis with GravSphere in Appendices A and B, co-produced Figures A.1–A.3 and B.4–B.13, and co-wrote the text.

Proceedings:

1. A. Reguitti, P. Ochner, H. Addison, M. Valentini, B. Bandi, **M. P. Júlio**, A. Galkin, M. Cunningham, S. Philipsborn, & H. Mendez-Hernandez (May 2025). "Padova-Asiago Transient Classification Report for 2025-05-14". In: *Transient Name Server Classification Report* 2025-1785, 1.

2. **M. P. Júlio**, J. Brinchmann, J. I. Read, & M. Collaboration (Jan. 2025a). "The Dark Matter Density Profiles of Antlia B". in: *Dynamical Masses of Local Group Galaxies*. Vol. 379. IAU Symposium, 147–153. DOI: 10.1017/S1743921323001473.

3. **M. P. Júlio** & M. S. Pawlowski (July 2023). "Exploring satellite group infall in the Milky Way: the case of the Crater-Leo objects". In: *EAS2023, European Astronomical Society Annual Meeting*, 2121.

4. **M. P. Júlio** (July 2023). "The Dark Matter Density Profiles of Antlia B". in: *EAS2023, European Astronomical Society Annual Meeting*, 1863.

Press releases & media coverage:

- Decades-old dark matter debate narrows thanks to dwarf galaxies. *Leibniz Institute for Astrophysics Potsdam.* 27 October 2025
- Decades-old dark matter debate narrows as smallest galaxies reveal hidden forces at work. *University of Surrey.* 27 October 2025
- Dwarf galaxies tip the scales in favor of dark matter over modified gravity. *Phys.org*. 27 October 2025
- Dwarf Galaxies May Hold the Answers to the Debate on Dark Matter. *Universe Today.* 09 November 2025

Acknowledgements

Doing a PhD is not easy, and I will always be immensely grateful to all the people who supported me throughout this journey, in one way or another.

First and foremost, I would like to thank my supervisor, Marcel, for his constant guidance, support, and encouragement. Working with you has been a privilege, and your support made both this thesis and my development as a researcher possible. Thank you for always being there to answer my questions (and for teaching me how to ask them), for providing me with the resources and opportunities to succeed, and for believing in me even when I doubted myself. I am truly thankful for your mentorship and for the positive impact you had on my academic and personal growth. Thank you for helping me believe in myself and for being such an incredible supervisor.

A good team makes all the difference, and I was lucky to be surrounded by one. To Jamie, Salvatore, and Pengfei: it has been a pleasure working with you. Your ideas, discussions, and enthusiasm made this process not only productive but also enjoyable. I learned a lot from all of you. I would also like to thank to everyone in my group, Dwarf Galaxies and the Galactic Halo, and our neighbouring group, Milky Way and the Local Volume, for the research environment and support throughout these years.

I would also like to acknowledge my co-authors and collaborators. To Andrés, Bas, Daniel, Jarle, Justin, Nick, Noam, Oliver, and Tony: thank you for your valuable insights and thoughtful feedback, which significantly improved the quality of this work. It has been a privilege to collaborate with such inspiring people. A special thanks to Nick and Oliver for their friendship throughout these years, and for making one of my dreams come true by allowing me to observe in Chile. Nick, even when everything seemed determined to work against us getting decent data, you somehow managed to keep it fun. A special thanks also to Bas, who always had time to give me advice and support since my Bachelor days, and for providing the template for this thesis.

To my PhD sister, Léna: thank you for being there from the very beginning and for sharing this journey with me. It wasn't easy (and at times it was really hard), but you were always there, for the good parts and the super challenging ones. Together with Abinaya, Azlizan, Léa and Desmond, thank you for the laughter, the support, and the many wonderful meals, movies, crafts, and game nights that made even the coldest and darkest German winter feel more bearable. Anna, Elena, and Samir, I am very grateful to have had you by my side throughout this time. Özgün, you were a great sidekick in our student representative adventure. All of you made me feel at home in a place where I often felt it wasn't mine.

To Šárka, and all my other friends from the FLINTA* Bookshelf Collective — Julia, Marie, Niranjana, Patty, and Sonali: thank you for giving me a community, for reminding me how much I love books (and feminism), and for letting me contribute to something meaningful while being far from where I used to.

To my friends back from Portugal — those who stayed and those who moved — André, Andreia, Artur, Carolina, Bernardo, Fabrizio, Mário, and Rodrigo: thank you for your constant encouragement, for visiting me wherever I ended up, and for always making me feel at home when I returned. Your support, even from afar, meant more than I can express.

To momor, Nuno: this would not have been possible without you. I moved to another country to follow my dreams, and you made sure they came true. You supported me in every possible and imaginable way, even when you were not physically here. Thank you for being my home wherever we were and for sharing this adventure with me. Thank you for making my life easier when everything else felt impossible, for being my number one fan, and for always believing in me. Thank you for all the discussions, for taking the time to learn so many concepts and ideas from a completely different field just to help me, and for asking so many questions that helped me learn how to explain things better. Thank you for sharing your knowledge with me, because now I know a bit more about coding (and food). I am so grateful to have you by my side. És o melhor de todos os mundos.

To my siblings, Francisco and Madalena: watching you grow up from afar was one of the hardest things I have ever done (even harder than writing this thesis). I was your big sister before being anything else, and being far away from you was never easy. I am incredibly proud of you and deeply

grateful for your love and support. I missed you so much over these years, and I am so thankful for all your visits. Without you, I would not have been where I am now. And to Milky, our dog named after our galaxy, I missed you and your barks more than you will ever know.

Para os meus pais, em português, para que possam ler e perceber alguma coisa desta tese: obrigada por acreditarem em mim desde o início, por me encorajarem sempre a seguir os meus sonhos — mesmo quando eram difíceis, e mesmo quando mais ninguém achava possível. Se cheguei até aqui, foi porque vocês acreditaram primeiro, e nunca deixaram de o fazer. Obrigada por me deixarem seguir o meu caminho, mesmo que isso implicasse estar longe.

E para o resto da família — avós, tios e primos — obrigada por torcerem sempre por mim. Foi um privilégio levar-vos comigo em todas as minhas aventuras e partilhar um bocadinho de cada uma delas convosco ao longo destes anos.

This thesis is dedicated to all of you, and to all girls, women and queer people who sometimes feel like they do not belong in science or have been made feel like they could not. I did it, and we can. I hope this thesis can be a reminder that there is space for us here too.